Measurement of f_{LT}, f_{TT} and $f_{LT'}$ Response Functions in the Quasi-elastic $^2H(\vec{e}, e'p)$ Reaction at 200 (MeV/c) Missing Momentum

by

Shiao-Bin Soong

B.S., Physics and Computer Science
Tsinghua University, Beijing
July, 1989

Submitted to the Department of Physics
in partial fulfillment of the requirements for the degree of

Doctor of Philosophy

at the

MASSACHUSETTS INSTITUTE OF TECHNOLOGY

September 1998

© Massachusetts Institute of Technology 1998. All rights reserved.

Author .....
Department of Physics
July 29, 1998

Certified by.....
Stanley Kowalski
Professor of Physics
Thesis Supervisor

Certified by...
Aron Bernstein
Professor of Physics
Thesis Supervisor

Accepted by.....
Professor Thomas J. Greytak
Associate Department Head for Education

MASSACHUSETTS INSTITUTE OF TECHNOLOGY
OCT 09 1998
LIBRARIES

Measurement of f_{LT}, f_{TT} and $f_{LT'}$ Response Functions in the Quasi-elastic $^2H(\vec{e}, e'p)$ Reaction at 200 (MeV/c) Missing Momentum

by

Shiao-Bin Soong

Submitted to the Department of Physics
on July 29, 1998, in partial fulfillment of the
requirements for the degree of
Doctor of Philosophy

Abstract

We report in this thesis the simultaneous measurement of the logitudinal- transverse response functions, f_{LT} and $f_{LT'}$, and the transverse-transverse response function f_{TT} of the deuteron. The quasi-elastic $^2H(\vec{e}, e'p)n$ experiment reported here was conducted at the MIT/Bates Linear Accelerator Center in February, 1997.

The experiment was carried out with a 40% polarized, 800 MeV electron beam. The measurement took place in the Bates South Hall using the One Hundred Inch Proton Spectrometer(OHIPS) as the electron spectrometer. It was placed at an angle of 37.27° and the energy transfer, ω, was set for quasi-elastic kinematics with the square of the four-momentum transfer, Q^2, equal to -0.22 $(GeV/c)^2$. Three out-of-plane proton spectrometers (OOPS) were positioned at $\phi_{pq}^{cm} = (0°, 90°, 180°)$, respectively, for a given θ_{pq}^{lab} of 23.5°. This allowed the simultaneous measurement of f_{LT}, f_{TT} and $f_{LT'}$ at a central missing momentum of $\sim$ 200 (MeV/c).

The measured asymmetries, cross sections and response functions are compared with different theoretical models.

Thesis Supervisor: Stanley Kowalski
Title: Professor of Physics

Thesis Supervisor: Aron Bernstein
Title: Professor of Physics

Acknowledgments

There are many people I would like to thank, both professionally, for their contributions to this experiment and personally, for their contributions to my graduate education.

First I would like to thank my advisors, Stanley Kowalski and Aron Bernstein, for their guidance, encouragement and support throughout my graduate career. I particularly appreciate Stanley's effort of proof reading this thesis. I am also grateful to my thesis committee members, Bill Donnelly and Takashi Imai, for reading this thesis and making valuable suggestions.

I am indebted to the members of the OOPS collaboration. Without their efforts, this work would never be finished. I would like to particularly thank Zilu Zhou, for his tireless involvement in the experiments and data analysis, and his endless push for perfection. Without his help, this thesis would have taken significantly longer. My special thanks also go to Ricardo Alarcon, Adam Sarty, Steve Dolfini, Jeff Shaw, Bill Bertozzi, Shalev Gilad, Christian Kunz, Karen Dow, George Dodson, Dan Tieger and Bates staff for their contributions to the OOPS project. I thank Jyungseon Joo and Townsend Zwart for their assistance in setting up the South Hall Møller polarimeter. I am grateful to Costas Vellidis for many useful physics discussions and his tremendous effort to write the Monte Carlo simulation program "AEEXB". Many of us have greatly benefited from this program. I thank Michael Distler to reanalyze the OHIPS optics data and provide us the improved OHIPS matrix elements. I also appreciate Wolfgang Korsch and Betsy Beise for their help during the early years of my graduate study.

I should thank my fellow OOPS graduate students Jiang Chen, Xiaodong Jiang and Alaine Young. Without their contributions, this experiment would not be possible. We spent a lot of time together preparing the equipment, running the experiments

and analyzing the data. It has always been fruitful to work with them.

I thank my friends and colleagues who have provided help and companionship. I would like to thank Jianguo Zhao for all the fun time we spent together, and other friends Jian Tang, Li Cai, Dapeng Xu, Hojoon Park and Kevin Lee for making my graduate student experience as educational as it has been enjoyable.

Finally I would like to thank my wife, Hairong, for her patience and support during my time in graduate school and my long time friend Wenyi for his confidence in me. Without them, I would be writing this now.

In memory of my grandmother

Contents

List of Figures

List of Tables

Chapter 1

Introduction

One of the fundamental problems of nuclear physics has been to develop a complete understanding of the nucleon-nucleon (NN) interaction and the electromagnetic structure of the nucleus. The deuteron is the only nucleon-nucleon system in nature. It plays an essential role in nuclear physics because this two-nucleon bound system contributes to our basic understanding of the nucleon-nucleon interaction and serves as the microscopic input for all fundamental models of heavier nuclei. Furthermore, precise calculations of the wave function are possible for a given nucleon-nucleon potential, thus the sub-nuclear degrees of freedom can be studied without the complications arising from multinucleon effects that occur in heavier nuclei. This feature makes the deuteron an important testing ground for models of NN potentials and their electromagnetic properties.

The use of electron scattering from nuclei has been a fruitful approach for the determination of nuclear electromagnetic structure. Underlying such studies, the electron and virtual photon are described by the fundamental theory of quantum electrodynamics (QED), which means the interaction is well understood and calculable. It allows precise studies of the structure and dynamics of the nucleus. In particular, the coupling strength in electron scattering, characterized by the fine-structure constant $\alpha \equiv e^2/\hbar c \approx 1/137.036$, is relatively small so that only the lowest order

scattering processes need to be considered and one obtains a simple interpretation of experimental data in terms of charges and nuclear currents.

The deuteron consists of a pair of loosely bound proton and neutron. It has no excited bound states. It has a magnetic dipole moment of $0.8574\mu_N$, and an electric quadrupole moment of $0.2859fm^2$. The non-zero quadrupole moment of the deuteron implies that the deuteron wave function cannot be a pure S-wave, since the S-wave has spherical symmetry and consequently, a zero quadrupole moment. The deuteron wave function is a mixture of S-wave and D-wave. This mixture is due to the tensor force of the NN interaction. Various NN models predict a D-state probability P_D ranging from 4% to 7% in the ground state of the deuteron. Accurate knowledge of this probability is essential to understand the structure of the deuteron. However, P_D is not directly an experimental observable. One observable that is sensitive to the D-wave is the cross section of the reaction $^2H(e,e'p)$, measured at high initial momenta of the proton. Other observables sensitive to the D-wave are the deuteron tensor analyzing power T_{20}, derived from $^2H(e,e'\vec{d})$ polarization experiments [1, 2], and the tensor analyzing power A_D^T from the $^2\vec{H}(e,e'p)$ asymmetry measurements [3]. It is important to study different reactions that are sensitive to the deuteron wave functions, as each of these measurements is based on a different reaction mechanism.

An exciting and fundamental issue is the electromagnetic structure of the neutron. The knowledge on the electric form factor of the neutron (G_E^n) is still poor and controversial. This is due to the absence of free neutron targets and to the fact that G_E^n is very small. However, the polarized ^2H nucleus is a good approximation of a polarized neutron. It has been suggested [4] that a $^2\vec{H}(\vec{e},e'n)p$ experiment with longitudinally polarized electrons and a vector polarized deuteron target can provide relatively model independent data on G_E^n. Reaction $^2H(\vec{e},e'\vec{n})$ has also been used to measure G_E^n [5, 6]. In addition, polarized targets have provided a branch of new experiments for the study of the deuteron [7, 8, 9].

By using the exclusive $^2H(\vec{e},e'p)$ reaction, information on not only the deuteron

ground state wave function can be obtained, but also information on the electromagnetic currents which connect to the continuum np system. These currents are partly related to the NN potentials based on one-boson-exchange, via Meson Exchange Currents (MEC), and are also connected to the internal structure of the nucleon, via Isobar Configurations (IC). The nucleons are also subject to rescattering and exchange processes during breakup, which are known as final state interactions (FSI). By separating the electron scattering cross section into longitudinal (L), transverse (T), longitudinal-transverse (LT) and transverse-transverse (TT) interference response functions, further and more stringent constraints can be provided for the NN potential and reaction models. Furthermore, when the polarization of the ejected proton is measured by a focal-plane-polarimeter (FPP), a total of 18 independent response functions are available [10, 11, 12, 13]. By requiring consistent results for such measurements, reliable information on the deuteron wave function and interaction mechanism can be obtained. For example, at the quasi-elastic ridge, where the energy and momentum transfer are completely absorbed by a single nucleon, theoretical calculations indicate that MEC, IC and FSI are suppressed. All three effects become important in the non-quasi-elastic regions. IC become important at low momentum transfer and high energy transfer. MEC effects become important at high momentum transfer and low energy transfer. The response functions themselves exhibit varying degrees of sensitivity to these effects depending on the kinematic region chosen. The helicity dependent longitudinal-transverse interference response function $f_{LT'}$ (the so called fifth structure function), is always sensitive to final state interactions. f_{LT} is sensitive to the NN potential and relativistic effects in certain kinematic regions; f_{TT} is sensitive to IC in certain kinematic regions and is sensitive to MEC at threshold.

This thesis describes the simultaneous measurements of the response functions f_{LT}, f_{TT} and $f_{LT'}$ of the deuteron at the quasi-elastic ridge. It is one of the measurements conducted at the MIT Bates Linear Accelerator Center to systematically extract the coincidence cross section response functions accessible only through out-of-

plane techniques [14, 15]. During this experiment, three out-of-plane spectrometers were used to detect protons, and the scattered electrons were detected in coincidence with the knocked-out protons. The simultaneity and symmetry of the measurements minimizes the systematic uncertainty. The system was optimized to measure small effects with relatively high luminosity and consequently low statistical uncertainty.

In this chapter, we will present the electron scattering formalism in the framework of one-photon exchange, discuss theoretical calculations of the deuteron structure functions, summarize the previous measurements in electron scattering as they pertain to this experiment, and give the motivation for performing this experiment.

1.1 Inclusive Electron Scattering

Electron scattering experiments can be classified according to how many particles are detected. If only one particle in the final state is detected, the reaction is called "inclusive", or single-arm scattering. If multiple particles in the final state are detected, the reaction is called "exclusive", or coincidence scattering. Here "inclusive" means all the final states during the reaction are integrated, and "exclusive" means one of the final states is selected. Examples of inclusive electron scattering include single-arm (e, e') elastic scattering and excitation of discrete nuclear states. The coincidence $(e, e'p)$ reaction, which is described in the following sections, is an example of exclusive electron scattering.

A typical inclusive electron scattering spectrum is shown in Figure 1-1. This shows the inclusive cross section as a function of energy transfer ω for a fixed Q^2. The sharp peaks at low ω correspond to elastic scattering and excitations of discrete inelastic states. At larger energy transfer, a set of broad bumps are associated with nuclear collective modes of motion, which is called the "giant resonance". At still higher ω, the wavelength of the virtual photon probe is small enough that it can interact primarily with a single nucleon in the nucleus, and the quasi-elastic peak

results. Broad peaks at larger energy transfers are excitations of hadronic states such as the Δ and N^*. The region between quasi-elastic scattering and Δ excitation is called the "dip" region. The kinematics for this experiment is at the quasi-elastic ridge.

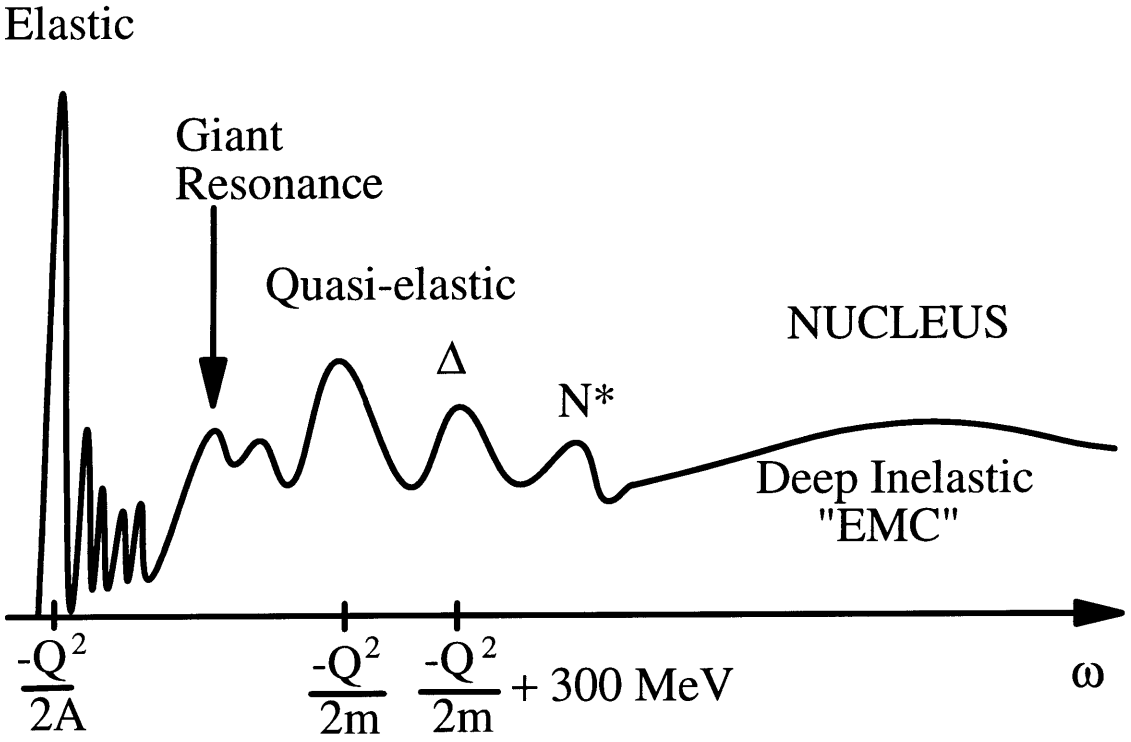

Figure 1-1: A typical inclusive electron scattering spectrum. Figure taken from [16].

In the first Born approximation (single virtual photon exchange), the (e, e') cross section can be written as[17]

$$\frac{d^3\sigma}{d\omega d\Omega_e} = \sigma_{Mott}\left\{\left(\frac{Q^2}{q^2}\right)^2 R_L(\vec{q},\omega) + \left[-\frac{1}{2}\left(\frac{Q^2}{q^2}\right) + \tan^2(\theta_e/2)\right] R_T(\vec{q},\omega)\right\}, \quad (1.1)$$

where R_L and R_T are the longitudinal and transverse response functions, and σ_{Mott} is the Mott cross section,

$$\sigma_{Mott} = \frac{\alpha^2\cos^2(\theta_e/2)}{4\epsilon^2\sin^4(\theta_e/2)}. \quad (1.2)$$

1.2 Coincidence Electron Scattering

In this section we first define the coincidence electron scattering kinematics, then we present a brief review of the derivation of the $(\vec{e}, e'p)$ cross section in the first Born approximation (single virtual photon exchange) and the separation of the nuclear response into contributions from L, T, LT, TT and LT′ components.

1.2.1 Kinematics

The basic diagram describing the coincidence electron scattering reaction $A(\vec{e}, e'x)B$ in the one-photon exchange framework is shown in Figure 1-2.

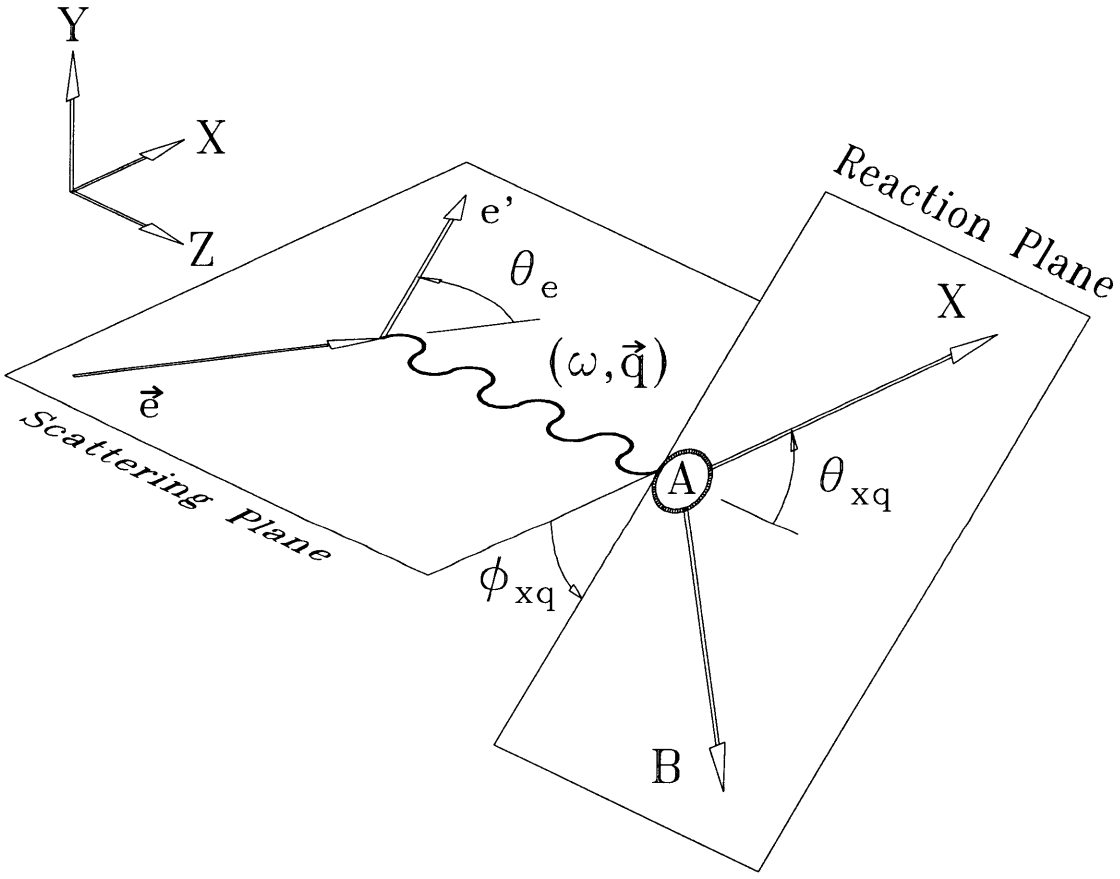

Figure 1-2: Kinematic definitions for the $A(\vec{e}, e'x)B$ reaction in the one photon exchange approximation.

An electron with 4-momentum $K^\mu = (\epsilon, \vec{k})$ is scattered through an angle θ_e to

4-momentum $K'^{\mu} = (\epsilon', \vec{k}')$. The virtual photon exchanged in the process carries 4-momentum transfer $Q^{\mu} = (\omega, \vec{q})$. We denote $P_A^{\mu} = (\epsilon_A, \vec{p}_A)$ as the 4-momentum of the target nucleus; the target is at rest in the laboratory frame, so that $\vec{p}_A = 0$ and $\epsilon_A = M_A$, which is the rest mass of the nucleus. The knocked-out particle x has 4-momentum $P_x^{\mu} = (\epsilon_x, \vec{p}_x)$ and the residual, recoiling nucleus (of mass M_B) has 4-momentum $P_B^{\mu} = (\epsilon_B, \vec{p}_B)$. In the ultra-relativistic limit (URL), the electron mass is neglected.

Conservation of 4-momentum implies that

$$Q^{\mu} = K^{\mu} - K'^{\mu} = P_x^{\mu} + P_B^{\mu} - P_A^{\mu} \ , \tag{1.3}$$

and

$$Q^2 = Q^{\mu} Q_{\mu} = \omega^2 - |\vec{q}|^2 \approx -4\epsilon\epsilon' \sin^2(\theta_e/2) \ . \tag{1.4}$$

The energy and momentum transfer are determined by the electron kinematics:

$$\omega = \epsilon - \epsilon' \ , \tag{1.5}$$

$$\vec{q} = \vec{k} - \vec{k}' \ . \tag{1.6}$$

Conservation of energy for the reaction yields

$$\omega + M_A = \epsilon_x + \epsilon_B \ , \tag{1.7}$$

$$= M_x + T_x + M_B + T_B \ , \tag{1.8}$$

where T_x and T_B are the kinetic energies of the knocked-out particle x and the recoiling nucleus B.

The "missing energy" is defined as

$$E_m \equiv M_B + M_x - M_A \ , \tag{1.9}$$

$$= \omega - T_x - T_B \ . \tag{1.10}$$

E_m is also called the "missing mass". They are used interchangeably in this thesis.

If the reaction is $^2H(e,e'p)$, then the knocked-out particle x is a proton and the recoiling nucleus B is simply the neutron, the corresponding missing mass is

$$\begin{aligned} E_m &= M_p + M_n - M_D \\ &= \epsilon_b \ , \end{aligned} \tag{1.11}$$

where M_D is the deuteron mass and $\epsilon_b \approx 2.2MeV$, which is the binding energy of the deuteron. For $^2H(e,e'p)$, the missing mass has only one value, ϵ_b.

Another very useful quantity, called the "missing momentum", is defined as

$$\vec{p}_m = \vec{q} - \vec{p}_x \ . \tag{1.12}$$

In the Plane Wave Impulse Approximation (PWIA), we assume that the entire momentum transfer is absorbed by the knocked-out particle x, and particle x has no further interaction with the residual nucleus B. With these assumptions, the missing momentum is simply the recoiling nucleus momentum or the negative initial x momentum inside target nucleus A. Thus the initial momentum distribution of x can be studied by selecting different missing momenta.

The quasi-elastic peak occurs when the energy and momentum transfers are completely absorbed by a single nucleon. The energy needed to eject a nucleon is

$$\omega_{QE} = \frac{|Q^2|}{2M_N} + \epsilon_b \ , \tag{1.13}$$

where M_N is the nucleon mass.

The quasi-elastic peak is broadened by the Fermi motion of the nucleon and is shifted by the separation energy.

1.2.2 Coincidence Cross Section Formalism

The cross section for the process shown in Figure 1-2 follows by applying the Feynman rules and involves the electron current j^μ, the photon propagator $g_{\mu\mu'}/Q^2$ and the nuclear matrix element, $J^{\mu'}_{fi}$ [18]:

$$d\sigma \sim \left| j_\mu \frac{1}{Q^2} J^{\mu'}_{fi} \right|^2 = \frac{1}{Q^4} j^*_\mu j_\nu \cdot J^{\mu *}_{fi} J^\nu_{fi} \sim \frac{1}{Q^4} \eta_{\mu\nu} W^{\mu\nu} \ . \tag{1.14}$$

Here $\eta_{\mu\nu}$ and $W^{\mu\nu}$ are the leptonic and hadronic tensors averaged over initial states and summed over final states:

$$\eta_{\mu\nu} \equiv \overline{\sum}_{electrons} j^*_\mu j_\nu \ , \tag{1.15}$$

$$W^{\mu\nu} \equiv \overline{\sum}_{hardrons} J^{\mu *}_{fi} J^\nu_{fi} \ . \tag{1.16}$$

The general cross section for exclusive (coincidence) electron scattering in the laboratory system can be written as

$$\frac{d^6\sigma}{d\omega d\Omega_e de_x d\Omega_x} = \frac{2\alpha^2}{Q^4} \left(\frac{\epsilon'}{\epsilon} \right) \frac{p_x M_x M_B}{(2\pi)^3 \epsilon_B} \eta_{\mu\nu} W^{\mu\nu} \delta(\epsilon_x + \epsilon_B - M_A - \omega) \ . \tag{1.17}$$

Integrating the delta function over ϵ_x yields

$$\frac{d^5\sigma}{d\omega d\Omega_e d\Omega_x} = \frac{2\alpha^2}{Q^4} \left(\frac{\epsilon'}{\epsilon} \right) \frac{p_x M_x M_B}{(2\pi)^3 M_A} f^{-1}_{rec} \eta_{\mu\nu} W^{\mu\nu} \ , \tag{1.18}$$

where f_{rec} is the recoil factor:

$$f_{rec} = 1 + \frac{2\epsilon \sin^2 \theta_e/2}{M_A} \ . \tag{1.19}$$

For longitudinally polarized electrons, the leptonic tensor has the form

$$\eta_{\mu\nu} = \frac{1}{4m_e^2} (K_\mu K'_\nu + K'_\mu K_\nu - g_{\mu\nu} K \cdot K' - ih\epsilon_{\mu\nu\alpha\beta} K^\alpha K'^\beta) \ , \tag{1.20}$$

where $h = \pm 1$ is the electron helicity, and $\epsilon_{\mu\nu\alpha\beta}$ is an anti-symmetric tensor.

The hardronic tensor $W^{\mu\nu}$ can be decomposed into a symmetric part $W_s^{\mu\nu}$ and an anti-symmetric part $W_a^{\mu\nu}$. By contracting the leptonic and hardronic tensors, the differential cross section can be written as

$$\begin{aligned}\frac{d^5\sigma}{d\omega d\Omega_e d\Omega_x} &= \frac{1}{(2\pi)^3}\sigma_{Mott} C_{kin} f_{rec}^{-1}[\nu_L W_L + \nu_R W_R + \nu_{LT} W_{LT}\cos(\phi_{xq}) \\ &\quad + \nu_{TT} W_{TT}\cos(2\phi_{xq}) + h\nu_{LT'} W_{LT'}\sin(\phi_{xq})] \ , \end{aligned} \tag{1.21}$$

where the subscripts L and T refer to the longitudinal and transverse components of the virtual photon polarization, LT and TT denote the longitudinal-transverse and transverse-transverse interference terms. The dependences of the structure functions on the out-of-plane angle ϕ_{xq} are made explicit. σ_{Mott} is the Mott cross section, and the constant C_{kin} is given by

$$C_{kin} = \frac{p_x M_x M_B}{M_A} \ . \tag{1.22}$$

The kinematic factors, ν's, are given by

$$\nu_L = \left(\frac{Q^2}{q^2}\right)^2 \ , \tag{1.23}$$

$$\nu_T = -\frac{1}{2}\left(\frac{Q^2}{q^2}\right) + \tan^2\frac{\theta_e}{2} \ , \tag{1.24}$$

$$\nu_{TT} = \frac{1}{2}\left(\frac{Q^2}{q^2}\right) \ , \tag{1.25}$$

$$\nu_{LT} = \frac{1}{\sqrt{2}}\left(\frac{Q^2}{q^2}\right)\sqrt{-\left(\frac{Q^2}{q^2}\right) + \tan^2\frac{\theta_e}{2}} \ , \tag{1.26}$$

$$\nu_{LT'} = \frac{1}{\sqrt{2}}\left(\frac{Q^2}{q^2}\right)\tan\frac{\theta_e}{2} \ . \tag{1.27}$$

The response function W's can be expressed in terms of the nuclear electromag-

netic current,

$$W_L = |\rho_{fi}(\vec{q})|^2 = (q/\omega)^2 |J^0_{fi}(\vec{q})|^2 \ , \tag{1.28}$$

$$W_T = |J^{+1}_{fi}(\vec{q})|^2 + |J^{-1}_{fi}(\vec{q})|^2 \ , \tag{1.29}$$

$$W_{LT} = -2Re[\rho_{fi}(\vec{q})^*(J^{+1}_{fi}(\vec{q}) - J^{-1}_{fi}(\vec{q}))] \ , \tag{1.30}$$

$$W_{TT} = 2Re[J^{+1}_{fi}(\vec{q})^* J^{-1}_{fi}(\vec{q})] \ , \tag{1.31}$$

$$W_{LT'} = -2Re[\rho_{fi}(\vec{q})^*(J^{+1}_{fi}(\vec{q}) + J^{-1}_{fi}(\vec{q}))] \ . \tag{1.32}$$

These basic response functions can also be written in terms of Cartesian projections of the currents, $J^x_{fi} = -(J^{+1}_{fi} - J^{-1}_{fi})/\sqrt{2}$, $J^y_{fi} = i(J^{+1}_{fi} + J^{-1}_{fi})/\sqrt{2}$ and $J^z_{fi} = J^0_{fi}$:

$$W_L = (q/\omega)^2 |J^z_{fi}(\vec{q})|^2 \ , \tag{1.33}$$

$$W_T = |J^x_{fi}(\vec{q})|^2 + |J^y_{fi}(\vec{q})|^2 \ , \tag{1.34}$$

$$W_{TT} = -|J^x_{fi}(\vec{q})|^2 + |J^y_{fi}(\vec{q})|^2 \ , \tag{1.35}$$

$$W_{LT} = 2\sqrt{2}(q/\omega) Re[J^z_{fi}(\vec{q})^* J^y_{fi}(\vec{q})] \ , \tag{1.36}$$

$$W_{LT'} = -2\sqrt{2}(q/\omega) Im[J^z_{fi}(\vec{q})^* J^y_{fi}(\vec{q})] \ . \tag{1.37}$$

Thus one can see that W_L and W_T measure the response of the longitudinal and transverse components of the nuclear current, respectively, to the virtual photon probe; W_L depends on the charge component of the nuclear current, and is predominantly sensitive to the deuteron wave function. The transverse and transverse-transverse interference structure functions W_T and W_{TT} contain additional sensitivity to the transverse processes such as MEC and IC. W_{LT} is the response resulting from interference between the longitudinal and transverse components; and W_{TT} is the response resulting from interference between the two transverse components of the current. The response functions W_{LT} and $W_{LT'}$ are directly related to the real and imaginary parts of the term $J^z_{fi}(\vec{q})^* J^y_{fi}(\vec{q})$, respectively. Therefore, by measuring the interference response functions, more detailed understanding of the nuclear current

can be obtained.

For inclusive electron scattering, in which one effectively integrates over all proton angles, the contributions arising from the interference terms vanish; thus the (e, e') reaction is fully characterized by only two response functions, the longitudinal and transverse, as described in Section 1.1.

1.3 Theoretical Calculations

Two different approaches have been used to describe the deuteron electrodisintegration process: the Schrödinger equation and the Bethe-Salpeter (BS) equation. The Schrödinger equation offers a non-relativistic description, whereas the BS equation is used to obtain a Lorenz-covariant description. However, the BS equation is more difficult to solve and calculations on deuteron disintegration only became available recently. Fortunately, it is possible to modify the Schrödinger equation to include relativistic effects and the range of its validity can be extended.

Various models have been developed specifically to describe the electromagnetic interactions with the deuteron. The most systematic theoretical calculations for the deuteron electrodisintegration structure functions were performed by Arenhövel and coworkers [19, 20, 21, 22, 23, 24, 25], and we refer them as the Mainz group. These calculations were based on the Schrödinger equation. The calculations can be done in conjunction with any standard parameterization of the NN interaction such as the Bonn [26] or Paris potentials [27]. The calculations also include the effects due to meson exchange currents, isobar configurations and final state interactions. They have been refined and extended to include polarization observables and relativistic corrections [22, 23, 24, 25]. Another model based on the original calculations of the Mainz group was developed by Mosconi *et al.* [28]. At the same time, Laget developed an approach in which specific diagrams for MEC, IC and FSI were taken into account [29]. A covariant approach based on an approximation of the BS equation

of the deuteron was also developed by Tjon and coworkers [30].

As to relativistic corrections, a recent approach is employed to the non-relativistic reduction of the electromagnetic current operator in calculations of electronuclear reactions [31]. In contrast to the traditional scheme, where the full relativistic electromagnetic current operator is normally not used, an improved current operator is provided to incorporate relativistic effects without any approximation in the transferred momentum or transferred energy. It has been shown that the relativistic effects in the current alone are large, and one can conjecture that up to transferred energies and momenta of a few GeV the relativistic effect in the current make up the bulk of the total relativistic contributions. Specially, the effect on the longitudinal-transverse response function is tremendous. The LT response consists of two different contributions: one contains the product of the first-order spin-orbit term and the zeroth-order magnetization current, the other one contains the product of the zeroth-order charge operator and the first-order convection current [32, 33]. The former amounts to roughly two thirds of the total response, the latter to one third. As the spin-orbit operator appears only in the relativistic treatment, it is clear that the major contribution to the response is completely missed in the strict non-relativistic limit.

The theoretical cross sections and response functions that are used in this thesis were provided by Arenhövel [34]. In this section, we give a brief presentation of the Mainz group's formalism and their treatment for the $^2H(\vec{e}, e'p)$ cross section.

The Mainz group's conventions for the response functions and the kinematic factors are slightly different from those presented in Section 1.2.2. Their calculations were performed in the deuteron center-of-mass frame. The cross section depends on the following variables: the laboratory energy transfer ω^{lab}, the laboratory electron solid angle Ω_e^{lab} and the center-of-mass solid angle Ω_{pq}^{cm}. The decomposition of the coincidence cross section into pieces characterized by the polarization states of the

exchanged virtual photon can be written as [22]

$$\frac{d^5\sigma}{d\omega^{lab}d\Omega_e^{lab}d\Omega_{pq}^{cm}} = C\Big\{\rho_L f_L \;+\; \rho_T f_T + \rho_{LT} f_{LT}\cos\phi_{pq}^{cm} \\ +\; \rho_{TT} f_{TT}\cos 2\phi_{pq}^{cm} + h\rho_{LT'} f_{LT'}\sin\phi_{pq}^{cm}\Big\}\,, \tag{1.38}$$

where the variable C is a function of the electron kinematics:

$$C = \frac{\alpha}{6\pi^2}\frac{1}{Q^{\mu 4}}\frac{e_f^{lab}}{e_i^{lab}}\,, \tag{1.39}$$

and the kinematic factors are defined as

$$\begin{aligned} \rho_L &= \beta^2 Q^2 \tfrac{\xi^2}{2\eta}\,, & \rho_T &= \tfrac{1}{2}Q^2\left[1+\tfrac{\xi}{2\eta}\right]\,, \\ \rho_{LT} &= \beta Q^2 \tfrac{\xi}{\eta}\left[\tfrac{\xi+\eta}{8}\right]^{1/2}\,, & \rho_{TT} &= -Q^2\tfrac{\xi}{4\eta}\,, \\ \rho'_{LT} &= \tfrac{1}{2}\beta Q^2\tfrac{\xi}{\sqrt{2\eta}}\,, \end{aligned} \tag{1.40}$$

with

$$\beta = \frac{|\vec{q}_{lab}|}{|\vec{q}_{cm}|}\,, \quad \xi = \frac{Q^2}{\vec{q}_{lab}^{\,2}}\,, \quad \eta = \tan^2\left[\frac{\theta_e^{lab}}{2}\right]\,,$$

and the center of mass momentum transfer,

$$|\vec{q}_{cm}| = \frac{M_D}{\sqrt{\left(\omega^{lab}+M_D\right)^2 - \vec{q}_{lab}^{\,2}}}\;|\vec{q}_{lab}|\,. \tag{1.41}$$

The response functions depend on θ_{pq}^{cm}, $\mathrm{E}_{\mathrm{np}}^{\mathrm{cm}}$, $|\vec{q}_{cm}|$, where $\mathrm{E}_{\mathrm{np}}^{\mathrm{cm}}$ is the final np state energy and is given by:

$$E_{np}^{cm} = \sqrt{\left(\omega^{lab}+M_D\right)^2 - \vec{q}_{lab}^{\,2}} - M_n - M_p\,. \tag{1.42}$$

This cross section can be transformed into the laboratory frame by using the

Jacobian [20]:

$$J \equiv \frac{\partial \Omega_{pq}^{cm}}{\partial \Omega_{p}^{lab}} = \left(\frac{p_p^{lab}}{p_p^{cm}}\right)^3 \frac{M^{lab}}{E^{lab}} \left(1 + \frac{q^{lab} M^{lab}}{2 p_p^{cm} E^{lab}} \cos\theta_{pq}^{cm}\right)^{-1} , \tag{1.43}$$

$$M^{lab} = E_{np}^{cm} + 2M_p , \quad E^{lab} = \left(\left(M^{lab}\right)^2 + \left(\vec{q}^{lab}\right)^2\right)^{1/2} .$$

The response functions are related to the W's presented in the previous section by

$$f_L = 12\pi^2 \alpha J W_L , \tag{1.44}$$

$$f_T = 12\pi^2 \alpha J W_T , \tag{1.45}$$

$$f_{LT} = -12\pi^2 \alpha J W_{LT} , \tag{1.46}$$

$$f_{TT} = 12\pi^2 \alpha J W_{TT} , \tag{1.47}$$

$$f_{LT'} = 12\pi^2 \alpha J W_{LT'} , \tag{1.48}$$

where α is the fine structure constant and J is the Jacobian defined in Equation 1.43.

The Mainz group's treatment for the deuteron includes a "normal" theory (N). MEC and IC corrections can be added to the normal theory to get a "total" theory (N + MEC + IC). Recently relativistic corrections have been made to the nucleon charge and current densities in the normal theory, which constitutes a "full" theory (N + RC + MEC + IC). Figure 1-3 shows the most important lowest-order diagrams included in the calculation.

In the normal theory, the deuteron initial state wave function is obtained by solving the Schrödinger equation numerically with a realistic model of the NN potential, such as the Bonn and Paris potentials. One-body non-relativistic charge and current densities are used, which include nucleon form factors and assume "on-shell" form factors for the two nucleons. The nuclear current density J^μ is expanded in terms of Coulomb and transverse electric and magnetic multipoles. To include final state

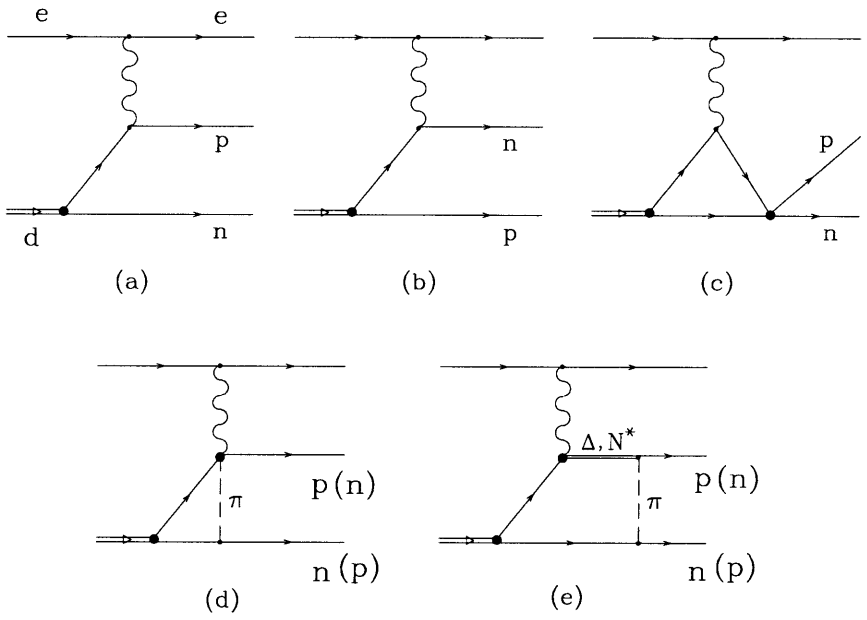

Figure 1-3: Most important lowest-order diagrams contributing to the $^2H(e,e'p)n$ cross section. (a) PWIA e-p scattering, (b) PWIA e-n scattering, (c) final state interactions, (d) pion exchange one-body, pair, contact and meson current, and (e)Meson exchange contribution including Δ's and N^*'s.

interactions, the final np state wave function is calculated by using the same NN potential as for the deuteron initial state wave function. As will be shown later, the normal theory N describes the structure functions very well near the quasi-elastic ridge. In other energy and momentum transfer domains, the non-nucleon degrees of freedom MEC and IC can also play important roles.

Meson exchange currents arise when two nucleons exchange a virtual meson, as shown in the diagram (d) of Figure 1-3. An isovector π two-body exchange term is included for the dominant long-range MEC. For the shorter range MEC, ρ and ω exchange current terms are added. A fraction of the long-range part is subtracted out since it is already implicitly included in the N theory. MEC effects are not expected to contribute greatly to the cross section at the quasi-elastic peak, since this is the

region where one-body processes are expected to dominate.

Contributions also occur by including Δ's and N^*'s, in which the photon-hadron vertex contains a Δ form factor or other nucleon excited states, as shown in the diagram (e) of Figure 1-3. Several types of transition currents, such as NN^* and N^*N^* currents, are also possible. In addition, the deuteron wave functions may contain isobar configurations such as $\Delta\Delta$ or N^*N components in the ground state.

Starting from the non-relativistic theory, the relativistic effects are included in the electromagnetic charge and current operators by a $\frac{p}{M_N}$ expansion. The relativistic corrections are discussed in more detail in references [24, 25].

Figure 1-4 shows Arenhövel's calculations of the deuteron response functions for the kinematics of this experiment, with different ingredients added.

From this figure, one can see that MEC, IC and FSI are suppressed at the quasi-elastic ridge. One can further see that f_{LT} is generally sensitive to relativistic corrections (i.e. the largest differences occur between the "normal" calculation and the "full" calculation with relativistic corrections included). The difference between PWBA and the "normal" theory shows that final state interactions are important for f_{LT} at high missing momentum. The helicity dependent response function $f_{LT'}$ is very sensitive to final state interactions. At higher and higher missing momentum, f_{TT} shows more and more sensitivity to MEC, IC, FSI and RC, specially to IC. One can also see that the combined response function $f_L + \frac{\rho_T}{\rho_L} f_T + \frac{\rho_{TT}}{\rho_L} f_{TT}$ is not sensitive to any of these effects. That's one of the reasons that it is essential to measure the interference response functions.

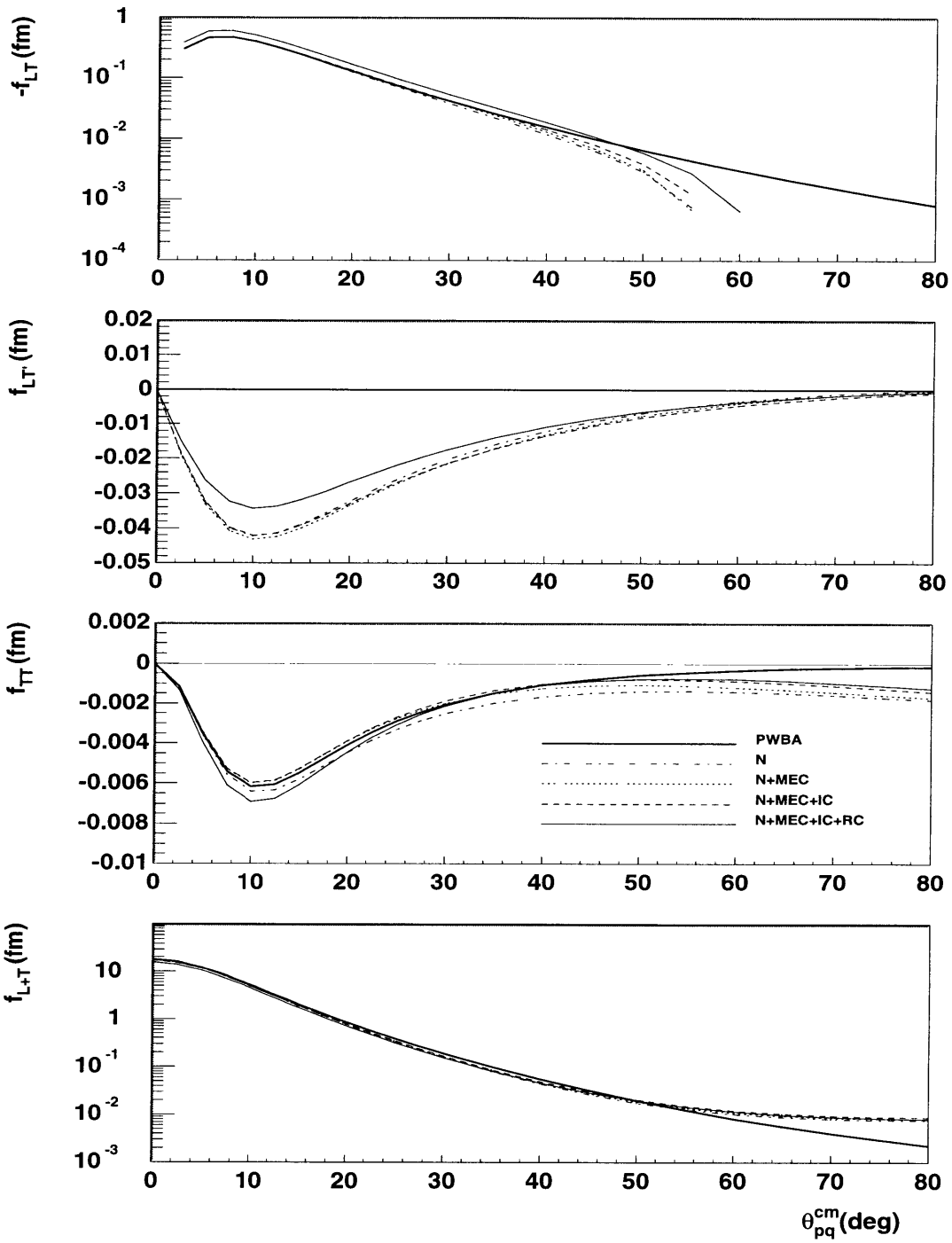

Figure 1-4: Deuteron response functions f_{LT}, $f_{LT'}$, f_{TT} and f_{L+T} calculated by Arenhövel *et al.* for the kinematics of this experiment, plotted as a function of the azimuthal angle θ_{pq}^{cm}. Different curves represent different ingredients included in the calculations. Note that the sign of f_{LT} is negative, and f_{L+T} is a combined response function defined in Equation 1.55.

1.4 Response Function Extraction

From Equation 1.38 we see that the different response functions f_{LT}, f_{TT} and $f_{LT'}$ can be formed by measuring coincidence cross sections at integer multiples of $\pi/4$ in ϕ_{pq}^{cm} angles. Asymmetry ratios that are proportional to the response functions can also be taken between various combinations of measurements at $n \cdot \frac{\pi}{4}$. Ideally four out-of-plane spectrometers should be placed symmetrically either at $n \cdot \frac{\pi}{2}$ corresponding to a "+"-configuration, or at $(n + 1/2) \cdot \frac{\pi}{2}$ corresponding to an "x"-configuration. The schematic diagram of the "+"-configuration is shown in Figure 1-5. During this experiment, three OOPS modules were used. They were aligned at $\phi_{pq}^{cm} = 0°, 90°, 180°$ respectively, which represented a half "+"-configuration. The reason multiple OOPS modules were employed is that it enables us to measure LT, TT and LT' response functions simultaneously and systematic errors are well under control.

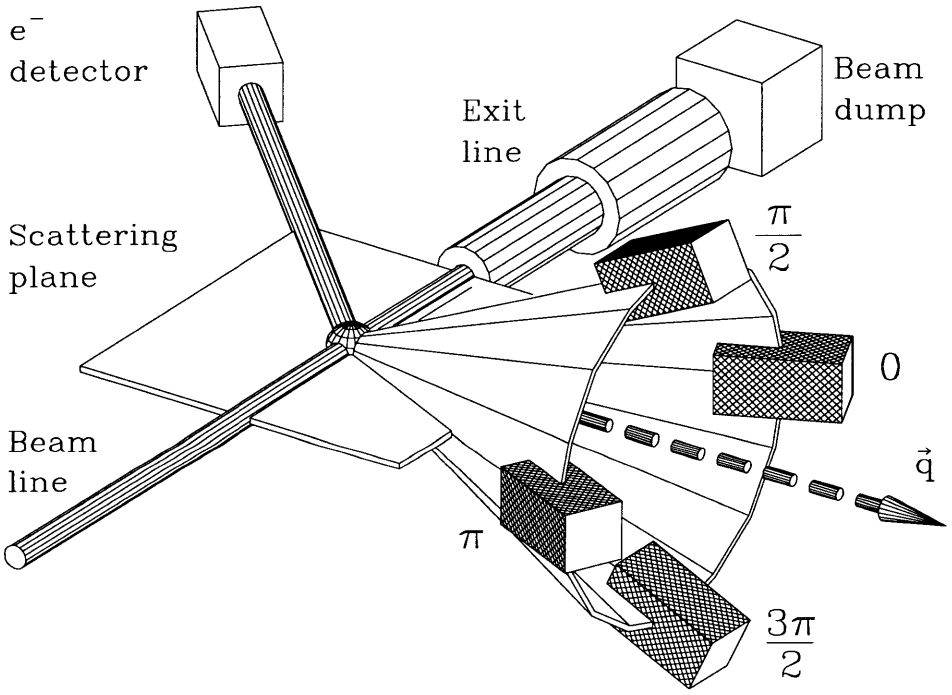

Figure 1-5: Schematic representation of the experimental geometry in the "+" configuration. Each proton detector (hatched) is labeled with its ϕ_{pq}^{cm} angle .

The technique used to extract response functions with minimum systematic error

is called the separation through asymmetries method (STAM) [35]. Many systematic uncertainties such as luminosity, phase space, detector efficiencies cancel out in the formation of asymmetries.

The helicity dependent asymmetry $A_{LT'}$ can be formed for each individual OOPS just by flipping the helicity of the electron beam. This asymmetry vanishes for any in-plane measurement because of the $\sin\phi_{pq}^{cm}$ factor in Equation 1.38. For the out-of-plane angle $\phi_{pq}^{cm} = 90°$, the asymmetry is given as

$$A_{LT'} \equiv \frac{\sigma_{\pi/2}^{+} - \sigma_{\pi/2}^{-}}{\sigma_{\pi/2}^{+} + \sigma_{\pi/2}^{-}} = \frac{\rho_{LT'} f_{LT'}}{\rho_L f_L + \rho_T f_T - \rho_{TT} f_{TT}}, . \tag{1.49}$$

where superscripts + and - denote the electron helicity.

By forming the difference between the forward and backward OOPS, the LT asymmetry can be written as

$$A_{LT} \equiv \frac{\sigma_0 - \sigma_\pi}{\sigma_0 + \sigma_\pi} = \frac{\rho_{LT} f_{LT}}{\rho_L f_L + \rho_T f_T + \rho_{TT} f_{TT}} , \tag{1.50}$$

which is proportional to the response function f_{LT}.

A_{TT} is determined using cross sections from all three OOPS's:

$$A_{TT} \equiv \frac{\sigma_0 + \sigma_\pi - 2\sigma_{\pi/2}}{\sigma_0 + \sigma_\pi - 2\sigma_{\pi/2}} = \frac{\rho_{TT} f_{TT}}{\rho_L f_L + \rho_T f_T} . \tag{1.51}$$

The extraction of the response functions is straight forward:

$$f_{LT'} = \frac{\sigma_{\pi/2}^{+} - \sigma_{\pi/2}^{-}}{2C\rho_{LT'}} , \tag{1.52}$$

$$f_{LT} = \frac{\sigma_0 - \sigma_\pi}{2C\rho_{LT}} , \tag{1.53}$$

$$f_{TT} = \frac{\sigma_0 + \sigma_\pi - 2\sigma_{\pi/2}}{4C\rho_{TT}} , \tag{1.54}$$

where C, $\rho_{LT'}$, ρ_{LT} and ρ_{TT} are the kinematic factors defined in Section 1.3.

It is also interesting to define the combined response function, $f_{L+T} = f_L + \frac{\rho_T}{\rho_L} f_T + \frac{\rho_{TT}}{\rho_L} f_{TT}$, which is extracted as

$$f_{L+T} = \frac{\sigma_0 + \sigma_\pi}{2C\rho_L} \ . \tag{1.55}$$

1.5 Previous Measurements

The cross section for the reaction $^2H(e, e'p)n$ has been measured extensively to study the deuteron. A complete review of the recent measurements and their comparison to theory can be found in [36].

The longitudinal and transverse responses f_L and f_T have been measured in three previous experiments using the Rosenbluth separation method. All measurements were performed at quasi-elastic kinematics with $Q^2 = -0.2(GeV/c)^2$ and at a relatively low missing momentum range of 0-100 MeV/c. In Figure 1-6, a comparison is presented of the longitudinal and transverse responses for NIKHEF data [37] and Bates data [41, 54]. While both data sets agree for the transverse part, they disagree significantly for the longitudinal part.

In Figure 1-7, both Saclay [40] and Bates data [41, 54] are compared to the full calculations by Arenhövel *et al.*. Again, both data sets agree for the transverse response. It is also noted that calculations by Arenhövel *et al.* reproduce the transverse response and they disagree with the longitudinal response as measured by both Saclay and Bates. Hence the experimental data are not conclusive, and the theory cannot reproduce the experimental longitudinal and transverse responses simultaneously.

There are several measurements of the longitudinal-transverse interference response function f_{LT} and the asymmetry A_{LT} from NIKHEF [38], Bonn [39], Saclay [40] and Bates [41]. The measured asymmetries are shown in Figure 1-8. All these measurements were performed in the quasi-elastic region with $Q^2 \sim -0.2(GeV/c)^2$. The asymmetries are compared to the calculations of Arenhövel *et al.*[23, 24, 25] with and without relativistic corrections. In addition, the NIKHEF data are also compared

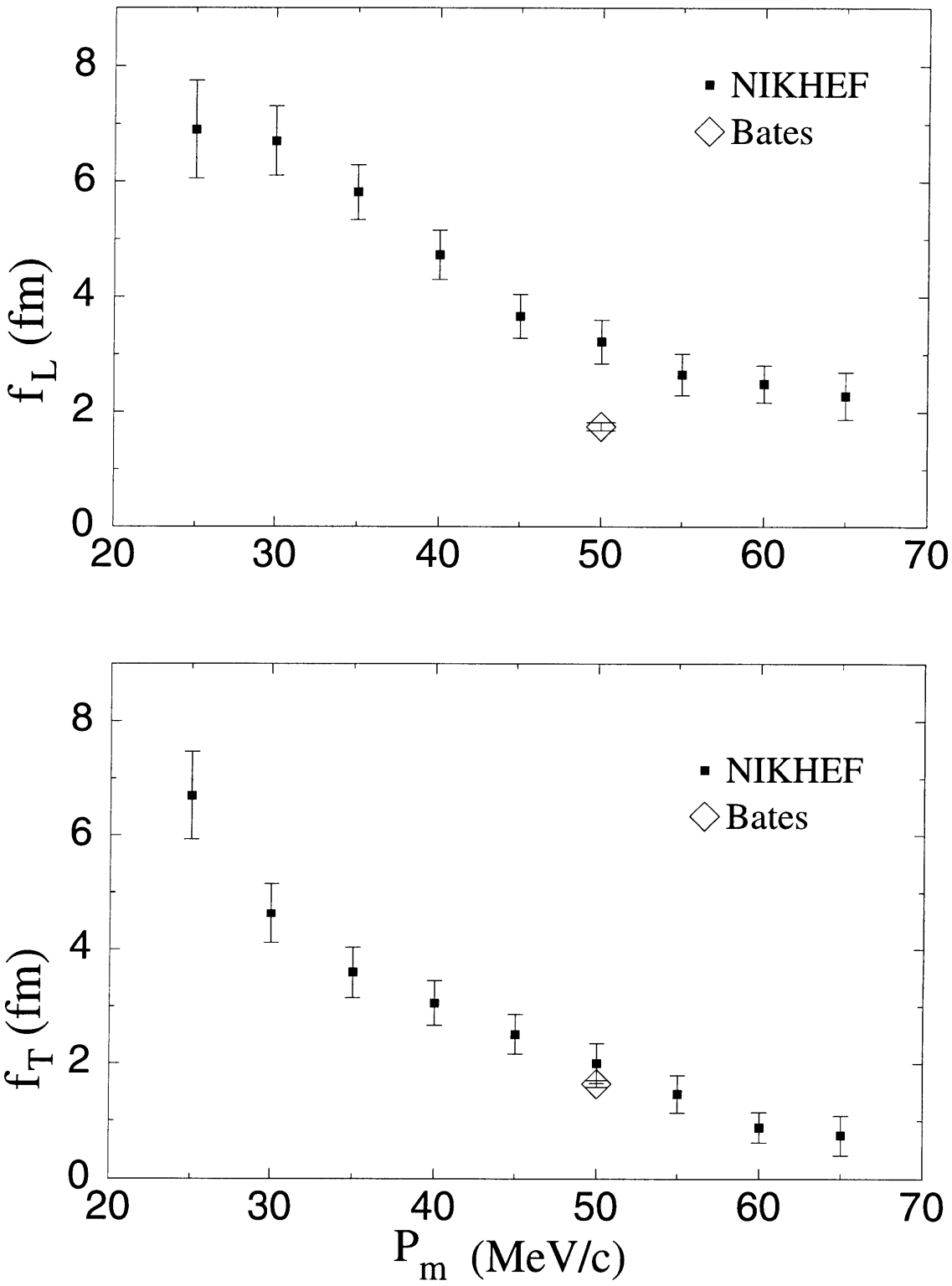

Figure 1-6: Separated f_L and f_T response functions from experiments at NIKHEF [37] and Bates [41, 54].

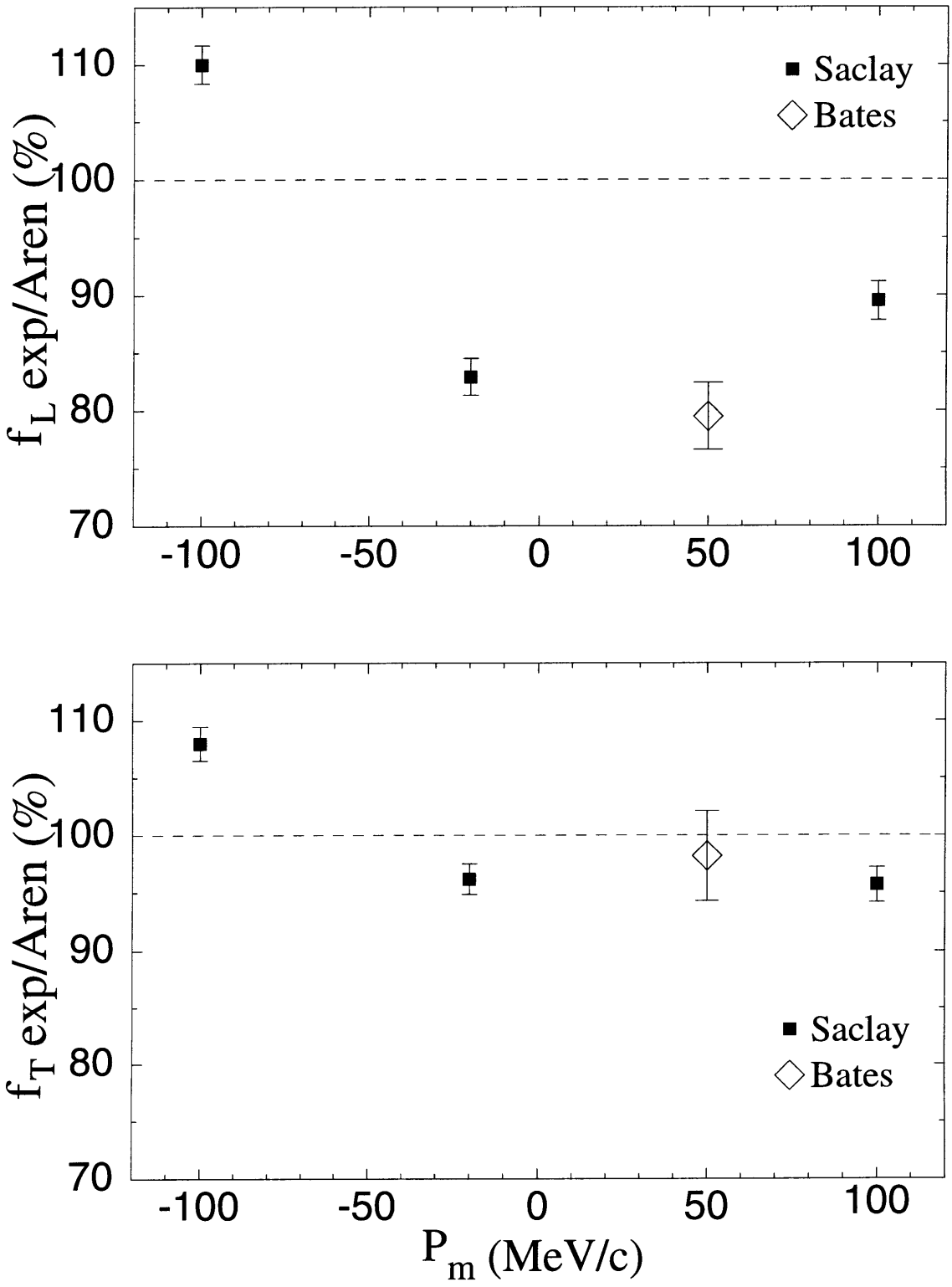

Figure 1-7: Ratio of the measured response functions to Arenhövel's calculations for experiments at Saclay [40] and Bates [41, 54].

to the relativistic calculations of Tjon *et al.* [42, 43, 44] and both the NIKHEF data and Saclay data are compared to the calculations of Mosconi *et al.*[28, 45] with relativistic corrections. Arenhövel's treatment of the electromagnetic current and the NN interaction is based on a one-boson exchange model which includes MEC and FSI. IC contributions are not included in the calculations. As mentioned earlier, Tjon's calculations use a fully covariant approach based on an approximation of the Bethe-Salpeter equation for the deuteron. Mosconi's calculations are very similar in nature to those of Arenhövel. In all cases, the calculations which include relativistic effects reproduce the A_{LT} asymmetries much better than those which do not. It is noteworthy, however, that in the calculations by Arenhövel *et al.*, it is the one without relativistic corrections which reproduces the response function f_{LT} better than the calculations which include those corrections[40, 41]. This indicates that the theoretical description of the deuteron is not complete or better quality experimental data are needed.

More recently, the f_{LT} response function and the cross section asymmetry A_{LT} for the reaction $^2H(e,e'p)$ have been measured at NIKHEF [46] with $Q^2 = -0.2(GeV/c)^2$, which is slightly above the quasi-elastic ridge. The data are presented in Figure 1-9 together with calculations by Tjon *et al.* [42, 43, 44] and Mosconi *et al.*[28, 45] (with and without relativistic corrections). To describe f_{LT} and A_{LT} properly, the calculations that include a relativistic form of the nucleon current operator are favored. It demonstrates that the relativistic corrections are needed at Q^2 values as low as $-0.2(GeV/c)^2$.

It is also not surprising that the SLAC data [47] for A_{LT} at $Q^2 = -1.2\ (GeV/c)^2$, as shown in Figure 1-10, are reproduced well by the relativistic calculation of Tjon *et al.* [42, 43, 44] and also by calculations which include relativistic corrections of Arenhövel *et al.*[23, 24, 25], and are not well described by non-relativistic calculations. It is remarkable that the differences between the various models are so large. One can see that up to p_m of about 120 MeV/c these data are described well by the

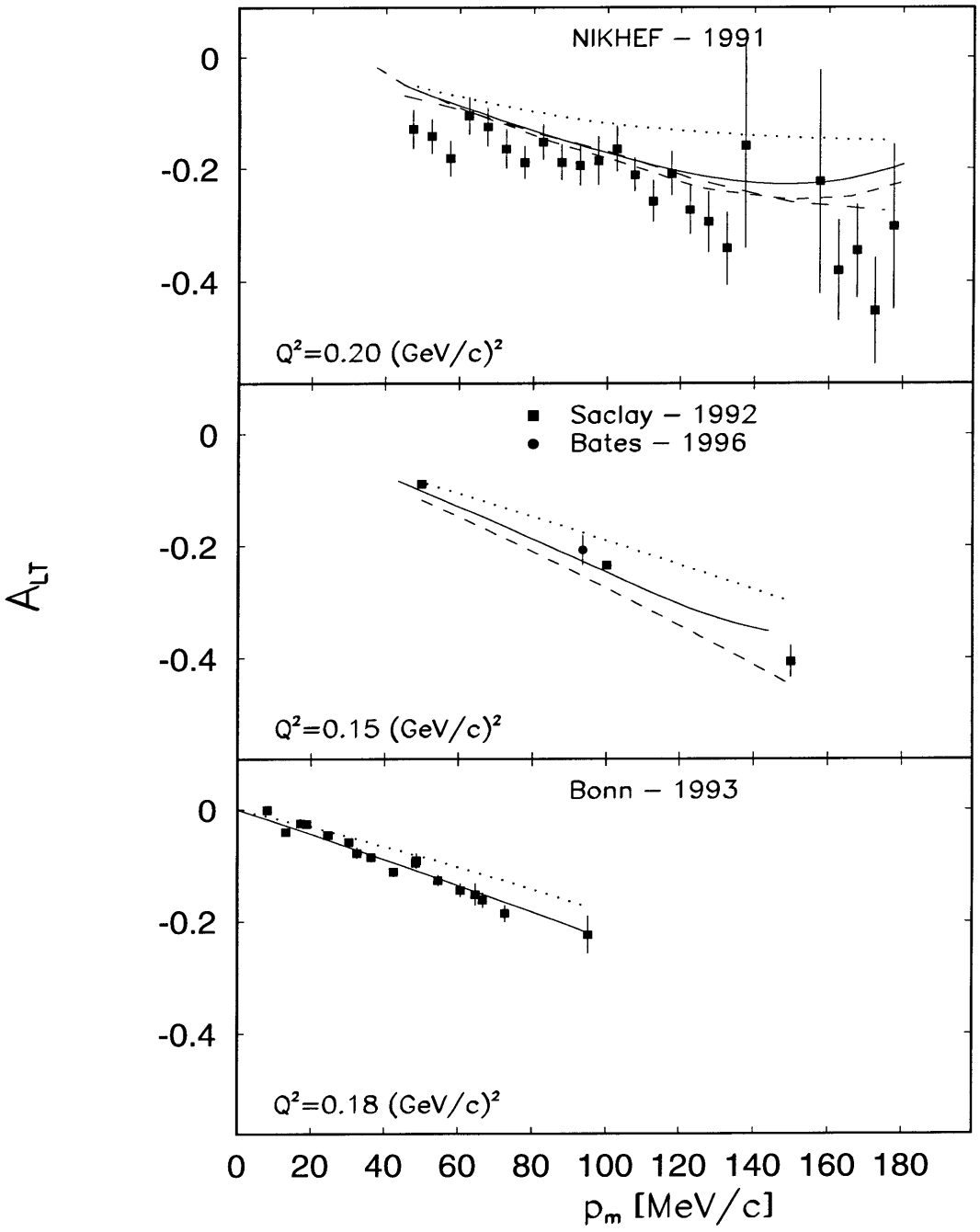

Figure 1-8: A_{LT} asymmetry for the reaction $^2H(e,e'p)n$ measured at NIKHEF [38], Bonn [39], Saclay [40] and Bates [41]. Solid curves (dotted curves) are calculations by Arenhövel *et al.* with (without) relativistic corrections. Also shown are the relativistic calculations of Tjon *et al.* (long-dashed curve) for the NIKHEF data and the calculations of Mosconi *et al.* with relativistic corrections (short-dashed curve) for both NIKHEF and Saclay data.

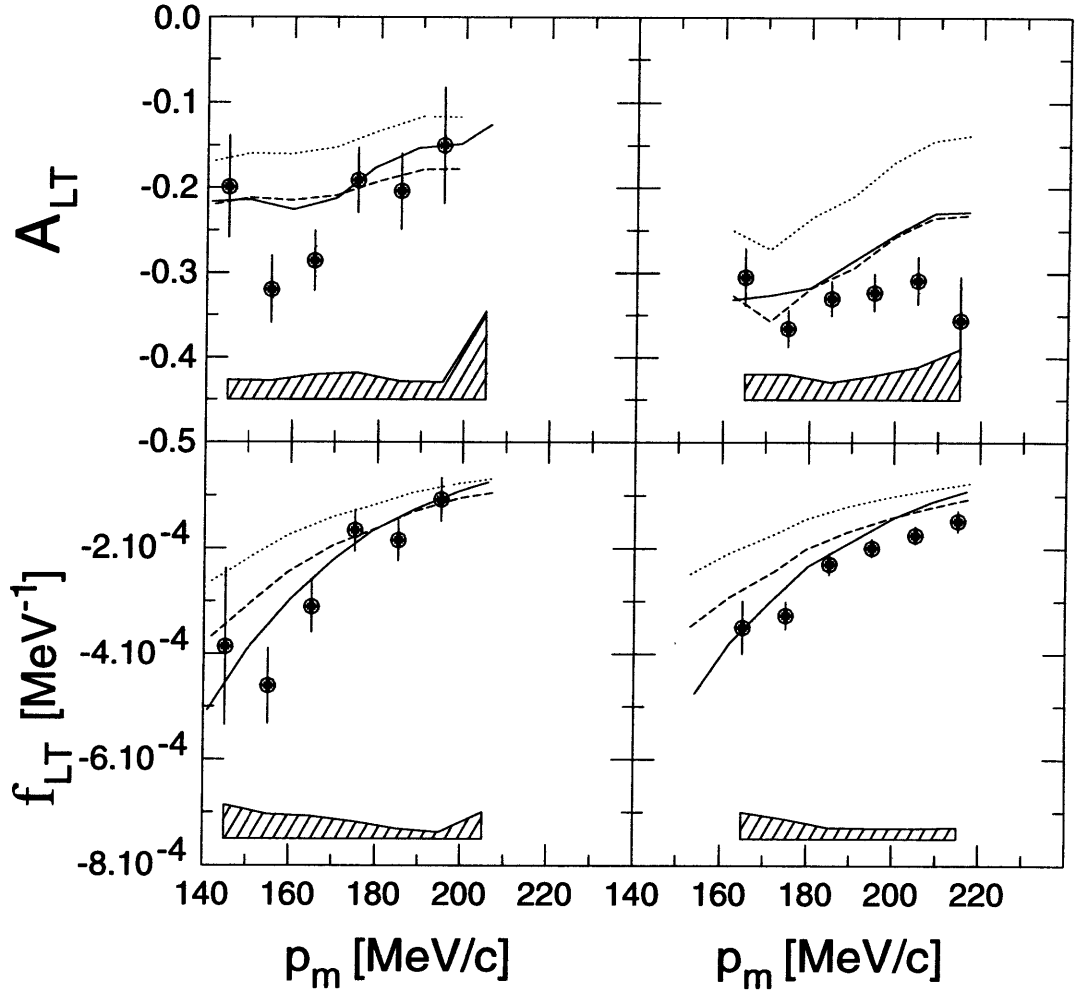

Figure 1-9: A_{LT} and f_{LT} measured at NIKHEF [46]. The shaded areas indicate the size of the systematic errors. The solid curve represents the relativistic calculation of Tjon *et al.*, the dashed (dotted) curves are calculations of Mosconi *et al.* with (without) relativistic corrections.

PWIA calculations using the σ_1^{cc} off-shell prescription of de-Forest [48] and the Paris spectral function for the deuteron [27]. We note again, that all data are at low to modest missing momenta, and hence the dependence of the calculations on the NN potential used is very small. Furthermore, a conclusion can be drawn that at least for $p_m < 150\ MeV/c$ the asymmetry A_{LT} and the interference response f_{LT} are very sensitive to relativistic effects (and are not sensitive to MEC, FSI or IC). A_{LT} is consistently described better when relativistic effects are included, while for f_{LT}, the data from NIKHEF and Bates are not consistent.

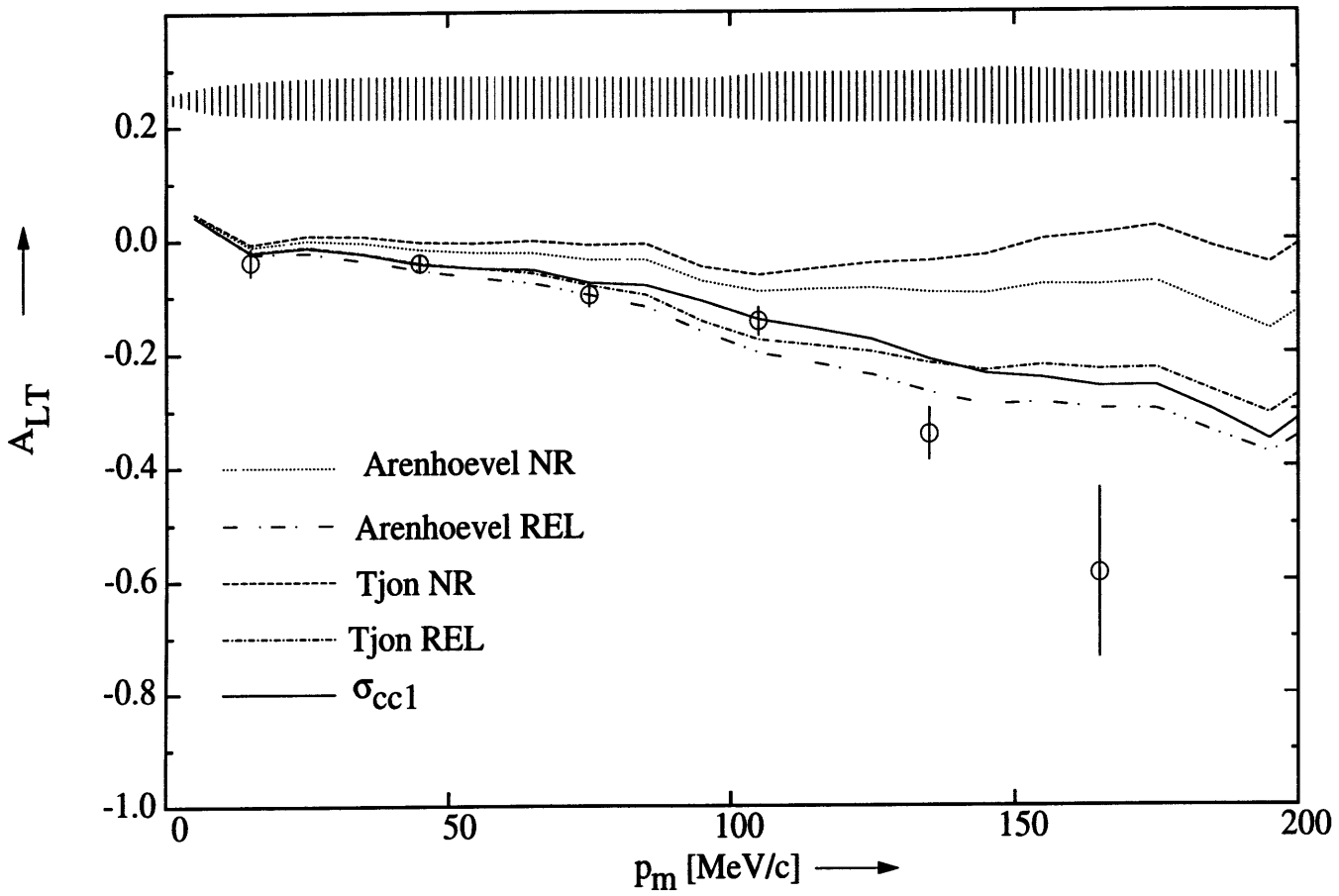

Figure 1-10: A_{LT} as a function of missing momentum at $Q^2 = -1.2(GeV/c)^2$ measured at SLAC [47] compared with various non-relativistic (NR) and relativistic (REL) models.

Both response functions f_{TT} and $f_{LT'}$ require the detection of the hadron out of the electron scattering plane. Hence, the experimental data are scarce.

There exists only one measurement of the transverse-transverse interference response function f_{TT} from NIKHEF [49]. The measurement was done in the Δ resonance region. These NIKHEF data are shown in Figure 1-11, together with calculations by Arenhövel *et al.*. The experimental results show that Δ IC plays a dominant role in the Δ region. The results of a coupled-channel calculation, including explicit pion, nucleon and Δ degrees of freedom, are in agreement with the cross section data. However, the f_{TT} data are systematically underestimated by 30% to 40%. Further theoretical studies are needed to clarify the observed discrepancies.

There also exists only one measurement of the helicity-dependent longitudinal-transverse interference response $f_{LT'}$, from Bates [50]. A polarized electron beam and an out-of-plane OOPS were used in the measurement. The data, as shown in Figure 1-12, seem to indicate that $A_{LT'}$ is non-zero for the range of p_m measured, but the statistical accuracy is very low, and hence no firm conclusion can be drawn from these data. These results clearly demonstrate that measurements of small out-of-plane observables with reduced systematic errors are now possible.

In conclusion, the existing measurements of response functions and the state-of-the-art calculations depict a less-than satisfactory level of our understanding of the electrodisintegration of the deuteron. Despite the fact that within the relatively low missing momentum for these data, hence the insensitivity to the different modern NN potentials, and despite the relatively low momentum transfers of these experiments, no theoretical model can describe adequately and consistently all the experimental data. One reason may be the fact that the data were taken at different kinematics such that a consistent theoretical and experimental comparison is not possible. Thus, it is desirable to measure several responses at the same kinematics. Also, simultaneous measurements allow a better control over kinematic parameters and the systematic uncertainties. Furthermore, it is desirable to measure as many responses as possible,

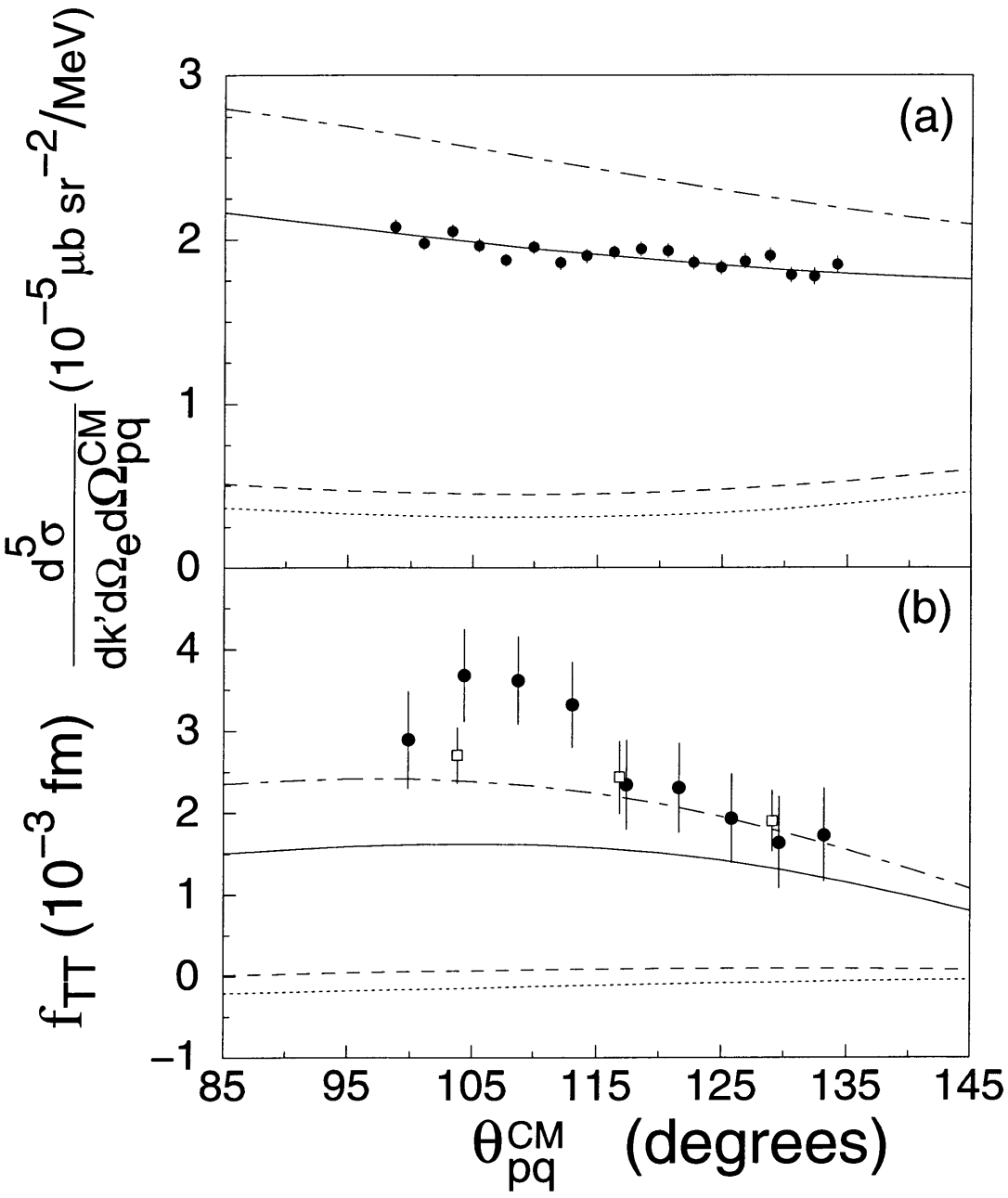

Figure 1-11: Differential cross section (a) and f_{TT} structure function (b) for the $^2H(e,e'p)n$ reaction as a function of θ^{cm}_{pq} measured at NIKHEF [49]. Only statistical errors are shown. The various curves represent calculations by Arenhövel *el al.*. Dotted curve: N; dashed curve: N + MEC; solid curve: N + MEC + IC, calculated within the coupled-channel (CC) model; dot-dashed curve: N + MEC + IC, calculated in the impulse approximation (IA) framework.

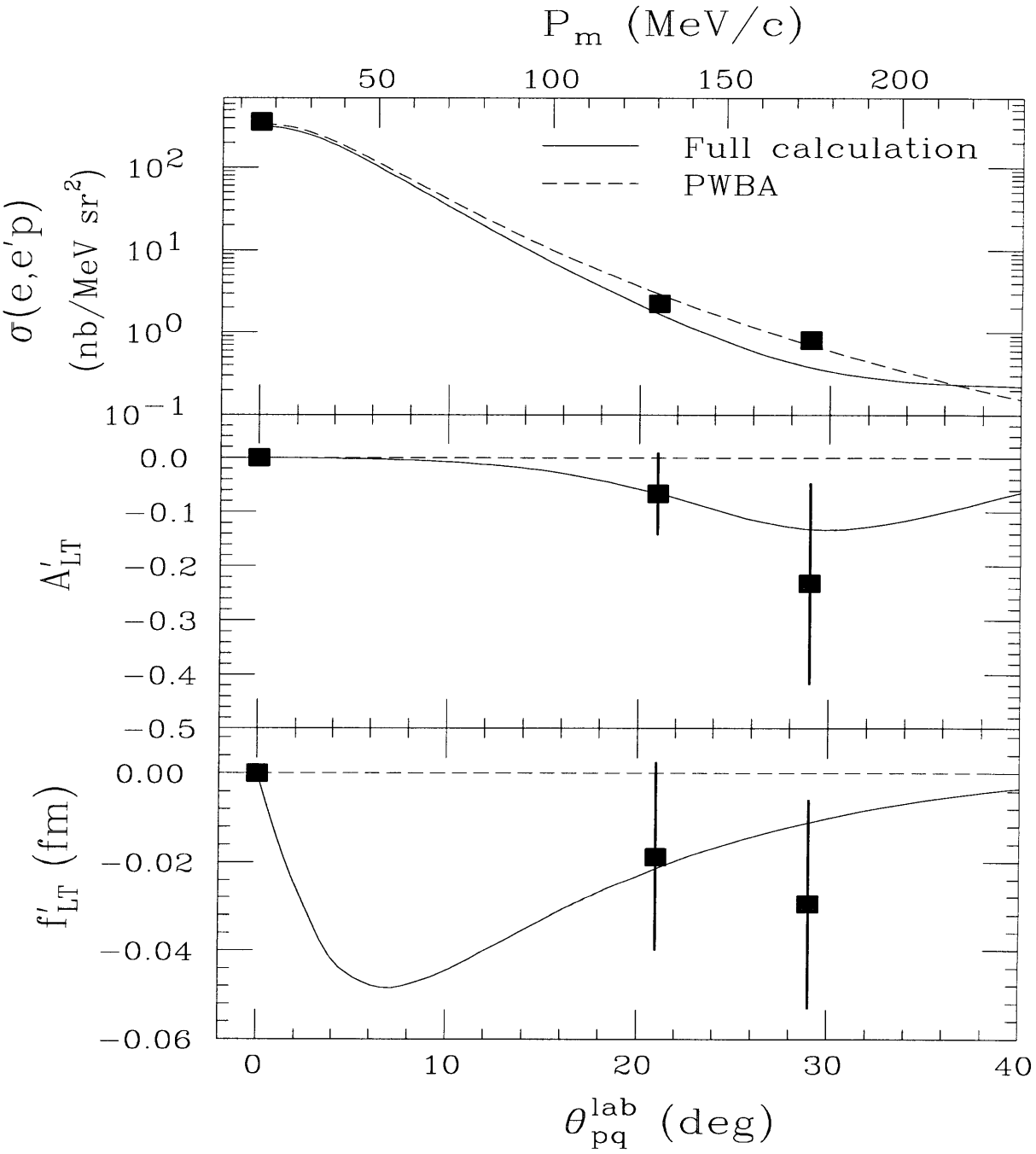

Figure 1-12: The helicity-independent cross section σ (top), the helicity asymmetry $A_{LT'}$ (center), and the structure function $f_{LT'}$ (bottom) as a function of θ_{pq}^{lab} and p_m, measured at Bates [50]. The curves correspond to calculations performed in the non-relativistic framework of Arenhövel *et al.* using the Paris potential. The errors shown are statistical only.

as these are independent observables which are needed to fully constrain theoretical models.

In this experiment, we measured f_{LT}, f_{TT} and $f_{LT'}$ response functions simultaneously in the quasi-elastic region. It is one of several proposed measurements of the deuteron response functions at Bates [14, 15]. To fully constrain the potential and interaction models, information on all deuteron responses are required over a varied range of kinematics.

Chapter 2

Experimental Apparatus and Data Acquisition System

In this chapter we will discuss the experimental setup and the major hardware elements of the measurement, which include the accelerator, polarized electron source, cryogenic target system, OOPS and OHIPS spectrometers, data acquisition system and the Møller polarimeter.

2.1 Overview of Setup

The measurements described in this thesis were carried out in the South Experimental Hall of the M.I.T. Bates Linear Accelerator Center (see Figure 2-1) in February, 1997. The Bates linear accelerator was designed to deliver a pulsed electron beam with duty factor of 1% and beam energies up to 1 GeV. It is currently being upgraded to produce a continuous beam (near 100% duty factor) with internal target capabilities, through the use of a new stretcher-storage ring.

An achromatic beam tune into the South Hall was utilized in order to achieve the smallest possible spot size on the target to maximize the missing energy resolution. Some key parameters of the beam employed in the measurements are listed in

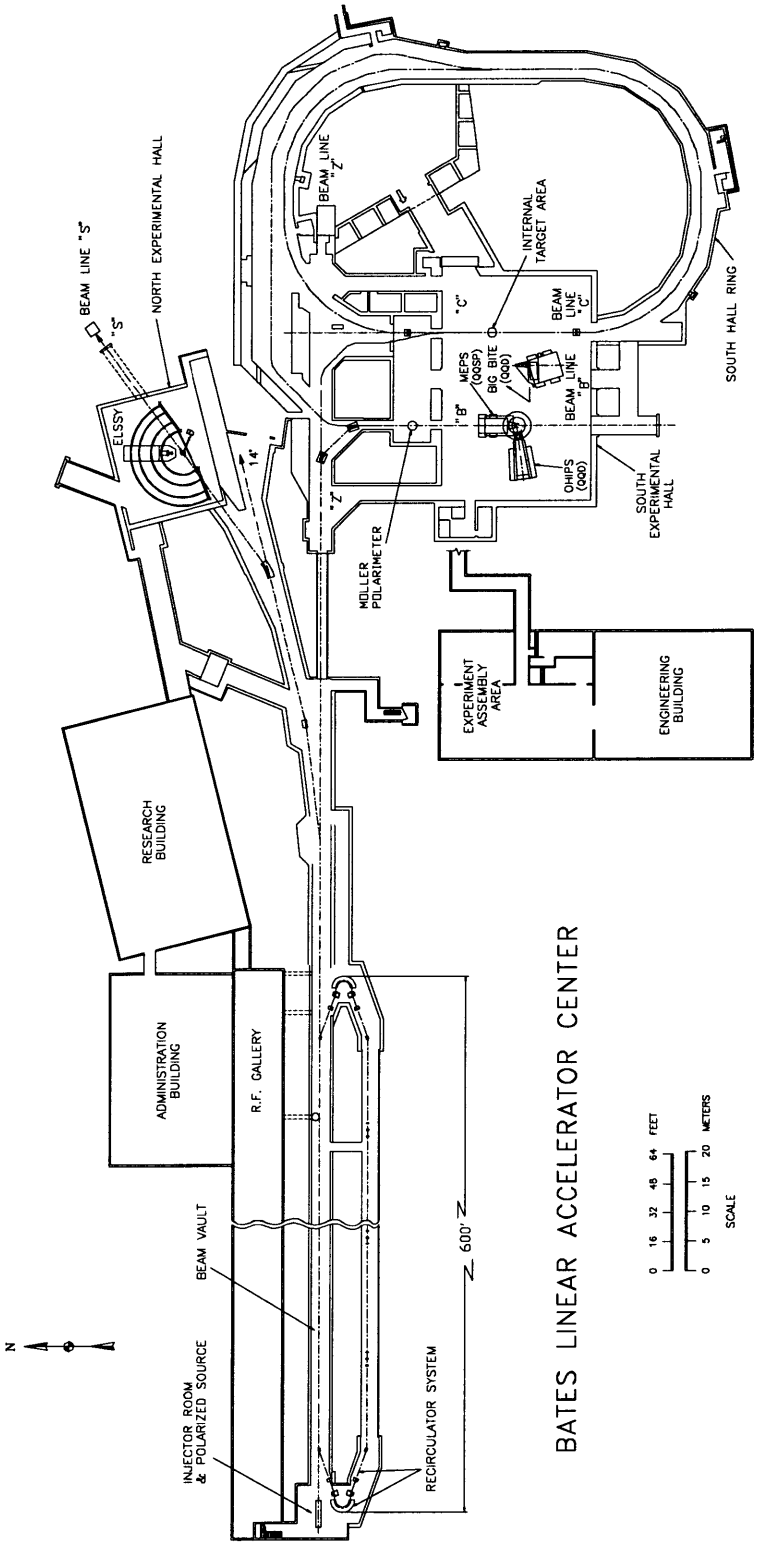

Figure 2-1: A plan view of the M.I.T. Bates Linear Accelerator Center.

Table 2.1.

Table 2.1: Beam parameters for the experiment.

Energy	800 ± 0.8 MeV	Pulse Width	15 μs
Tune	Recirculated, Achromatic	Duty factor	0.8%
Polarization	38.1 ± 5.3%	Peak Current	0.33 mA
Rep. Rate	580 Hz	Average Current	2.6 μA
Energy Slit	1%		

The One-Hundred-Inch Proton Spectrometer (OHIPS) was modified to detect electrons and was tuned for quasi-elastic kinematics on the deuteron. The electron central kinematic quantities are given in Table 2.2.

Three out-of-plane proton spectrometers (OOPS) were used to detect protons in coincidence with electrons. The proton central kinematic parameters are given in Table 2.3. The three OOPS modules were positioned at ϕ_{pq}^{cm} angles of 0°, 90° and 180° respectively. They formed a half "+"-configuration. In Table 2.3, θ_p and ϕ_p are OOPS angles in the laboratory frame; θ_p is the angle between the beam line and the projected central ray of an OOPS module onto the horizontal plane, and ϕ_p is the out-of-plane angle. The proton central momentum and missing momentum are denoted by p_p and p_m.

A schematic view of the experimental setup is shown in Figure 2-2. OHIPS is on the left side of the beam line with $\theta_e = 37.27°$, three OOPS's are shown on the right side of the beam line.

Table 2.2: Electron Central Kinematics.

ω	= 118.6 MeV	e_f	= 681.4 MeV
Q^2	= -0.22 (GeV/c)^2	$\|\vec{q}\|$	= 486.52 MeV/c
θ_e	= 37.27°	θ_q	= 58.01°

Table 2.3: Proton Central Kinematics.

	OOPS A	OOPS B	OOPS C
$\phi_{pq}^{cm}(^\circ)$	0	90	180
$\theta_p(^\circ)$	34.51	58.01	81.51
$\phi_p(^\circ)$	0	23.5	0
$\theta_{pq}(^\circ)$	23.5		
$\theta_{pq}^{cm}(^\circ)$	48.8		
$p_p(MeV/c)$	436.4		
$p_m(MeV/c)$	194.0		

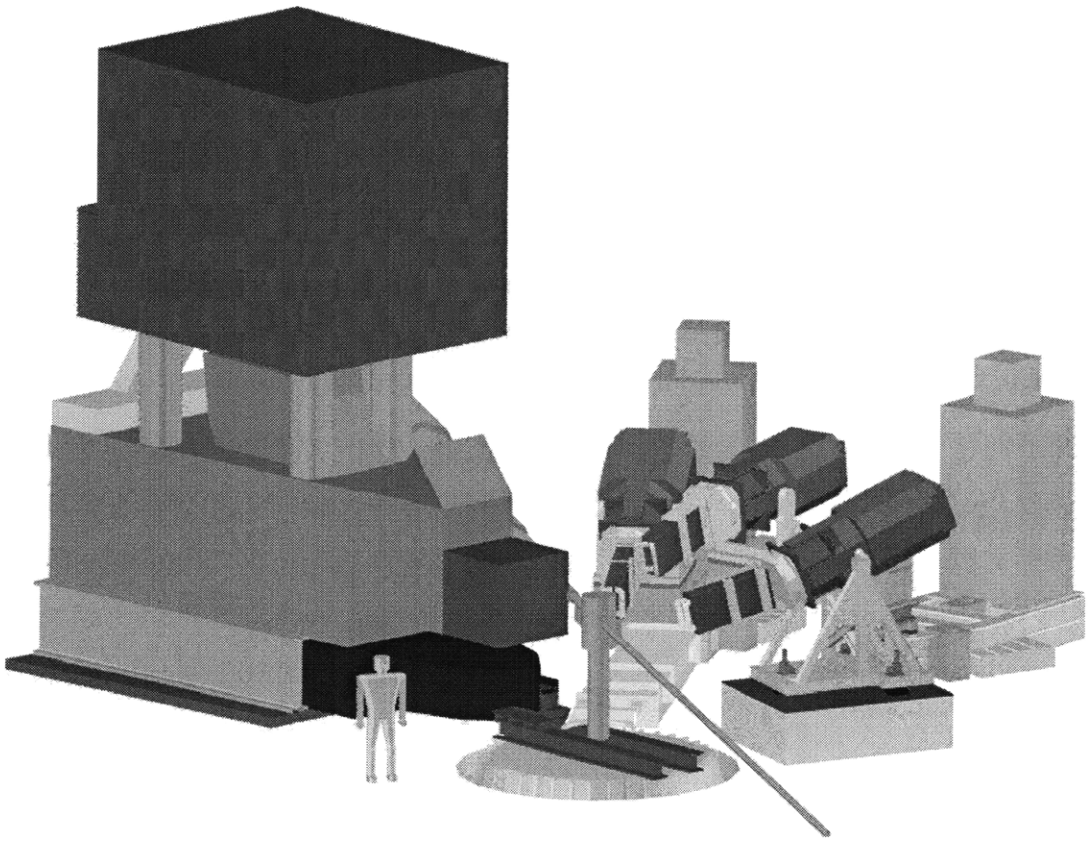

Figure 2-2: A schematic view of the experimental setup showing OHIPS and three OOPS modules.

2.2 Electron Beam

The experiment used a pulsed, polarized electron beam, which was produced by the polarized injector. Longitudinally polarized electrons are needed at the target. The electron spin precession in the beam line bending magnets has to be compensated for. It is also necessary to monitor all the beam quantities, such as the beam energy, halo, position, charge etc., which are described in this section.

2.2.1 Polarized Electron Source

The polarized electron source used in this experiment was similar to the ones in use at SLAC [51] and TJNAF. Longitudinally polarized electrons were produced by the photo-emission of electrons from a gallium-arsenide (GaAs) crystal bombarded by circularly polarized laser light.

GaAs is a semiconductor material with a valence band and a conduction band. The energy gap between the top of the valence band and the bottom of the conduction band is $E_g = 1.52\ eV$. When circularly polarized photons are incident upon a GaAs crystal, electrons with a given spin state are preferentially pumped into the conduction band due to angular momentum conservation. Electrons are emitted from the conduction band with a possible maximum polarization of 50%. The energy it takes for the electrons to escape the conduction band is about 2.5 eV. By treating the surface of GaAs with Cs and NF_3, this energy is reduced to a negative value. This procedure is called cesiation. Periodic recesiations are needed to maintain the quantum efficiency [1] of the crystal at an acceptable value. Typical quantum efficiencies were in the range of 0.5% to 2.0% for this experiment.

When the helicity of the incident photons changes, the helicity of the emitted electrons also changes. It allows for rapid electron helicity reversal.

[1] Quantum efficiency is the probability that an electron is emitted when a photon is incident upon the photo-cathode surface.

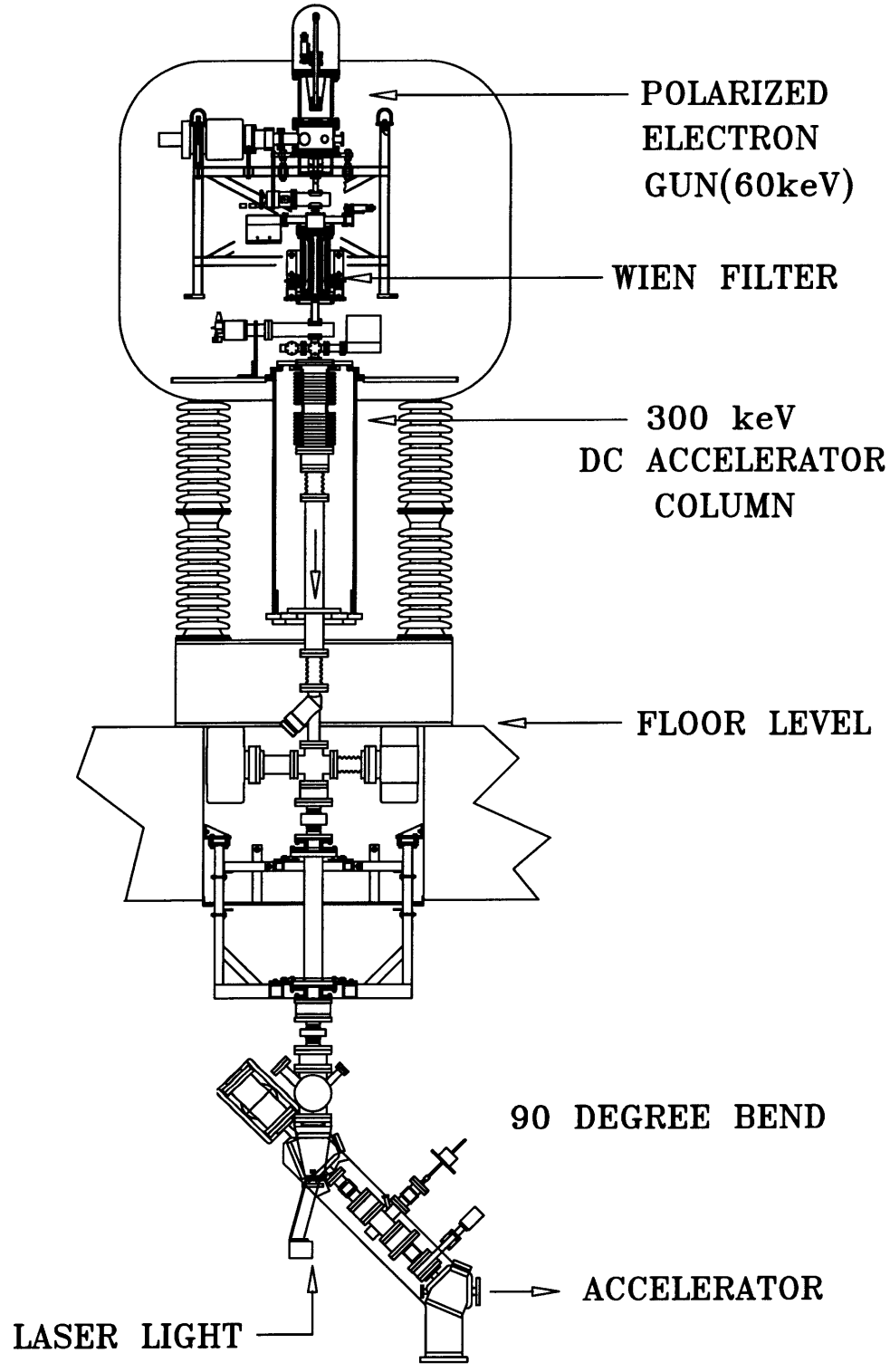

Figure 2-3: An elevation view of the Bates polarized electron source.

The laser system consisted of a Ti-sapphire laser driven by an argon laser, which delivered a photon beam at a wavelength of about 750 nm. Several optical elements were used to create circularly polarized light modulated to the duty factor of the accelerator. A shutter Pockels cell[2] was used to modulate the laser light. A helicity Pockels cell was used to convert linearly polarized laser light to right or left-circularly polarized light, depending on the polarity of the voltage applied to the cell.

The helicity of the beam was selected randomly on a pulse-by-pulse basis. For an electron beam with repetition rate of 600 Hz, the helicities of the first ten beam pulses were selected randomly, and the helicities of the next ten beam pulses were taken as the complement of the previous ten. This pseudo-random choice of the helicity states ensures that noise sources of any frequency in the experiment cannot couple to the asymmetry measurement. This also ensures that the total numbers of beam bursts with "+" and "–" helicities are equal.

An elevation view of the polarized source is shown in Figure 2-3.

2.2.2 Spin Precession

For this experiment, longitudinally polarized electrons were needed at the target. However, electrons are not necessarily longitudinally polarized at the target except for certain "magic energies" [3] due to the spin precession through bending magnets along the beam transport line. A Wien filter, coupled with the injector solenoids, was used to compensate for the spin precession caused by the bending magnets. In this section, we detail the principles of spin precession and Wien filter.

The equation of motion of the electron spin vector $\vec{s}$ through an electromagnetic

[2] A Pockels cell is an electro-optical device which introduces a phase retardation proportional to the voltage applied across the cell.

[3] "Magic energies" are beam energies chosen so that electron spins precess an integer number of half flips($\phi_s = \pi$) along the beam transport line from the polarized injector to the target.

field ($\vec{E}$ & $\vec{B}$) is given by Thomas's equation (Equation 11.170 of reference [52]):

$$\frac{d\vec{s}}{dt} = \frac{e}{mc}\vec{s} \times \left[\left(\frac{g}{2} - 1 + \frac{1}{\gamma} \right) \vec{B} \; - \; \left(\frac{g}{2} - 1 \right) \left(\frac{\gamma}{\gamma + 1} \right) \left(\vec{\beta} \cdot \vec{B} \right) \vec{\beta} \right. \\ \left. - \; \left(\frac{g}{2} - \frac{\gamma}{\gamma + 1} \right) \vec{\beta} \times \vec{E} \right] , \tag{2.1}$$

where $\vec{\beta} = \vec{p}/E$ and $\gamma = E/m$. This equation applies to a particle of total energy E, momentum $\vec{p}$, mass m, charge e and a magnetic dipole moment with a Landé g-factor. The direction of the spin vector is given in the rest frame of the particle, whereas $\vec{\beta}$ and the electromagnetic fields are given in the laboratory frame.

The spin precession angle $\Delta\phi_s$ with respect to the momentum of the electron can be found for a given magnet bending angle $\Delta\phi_{bend}$ as [55]:

$$\Delta\phi_s = \gamma(\frac{g}{2} - 1)\Delta\phi_{bend} \; , \tag{2.2}$$

where the Landé g-factor for the electron has the value of 2.002319304.

Figure 2-4 is a simple schematic of the Bates beam transport line. Since the recirculator was used in this experiment, the electron spin precession arose from

1. The 90° bend from the injector to the accelerator. Since the injection energy was small (360 KeV), the spin precession caused by this bend was negligible.

2. The 360° bend in the recirculator.

3. The 90° bend of the switchyard magnet that directed the beam into the South Hall B-line.

The final total spin precession angle is determined as

$$\Delta\Phi_s^{total} = (\frac{g}{2} - 1)(\gamma_M\phi_M + \gamma_f\phi_f) \; , \tag{2.3}$$

where $\gamma_M = E_M/m_e$, E_M was the electron energy before it entered the recirculator;

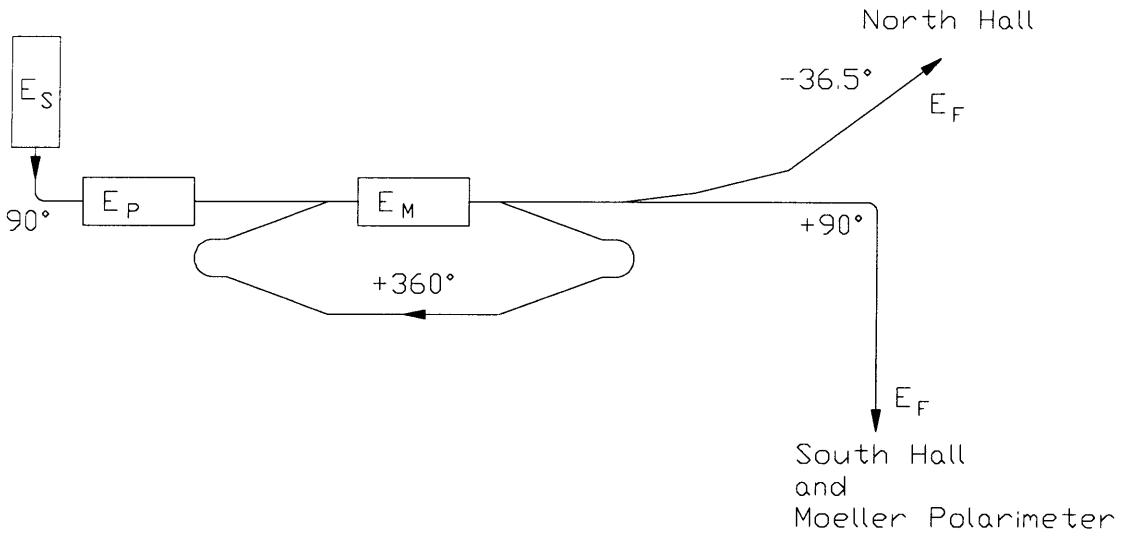

Figure 2-4: A schematic of the Bates beam transport line.

$\gamma_f = E_f/m_e$, E_f was the final beam energy; and $\phi_M = 360°$, $\phi_f = 90°$ are bending angles for the recirculator and the B-line switching magnets.

To compensate for the spin precession caused by the bending magnets, a Wien filter, coupled with the injector solenoids, was used to introduce a preset spin rotation before electrons entered the accelerator. The Wien filter was located just below the polarized injector floor.

A Wien filter is a device with independent E and B fields. The E and B fields are perpendicular to each other, and they are both perpendicular to the electron momentum. The E and B fields are adjusted in such a way that there is no net force exerted on the electrons, which requires

$$\vec{E} + \frac{\vec{v}}{c} \times \vec{B} = 0 \; . \tag{2.4}$$

Substituting this relation into Equation 2.1, the equation of motion of the spin vector inside the Wien filter becomes

$$\frac{d\vec{s}}{dt} = \frac{e}{mc}\vec{s} \times \left[\left(\frac{g}{2} - 1 + \frac{1}{\gamma} \right) - \beta^2 \left(\frac{g}{2} - \frac{\gamma}{\gamma+1} \right) \right] \vec{B} = \vec{s} \times \vec{\omega}_s \; , \tag{2.5}$$

$$\vec{\omega}_s \equiv \frac{e}{mc}\left[\left(\frac{g}{2}-1+\frac{1}{\gamma}\right)-\beta^2\left(\frac{g}{2}-\frac{\gamma}{\gamma+1}\right)\right]\vec{B}\,, \tag{2.6}$$

where ω_s is the angular velocity of the electron spin rotation inside the Wien filter.

If the effective path length for electrons inside the Wien filter is L, the time that electrons travel through the Wien filter is L/v. Then the spin precession angle induced by the Wien filter is

$$\Delta\Phi_w = \frac{L}{v}\omega_s. \tag{2.7}$$

The E and B fields are set to compensate precisely for the precession of the spin produced by the dipoles in the recirculator and the experimental beam lines, and the field strength is determined by setting $\Delta\Phi_w$ and $\Delta\Phi_s^{total}$ equal but with opposite signs.

Solenoids were used to rotate the ϕ angle of the electron spin around the electron momentum direction. They were adjusted to ensure that the electron spin was always in the horizontal plane. The details are given in reference [53].

2.2.3 Energy Compression System

The electron injection energy was about 360 KeV. A single pass through the linear accelerator boosted the electrons up to 400 MeV. Since the maximum energy was greater than 400 MeV, the recirculator was used to accelerate the electron beam a second time. The final beam energy for this experiment was 800 MeV. Before the beam entered the switchyard, it traveled through the energy compression system (ECS). The ECS reduced the total energy spread and provided a reliable measurement of the beam energy.

The ECS consisted of a chicane, an energy defining slit and a RF cavity, as shown in Figure 2-5. The chicane was composed of four dipole magnets. As the beam passes through the dipoles, the more energetic electrons are deflected less than the least energetic ones. This introduces a path length difference for electrons with different

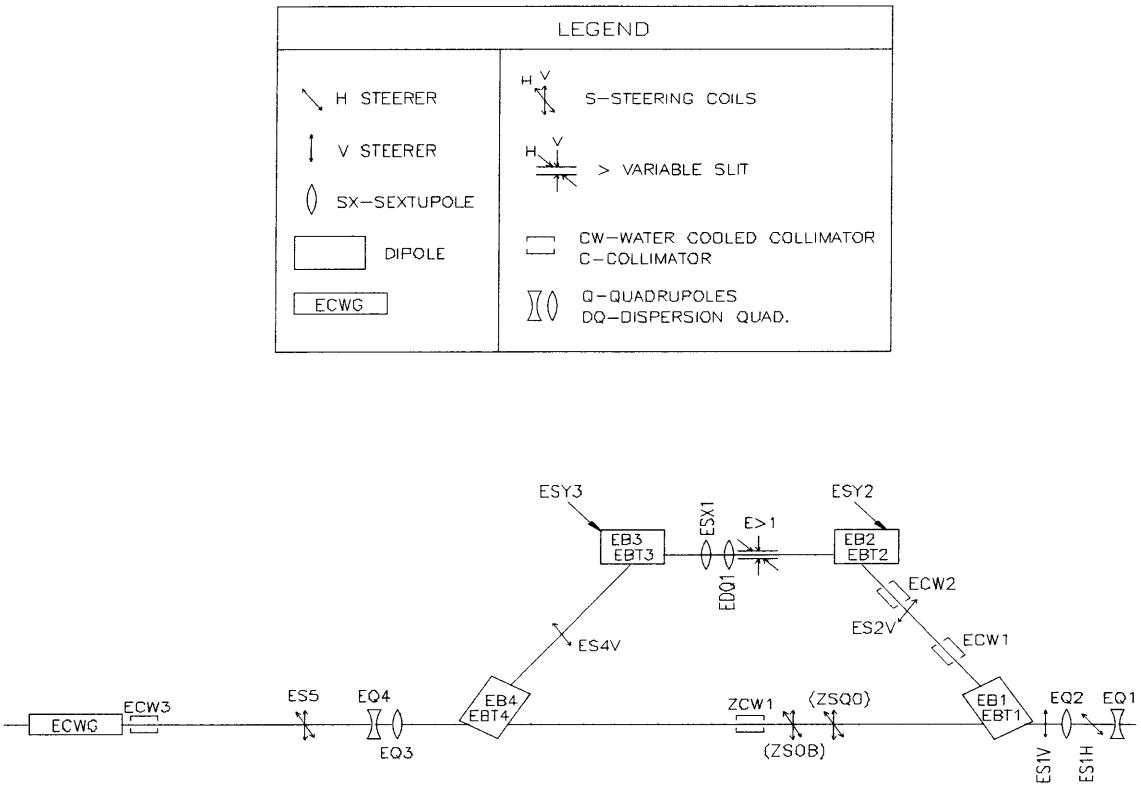

Figure 2-5: Schematic of the Energy Compression System.

energies. An RF cavity takes advantage of this phase difference and reduces the spread in the beam energy.

The energy defining slit was located between the second and the third dipole. By collimating the beam at this location, the maximum range of beam energies was selected.

2.2.4 Electron Beam Monitors

There were three ferrite-core toroidal transformers mounted on the beam line entering the South Hall. They are labeled as BT1, BT2 and BT3. These toroids provided a continuous non-interfering measurement of the beam current. BT1 was positioned about 10 m upstream of the Møller scattering chamber. BT2 and BT3 were about one meter upstream of the South Hall scattering chamber. Signals from BT1 and BT2 were digitized by ADCs to measure the beam charge pulse-by-pulse. The BT3

signal was sent to a BIC integrator in the counting bay to measure the total charge delivered during a given time and at the same time monitored the online average beam current. BT3 signals were not vetoed by the Computer Busy (CB) signal.

To accurately determine the beam charge, BT1, BT2 and BT3 were carefully calibrated. The calibration procedure was:

1. Each beam toroid had a built-in Q-loop. The current output from a precise charge pulser was fed to the Q-loop to simulate the pulsed electron beam. By varying the peak current and the pulse width of the charge pulser, the relation between the toroid ADC channels and the input charge was determined.

2. The charge pulser was calibrated against the BIC integrator, which was a very precise charge integrator with an accuracy of 0.1%.

It was found that the measured charge from BT2 and BT3 agreed with each other, but there were discrepancies between BT1 and BT2 of up to 1-2%, which was attributed to beam halo.

Two NIKHEF beam position monitors (BPM) were mounted about 2 m and 12 m upstream of the target chamber. They provided information on the horizontal (X) and vertical (Y) positions of the electron beam. It was also possible to monitor the beam incoming angle relative to the beam line. The devices can monitor the beam position to better than 1 mm. The analog signal outputs of the BPMs (one each for X and Y) were digitized and histogrammed. The centroid of the resulting pulse-height distribution provided a measure of beam position. Both BPMs were calibrated against a LUTE during the experiment. Unfortunately, later off-line data analysis revealed significant discrepancies between positions measured by the BPMs and the actual positions (as determined from the illuminated spot on the BeO target).

Two scintillator/photomultiplier tubes (PMT) were attached to the beam line as beam halo monitors. One was located upstream of the Møller scattering chamber, the other one was upstream of the South Hall scattering chamber. The output of the

PMTs were digitized and histogrammed. One could use the beam halo spectra to help guide the accelerator operators in tuning the beam.

2.3 Cryogenic Target

2.3.1 Overview

The M.I.T. Basel loop target was used for this experiment. It had two loops; one was filled with liquid hydrogen, and the other with liquid deuterium. Liquid hydrogen was used for calibration and normalization purposes. Between the two loops was a solid target ladder with a ^{12}C, a BeO and a slant carbon target.

The target cell was made of Havar, an alloy of Cobalt(42.0%), Chromium(19.5%) , Iron(19.1%), Nickel(12.7%), Tungsten(2.7%), Molybdenum(2.2%), Manganese(1.6%) and Carbon(0.2%). The characteristics of the target cells are given in Table 2.4.

Table 2.4: Cryogenic target cell specifications.

Cell Diameter	1.6 cm
Out-of-plane Angle	-30° to 60°
Wall Material	Harvar
Thickness	0.17 mil (4.3 μm)
Density	8.32 g/cm^3

A schematic of the cryogenic target is shown in Figure 2-6. A similar target was user for several earlier experiments[13, 56]. Each loop consisted of a heat exchanger to cool the liquid, a heater to keep a constant liquid temperature, two temperature sensors to measure the liquid temperature, an electric fan to circulate the liquid and a sensor to monitor the target pressure. A 200-Watt Koch model 1420 refrigerator provided cooled Helium gas for the heat exchangers. The two loops were cooled in tandem.

For each target cell, a carbon glass resistor temperature sensor was located im-

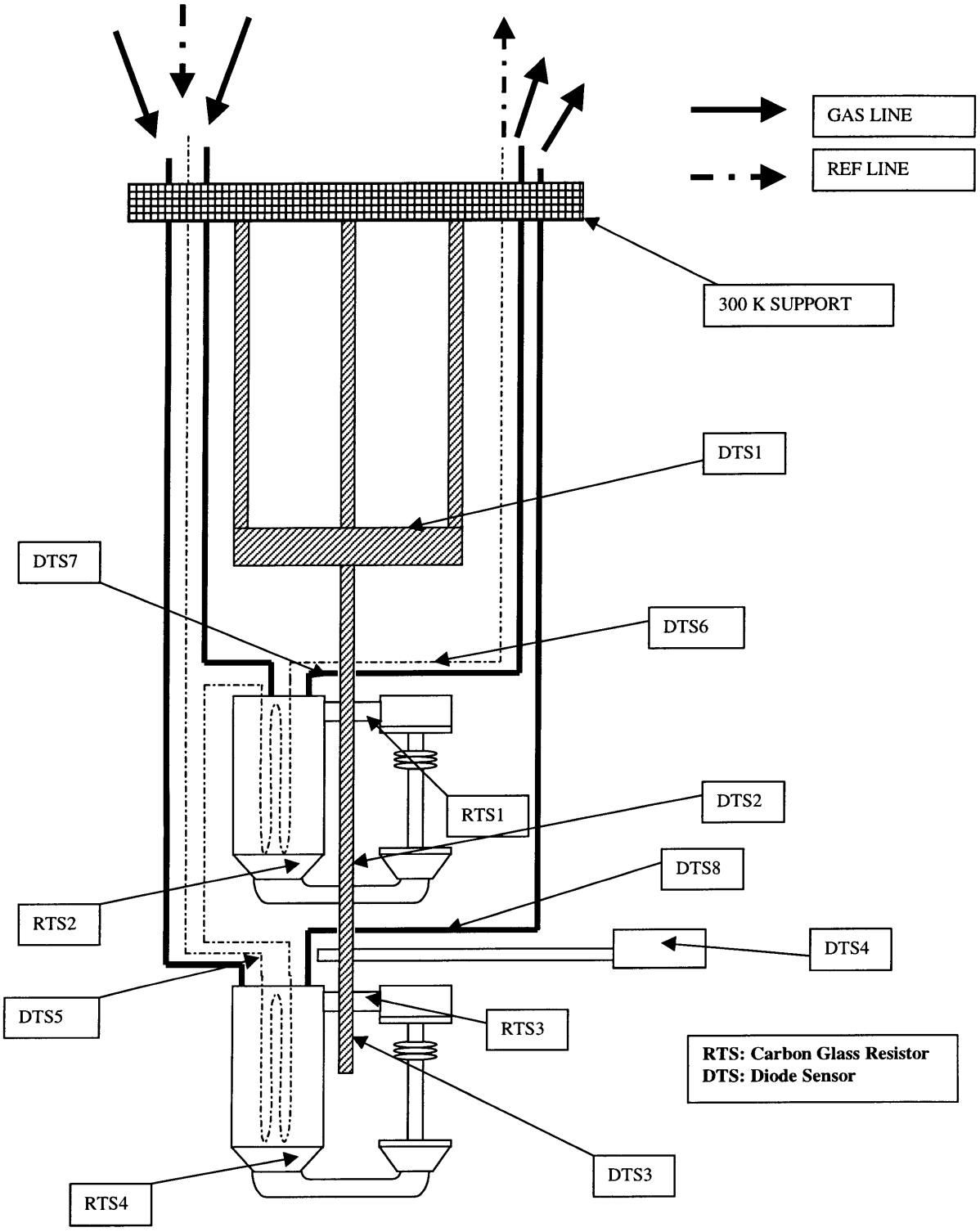

Figure 2-6: Schematic of the M.I.T.-Basel Loop Target.

mediately downstream of the heat exchanger while another was located immediately downstream of the heater and fan. Their accuracy was within 0.1° K. Eight diode temperature sensors were placed through out the target system. Diode temperature sensors are less accurate and more susceptible to radiation damage but are significantly less expensive than the carbon glass resistor sensors.

The target cells were filled through a gas handling system. Some of the valves of this system were remotely controlled from the counting bay. When the target pressures were too low or too high, hydrogen or deuterium could be added to or released from the cells without going into the experimental hall.

The target instrumentation was monitored and controlled by a PC. The computer was located in the counting bay and ran a LabView Virtual Instrument program. Through a GPIB (General Purpose Interface Bus), this program controlled two ADCs and two Lakeshore temperature controllers. The ADCs digitized signals from the vacuum gauges, pressure transducers, temperature sensors and the beam toroid. Once a minute, the program wrote information to a CAMAC module over a serial port. The information written included the date and time, the top and bottom temperatures of the target cells and the pressure for each cell. The target information was Event 13 in the data stream. With this information, the liquid hydrogen or deuterium temperature and pressure changes were monitored constantly during the experiment and it enabled the target densities to be accurately calculated.

2.3.2 Target Thickness and Liquid Densities

The basic properties of liquid H_2 and liquid D_2 are listed in Table 2.5.

The equation for the density of liquid hydrogen was taken from [57]. The density of liquid parahydrogen in moles/cm^3 under the condition of liquid-vapor coexistence is

$$\rho_{LH_2} = \rho_c + A_1 \cdot \Delta T^{0.380} + A_2 \cdot \Delta T + A_3 \cdot \Delta T^{4/3} + A_4 \cdot \Delta T^{5/3} + A_5 \cdot \Delta T^2 \ , \quad (2.8)$$

Table 2.5: Properties of LH_2 and LD_2 targets.

	Liquid H_2	Liquid D_2
Nominal Temperature	20.3 K	23.7 K
Nominal Pressure	1 atm	1 atm
Atomic Mass	1.6737×10^{-24} g	3.3443×10^{-24} g
Scattering Density	0.071 moles/cm^3	0.080 moles/cm^3
Density	0.071 g/cm^3	0.160 g/cm^3
Stopping Power	5.6 MeV $\cdot$ cm^2/g	2.8 MeV $\cdot$ cm^2/g

for $T \leq T_c$ and

$$\begin{aligned}
\rho_c &= 0.01559 \text{ moles/cm}^3 \ , \\
T_c &= 32.976^\circ \text{ K} \ , \\
\Delta T &= T_c - T \ , \\
A_1 &= 7.3234603 \times 10^{-3} \ , \\
A_2 &= -4.4074261 \times 10^{-3} \ , \\
A_3 &= 6.6207946 \times 10^{-3} \ , \\
A_4 &= -2.9226363 \times 10^{-3} \ , \\
A_5 &= 4.0084907 \times 10^{-3} \ .
\end{aligned}$$

A similar equation for the density of liquid deuterium is not available. The equation below was determined by fitting the data taken from a plot in [58]. The density of liquid deuterium in moles of nuclei per cm^3 is

$$\rho_{LD_2} = \frac{0.210 - 0.002T}{N_A A_{LD_2}} \ , \tag{2.9}$$

for $19.0^\circ\ K \leq T \leq 24.0^\circ\ K$, where N_A is Avogadro's Number and A_{LD_2} is the atomic mass of deuterium.

2.4 OOPS Spectrometers

Three OOPS spectrometers were used for his experiment. They are all of identical design. A more detailed description of the design and the measured properties of the prototype OOPS can be found in [59, 60]. In order to investigate the systematic differences among the OOPS spectrometers, the same LT asymmetry was measured twice by swapping two OOPS's. It turned out that the basic characteristics are almost identical for all OOPS's. A detailed description of these measurements is presented in [61].

2.4.1 Design

The OOPS is a DQ (dipole-quadrupole) magnetic spectrometer. An elevation view of the spectrometer is shown in Figure 2-7.

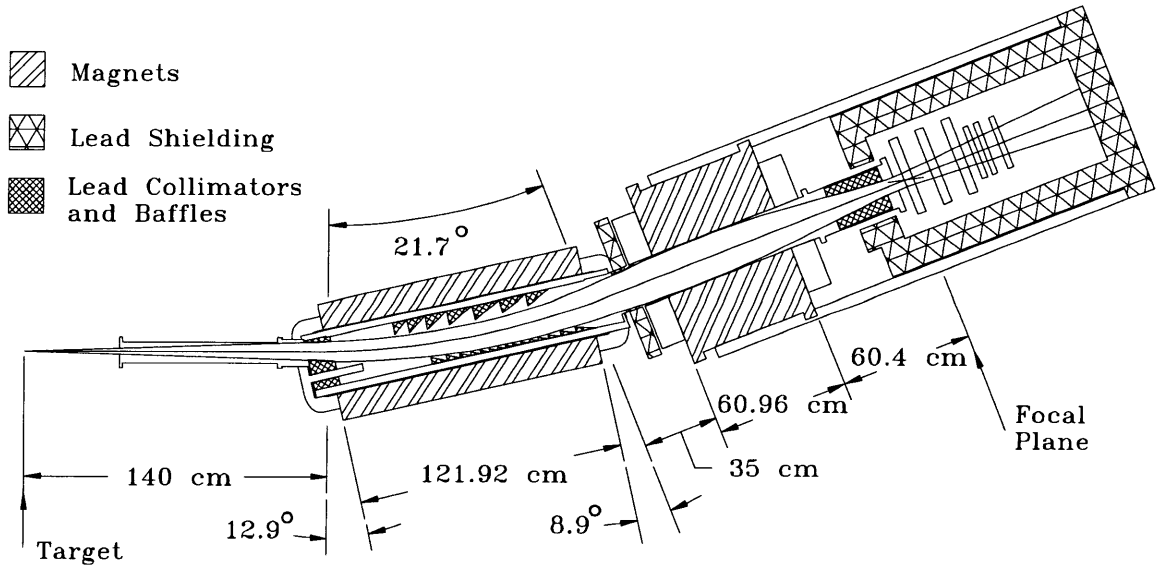

Figure 2-7: An cross section elevation view of OOPS.

The dipole magnet deflects particles through 21.7° with a 3.47 m bend radius. The detector system was enclosed in a lead compartment at the rear of the spectrometer. The compartment is made of 15 cm thick lead walls and is supported by a 5 cm thick

steel octagonal support tube. A baffling system was implemented in the dispersion plane of the dipole magnet to reduce the number of particles entering the detector system via small angle scatting.

The OOPS module is relatively light (~16 tons), which makes it easy to place out of the electron scattering plane. Its maximum central momentum is 832 MeV/c. The focal plane is tilted at an angle of 12.7° to the central ray and its dispersion is 0.22 cm/%. The OOPS momentum resolution is approximately 1%. Optics measurements performed with a sieve slit collimator have demonstrated angular resolutions of about 1 mr for both the in-plane and out-of-plane scattering angles. The OOPS design characteristics are given in Table 2.6. The measured optical matrix elements are listed in Appendix A.

Table 2.6: OOPS design characteristics.

Geometry	DQ
Solid angle	1.2 msr
Angular opening	±25.0 × ±12.0 mr
Initial drift distance	1.4 m
Total bend angle	21.7°
Total distance to detectors	4.2 m
Weight	16.0 tons
Dispersive plane optics	Point-to-point
"Flat" momentum bite	10.0 %
Focal plane angle	12.7°
δP/P	1.0 %

2.4.2 OOPS Detector Package

The OOPS detector system consisted of three horizontal drift chambers (HDC) and three scintillators. Three HDCs, each composed of two orthogonal wire planes, were used to track particles passing through the focal plane region of the spectrometer. Only two chambers were needed to give position and angle information about particle

trajectories, but three were used to increase the overall detection efficiency. Three plastic scintillators, with photomultiplier tubes on each end were located behind the three wire chambers. A six-fold coincidence was formed among the scintillator signals to generate the OOPS trigger and provided the timing fiducial for the HDC delay lines.

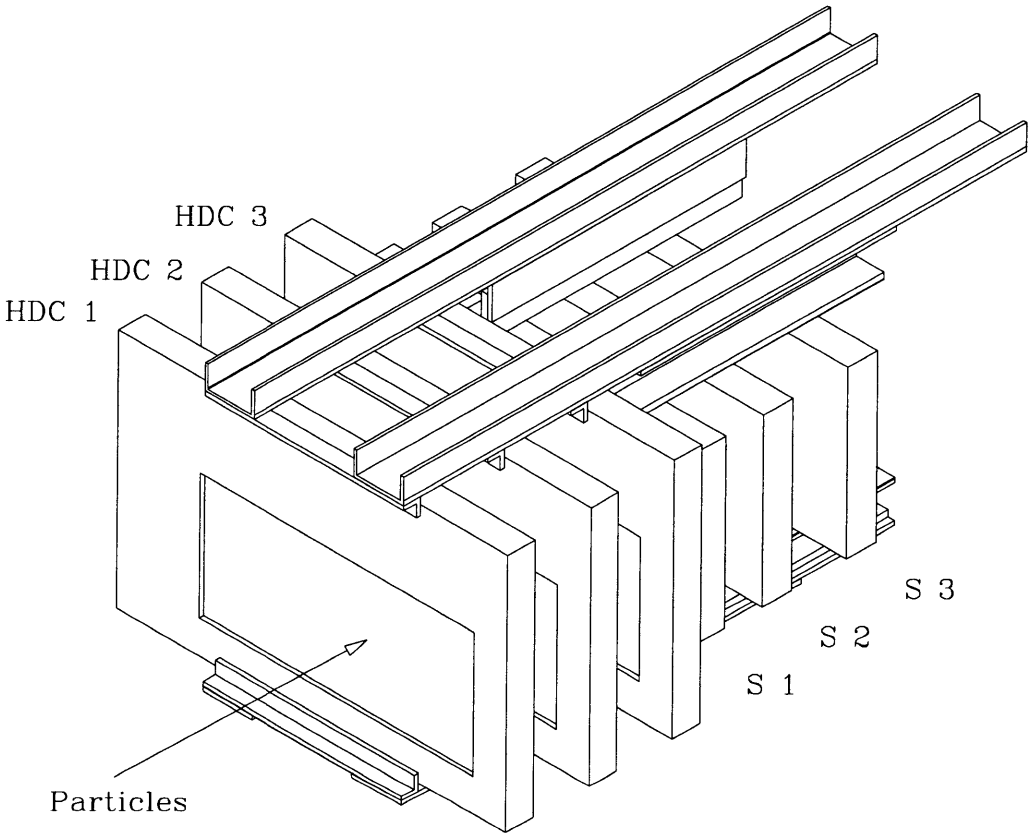

Figure 2-8: A schematic of the OOPS detector package. The OOPS detector system [62] consists of three horizontal drift chambers (HDC1-3), each containing two orthogonal wire planes, and three scintillators (S1-3) with photomultiplier tubes on both ends (not shown).

A schematic of the OOPS detector package is shown in Figure 2-8. The HDCs and scintillators are labeled as HDC 1–3 and S1–3 respectively. The thicknesses of the scintillators (1/16", 3/16" and 3/16" along the direction of the particle travel) allowed particle identification and detection of relatively low energy protons. Two U-shaped aluminum channels fixed to the top of the detector package form its rigid

spine. An aluminum plate mounted on the bottom forms a rigid surface to attach the package to the rail system. The modularity of the detector system aided in its easy removal and installation as well as providing a rigid unit that can be mounted in any spectrometer orientation.

2.4.3 OOPS Trigger and Electronics

The OOPS scintillator trigger logic is shown in Figure 2-9. One phototube each was mounted on the left and right end of each scintillator. A left and right coincidence signal was formed for each scintillator. A 3-fold coincidence signal was generated as the OOPS trigger.

The OOPS HDC readout was a delay line readout system. Each wire chamber had two delay lines (one delay line for each of the x and y planes). The logic pulse from the delay line served as the STOP signal for a TDC; the START signal came from the OOPS scintillator trigger.

The OOPS HDC's used the current pulses induced on the field-defining cathode wires (which alternate with the anode wires) to make a "left-right" decision (on which side of the signal wire the particle passed). Every other cathode wire in a wire plane was bussed together, giving two cathode output signals per plane. A voltage-sensitive differential amplifier measured the difference in the induced current for the two sets of cathode wires. The output from the amplifier was sent to an ADC. The ADC reading determined on which side of the signal wire the particle traveled. A detailed description of the OOPS HDC and the associated electronics can be found in references [62, 63, 64].

2.5 OHIPS Spectrometer

The One-Hundred-Inch-Proton-Spectrometer (OHIPS), as its name implies, was originally designed to be a proton spectrometer. Its focal plane detector was overhauled

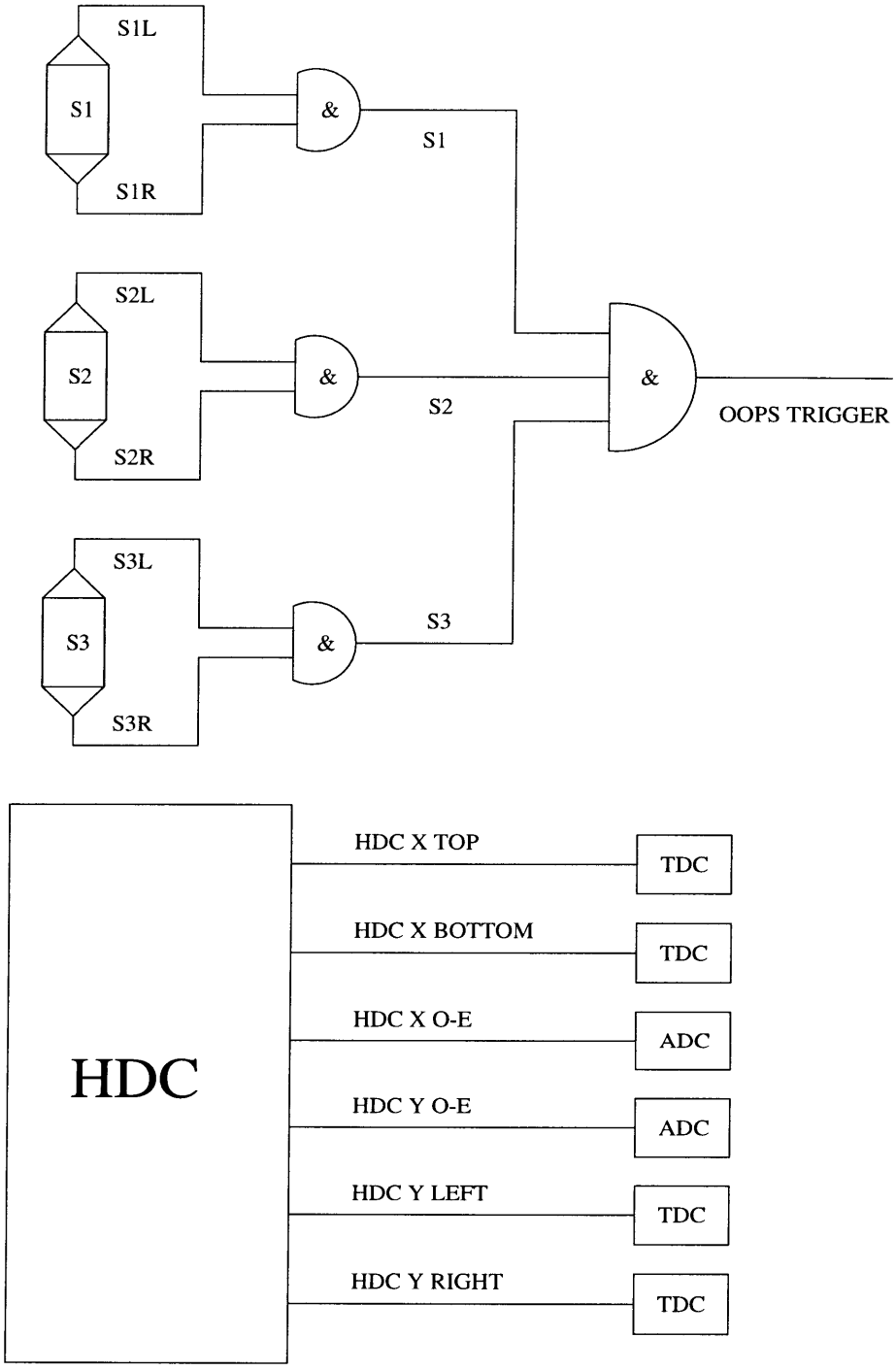

Figure 2-9: Logic diagram of the OOPS scintillator trigger and HDC readout system. A left and right coincidence signal was formed for each scintillator. A 3-fold coincidence signal was generated as the OOPS trigger.

and converted into a high efficiency, low background electron spectrometer. A second wire chamber, a Cherenkov detector and two layers of lead glass shower counter were added to the detector system. The details of the modification can be found in [68].

2.5.1 Design

OHIPS is a QQD (quadrupole-quadrupole-dipole) magnetic spectrometer. The layout of OHIPS and its detector package is shown in Figure 2-10.

OHIPS was designed to be a point-to-point focusing spectrometer in both bending and transverse planes. It has two quadrupole focusing modes. One is called the Normal Mode (Horizontal-Vertical mode). In this mode, the first quadrupole focuses in the transverse (horizontal) direction and the second quadrupole focuses in the dispersion (vertical) direction. The other mode is called the Reverse Mode (Vertical-Horizontal mode) which is just the opposite of the Normal Mode. In this mode, the first quadrupole focuses in the dispersion direction and the second quadrupole focuses in the transverse direction. The HV mode, focusing first in the transverse plane, provides a larger scattering angle acceptance and therefore a larger range of momentum transfer. On the other hand, the VH mode has a larger angular acceptance in the vertical direction and the variation in the momentum transfer vector would be more limited, which makes the forward and backward OOPS more symmetrical along the momentum transfer. It also provided a factor of 3 better scattering angle resolution than the HV mode. In return, it defined the momentum transfer direction better, which is essential for the A_{LT} and A_{TT} measurements. The VH mode was used in this experiment.

The front collimator was an 8-inch thick rectangular lead block. It had a 7.5cm $\times$ 17.3cm opening. Its distance to the target was 156 cm. The front collimator solid angle was 5.4 msr. The actual acceptance was reduced to about 4.34 msr because some internal spectrometer structures cut off the acceptance in the transverse direction. A summary of the OHIPS properties are listed in Table 2.7. Further information on

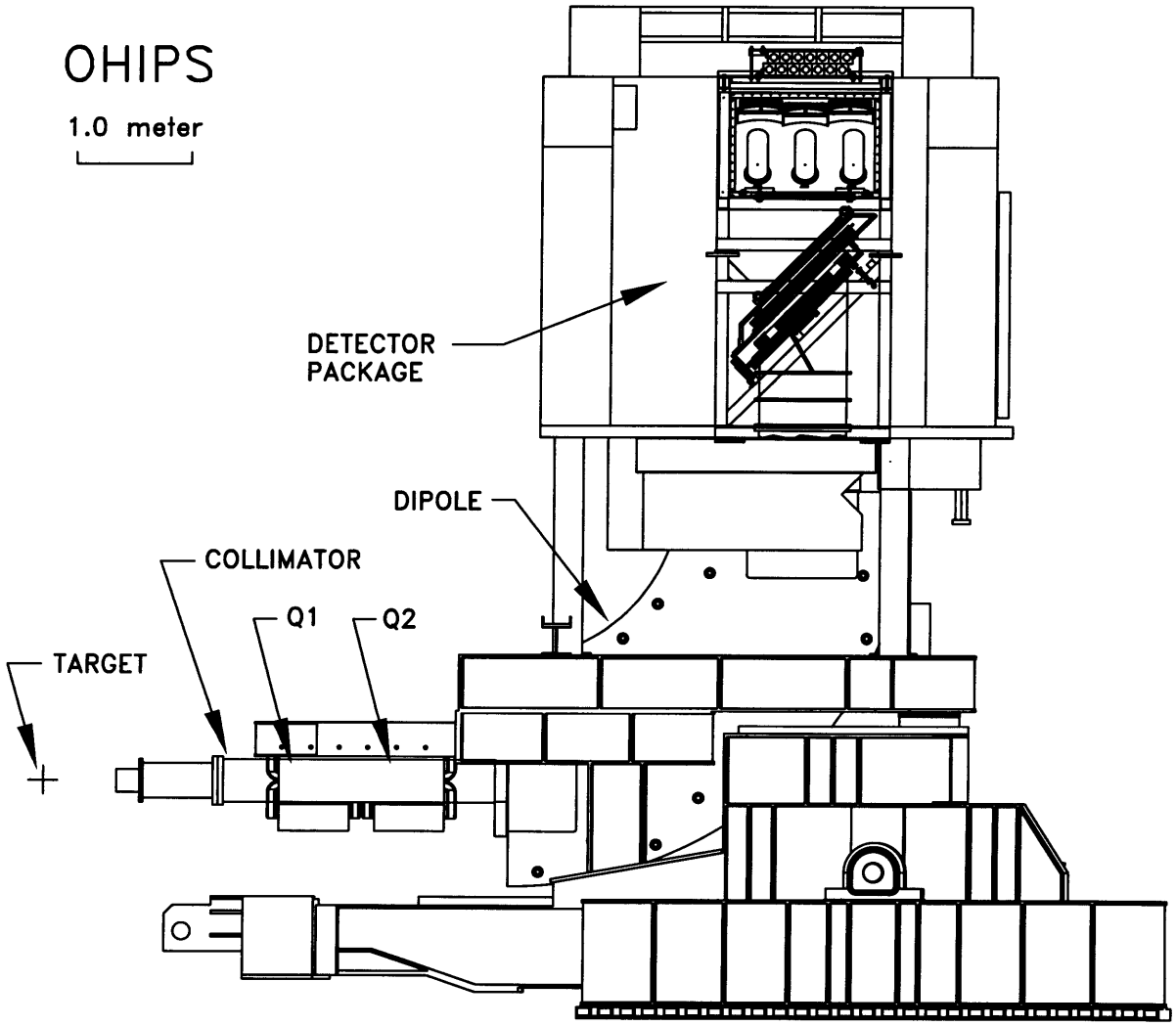

Figure 2-10: A schematic layout of OHIPS.

OHIPS can be found in reference [68].

Table 2.7: A summary of OHIPS properties.

Drift Distance	2.04 m
Quadrupole Focusing Mode	VH mode
Nominal Solid Angle	4.34 msr
θ Acceptance	$\pm 55.0mr$
ϕ Acceptance	$\pm 19.7mr$
Accessible Angular Range	$17° - 160°$
Maximum Central Momentum	1300 MeV/c
Maximum Momentum Acceptance(design)	$\pm 7.0\%$
Momentum Acceptance Instrumented	-4.75% *to* 4.0%
Momentum Resolution(FWHM)	1.18×10^{-3}
Radius of Curvature	2.54 m
Bending Constant	$77.82\ MeV/kG$
Bending Angle	90°
Path Length to Focal Plane	9.7 m

2.5.2 OHIPS Detector Package

The OHIPS detector package consisted of two cross-wire vertical drift chambers (VDCX1 and VDCX2), three scintillators (S1, S2 and S3), a gas Cherenkov detector and two layers of lead-glass shower counters. A schematic of the OHIPS detector package is shown in Figure 2-11.

The OHIPS scintillators were made of Bicron BC-408 plastic. Scintillator S1 and two VDCs were tilted at an angle of 45° with respect to the center line of the spectrometer so that they overlapped with the focal plane as much as possible to achieve an optimal spectrometer resolution. S2 and S3 were mounted on the front and rear of the Cherenkov tank. Each scintillator had two photomultiplier tubes, one on each side. A five-fold coincidence is formed among the scintillator signals to

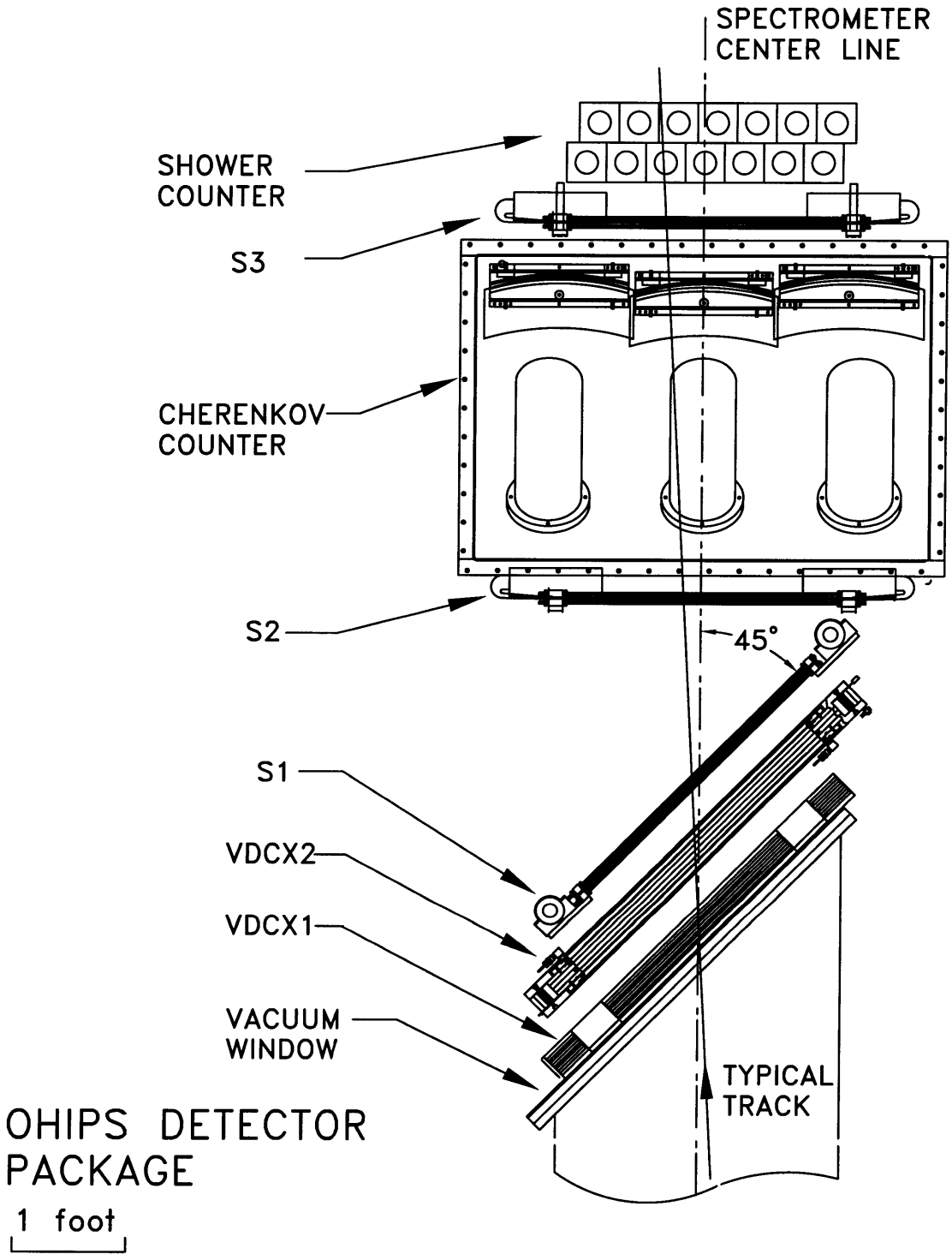

Figure 2-11: A schematic of the OHIPS detector package.

generate the OHIPS single arm trigger, and the left photomultiplier tube signal of S2 provided the timing of the OHIPS trigger.

Charged particle tracking in OHIPS was reconstructed by the two wire chambers, VDCX1 and VDCX2. They were mounted in parallel with each other with a separation of 0.1 m. Compared with only one wire chamber, two chambers provide better angular and position resolutions and higher efficiency.

The threshold gas Cherenkov detector and two layers of lead glass shower counters provided particle identification information.

2.5.3 OHIPS Trigger and Electronics

A DCOS wire chamber readout system was employed to measure the drift times. The DCOS system used was the LeCroy 4290 Drift Chamber Time Digitizing System.

The LeCroy 4290 system was a commercially available readout system for multi-wire drift chamber data acquisition. The system consisted of a dedicated CAMAC crate, amplifier-discriminator cards, time digitizer modules (LeCroy Model 4291B), control-readout units (LeCroy Model 4298) and CAMAC interface buffers (LeCroy Model 4299). The OHIPS DCOS readout system is illustrated in Figure 2-12.

DOCS was a relatively high density, low cost system. It allowed one TDC per wire readout for the drift chambers, thus eliminating the TDC corruption problems which often occur in a traditional delay line readout system when the event rate is too high. A detailed description of the DCOS encoding and decoding procedures can be found in [68].

A five-fold coincidence from Scintillators S1, S2 and S3 provided an OHIPS single arm trigger, it also acted as the common stop signal for the OHIPS wire chamber TDCs. The OHIPS single arm trigger logic diagram is shown in Figure 2-13.

The OHIPS single-arm trigger is called the pilot signal. The pilot signal was sent to the OOPS electronics system to form a coincidence with OOPS. If the OHIPS electronics did not receive a reply in 470 ns, the gate generator would issue a self clear

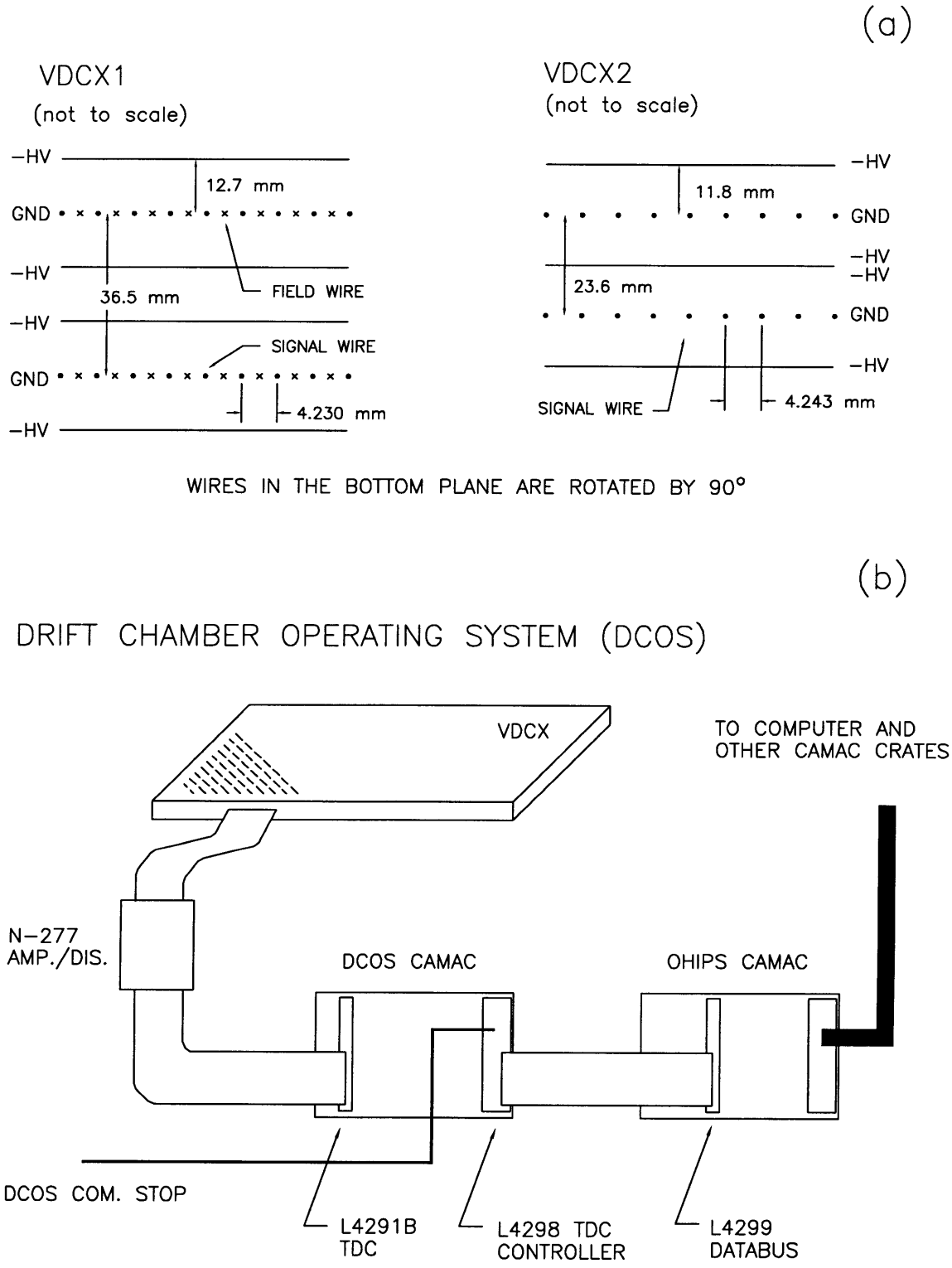

Figure 2-12: The OHIPS VDCX wire layout and DCOS readout system.

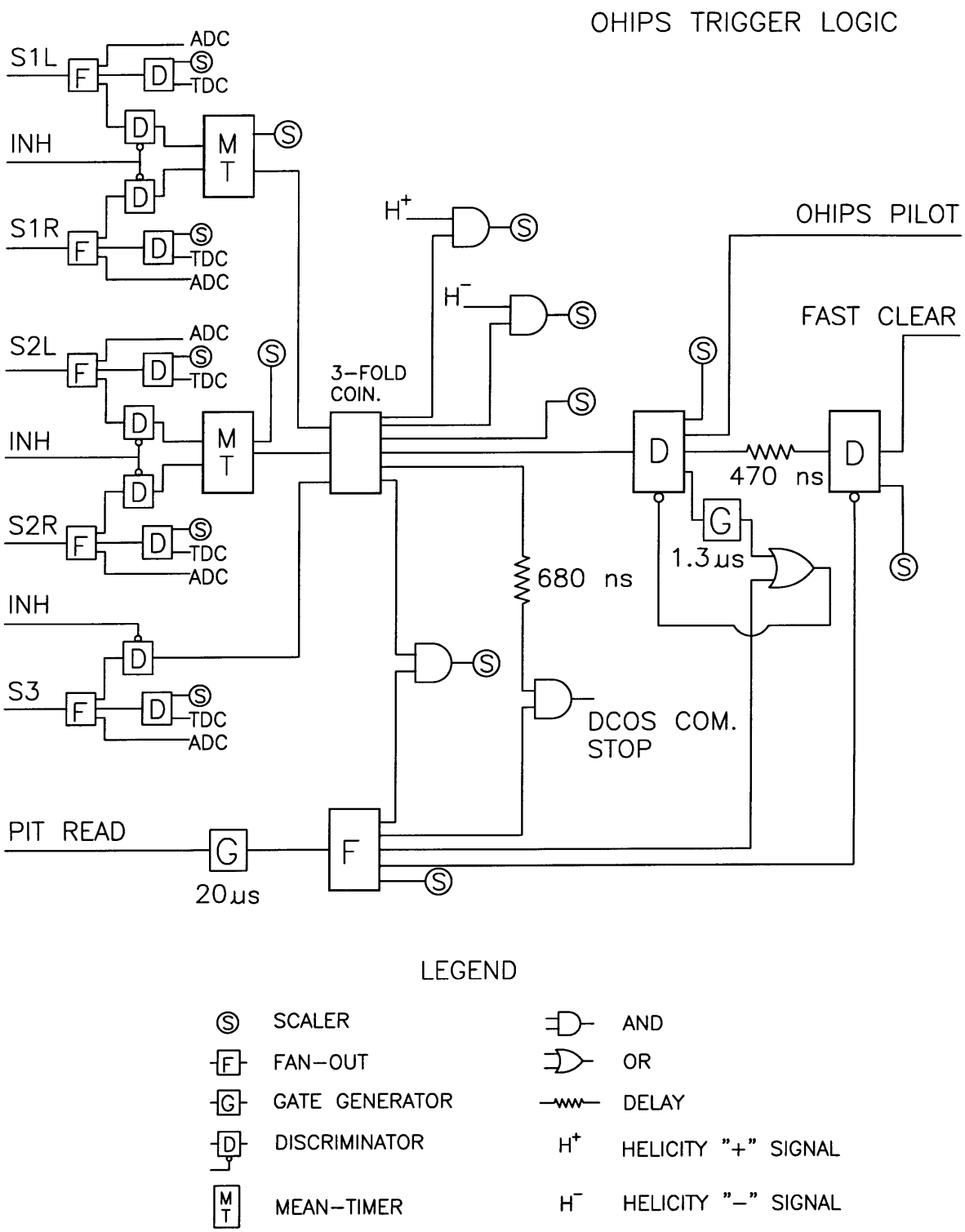

Figure 2-13: The OHIPS single arm trigger logic diagram.

signal to clear all OHIPS ADCs and TDCs. This prepared the OHIPS electronics for the next trigger. The self clear time was about 1.2 μs. During this time, all triggers were inhibited. The inefficiency caused by this inhibit is called the OHIPS self-inhibit inefficiency. The data were corrected for this inefficiency by using the related scaler information.

2.6 Coincidence Trigger and Electronics

The coincidence trigger circuit processed triggers from OHIPS and the three OOPS spectrometers. The logic diagram of the coincidence electronics is shown in Figure 2-14. OOPS A, B, C and OHIPS trigger signals were sent to a programmable logic unit. The logic unit can selectively perform "AND" or "OR" operations among any combination of the input signals. The coincidence signals between OOPS A, B, C and OHIPS together with OOPS A, B, C and OHIPS prescale signals formed the Event 8 trigger. The trigger signal, reshaped by a gate generator, was used to disable the "OR" logic modules, preventing the creation of further triggers during one beam burst. This is called the one per beam burst veto. At the same time, the trigger signal also served as the strobe for the latch word.

OOPS re-timing signals (from S2L of each OOPS), together with coincidence or OOPS prescale signals, formed the start signal to the time-of-flight TDC. The TDC was stopped by an OHIPS trigger.

In addition, the coincidence circuit has a number of other features:

1. It provided a 100 ns timing window to detect coincidence events between OOPS and OHIPS. Thus in addition to the true $(e, e'p)$ coincidence events, the accidental coincidences were also sampled extensively. This information was used to subtract the background in the time-of-flight spectra.

2. The coincidence triggers had the highest priority. They were always processed when the MBD and computer were available. The OOPS and OHIPS single-

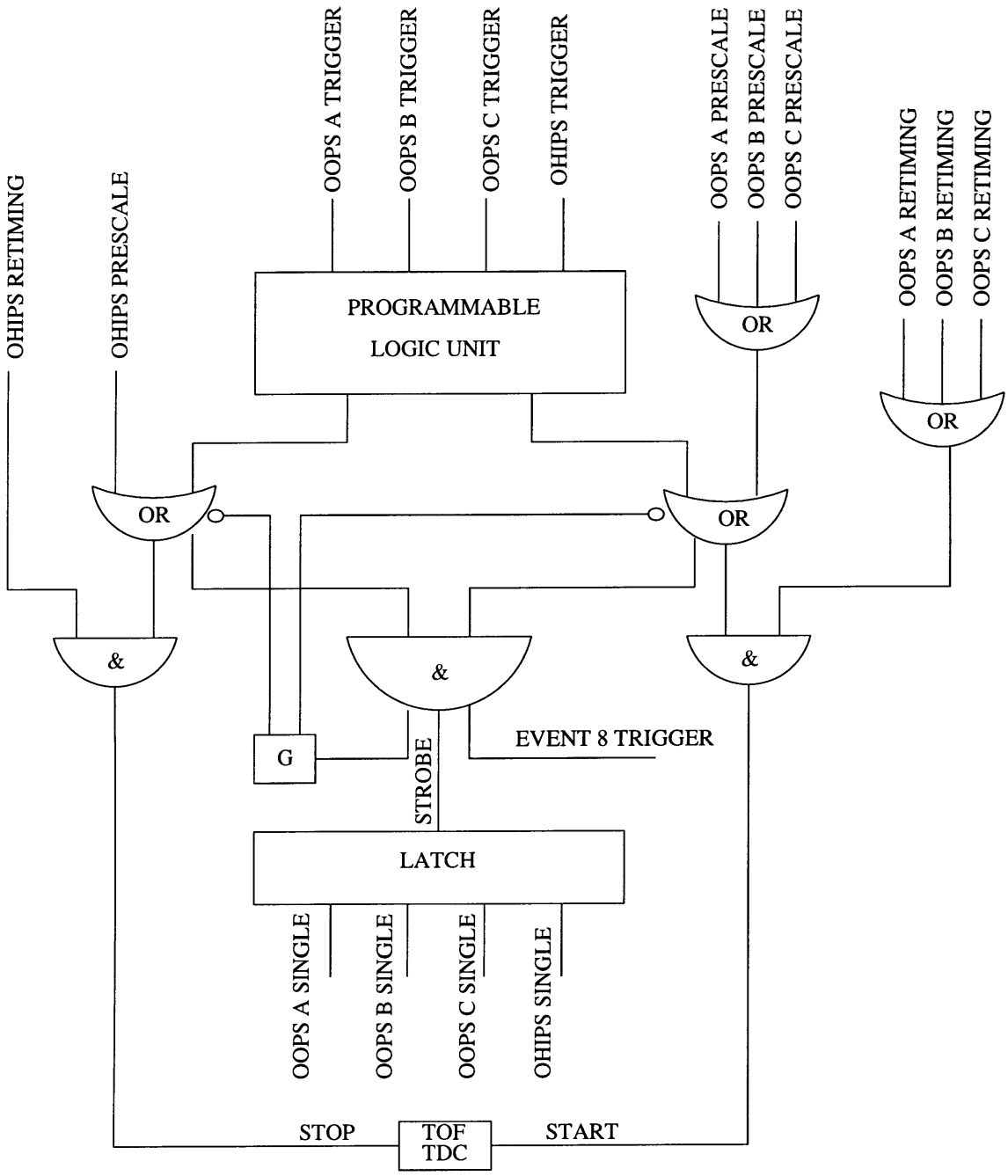

Figure 2-14: The logic diagram of the coincidence electronics.

arm events were processed only for a fraction of their occurrences, which were determined by the prescale modules. The prescaled single-arm triggers were the coincidences between the original single-arm triggers and the signals generated by a pulse generator. By adjusting the frequency and width of the pulse generator, the prescaling factors could be changed arbitrarily. By prescaling OOPS and OHIPS, one ensured that the data acquisition computer had time to accept practically all of the coincidence events; while at the same time, a small fraction of the single-arm events could be recorded to help monitor the behavior of the spectrometers.

3. The latch word was used to identify the event type according to whether it was an OOPS prescale, an OHIPS prescale, or a coincidence event, or a combination of these. The latch word was set by the single-arm or coincidence triggers and strobed by an Event 8 trigger.

4. The computer and the CAMAC modules could process only one event in each beam burst. It was achieved by the one per beam burst veto circuit. Once the circuit was activated, it would inhibit other triggers during the same beam burst.

5. It was possible to have more than one coincidence trigger during a beam burst, but only one coincidence event could be recorded for that beam burst. To correct for this inefficiency, scalers counted all the coincidence triggers which were not affected by the one per beam burst veto. In addition to the coincidence scalers, other scalers were used to count OOPS and OHIPS prescaled triggers and other useful information.

2.7 Data Acquisition and Experiment Control

The data acquisition system consisted of the electronics that formed the logic and digitization as well as the computers and software that controlled it. The computer used for the data acquisition was a MicroVax III workstation. The MicroVax was interfaced to CAMAC by a Microprogrammable Branch Driver (MBD), which did the actual data acquisition. A key piece of hardware needed for this system was the LAMPF CAMAC trigger module, which was used to identify an event type. There were four different event types. Event 5 was the scaler event, which was triggered every 10 seconds. Event 8 contained the OOPS and OHIPS detector readout data. It could be an OOPS singles, or an OHIPS singles or a coincidence event. Event 10 contained beam information, such as charge, position, halo and helicity. Event 13 had the target information. The event data structures are presented in Appendix C.

The data acquisition software was based on the "Q" system that was developed at the Los Alamos Meson Physics Facility (LAMPF) [65]. It included a histogram package, a test package, a dynamic parameter package, a data storage/retrieval package and some user-supplied subroutines. The user-supplied subroutines were used to extract all the scaler and target information, decode the wire chamber information and construct the focal plane and target coordinates of each event.

2.7.1 Experimental Control and Beam Line Electronics

An experimental gate controller was used to control the experimental data taking, as shown in Figure 2-15.

The experimental gate controller was connected to a CAMAC output register, which in turn was controlled by the Q data acquisition software. From the outputs of the gate controller, various gates and an Event 10 trigger were created. Two sets of BPM signals (TGTX, TGTY, MOLX and MOLY) and two beam toroid signals (BT1 and BT2) were digitized on a pulse-by-pulse basis and recorded in the data

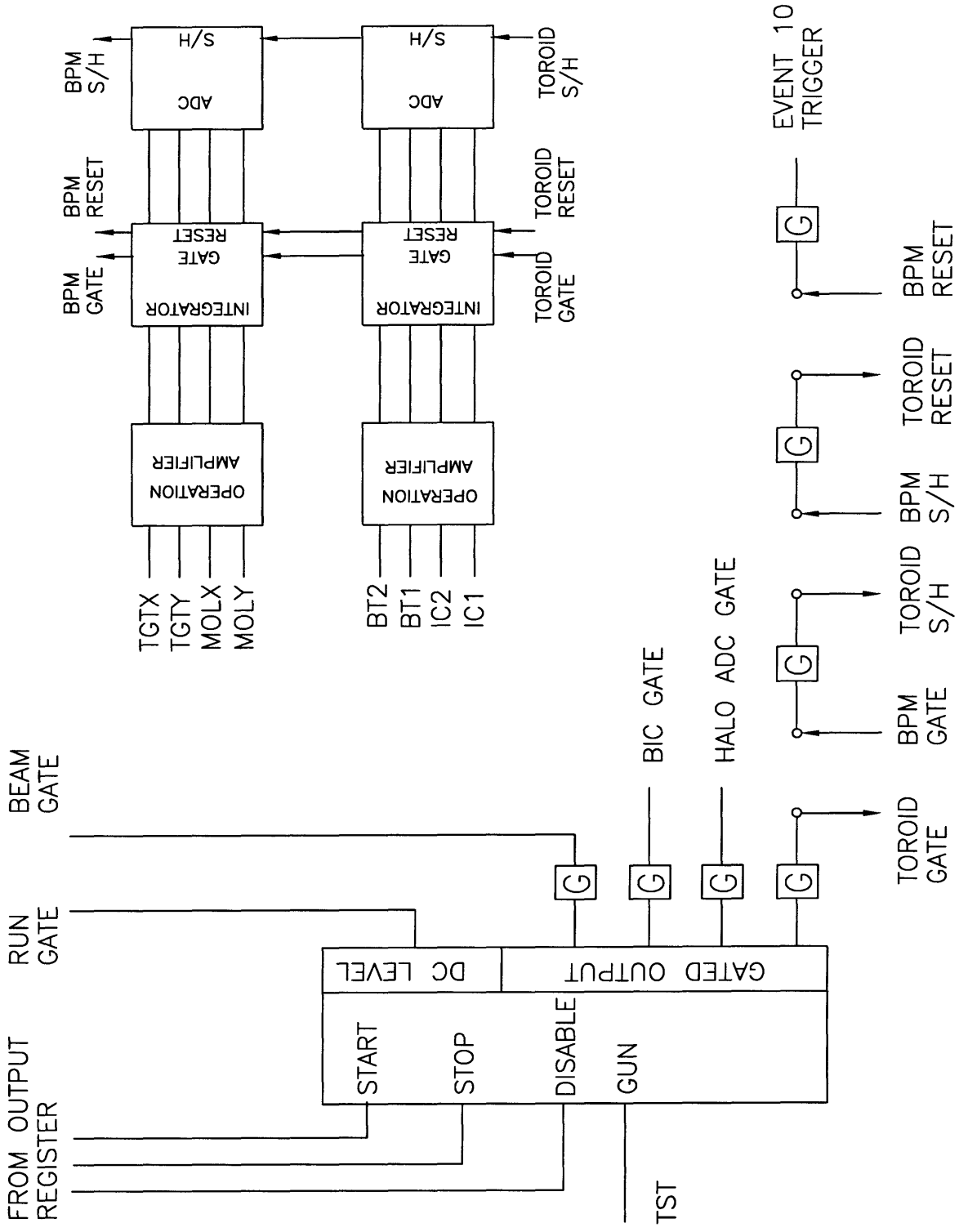

Figure 2-15: The experimental control and beam line electronics diagram.

stream. The integrators and ADCs were specially designed and built to provide long integration times.

The same electronics was also used for the Møller measurements. IC1 and IC2 were the two Cherenkov detector signals from the Møller polarimeter.

2.7.2 Front-end Veto Electronics

There were several considerations for the front-end veto design:

1. When the computer was busy with data taking, no additional events could be accepted. A veto signal was used to inhibit all the OOPS and OHIPS scintillator discriminators during this computer busy time. No new triggers were allowed during this period of time.

2. The beam gate was only open about 40 μs for every beam burst. This greatly reduced the background counts.

3. Since the charge for a fraction of a beam burst could not be accurately measured, the computer busy veto signal was extended to the end of a beam burst even if it occurred in the middle of the beam burst.

4. When an OOPS or OHIPS chamber high voltage tripped, data taking was stopped. This was achieved by connecting the chamber trip output (from the H.V. power supplies) to the disable input of the experimental gate controller.

The front-end veto electronics diagram is shown in Figure 2-16. This signal was used to inhibit all the OOPS and OHIPS scintillator discriminators. It means that whenever the computer was busy, or the beam burst gate was not present, or the run gate was not there, no single arm or coincidence triggers were formed. The extended computer busy was achieved by a gate generator. The gate generator was working in the trigger-reset mode. The leading edge of the computer busy signal triggered the gate generator, and the trailing edge of the computer busy or beam burst gate signal

reset the gate generator, whichever came later. The biggest advantage of this setup

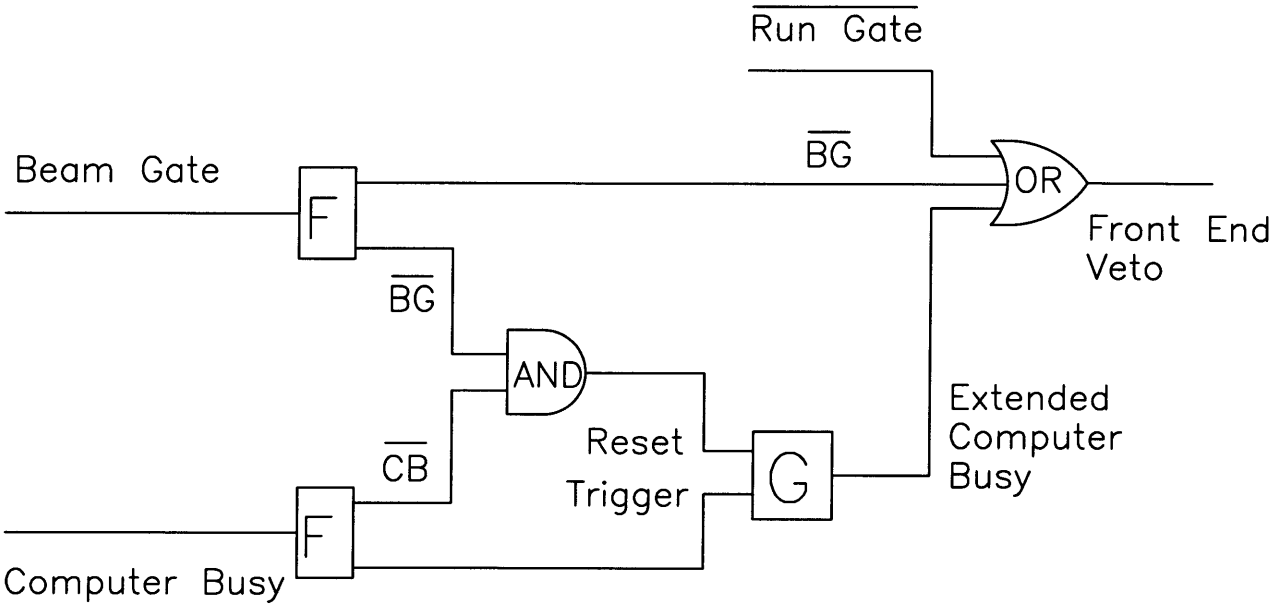

Figure 2-16: Front-end veto electronics diagram.

is that computer busy corrections were no longer needed for all the asymmetry and cross-section calculations, because when the computer was busy, no charge or events were accepted.

2.8 Møller Polarimeter

The B-line Møller polarimeter [66] was used to measure the electron polarization. The idea is to infer the electron polarization by measuring the asymmetry in the $\vec{e}(\vec{e}, e')$ elastic scattering cross section from a target of known polarization.

The Møller scattering cross section for polarized, elastic electron-electron scatter-

ing can be written as

$$\frac{d\sigma}{d\Omega} = \frac{d\sigma_0}{d\Omega}\left(1 + \sum_{i,j=x,y,z} P_B^i A_{ij} P_T^j\right) , \tag{2.10}$$

where P_B^i, P_T^i, $i = x, y, z$ are the beam and target polarization components respectively. The z-axis points along the beam momentum, and the y-axis is normal to the electron scattering plane. $\frac{d\sigma_0}{d\Omega}$ is the unpolarized cross section. To lowest order in QED and by using the ultra-relativistic approximations, the unpolarized laboratory cross section and the nine asymmetries are

$$\frac{d\sigma_0}{d\Omega} = \left[\frac{\alpha(1+\cos\theta_{cm})(3+\cos^2\theta_{cm}}{2M_e \sin^2\theta_{cm}}\right]^2 , \tag{2.11}$$

$$A_{zz} = -\frac{(7+\cos^2\theta_{cm})\sin^2\theta_{cm}}{(3+\cos^2\theta_{cm})^2} , \tag{2.12}$$

$$-A_{xx} = A_{yy} = \frac{\sin^4\theta_{cm}}{(3+\cos^2\theta_{cm})^2} , \tag{2.13}$$

$$A_{xz} = A_{zx} = -\frac{2\sin^3\theta_{cm}\cos\theta_{cm}}{\gamma(3+\cos^2\theta_{cm})^2} , \tag{2.14}$$

$$A_{xy} = A_{yx} = A_{yz} = A_{zy} = 0 . \tag{2.15}$$

Here θ_{cm} is the electron scattering angle in the center-of-mass frame, and $\gamma = \sqrt{(E+m)/2m}$, which is the Lorentz factor relating the center of mass and the laboratory frames. E is the incident electron energy, and m is the electron mass.

When $\theta_{cm} = 90°$, the asymmetries A_{xx}, A_{yy}, and A_{zz} are maximized whereas the cross terms A_{xz} and A_{zx} disappear. The polarimeter was used in such a way that the asymmetries were maximized. The laboratory electron scattering angle corresponding to $\theta_{cm} = 90°$ is

$$\theta = \arctan\sqrt{\frac{2m}{E+m}} . \tag{2.16}$$

For example, at $E = 800MeV$ for this experiment, $\theta = 2.05°$.

Figure 2-17 is a plane view of the Bates South Hall Møller polarimeter. It con-

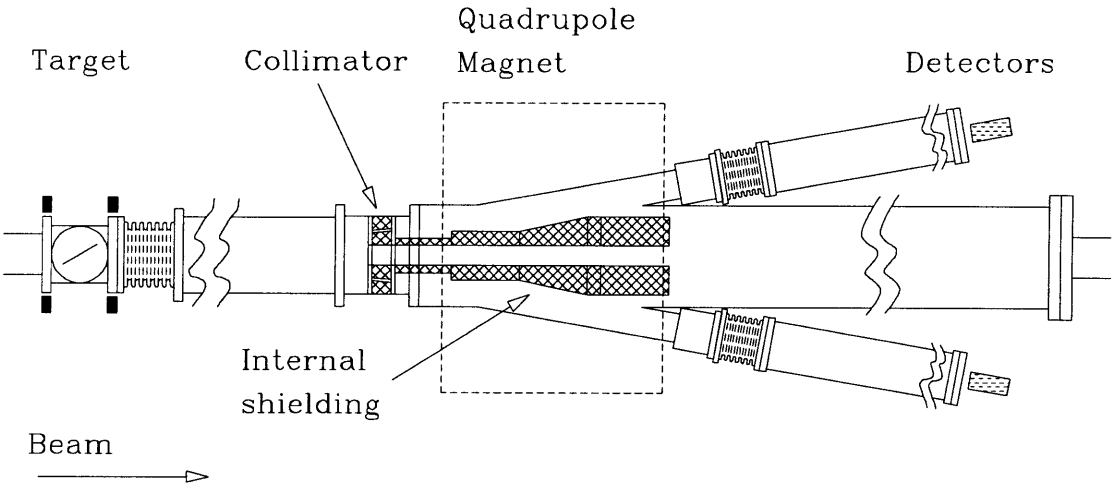

Figure 2-17: A plan view of the Bates South Hall Møller polarimeter.

sisted of a polarized target, a large bore quadrupole magnet to deflect the scattered electrons to larger angles, and two Cherenkov detectors for detecting the electrons. The polarized target was Supermendur alloy which can be magnetized to saturation in a relatively small magnetic field (~150 gauss). The target was surrounded by a set of Helmholtz coils which provided a uniform magnetic field. The target was rotated 30° relative to the beam line so that a large component of electron polarization existed along the beam. A 6-inch thick lead collimator was used to select the appropriately scattered electrons. There were four sets of holes in the collimator block which corresponded to four different scattering angles. By changing the distance between the target and the collimator, the beam polarization with different incident energies can be measured. Lead bricks were used in the bore of the quadrupole magnet to shield the detectors from the low energy background. The signals from the detectors were recorded by integrating the photomultiplier tube currents over the length of the incident beam pulse. The electric charge and helicity state of each beam pulse were also recorded. The same electronics setup was used to measure the beam polarization and to take the beam line information, which was discussed in more detail in section 2.7.1.

Chapter 3

Data Analysis Software and Methods

In this chapter, we discuss the data analysis software and tools, and describe how the OOPS and OHIPS wire chamber information was decoded. We also discuss the procedures for OOPS and OHIPS particle identifications. Successful Monte Carlo simulations are essential to understand the responses of the spectrometers. Monte Carlo simulations are used to calculate acceptance and radiative corrections. All aspects of the Monte Carlo simulation are discussed in the last section.

3.1 Data Analysis Software

The experimental data were taken with the Q data acquisition system. The online Q analyzer could be modified for the off-line data analysis, but this analyzer only ran on certain VAX machines and was very slow. A new off-line analyzer was developed in the object-oriented language C++. The advantages of a C++ analyzer are:

1. It is simple to write. The event data structures can make full use of the object-oriented design ideas.

2. It is easy to maintain. Each event class and its methods (functions) are relatively independent. Any changes in the data representation do not affect other parts of the program.

3. It can be easily ported to other machines. The analyzer runs on most platforms with little modifications.

The analyzer was developed on a Pentium PC running Red Hat Linux. All the data analysis was done on the same computer. A flow chart of the data analysis is shown in Figure 3-1, and the design of the analyzer can be found in Appendix D.

CD-ROMs were used to store and retrieve the experimental data, which greatly increased the data analysis speed. The analyzer read in raw data from a CD-ROM driver, then decoded the raw TDC and ADC information, and calculated the coordinates of the actual particle tracks in the spectrometers. Finally, the analyzer wrote the analyzed data event-by-event to ntuple files for further analysis. A program "h2root" was used to convert the ntuple files to a format that ROOT can interpret.

ROOT is a data analysis and histogram manipulating system developed at CERN (http://root.cern.ch). It is a successor of PAW and has a comprehensive package that provides a solid foundation on which large scale data analysis applications can be built. The ROOT system provides a set of object-oriented frameworks with all the functionality needed to handle and analyze large amounts of data in a very efficient way. Having the data defined as a set of objects, specialized storage methods are used to get direct access to the separate attributes of the selected objects, without having to manipulate the bulk of the data. Included are histograming methods in 1, 2 and 3 dimensions, curve fitting, function evaluation, minimization, graphics and visualization classes to allow the easy setup of an analysis system that can query and process the data interactively or in batch mode. The command language, the scripting, or macro language and the programming language are all C++. By using the ROOT system, we can extract asymmetries and calculate cross sections and response functions efficiently.

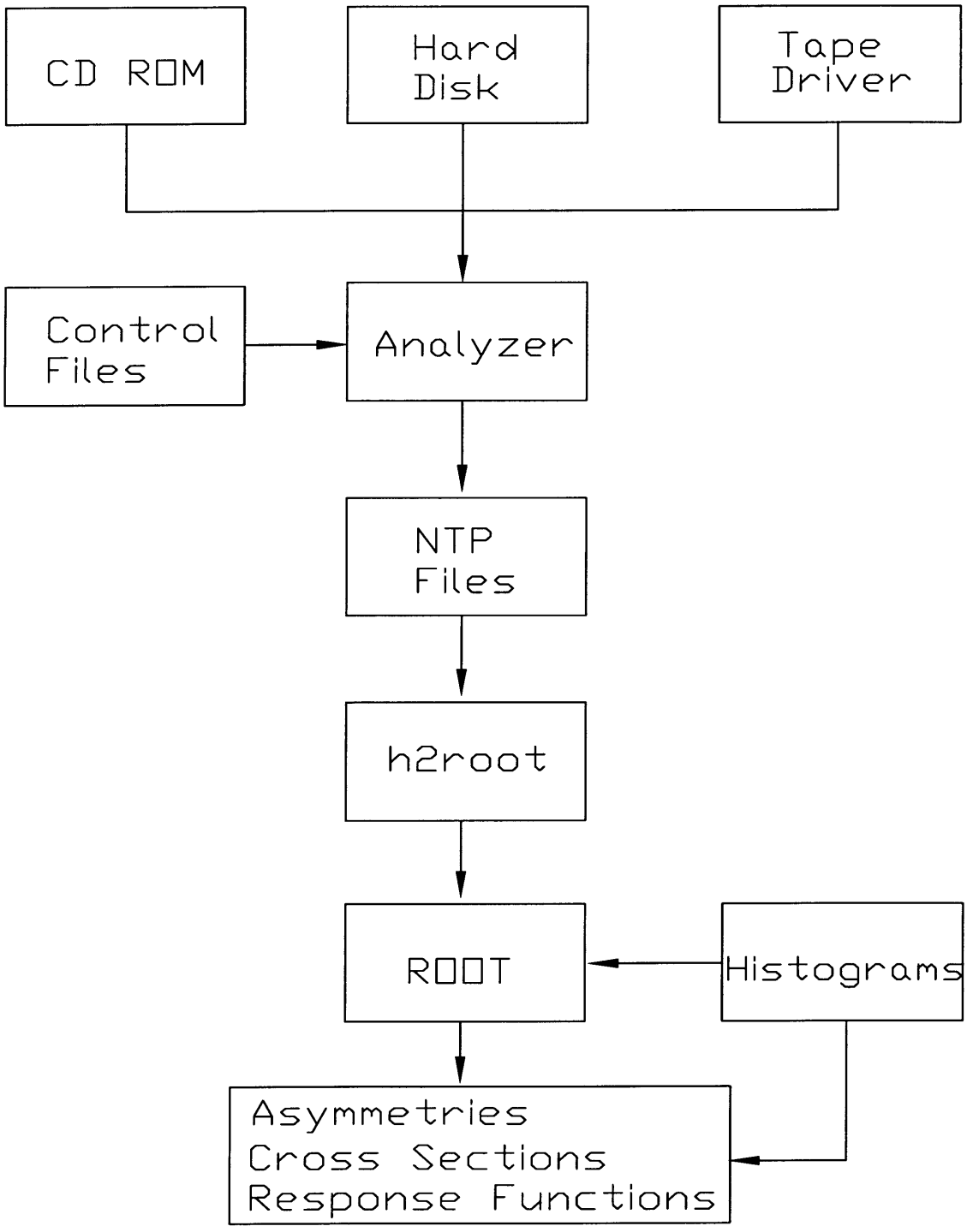

Figure 3-1: Data analysis flow diagram.

3.2 TRANSPORT Coordinates

TRANSPORT coordinates were used as the particle coordinate system in the spectrometers. At any specified position in the system an arbitrary charged particle is represented by a vector $(x, \theta, y, \phi, \delta)$. Here x is the horizontal displacement of the arbitrary ray with respect to the assumed central trajectory, θ is the angle this ray makes in the horizontal plane with respect to the central trajectory, y is the vertical displacement of the ray with respect to the central trajectory, ϕ is the vertical angle of the ray with respect to the central trajectory and δ is the fractional momentum deviation of the ray from the assumed central momentum.

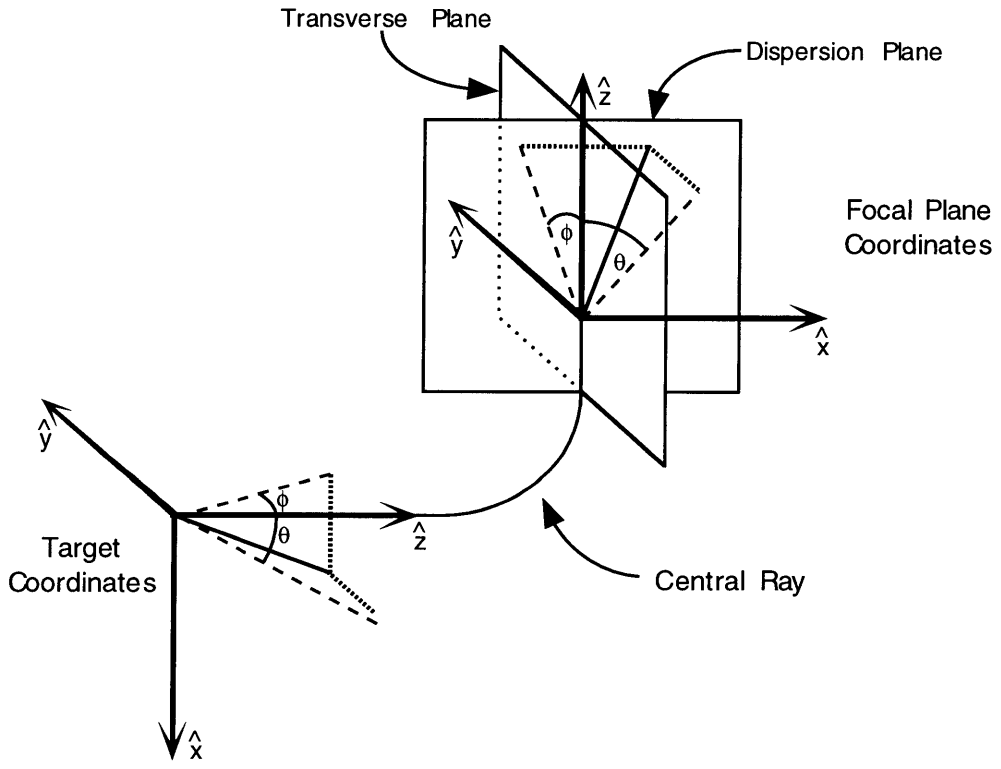

Figure 3-2: TRANSPORT coordinates at the target and at the focal plane.

There are two principle sets of TRANSPORT coordinates: the target coordinates and the focal plane coordinates. For vertical bending magnetic spectrometers such

as OOPS and OHIPS, the TRANSPORT target coordinates are x_t pointed toward the floor, z_t pointed to the spectrometer entrance and y_t is in the scattering plane. θ_t is the vertical angle and ϕ_t is the horizontal angle. Definitions of the TRANSPORT coordinates at the target and at the focal plane are shown in Figure 3-2.

3.3 Decoding OOPS HDC

The OOPS focal plane detector package used horizontal drift chambers (HDCs) to determine all particle positions and angles. Each HDC contained two orthogonal wire planes, an x wire plane and a y wire plane. Each wire plane was composed of alternating guard and signal wires. The guard wires were grounded, signal wires were applied a positive high voltage. The wire planes were sandwiched between two sets of thin aluminized mylar foils, which were also grounded. Each x wire plane had 21 signal wires, and each y wire plane had 49 signal wires. For each wire plane, all the signal wires were connected to a single delay line, even and odd numbered guard wires were attached to two different bus lines. A TDC was connected to each end of the delay line. The sum and the difference of the two bus line signals were sent to two ADCs to form left-right decisions. A single HDC chamber allowed the determination of x and y positions. The use of a second HDC allowed for the measurements of θ and ϕ angles and projection of the x and y locations to the focal plane. Figure 3-3 shows a typical proton trajectory passing through a wire chamber.

A gas mixture of 65% argon, 35% isobutane and 0.5% alcohol was used in the HDCs. When a charged particle transverses the chamber, it ionizes gas atoms. Electrons liberated from the gas atoms drift along the field lines toward the signal wire. The time measured from each end of the delay line (denoted as T_L and T_R) can be written as

$$T_L = T_{drift} + n\tau + T^L_{delay} , \tag{3.1}$$

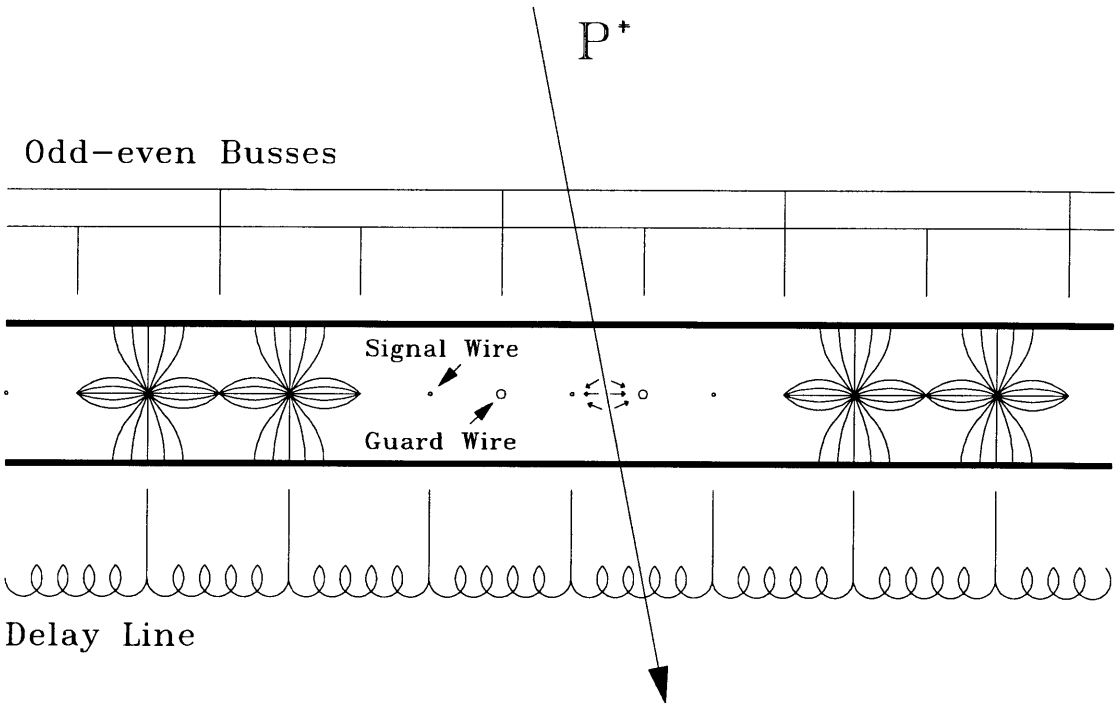

Figure 3-3: Schematic representation of a cross sectional view of the OOPS horizontal drift chambers.

$$T_R = T_{drift} + (N - n)\tau + T^R_{delay} , \tag{3.2}$$

where T_{drift} is the drift time for the electron to reach the signal wire, T^L_{delay} and T^R_{delay} are the sums of all electronic delays between two ends of the delay line and the TDC, n is the wire number that fired, N is the total number of wires in the wire plane, and τ is the delay time between two consecutive nodes on the delay line.

The wire number that fired is computed by subtracting Equation 3.2 from Equation 3.1 and solving for n:

$$n = \frac{T_L - T_R}{2\tau} + \frac{N}{2} - \frac{T^L_{delay} - T^R_{delay}}{2\tau} , \tag{3.3}$$

which is directly proportional to the time difference between the two ends of the delay line. Typical time difference spectra for an OOPS HDC are shown in Figure 3-4. From the figure, each individual wire that fired can be easily distinguished.

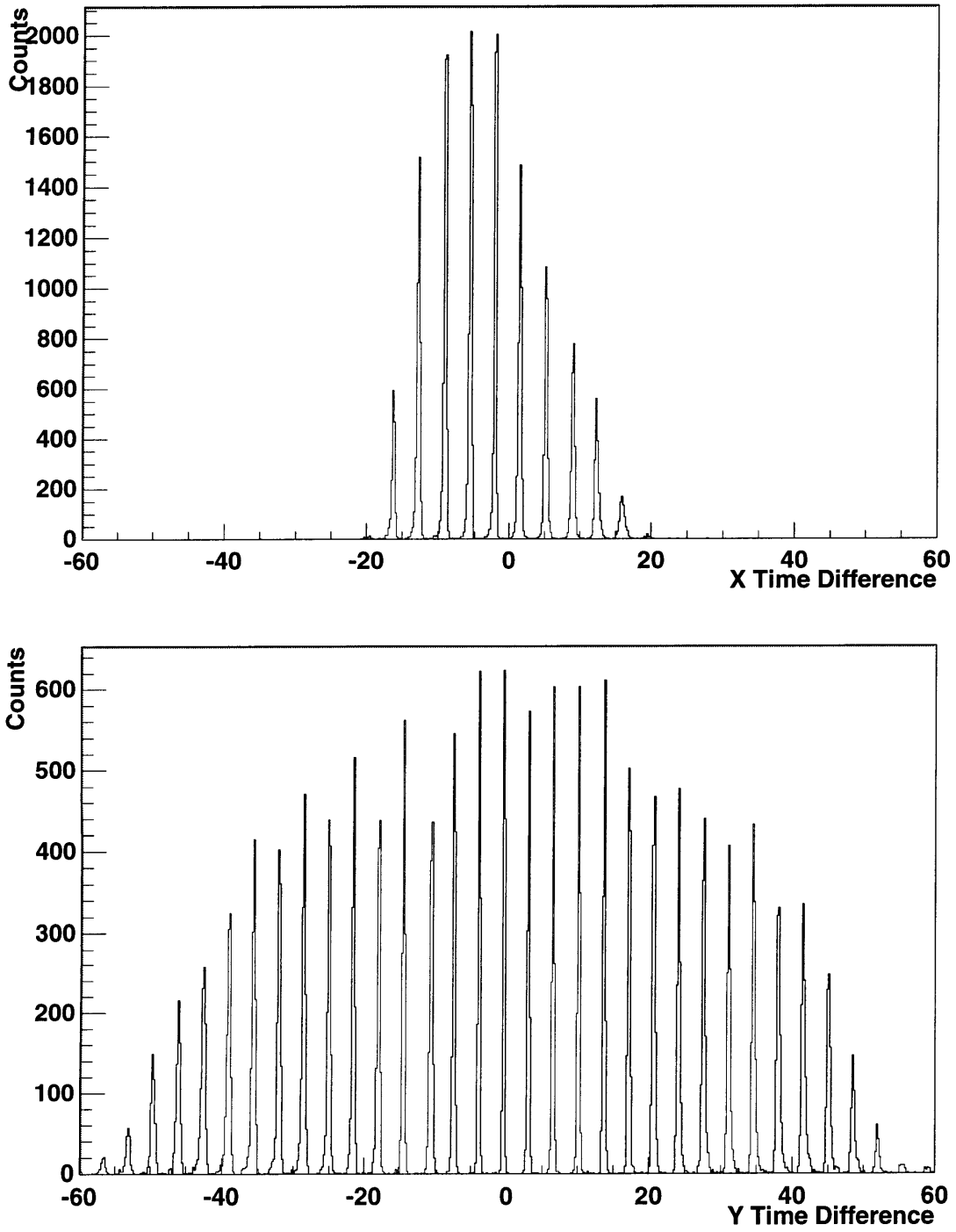

Figure 3-4: Typical OOPS HDC x and y plane delay line time difference spectra.

If one defines $T_{diff} = T_L - T_R$, the wire number n can be written as

$$n = a_0 + a_1 T_{diff} \ . \tag{3.4}$$

The parameters a_0 and a_1 for the wire planes of each wire chamber were calibrated. The center wire was labeled as wire number zero, which was the 11^{th} wire for the x wire plane and the 25^{th} wire for the y wire plane. The wire numbers are negative on the negative TRANSPORT x and y side and positive on the other side.

If the calculated wire number from Equation 3.4 was not an integer, the nearest integer was taken as the real wire number. The difference between these two numbers is a very important quantity, it gives the information about the goodness of the wire number fitting. It should center around 0, and the width should be no more than 0.5. Otherwise, something was wrong with the wire number fitting parameters, or the tracking was skewed. Simply putting a cut on this variable would eliminate most of the bad particle tracks.

The drift time for each delay line was obtained by adding Equation 3.1 and 3.2,

$$T_{drift} = \frac{T_L + T_R}{2} - \frac{N\tau}{2} - \frac{T^L_{delay} + T^R_{delay}}{2}. \tag{3.5}$$

The drift time was converted to drift distance by using a lookup table. Figure 3-5 shows typical drift time and drift distance histograms for one of the delay lines.

One of the special features of the OOPS HDCs was the ability to distinguish whether the charged particle passed on the right or on the left side of the wire. The details of the electronics which were used for this can be found in Section 2.4.3. A typical spectrum of the odd–even signal is presented in Figure 3-6.

Once the wire number that fired is known, so is the drift distance from the hit point to the signal wire. The positions (x and y) can be calculated as

$$x \ = \ nd + offset \pm D \ , \tag{3.6}$$

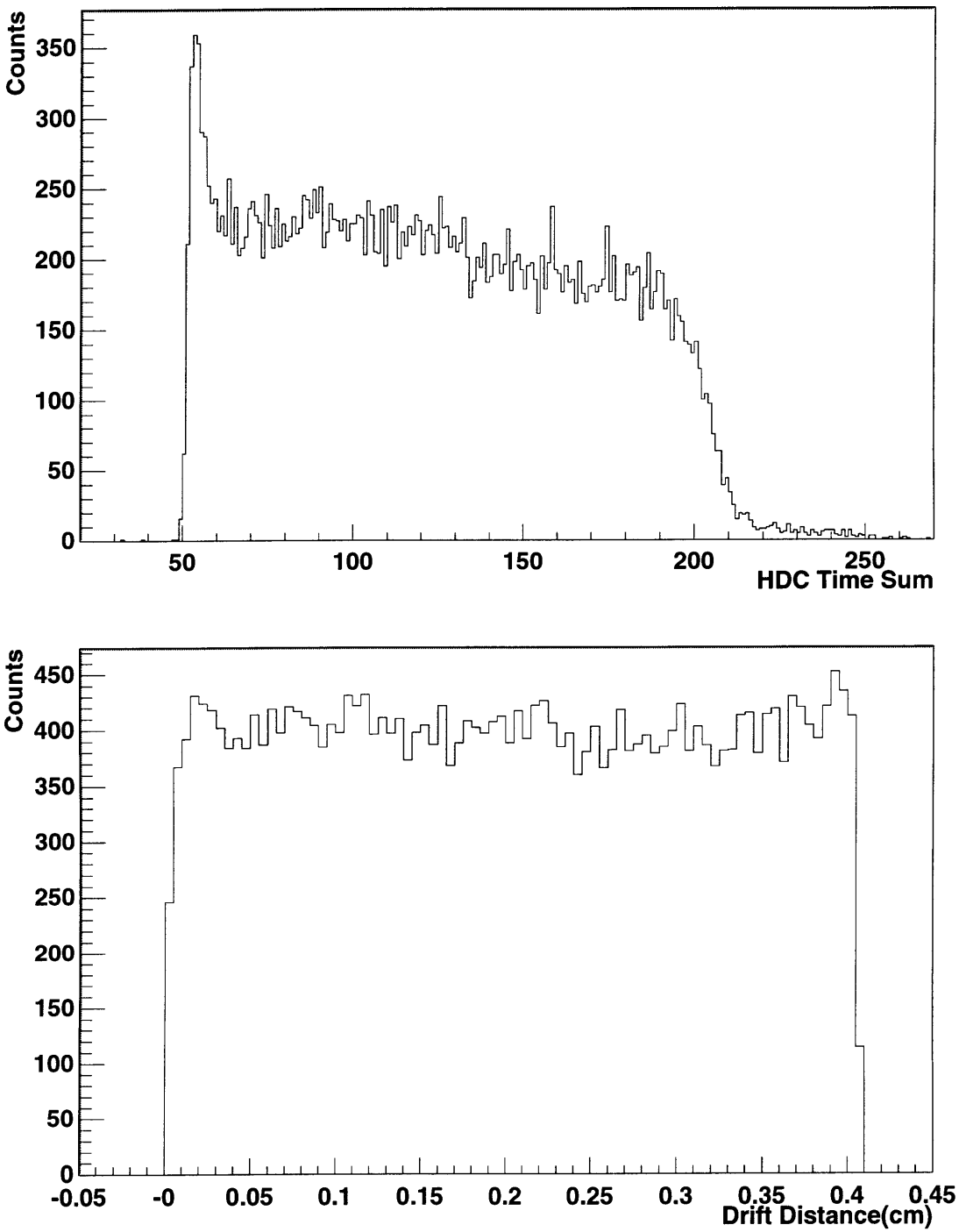

Figure 3-5: Typical OOPS HDC drift time and drift distance spectra.

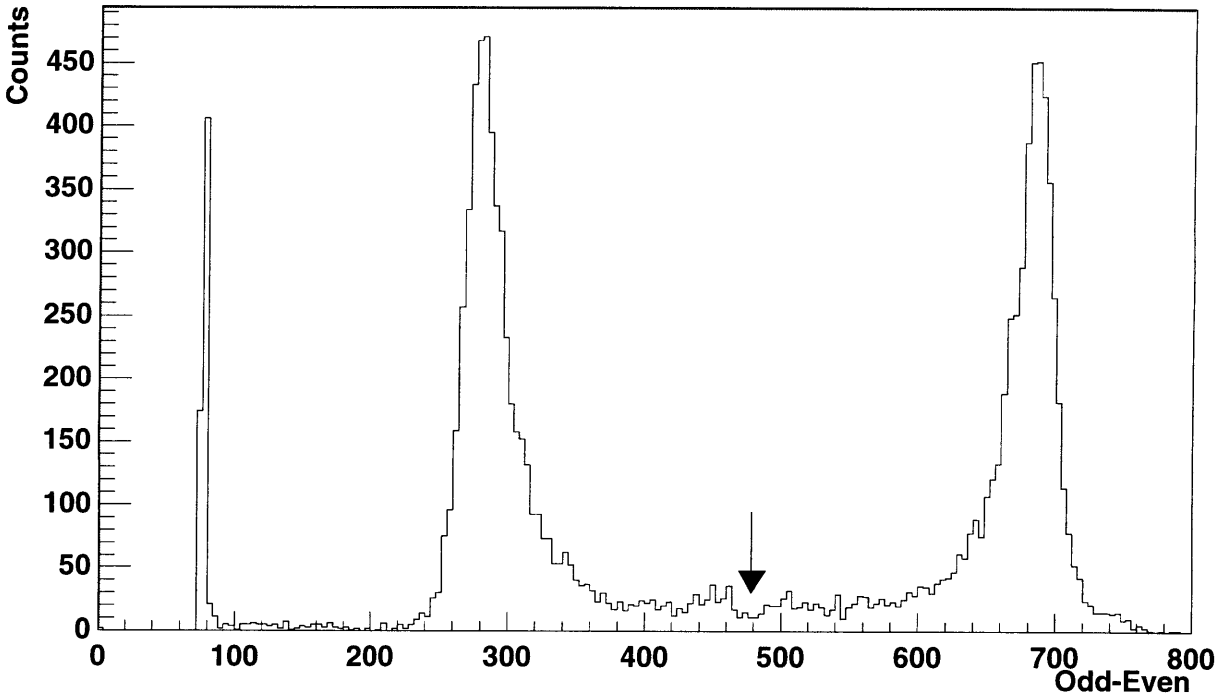

Figure 3-6: Typical HDC odd-even spectrum. The arrow represents a demarcation between events which fall on either side of the signal wire. The underflow signals were caused by the inefficiency of the odd-even circuit.

$$y = nd + offset \pm D \ , \tag{3.7}$$

where d is the wire spacing, $offset$ corresponds to the physical position of the center wire of this wire plane relative to the center of the transport coordinate, D is the drift distance, and the + or - sign depends on which side of the wire the particle passed.

The x wire plane of the first chamber is located on the OOPS focal plane. Three x positions and three y positions were fitted to straight lines, their interception with the first x wire plane are the focal plane x and y positions, which are denoted as x_f and y_f. The calculations of θ_f and ϕ_f are straightforward.

Two more diagnostic quantities were defined. They are called the "fitting resolu-

tions", and were used to test the tracking quality. They are defined as

$$x_d = x_f - x_1 \ , \tag{3.8}$$

$$y_d = y_f - y_1 \ , \tag{3.9}$$

where x_1 is the position given by the x wire plane of the first chamber, and y_1 is the projected y position on the x wire plane of the first chamber.

A typical x_d and y_d spectrum is shown in Figure 3-7. This spectrum gives useful information about the position fitting and left-right decisions. If the left-right decision was wrong, x_d and y_d would have more than one peak; if one of the wire planes misfired, the width would be much wider.

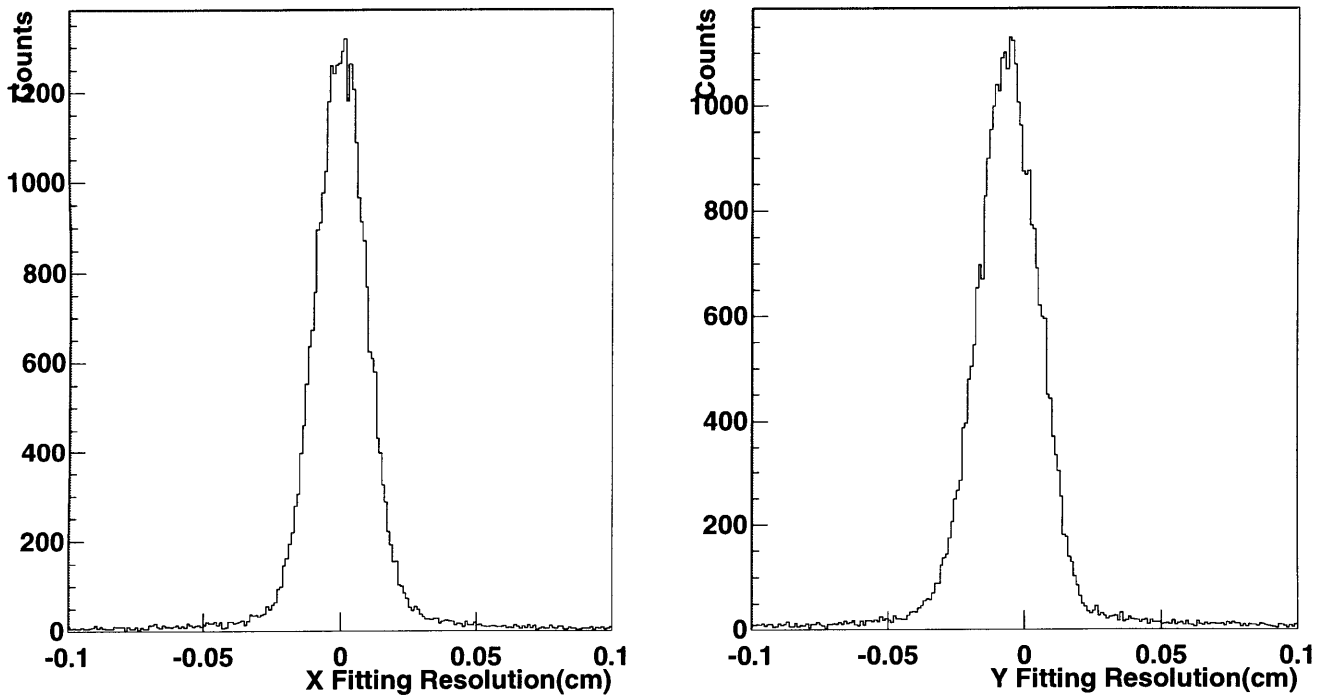

Figure 3-7: Typical OOPS HDC x and y fitting resolutions.

It is possible that only two chambers fired. In this case, it is still possible to extract

focal plane coordinates. But during this experiment, all the wire chambers were very stable and efficient, we did not consider two out of three chamber reconstruction. If it occurred, it was attributed to chamber inefficiencies to simplify the data analysis.

3.4 Decoding OHIPS VDCX

Two vertical drift wire chambers were used to provide the electron particle tracking information for OHIPS. Each wire chamber had two perpendicular wire planes (called the U plane and V plane). Each wire plane was sandwiched between two foils of 0.5 mil aluminized mylar. VDCX1 had four aluminized mylar foils which were kept at an operating voltage of -9.2 kV. VDCX2 had three aluminized mylar foils with the middle plane being a double-sided aluminized mylar, and were kept at operating voltages of -4.8 kV.

Signal wires for both VDCX1 and VDCX2 were made of gold plated tungsten wires with 20 μm diameters. Each wire plane in VDCX1 has 128 signal wires while each wire plane in VDCX2 has 201 wires. These signal wires were held at ground potential. In VDCX1, every two signal wires were separated by a 60 μm diameter beryllium-copper guard wire which was also held at ground potential. There were no guard wires between the signal wires for VDCX2.

The chambers were filled with flowing argon and isobutane gases mixed at approximately equal volume. The argon acts as an ionization medium while isobutane acts as a quenching gas. When a charged particle passes through a chamber drift cell, a discrete number of primary ionizing collisions takes place which liberates electron-ion pairs in the medium. The electrons generated by the primary collision can still have enough energy to further ionize and produce secondary ion pairs. The sum of the two contributions is the total ionization. A strong field causes the electrons produced by the ionization to migrate along the field lines to reach the anode wire where avalanche multiplication occurs and an analog pulse is generated. It has been demonstrated that

the electron drift velocity saturates at a level which is only related to the properties of the gas mixture, provided the electrical field is stronger than 2 kV/cm. By measuring the ionized electron drift time in each drift cell one can reconstruct the track of the charged particle if one knows the relation between the drift time and the location where the particle intercepts the drift cell.

OHIPS particle tracking was based on the drift time information for each hit-wire obtained from the four wire planes of two VDCX wire chambers. The wire orientation of each wire plane and the distances between them are shown in Figure 3-8.

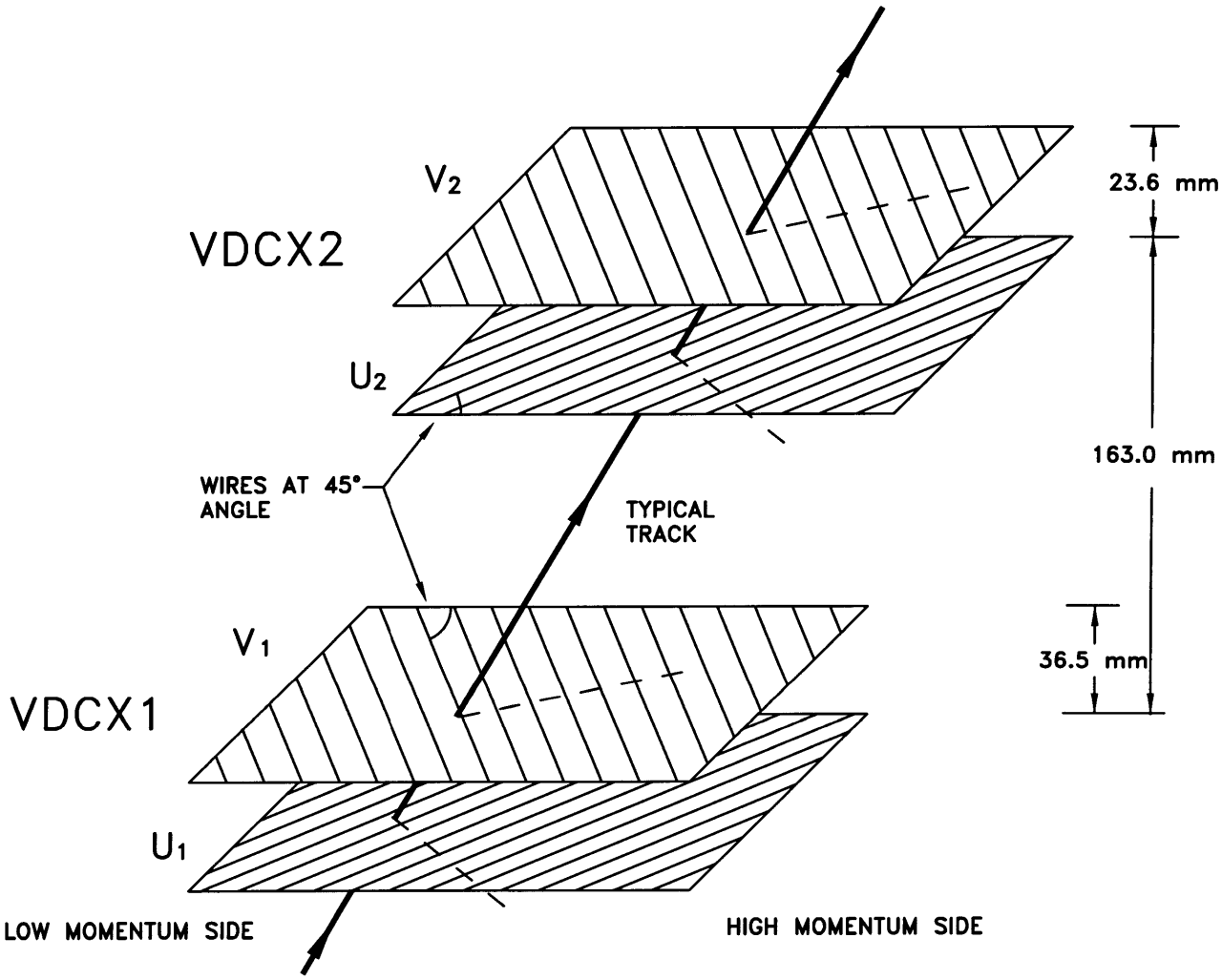

Figure 3-8: OHIPS VDCX wire orientations and distances between wire planes.

The OHIPS track reconstruction procedure includes the following steps:

1. Decode raw DCOS data. Extract drift time and wire number information for each wire that fired. A typical drift time spectrum is shown in Figure 3-9.

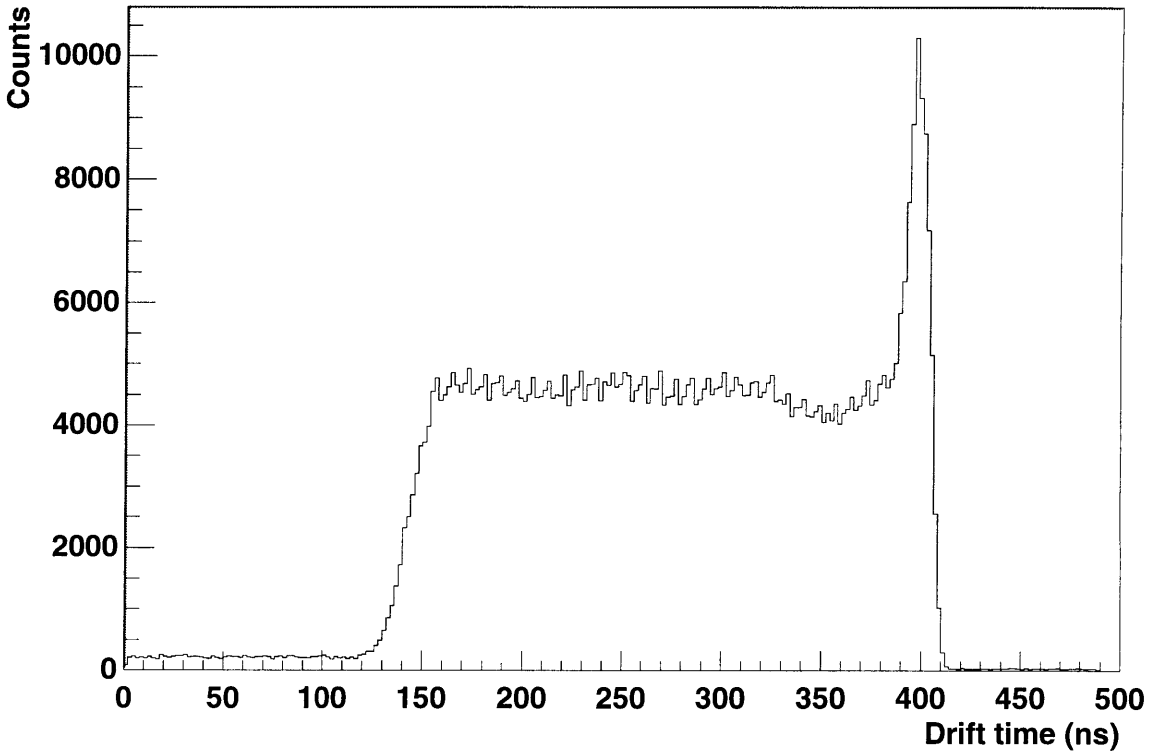

Figure 3-9: Typical OHIPS drift time spectrum. Since OHIPS DCOS was operated in common stop mode, the characteristic drift time peak showed up on the far right side of the spectrum.

2. For each wire plane, find wire-hit clusters, identify their pattern.

3. For each candidate cluster, identify the wire with the minimum drift time as the pivot wire.

4. For each hit in a cluster, convert drift time to drift distance multiplying by the drift velocity of the electron.

5. Determine the drift distance sign of the pivot wire by performing trial fits and locating the particle interception point with each wire plane.

6. Fit interception point of each wire plane to a straight line. Calculate the particle tracking variables $(x_c, \theta_c, y_c, \phi_c)$ in the chamber coordinates. Convert tracking variables to target variables $(\delta, \theta_t, \phi_t)$. The chamber coordinates are fixed to wire plane $U1$. The OHIPS matrix elements were obtained from these chamber coordinates and not from the OHIPS focal plane TRANSPORT coordinates [70]. Figure 3-10 shows the x_c, θ_c, y_c, and ϕ_c fitting uncertainties. They are good indications of the position and angle resolutions of OHIPS.

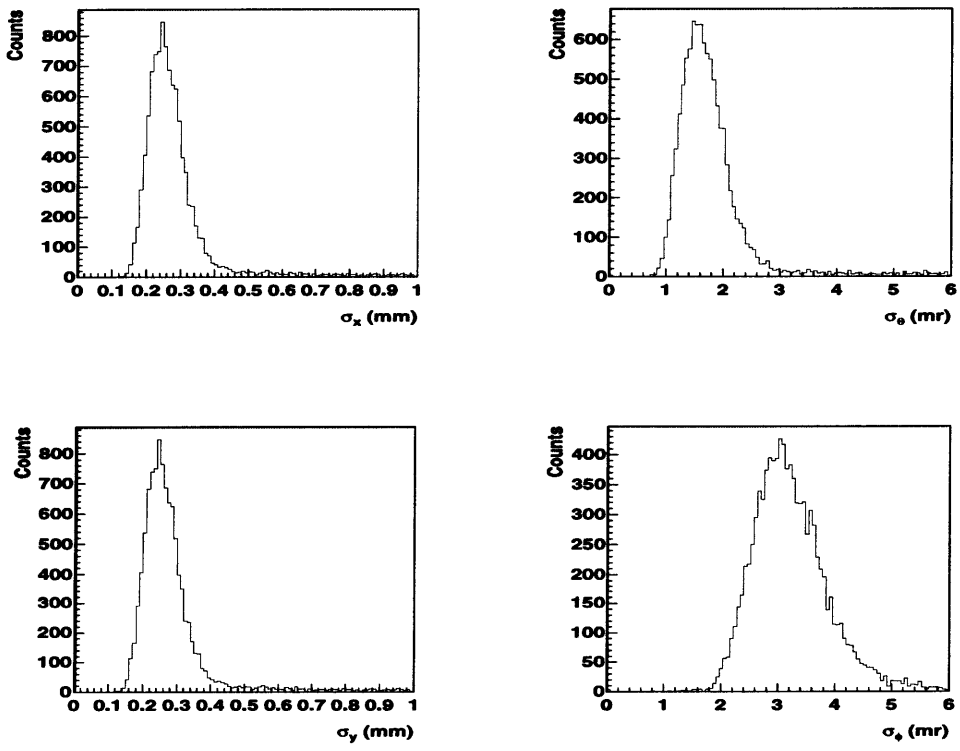

Figure 3-10: Typical fitting uncertainties for OHIPS x, θ, y and ϕ in the chamber coordinate.

More details of OHIPS particle tracking can be found in [68].

3.5 Particle Identification

Some reactions produce particles which are indistinguishable from protons or electrons in terms of momentum, charge and the relative timing between the two spectrometers. In our case pions were of concern in both the OOPS and OHIPS spectrometers. Special detectors were implemented in the spectrometers to eliminate the unwanted particles.

3.5.1 OOPS Particle Identification

The OOPS spectrometer detector package was designed to detect hardrons. Apart from protons, π^+ and deuterons with the same momentum could also be detected. The Bethe-Bloch equation [71] for the energy loss of heavy charged particles passing through materials is

$$\frac{dE}{\rho dx} = 0.307 cm^2/g \frac{Z}{A}\frac{1}{\beta^2}(ln\frac{2m_e\gamma^2\beta^2}{I} - \beta^2) \ , \tag{3.10}$$

where β and γ are the usual relativistic quantities, I is a phenomenological function, and ρ, Z and A are the target material density, charge and atomic number, respectively.

The strong β dependence of energy loss implies that protons, π^+ and deuterons deposit different energies in the scintillator materials when they pass through the scintillators. Therefore, the scintillator pulse height will be different for different particles. π^+ is the lightest particle, it will deposit the least energy. The deuteron is the heaviest particle and will deposit the most energy. Usually, the deuterons are stopped by the first two scintillators, and they cannot produce an OOPS trigger. A typical OOPS average scintillator pulse height spectrum is shown in Figure 3-11. The separation of π^+ and protons is quite clear.

By putting a cut on the proton peak, most of the pions could be eliminated.

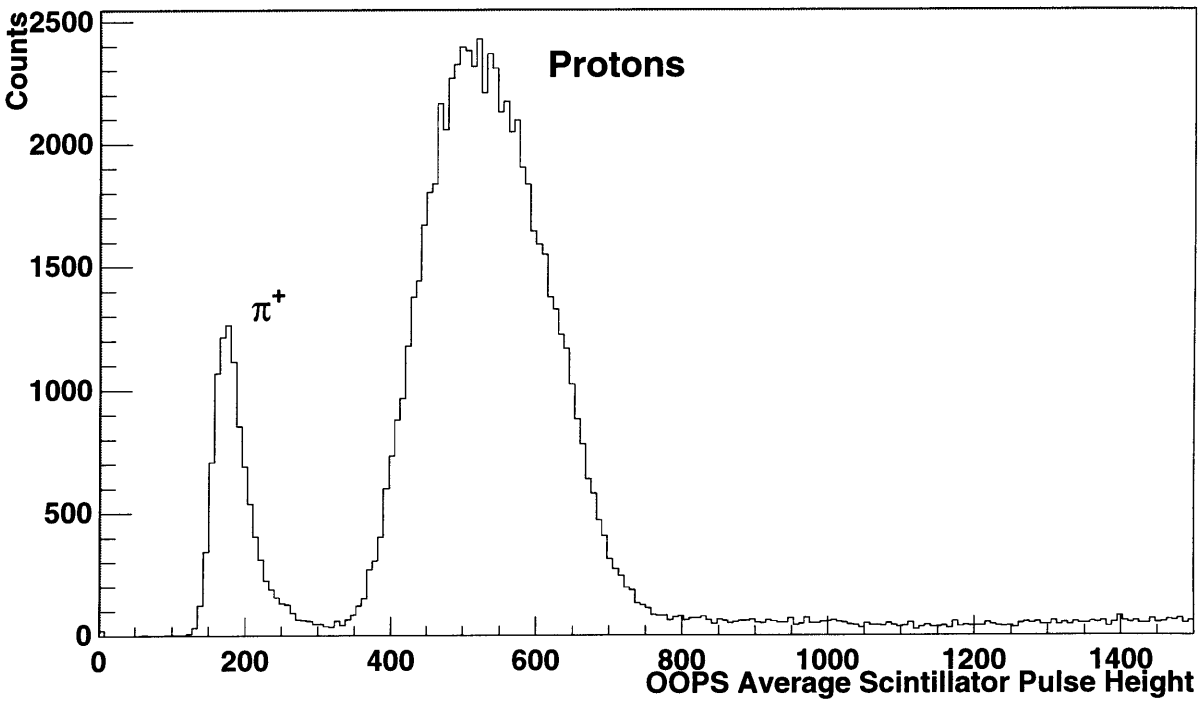

Figure 3-11: Typical OOPS average scintillator pulse height spectrum. The separation of pions and protons is clear.

3.5.2 OHIPS Particle Identification

The OHIPS detector package contained a gas Cherenkov counter and two layers of lead glass to discriminate between electrons and pions (π^-). The Cherenkov and scintillator signals together formed the OHIPS trigger.

Cherenkov radiation arises when a charged particle in a material medium moves faster than the speed of light in that same medium. The OHIPS Cherenkov counter was a gas threshold Cherenkov detector. It consisted of a gas tank, photomultiplier tubes and mirrors to focus Cherenkov light onto the photomultiplier tubes. The gas tank was filled with isobutane gas at atmospheric pressure and at room temperature. The index of refraction of isobutane is $n = 1.00127$. The velocity threshold is

$$\beta_{th} = \frac{1}{n} = 0.99873 \; . \tag{3.11}$$

The momentum threshold is 10 MeV/c for electrons, 2.0 GeV/c for muons and 2.8 GeV/c for pions. Obviously, beam related pions and muons will not produce Cherenkov light because of the limited beam energy. Thus a good Cherenkov signal will indicate the presence of an electron.

Behind the third scintillator, there were 14 individual lead-glass blocks separated into two layers serving as shower counters. They provided redundant and independent particle identifications, which produced a clear separation between pion events and electron events.

The lead-glass detectors measure the amount of Cherenkov light generated by a charge particle passing through it. Because the lead-glass has a very high index of refraction, $n = 1.80$, the Cherenkov momentum for electrons is only 0.34 MeV/c. Therefore, almost all the energy lost by an electron in the lead-glass will be ultimately converted into Cherenkov light.

When an electron passes through a lead-glass detector, it generates a large electromagnetic shower and deposits all of its energy within the lead glass. A pion, on the other hand, deposits much less energy since it only causes ionization. Furthermore, an electron deposits more energy in the first layer of the lead glass than in the second layer since most of the electromagnetic shower is created in the first layer. A pion, under minimum ionization, deposits similar amounts of energy in each layer. Thus, on a two-dimensional plot of the lead-glass ADC sum of the first layer against the second layer, pion events and electron events are well distinguished, as seen clearly in Figure 3-12.

In this experiment, not many pions were generated. A cut on the Cherenkov ADC spectrum eliminated most of them.

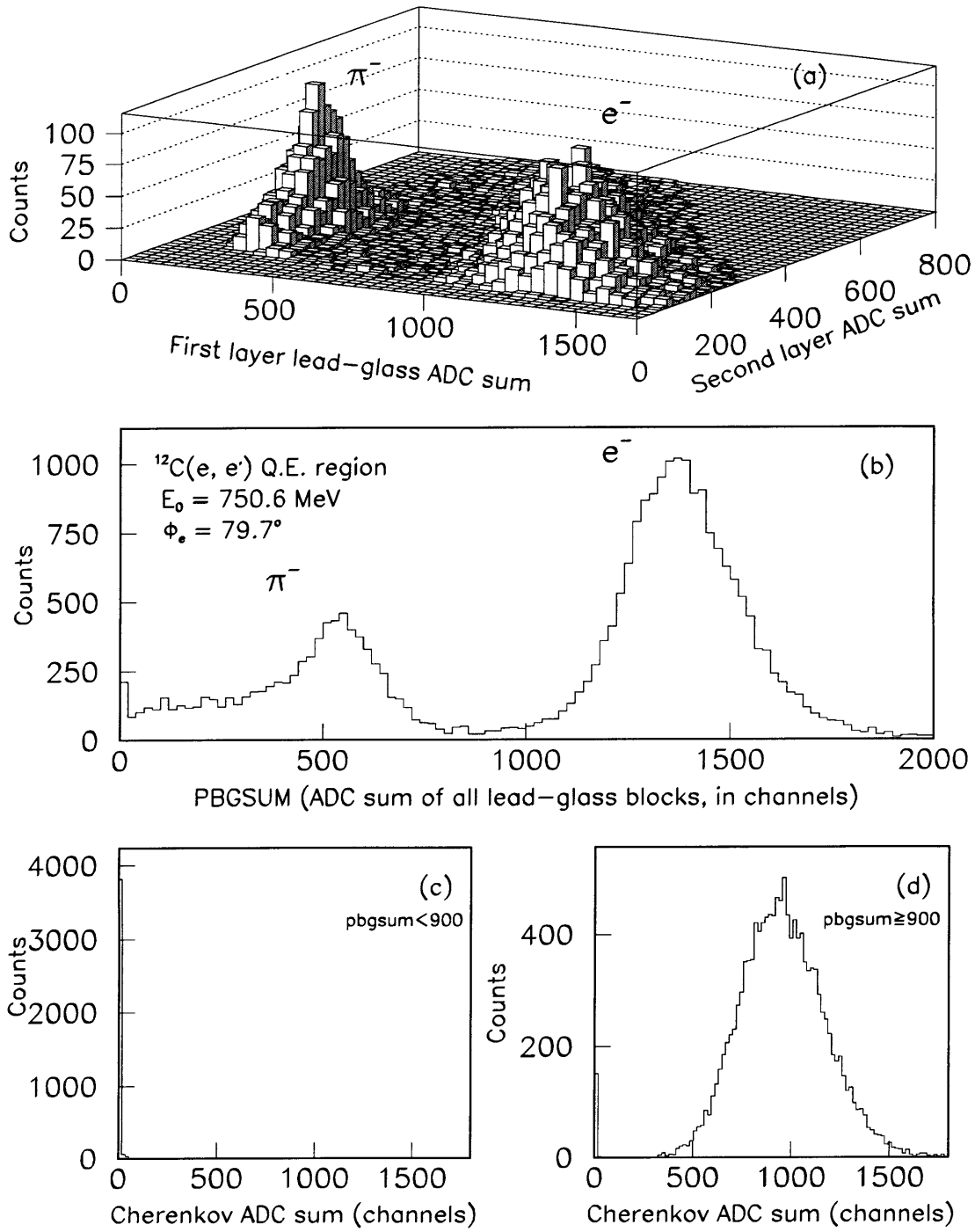

Figure 3-12: OHIPS particle identification. (a) Two-dimensional ADC sum histogram of the first layer lead-glass vs. the second layer lead-glass. The separation of electrons and π^- is clear. (b) Sum of all lead-glass ADC (pbgsum). (c) Cherenkov ADC sum with pbgsum < 900. (d) Cherenkov ADC sum with pbgsum > 900. Note no Cherenkov signal for π^- events can be seen in (c).

3.6 Monte Carlo Simulation

Monte Carlo simulations of the OOPS and OHIPS spectrometers were essential for the determination of absolute cross sections. A series of Monte Carlo simulations were performed to determine the coincidence acceptances, focal plane efficiencies and radiative corrections. The flow diagram of the Monte Carlo program AEEXB is shown in Figure 3-13. This is a program for simulation of coincidence electron scattering experiments of the type $A(\vec{e}, e'x)B$. The special features of this program include:

1. It allows the use of multiple secondary (X particle) spectrometers which can be placed in or out of the electron scattering plane.

2. It simulates magnetic spectrometers within the context of the ion optics program TURTLE [72].

3. Reaction cross sections are calculated separately on an event-by-event basis. Available theoretical models can be used for the simulation.

The key part of the program is the event generator. It processes events in the following way:

1. Two TRANSPORT rays, one for the scattered electron and one for the coincident particle X, are sampled within input-specified acceptances about their respective central values. In addition, the incident electron helicity (± 1), the Cartesian coordinates of the reaction point along the target length and beam diameter are randomly sampled.

2. The scattered electron momentum about the beam direction and the X particle momentum about the momentum transfer vector are calculated from the two TRANSPORT rays. The momentum transfer and X particle momentum 4-vectors are transformed to the hadronic center-of-momentum frame.

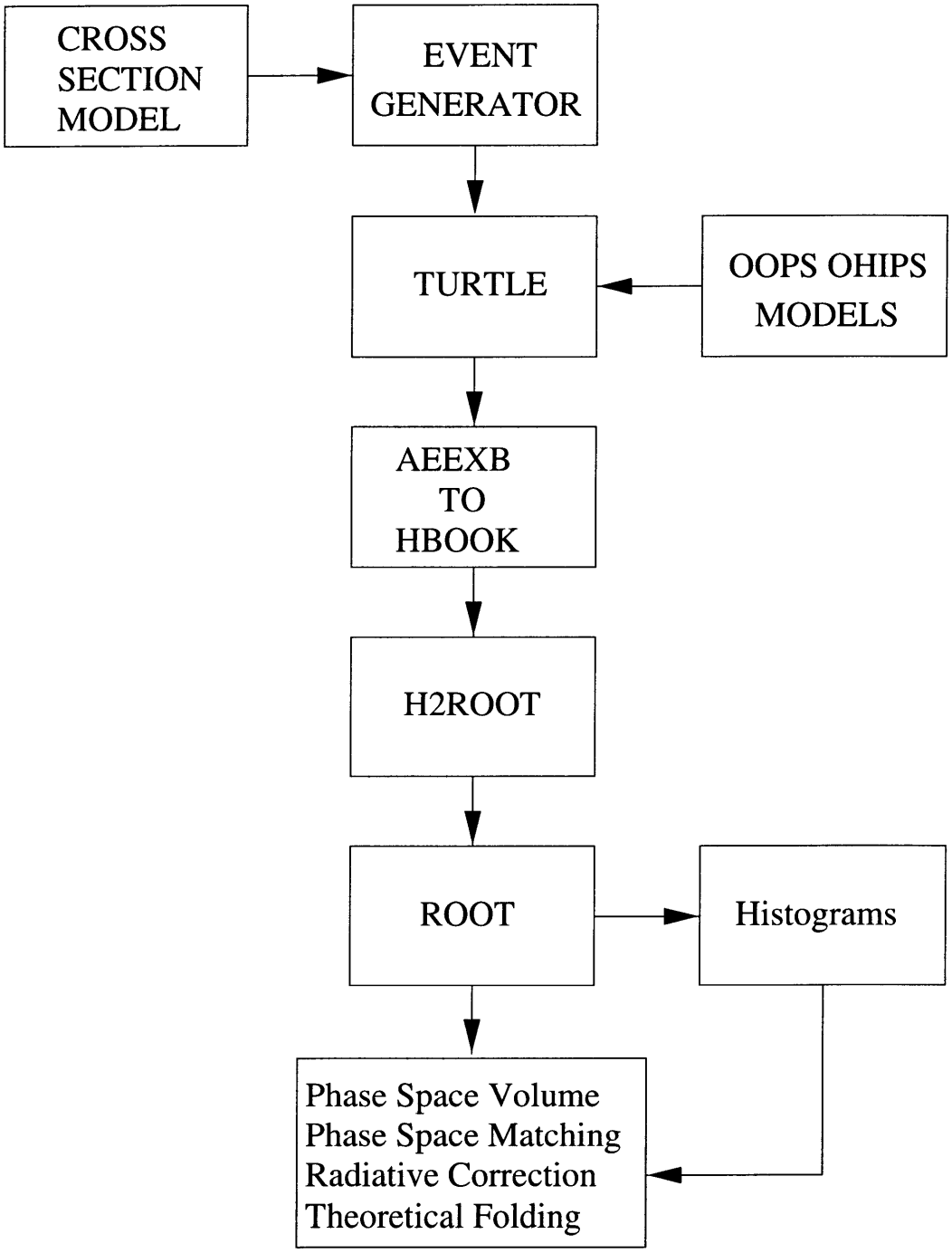

Figure 3-13: AEEXB flow diagram.

3. The five response functions, tabulated over a 3-dimensional grid in the independent dynamical variables $(e_f, \theta_e, \theta_{pq})$, are interpolated for any particular kinematic point using either a natural cubic spline or polynomial interpolation.

4. The cross section for a particular event is calculated in the hadronic center-of-momentum frame from the interpolated response functions, according to the conventions of the model in use, and then transformed to the laboratory frame.

5. Energy loss due to ionization, multiple scattering, and electron bremsstrahlung in the target is included for the incident and scattered electron and X particle momenta. The two TRANSPORT rays are then modified accordingly.

6. The two rays are transported through the corresponding spectrometers.

7. All relevant quantities are saved event-by-event to a binary file at any detector position specified in the spectrometer TURTLE_JBM models [73], which was derived from the program TURTLE. The binary file can be transformed to ntuple or ROOT file format. The detailed analysis is done by PAW or ROOT.

8. Radiative tails, radiative corrections and no radiation are included as separate options.

The program was originally written by J. Mandeville [69] and was rewritten by C. Vellidis [74]. It has been used for data analysis in several previous experiments [55, 56, 69]. A complete description of the program can be found in [74]. In the following subsections, we describe how AEEXB was used to calculate the coincidence acceptance, perform radiative corrections and fold theoretical calculations. The phase space match is discussed in Chapter 5.

3.6.1 Acceptance Calculations

The spectrometer acceptance is the product of the solid angle and momentum bite. The coincidence acceptance for elastic electron scattering is the solid angle of the

electron spectrometer cut by both the solid angle and momentum of the secondary spectrometer. It is calculated as

$$\Delta\Omega_{elas} = \Delta\theta_e \Delta\phi_e \cdot \frac{N_c}{N_T} \ , \tag{3.12}$$

where $\Delta\theta_e$ and $\Delta\phi_e$ are electron angle sampling ranges specified in the AEEXB parameter file, N_T is the total number of events generated and N_c is the number of acceptable coincidence events between OHIPS and OOPS.

The non-elastic coincidence acceptance is calculated as

$$\Delta\Omega = \Delta\omega_e \Delta\theta_e \Delta\phi_e \Delta\theta_p \Delta\phi_p \cdot \frac{N_c}{N_T} \ , \tag{3.13}$$

where $\Delta\theta_p$ and $\Delta\phi_p$ are proton angular sampling ranges, $\Delta\omega_e$ is the electron momentum sampling range.

AEEXB can also simulate extended target effects. For an extended target, the acceptance has one more physical dimension, the target length. The integrated solid angle is given by

$$< \Omega z >= \frac{\int P(x,y)\Omega(x,y,z)dxdydz}{\int P(x,y)dxdy} \ , \tag{3.14}$$

where $P(x,y)$ describes the reaction point and $\Omega(x,y,z)$ is the acceptance at each point in the target cell. For the coincidence acceptance, such as $^2H(e,e'p)$, it is evaluated by the Monte Carlo simulation as

$$< \Omega z >= \Delta L \Delta\omega_e \Delta\theta_e \Delta\phi_e \Delta\theta_p \Delta\phi_p \cdot \frac{N_c}{N_T} \ , \tag{3.15}$$

where ΔL is the nominal extended target length. The extended target efficiency is folded into the simulation. The extended target efficiencies were also measured by using a slant carbon target (see Section 4.4). The measured efficiencies agree very well with the Monte Carlo simulation with proper spectrometer models.

The accuracy of the acceptance calculations strongly depends on the OOPS and

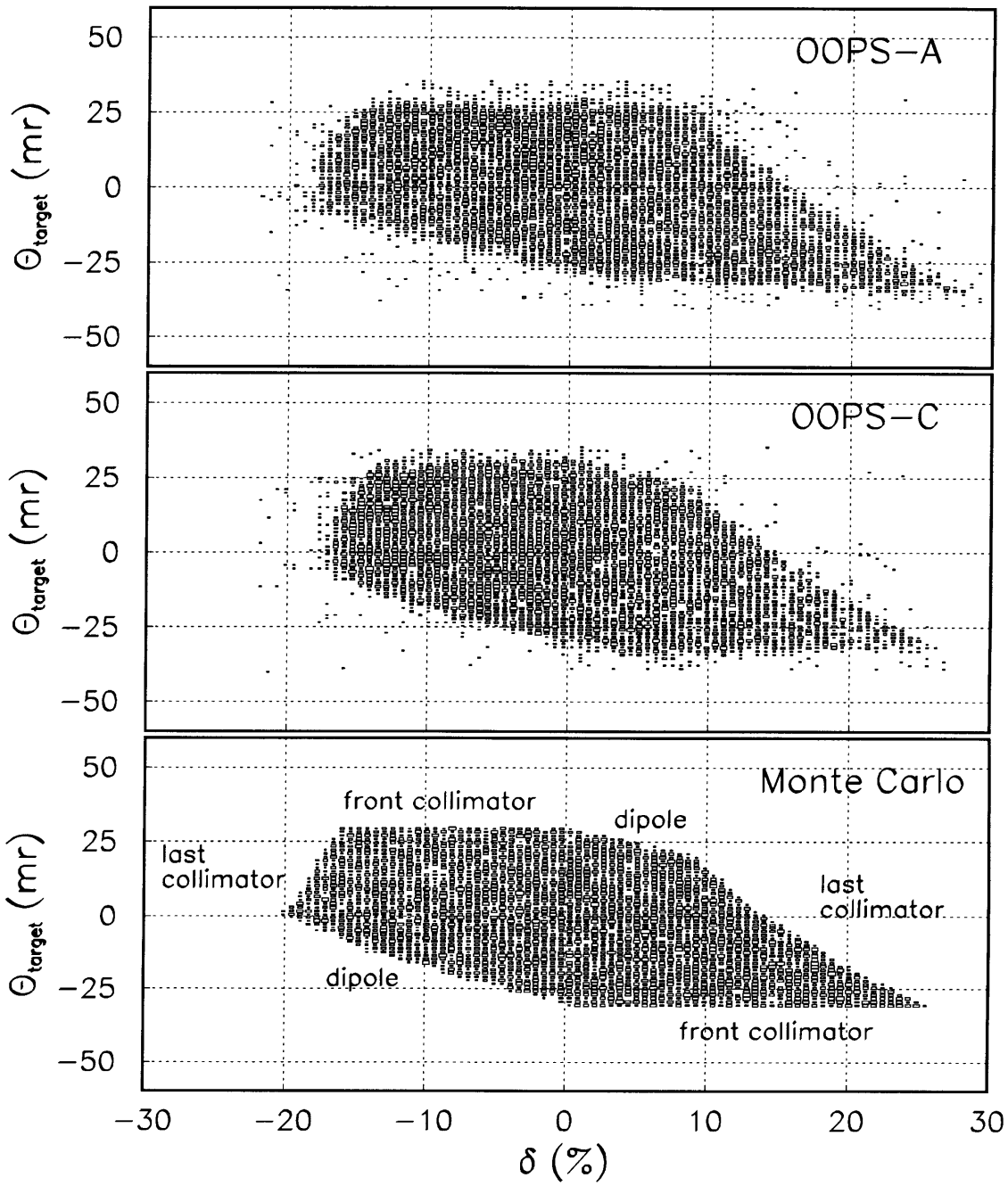

Figure 3-14: Comparison of the measured and simulated OOPS acceptance boundary. Angles at target dispersion direction θ_t are plotted against OOPS δ. The Monte Carlo simulation picture also shows the defining elements, which are labeled at the boundaries of the acceptance.

OHIPS TURTLE models. A lot of effort was spent to refine the spectrometer models. The OOPS and OHIPS TURTLE models are given in Appendix C. Figure 3-14 shows the measured phase space shapes for OOPS A and C and the simulated boundary. It can be seen that the simulation clearly resembles the actual performance.

3.6.2 Radiative Corrections

Electrons can radiate real or virtual photons during the scattering process. This will change the electron momentum and affect the results. The radiation processes add tails to peaks and reduce the observed cross sections. It is important to understand these processes and make corrections for them.

Basically there are three kinds of radiation:

1. *Internal Bremsstrahlung:* Emission of real and virtual photons in the field of the scattering nucleus.

2. *External Bremsstrahlung:* Emission of real photons in the presence of a nucleus other than the nucleus involved in the $(e, e'p)$ reaction.

3. *Ionization Loss (Landau Straggling):* Energy loss due to collisions with atomic electrons in the target.

It should be noted that protons can also produce bremsstrahlung radiation, but since the intensity is inversely proportional to the mass of the projectile squared [75] this effect is very small for our kinematics and was ignored.

The largest correction is due to internal bremsstrahlung. The Feyman diagrams for the internal bremsstrahlung processes are given in Figure 3-15.

Diagram a) describes an electron which radiates a real photon before and after the scattering, respectively. If the photon energy, k_γ, is greater than a cutoff energy ΔE (hard photons), this process causes a radiative tail. The strength is shifted outside the peak and must be accounted for. ΔE is the energy interval over which

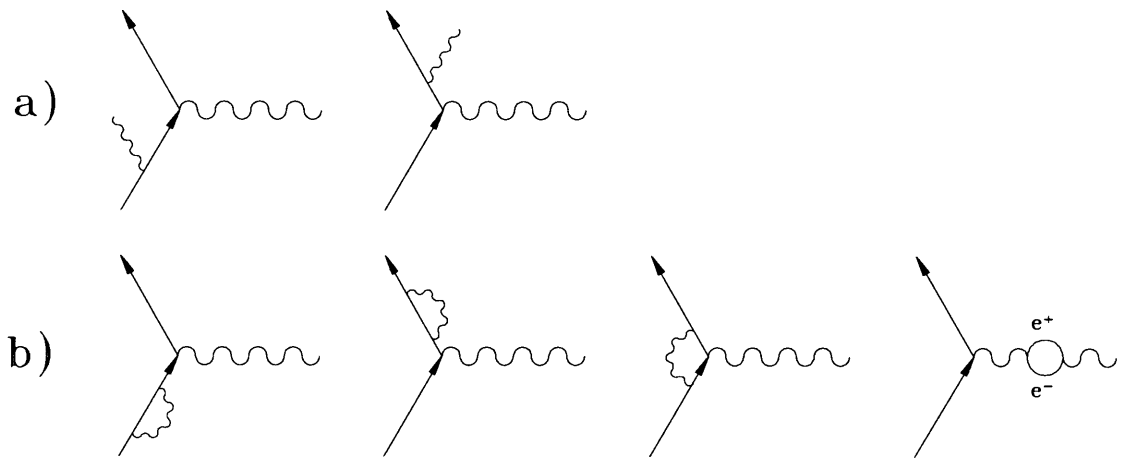

Figure 3-15: Feynman diagrams for internal bremsstrahlung processes.

the cross section is integrated and which may correspond to the energy resolution of the electron spectrometer. On the other hand, if the emitted photon energy is less than the cutoff energy (soft photons), no correction is needed since the strength is merely redistributed inside the peak.

Diagram b) depicts the renomalization of the electron mass, vertex correction and vacuum polarization of the exchanged photon.

AEEXB includes optional electron internal bremsstrahlung in the so-called "peaking approximation", which consists of letting the incident or scattered electron radiate one real photon of random energy along its direction of motion only.

To calculate the correction factor, the program uses the Schwinger correction [76] as was proposed by Penner [77]. The formalism was based on Mo and Tsai [78]. The correction factor takes the form

$$C_{Schw} = \frac{e^{\delta_{real}}}{1 - \delta_{virtual}} , \tag{3.16}$$

where

$$\delta_{real} = \frac{2\alpha}{\pi} \ln \frac{\sqrt{\epsilon\epsilon'}}{\Delta E} \left(2 \ln \frac{|\vec{q}|}{m_e} - 1 \right) , \tag{3.17}$$

$$\begin{aligned} \delta_{virtual} = \frac{2\alpha}{\pi} \Bigg\{ & - \frac{13}{12} \left(2 \ln \frac{|\vec{q}|}{m_e} - 1 \right) + \frac{17}{36} + \frac{1}{4} \ln^2 \frac{\epsilon}{\epsilon'} \\ & + \frac{1}{2} \left[\frac{\pi^2}{6} - L_2 \left(\cos^2 \frac{\theta_e}{2} \right) \right] \Bigg\} , \end{aligned} \tag{3.18}$$

and the Spence function

$$L_2(x) = \int_0^x \frac{\ln(1-y)}{y} dy . \tag{3.19}$$

The external bremsstrahlung correction factor C_{Brem} is $1/e^{-(\delta_0+\delta_e)}$, which is calculated as [79]

$$\delta_{0,e} = t_{0,e} \left[\frac{1 - k_{0,e}^2}{2} - b(1 - k_{0,e} + \ln k_{0,e} \right] , \tag{3.20}$$

with

$$k_{0,e} = \frac{\Delta E}{\epsilon_{0,e}} , \tag{3.21}$$

$$t_{0,e} = \frac{x_{0,e}}{X_0} . \tag{3.22}$$

Here $\epsilon_{0,e}$ are electron energies before and after scattering and $x_0(x_e)$ is the distance the incident (scattered) electron traverses through a medium with a radiation length X_0. The parameter b is defined as

$$b = \frac{4}{3} \left(1 + \frac{1}{12} \frac{Z+1}{ZL_r + L_r'} \right) , \tag{3.23}$$

where Z is the atomic number of the medium, L_r and L_r' are two parameters related to Z [80].

The ionization loss has been taken into account in the AEEXB event generator. No separate ionization loss correction is needed. The total radiative correction factor

that AEEXB returns for each event is

$$f_{rad} = C_{Schw} C_{Brem} \ . \tag{3.24}$$

The overall radiative correction factors are averaged over the proper phase spaces. Apart from the radiative corrections, AEEXB can also simulate radiative tails.

For inelastic coincidence electron scattering, the Borie-Drechsel equation [81] for the radiative cross section was used:

$$\begin{aligned} \frac{d^4\sigma_{tail}}{d\omega_e\, d\Omega_e\, d\Omega_p\, dk_\gamma} = \frac{\alpha}{\pi k_\gamma} \ \Bigg\{ & \ \frac{\epsilon^2 + (\epsilon - k_\gamma)^2}{\epsilon^2} \ln\left(\frac{2\epsilon}{m_e}\right) \frac{d^3\sigma(\epsilon - k_\gamma, \epsilon')}{d\omega_e\, d\Omega_e\, d\Omega_p} \\ & + \ \frac{(\epsilon' + k_\gamma)^2 + \epsilon'^2}{(\epsilon + k_\gamma)^2} \ln\left(\frac{2\epsilon'}{m_e}\right) \frac{d^3\sigma(\epsilon, \epsilon' - k_\gamma)}{d\omega_e\, d\Omega_e\, d\Omega_p} \ \Bigg\} \ . \end{aligned} \tag{3.25}$$

For elastic electron scattering, the following Mo-Tsai equation [78] for the radiative cross section was used:

$$\frac{d^3\sigma}{dk_\gamma d\Omega_e} = \frac{\alpha}{\pi k_\gamma} \Big\{ \frac{M_A + (\epsilon - k_\gamma)(1 - \cos\theta_e)}{M_A - \epsilon'} (1 - \cos\theta_e) t_0 \frac{d^2\sigma(\epsilon - k_\gamma)}{d\Omega_e} + t_e \frac{d^2\sigma(\epsilon)}{d\Omega_e} \Big\} \ , \tag{3.26}$$

where

$$t_{0,e} = \frac{1 + x_{0,e}^2}{2} \ln\frac{Q^2}{m_e^2} - x_{0,e} \ , \tag{3.27}$$

$$x_0 = \frac{\epsilon - k_\gamma}{\epsilon} \ , \tag{3.28}$$

$$x_e = \frac{\epsilon'}{\epsilon' + k_\gamma} \ . \tag{3.29}$$

All quantities were previously defined in Chapter 1 and in this section.

In both Equation 3.25 and 3.26, the first term corresponds to radiation before scattering and the second term to radiation after scattering. The factors multiplying the $A(e, e'x)B$ (or $A(e, e'A')$ elastic) cross section are the cross sections for one photon emission along the direction of motion of the incident or scattered electron,

respectively.

3.6.3 Averaging Over Acceptance

All the extracted asymmetries and response functions are not directly comparable with the theoretical calculations, because the extracted values are averaged over a range of finite acceptance. In order to compare the extracted asymmetries and response functions with theoretical models, AEEXB was used to fold theoretical calculations over the experimental acceptance. In addition, the same Monte Carlo simulation was used to average the radiative correction factors and some kinematic factors, which were needed for the response function extractions.

The average of any function F on any dynamical variables over a certain phase space volume V is

$$\langle F \rangle_V = \frac{1}{n} \sum_{i=1}^{n} F(i) \ , \tag{3.30}$$

where $F(i)$ is the value of the function F for event i under certain phase space cuts, n is the number of events satisfying the same cuts.

Chapter 4

Calibrations and Normalizations

In this chapter, we describe how the optical studies for OOPS and OHIPS were conducted, then we discuss the OOPS and OHIPS efficiencies, and the extended target and electronics efficiencies. Hydrogen normalization is used to calibrate the instrumentation and absolute efficiencies of the experimental setup. Section 4.6 presents the details about the $H(e, e'p)$ absolute cross section measurements. In the last two sections of this chapter, we also discuss how the beam energy and polarization were determined.

4.1 OOPS and OHIPS Optics

Full details of the procedures used to determine the ion-optic matrix elements for OOPS and OHIPS can be found in [61, 68]. Only a brief description of the principles involved are discussed here. The goal of the optics measurements is to find a relation between the target variables (x_t, θ_t, y_t,ϕ_t) and the focal plane variables (x_f, θ_f, y_f, ϕ_f, δ). The target and focal plane variables are given in TRANSPORT coordinates, which were defined in section 3.2.

During the experiment, the focal plane variables were measured, but what is needed are the target variables. One can express a target variable in terms of the

focal plane variables and measured matrix elements as

$$V_{tgt} = \sum_{i,j,k,l,m} \langle V_{tgt} | x_f^i \theta_f^j y_f^k \phi_f^l \delta^m \rangle x_f^i \theta_f^j y_f^k \phi_f^l \delta^m \ , \tag{4.1}$$

where V_{tgt} stands for one of the target variables x_t, θ_t, y_t and ϕ_t. The coefficients in Equation 4.1 are referred to as the optical matrix elements. All of the matrix elements used for the analysis of this experiment were measured during an OOPS/OHIPS commissioning run in September 1996, which immediately preceded the main coincidence runs.

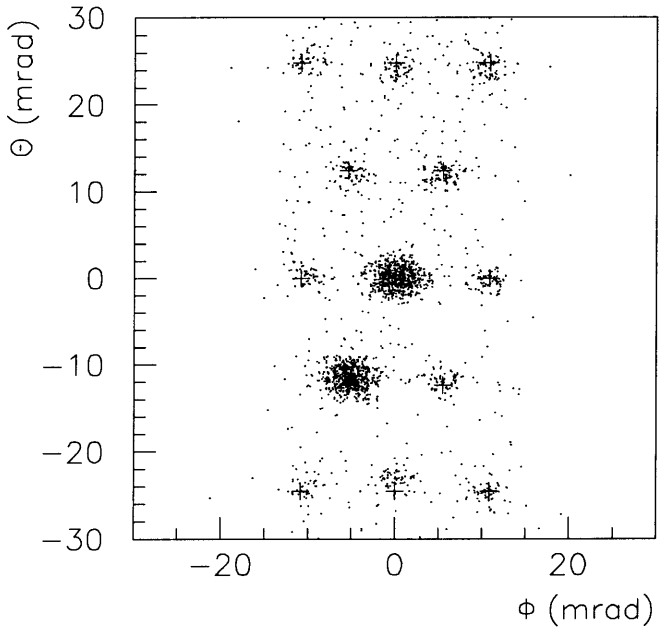

Figure 4-1: Images of the OOPS sieve-slit in the TRANSPORT target coordinates. The crosses are predicted sieve-slit hole positions. The images are reconstructed by using the OOPS θ_t and ϕ_t matrix elements.

Sieve-slits were used to measure the matrix elements for both OOPS and OHIPS. A sieve-slit is a collimator with an array of holes which is mounted in the snout at the front of the spectrometer. Particles passing through the sieve-slit holes arrive at the spectrometer focal plane at locations which correspond to the angular positions of the holes. Since the angular positions of the sieve-slit holes are known, one can trace

the measured focal plane variables back to the target variables. The sieve-slit hole sizes were designed to be asymmetric so that it was easy to recognize the orientation of the hole images in the focal plane. Typical sieve-slit images in the TRANSPORT target coordinates for OOPS and OHIPS are shown in Figures 4-1 and 4-2.

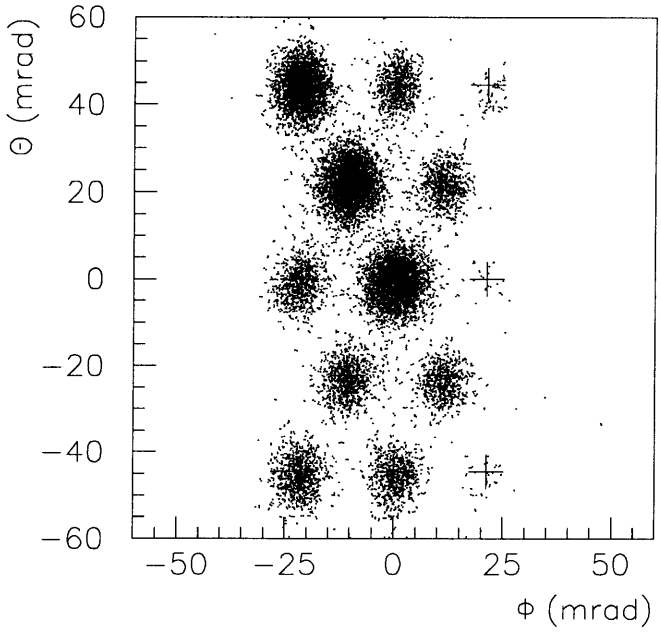

Figure 4-2: Images of the OHIPS sieve-slit in the TRANSPORT target coordinates. The crosses are predicted sieve-slit hole positions. The images are reconstructed by using the OOPS θ_t and ϕ_t matrix elements.

The measured OOPS and OHIPS matrix elements are listed in Appendix A.

4.2 OOPS Efficiency

The OOPS efficiency can be divided into an OOPS focal plane efficiency and an OOPS wire chamber efficiency, which are discussed separately in the following subsections.

4.2.1 OOPS Focal Plane Efficiency

An OOPS module has a rather large momentum bite. Design calculations show a region of flat efficiency (> 90%) over a total range of 15% of the central momentum.

The OOPS focal plane efficiencies were measured as a function of momentum by using the quasi-elastic electron scattering from $^{12}C(e,e')$ [67]. A broad quasi-elastic peak from $^{12}C(e,e')$ scattering was scanned through the OOPS momentum acceptance in small steps by changing the current settings of the spectrometers. The measured OOPS A focal plane profile is plotted in Figure 4-3.

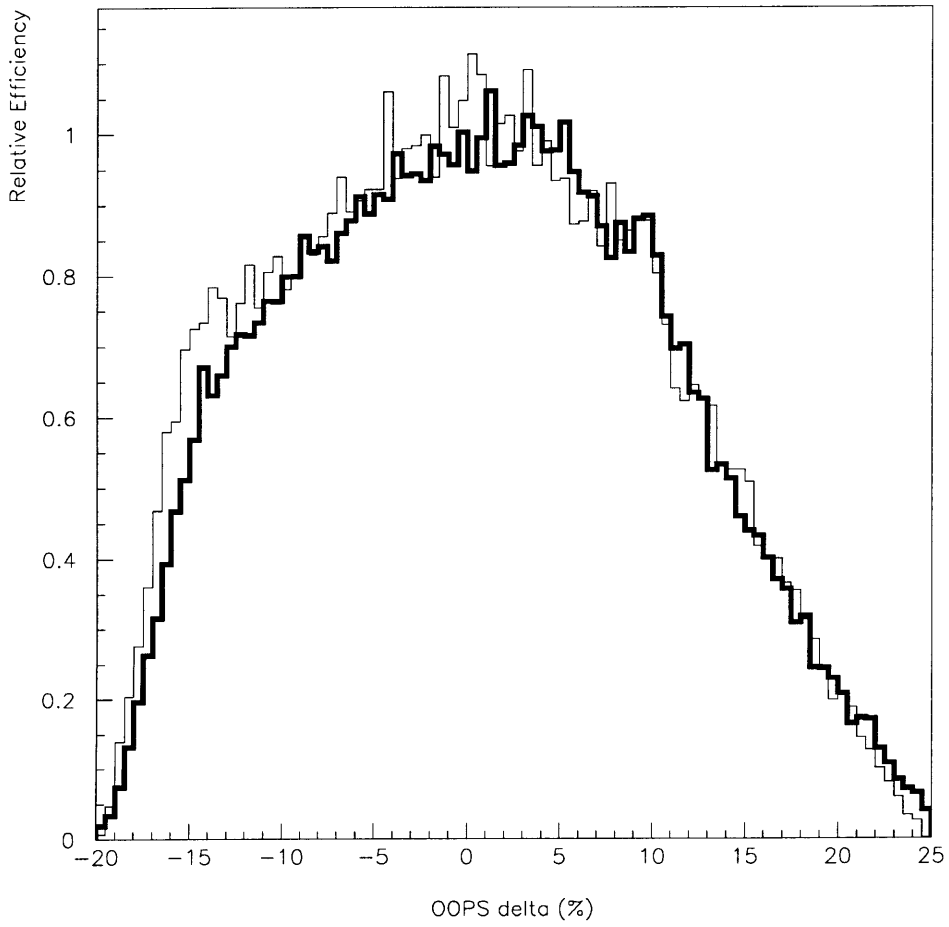

Figure 4-3: Measured OOPS focal plane relative efficiency and the TURTLE simulation. The thick line is the measured relative efficiency profile for OOPS A. The thin line is the result from the Monte Carlo simulation.

By comparing the measured efficiencies with a Monte Carlo simulation using the TURTLE model, it is concluded that the OOPS focal plane efficiency profile has been simulated very well. When the Monte Carlo simulations are used to calculate the acceptances, the focal plane efficiency is built into the calculations.

4.2.2 OOPS HDC Efficiency

Not each detected particle has a reconstructible track. This can be attributed to the OOPS HDC inefficiency. OOPS HDC inefficiencies arise from many sources, such as the inefficiency of the delay lines, slow response from the odd-even amplifier circuit and pile-up etc., but they were not distinguished. What is important is the number of proton triggers, and the number of good proton tracks. The overall OOPS wire chamber efficiency is defined as

$$\epsilon_{oc} = \frac{Number\,of\,protons\,that\,have\,good\,tracks}{Total\,number\,of\,proton\,triggers} \,. \tag{4.2}$$

The criteria for what constitutes a proton trigger and a proton with good track can be found in section 5.4.

4.3 OHIPS Efficiency

The acceptance of OHIPS has been studied extensively [68]. The OHIPS momentum acceptance for this experiment was about $\pm 4\%$, which was well within the "flat" region of the OHIPS full momentum acceptance. The OHIPS focal plane efficiency study through elastic electron scattering from $^{12}C(e,e')$ shows that the OHIPS TURTLE model simulates the spectrometer performance well.

Following the same reasoning as for the OOPS HDC efficiency, the overall OHIPS wire chamber efficiency is defined as:

$$\epsilon_{hc} = \frac{Number\ of\ electrons\ that\ have\ good\ tracks}{Total\ number\ of\ electron\ triggers} \ . \tag{4.3}$$

4.4 Extended Target Efficiency

Since a cryogenic liquid target was used in the experiment and three OOPS modules viewed the target from different angles, the extended target efficiency for different OOPS had to be determined.

The extended target response of each OOPS module was measured by detecting quasi-elastic protons from a slant carbon target. Motion of the target ladder up and down translated into movement of the interaction point along the beam line. The transverse interaction position in the spectrometer system was then just the projection of the beam position onto the line perpendicular to the spectrometer central ray. The measured focal plane relative efficiencies for OOPS A, B and C , compared with the Monte Carlo simulation, are shown in Figure 4-4.

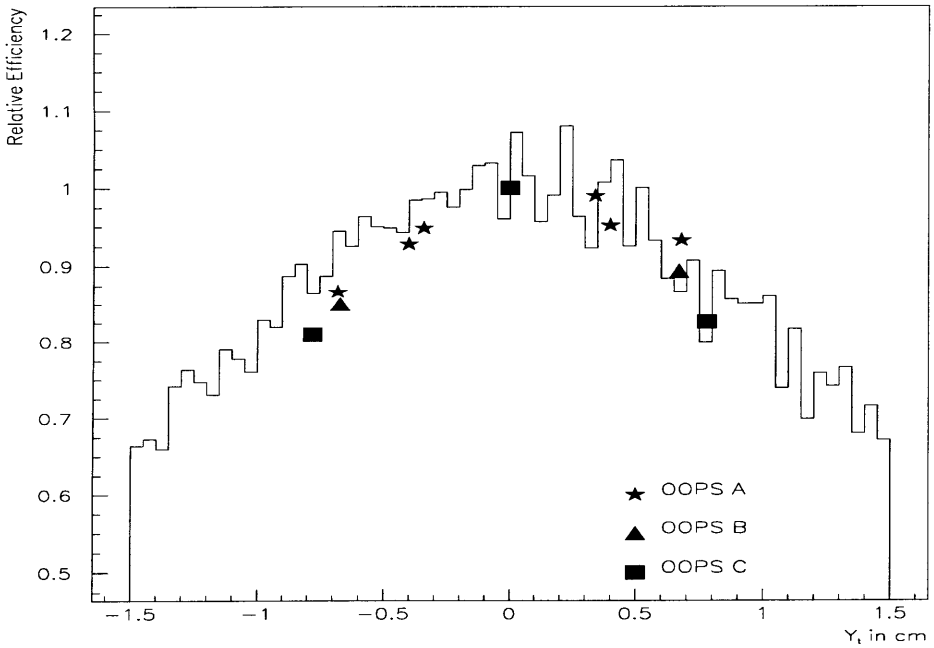

Figure 4-4: The measured OOPS extended target efficiencies, compared with a TURTLE simulation (solid line).

4.5 Electronic Dead Times

The front-end veto scheme did not eliminate all sources of electronic dead time. They include:

1. OOPS and OHIPS trigger pile-up inefficiencies. If more than one trigger comes too close in time (less than 30 ns), the OOPS and OHIPS scintillators can't discriminate them. This causes trigger inefficiency. A Poisson process was used to model this inefficiency.

2. One per beam burst veto. For each beam burst, only one single or coincidence event can be taken. If more than one event trigger occurs during a beam burst, they were recorded by scalers. The scaler information was used to calculate the one per beam burst veto efficiency.

3. OHIPS self-inhibit inefficiency.

For a given trigger rate and pulse width, one can simply calculate the probability that two or more pulses arrive close enough together in time that they overlap and become a single output pulse. The time distribution of events is modeled by the Poisson distribution,

$$P(n,t,\tau) = \frac{1}{n!}(t/\tau)^n e^{-t/\tau} \ , \tag{4.4}$$

which gives the probability of observing n events in a time interval t when the average pulse separation is τ. The time interval t can be considered as the signal pulse width of the scintillator discriminators. Typically it was approximately 30 ns.

The probability to have more than one trigger during the interval t is

$$P = 1 - P(0,t,\tau) - P(1,t,\tau) \ . \tag{4.5}$$

The triggering efficiency is

$$\epsilon_t = 1 - P = P(0,t,\tau) + P(1,t,\tau) \ . \tag{4.6}$$

Since the triggering rates were relatively low (less than 100 per beam burst) for this experiment, typical OOPS and OHIPS triggering efficiencies were more than 99%.

The one per beam burst veto efficiency is defined as

$$\epsilon_{1/BB} = \frac{Nubmer\ of\ coincidence\ events\ recorded\ in\ Event\ 8}{Total\ number\ of\ coincidence\ events\ counted\ by\ scalers} . \tag{4.7}$$

The typical one per beam burst veto efficiency for this experiment was 95%.

The OHIPS self-inhibit efficiency is calculated as

$$\epsilon_{si} = 1 - \frac{Number\ of\ OHIPS\ triggers\ during\ self\ inhibit\ period}{Total\ number\ of\ OHIPS\ triggers} . \tag{4.8}$$

The OHIPS self-inhibit time was about 2 μs, the average efficiency was about 85%.

4.6 $H(e, e'p)$ Normalization

Because the $H(e, e'p)$ cross sections are well known [82], a series of $H(e, e'p)$ runs were performed to understand the instrumentation and normalization issues. These measurements served as benchmark tests for the other cross section measurements, such as the $^2H(e, e'p)$ cross sections described in this thesis.

During the commissioning stage of the experiments, $H(e, e'p)$ elastic scattering data were collected for OHIPS and each OOPS module, using solid CH_2 targets. The analysis and interpretation of these data are given in reference [68].

At the end of the experiment, a liquid hydrogen target, which was identical to the liquid deuterium target, was used to take coincidence data between OHIPS and OOPS A. The setup was the same as for the deuterium experiment, except OOPS A was positioned along the momentum transfer $\vec{q}$ direction.

The coincidence $H(e,e'p)$ cross section is calculated as

$$\sigma_{(e,e'p)} \equiv \frac{d\sigma}{d\Omega_e} = \frac{N_c}{\Delta\Omega \cdot \frac{Q}{e} \cdot \rho \cdot t \cdot N_A \cdot t_{frac}} \cdot \frac{1}{\epsilon_{ot} \cdot \epsilon_{ht} \cdot \epsilon_{oc} \cdot \epsilon_{hc} \cdot \epsilon_{1/BB} \cdot \epsilon_{si}} \cdot f_{rad} \ , \quad (4.9)$$

where

N_c $\equiv$ Number of true coincidence events ,

$\Delta\Omega_e$ $\equiv$ The coincidence electron acceptance ,

Q $\equiv$ Total charge ,

e $\equiv$ Electron charge(1.602×10^{-19} coulomb/electron) ,

ρ $\equiv$ Target density ,

t $\equiv$ Effective target thickness ,

N_A $\equiv$ Avogadro's constant (6.02×10^{23} particles/mole) ,

t_{frac} $\equiv$ Hydrogen composition of the target (LH_2=1.0, CH_2=$\frac{1}{7}$) ,

ϵ_{ot} $\equiv$ OOPS trigger efficiency ,

ϵ_{ht} $\equiv$ OHIPS trigger efficiency ,

ϵ_{oc} $\equiv$ OOPS chamber efficiency ,

ϵ_{hc} $\equiv$ OHIPS chamber efficiency ,

$\epsilon_{1/BB}$ $\equiv$ One per beam burst veto efficiency ,

ϵ_{si} $\equiv$ OHIPS self-inhibit efficiency ,

f_{rad} $\equiv$ Radiative correction factor .

The definitions for the efficiencies can be found in previous sections. For an extended target (LH_2), the target thickness t is convoluted into the acceptance calculation, and hence the acceptance unit is $MeV \cdot msr \cdot cm$.

During the experiment, there was a power failure. After the power failure, the target cell was changed. It was discovered that the target cell was off center, and the electron beam was striking 0.5 cm away from the target center. The deuterium data taken before and after the power failure were used to infer the effective target thickness after the power failure. The effective target thickness was about 1.20 cm. A

target position survey after the experiment confirmed this result. The LH_2 calibration data were taken after the power failure.

The measured cross sections were compared with the $H(e,e')$ cross section derived from the Mainz fit of the proton form factors [82]. The comparison is listed in Table 4.1. The Mainz cross section was averaged over the experimental acceptance using a Monte Carlo simulation.

Table 4.1: $H(e,e'p)$ Cross Section Calculation. A liquid hydrogen target was used. The Beam energy was 800.0 MeV, $\theta_e = 37.27°$ and $\theta_p = 58.0°$.

N_c	133960
$\Delta\Omega_e(msr)$	1.290
$t(cm)$	1.20
$\rho(mol/cm^3)$	0.071
ϵ_{oc}	0.6124
ϵ_{hc}	0.9813
$\epsilon_{1/BB}$	0.9984
ϵ_{SI}	0.9254
ϵ_{ot}	1.0
ϵ_{ht}	1.0
f_{rad}	1.263
$\frac{d\sigma}{d\Omega_e}(\mu b/sr)$	0.2968 ± 0.0008
Dipole Fit$(\mu b/sr)$	0.3010

An OOPS momentum scan was performed by fixing the OHIPS current setting and changing the OOPS central momentum setting. By measuring the $H(e,e'p)$ cross section at different OOPS momentum settings, further understanding of the OOPS focal plane efficiency was obtained and the OOPS TURTLE model was tested at the extreme momentum settings. The $H(e,e'p)$ cross section as measured for different OOPS momentum settings is shown in Figure 4-5.

From this figure, one can see that the measured cross sections agree well with the Mainz fit except at the extreme OOPS momentum settings, where the deviations are up to 10%. This is because the TURTLE model cannot simulate the spectrometer

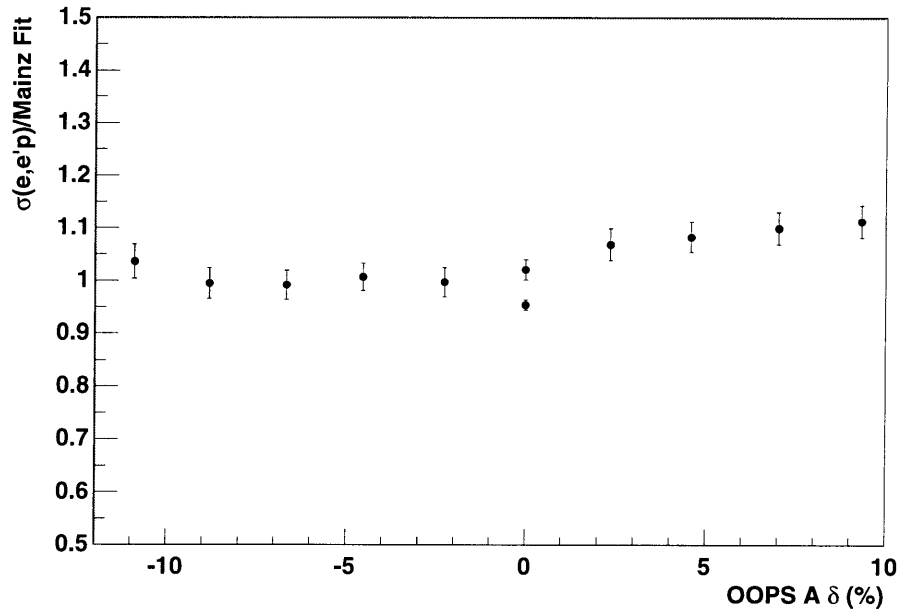

Figure 4-5: $H(e, e'p)$ cross section measured for different OOPS momenta.

boundary very well. This disagreement can help us set an upper limit on the systematic uncertainties of the cross section measurements. The dominant systematic uncertainty results from the phase space volume calculation.

The systematic uncertainties of the $H(e, e'p)$ cross section measurements came from the uncertainty in the beam energy, uncertainties in the target thickness and total charge, uncertainty in the coincidence acceptance determination, errors in the alignment of the spectrometers, momentum resolutions of the OHIPS and OOPS spectrometers and the uncertainties in the Mainz data set.

The dominant systematic uncertainties are the coincidence phase space volume and the target thickness. Based on different $H(e, e'p)$ cross section measurements in Figure 4-5, a 5% uncertainty is assigned to the phase space volume. A 0.2 mm beam position change on the target was translated to a 3% uncertainty in the target thickness. An uncertainty of 1% was assigned to the radiative correction factor. Table 4.2 lists all the known sources of systematic uncertainties and their estimated contributions to the $H(e, e'p)$ cross section measurements.

Table 4.2: Estimated systematic uncertainties in the $H(e,e'p)$ measurements.

Sources	Uncertainties	Contribution to Cross Section
Beam Energy	0.1%	0.4%
Beam Charge	0.1%	0.1%
OOPS Alignment	0.06°	0.5%
OOPS Momentum	1.0%	1.5%
OHIPS Alignment	0.1°	0.9%
OHIPS Momentum	0.25%	0.8%
Target Thickness	3.0%	3.0%
Acceptance	5.0%	5.0%
Mainz Data	1.0%	1.0%
Radiative Correction	1.0%	1.0%
Total		6.3%

Based on the above analysis, the systematic uncertainty in the absolute normalization of this experiment is about 6%. The same systematic error is expected for the $^2H(e,e'p)$ cross section determination.

4.7 Beam Energy Determination

The determination of the beam energy is essential to this experiment since we rely on the precise knowledge of the beam energy for calibration of the spectrometers. It also affects the systematic uncertainties.

For this experiment, the beam energy was determined by the settings of the the Energy Compression System (ECS). The dipole magnets of the ECS chicane were precisely mapped and calibrated. The mapping procedure is documented in detail in reference [83].

There were three factors contributing to the uncertainties in the beam energy as determined by the ECS [13]:

1. The absolute error in the field integral of the central ray through each dipole

was 0.035%.

2. Due to the finite range of momentum acceptance of the chicane, the uncertainty of the beam energy after the ECS was around 0.03%.

3. The mismatch of the beam phase with respect to the Radio Frequency (RF) electromagnetic waves in the cavity after the chicane induced an uncertainty of 0.11% in the beam energy, which was confirmed by the precise beam energy measurement conducted by measuring the spin precession frequency of the electrons in the South Hall Ring [84].

The beam energy for this experiment as determined by the ECS was 800.0 ± 0.8 MeV.

4.8 Beam Polarization Determination

The beam polarization is determined by measuring the asymmetry in the counting rates in the Møller spectrometer Cherenkov detector as the beam helicity is flipped,

$$A_N = \frac{Y^+/Q^+ - Y^-/Q^-}{Y^+/Q^+ + Y^-/Q^-} , \tag{4.10}$$

where $Y^\pm$ and $Q^\pm$ are yield and charge for each helicity state.

Theoretically, at $\theta_{cm} = 90°$,

$$A_N = A_{zz} P_B^z P + A_{xx} P_B^x P_T^x + A_{yy} P_B^y P_T^y , \tag{4.11}$$

and

$$P_B^x = P_B \sin\theta_0, P_B^y = 0, P_B^z = P_B \cos\theta_0 , \tag{4.12}$$

$$P_T^x = P_T \sin\theta_T, P_T^y = 0, P_T^z = P_T \cos\theta_T . \tag{4.13}$$

Here θ_0 is the angle between the direction of beam polarization and the beam direction, and θ_T is the angle between the target polarization and the beam direction. In our measurements, θ_T was set to 30°.

If the beam polarization is along the beam direction, i.e., there is no transverse component, we have

$$A_N = -\frac{7}{9} P_B P_T \cos\theta_T. \tag{4.14}$$

The measured asymmetry, A_{meas}, was diluted by background from processes other than Møller scattering. It can be written as

$$A_{meas} = \frac{A_N}{1 + B/S}\ , \tag{4.15}$$

where S is the rate from the Møller scattering and B is the background rate (assumed to be spin-independent).

Finally the beam polarization can be written as

$$P_B = -\frac{9A_{meas}(1 + B/S)}{7P_T \cos\theta_T}\ . \tag{4.16}$$

To determine the signal to noise ratio and the position of the Møller scattering peak, a quadrupole scan was performed. This was done by changing the quadrupole magnet currents. This procedure is called the "real scan". Figure 4-6 shows a typical real scan for one of the detectors. Then the normalized yield curve was fitted to the function

$$Y(x) = S exp\left[\frac{(-\frac{|x-c|}{w})^p}{p}\right] + B(x)\ , \tag{4.17}$$

where x is the quadrupole shunt voltage and $B(x)$ is a background function, S, w, c and p are fitted parameters. The background was fitted with both linear and exponential functions.

After the real scan was completed and the peak position was determined, a quadrupole scan was performed again near a narrower range which contained the

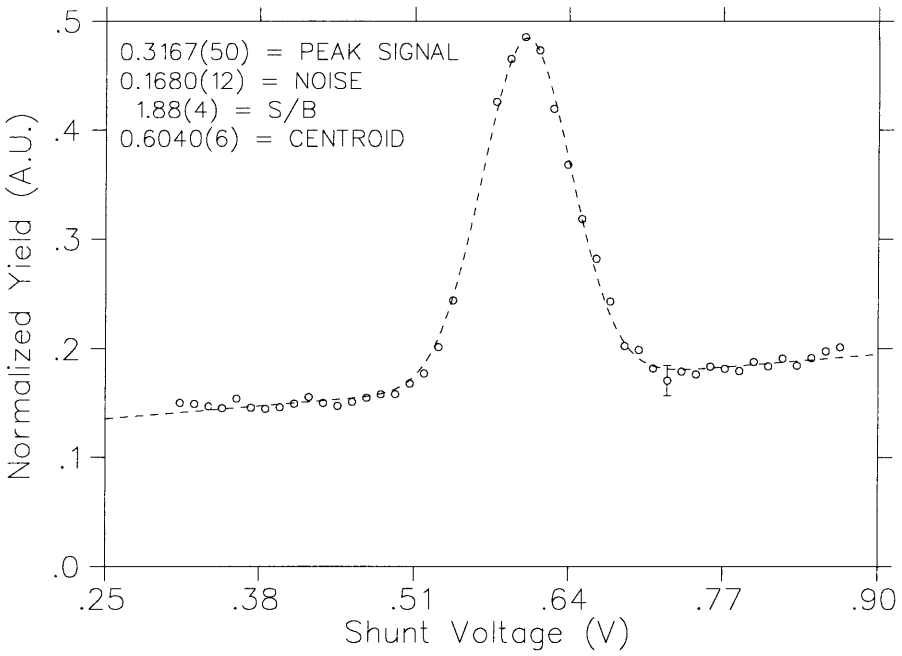

Figure 4-6: Quadrupole "real scan" peak from detector 1 of the Møller polarimeter.

Møller peak. This is called the "peak scan". The purpose of the peak scan was to take more data around the peak region, thus reducing the statistical errors of the measured asymmetries. Figure 4-7 shows typical measured asymmetries as a function of shunt voltage. The asymmetries were fitted to the shape of a Gaussian. The peak asymmetry was used to calculate the beam polarization.

From September 1996 to February 1997 when this experiment was finished, about 20 beam polarization measurements were performed. The measured polarization as a function of run number is plotted in Figure 4-8. Each Møller measurement usually took one hour. The Møller measurement was conducted once every 24 hours, sometimes once every 48 hours when beam conditions were stable.

From the figure, one can see the day-to-day variation of the beam polarization. It could be related to the quantum efficiency of the polarized source crystal which changed with time. Periodic recesiations were performed to keep the quantum efficiency high during the experiment. Among the polarization measurements, the last three are relevant to this experiment. They are listed in Table 4.3.

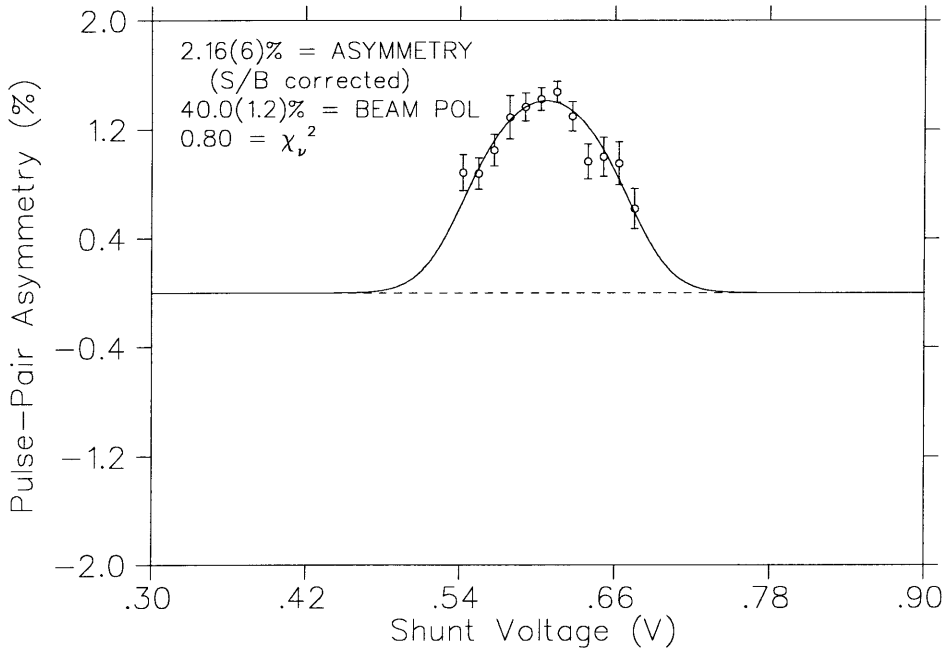

Figure 4-7: Helicity asymmetry in the quadrupole "peak scan".

The systematic errors for the polarization determination come from the following sources:

1. Fluctuations in the beam position cause a change in the scattering angle. The uncertainty associated with knowledge of the beam position leads to a systematic error of 1% in P_B.

2. Relative variations in thickness over the surface of the Supermendur foil. Thick-

Table 4.3: Measured beam polarizations. Statistical error only.

Run Number	Detector 1	Detector 2	Average
1191/1192	38.1 ± 2.4	37.8 ± 3.4	37.9 ± 2.1
1193/1194	35.4 ± 2.7	36.2 ± 1.9	35.8 ± 1.7
1195/1196	41.3 ± 2.4	39.1 ± 2.1	40.2 ± 1.6
Final			38.1 ± 1.8

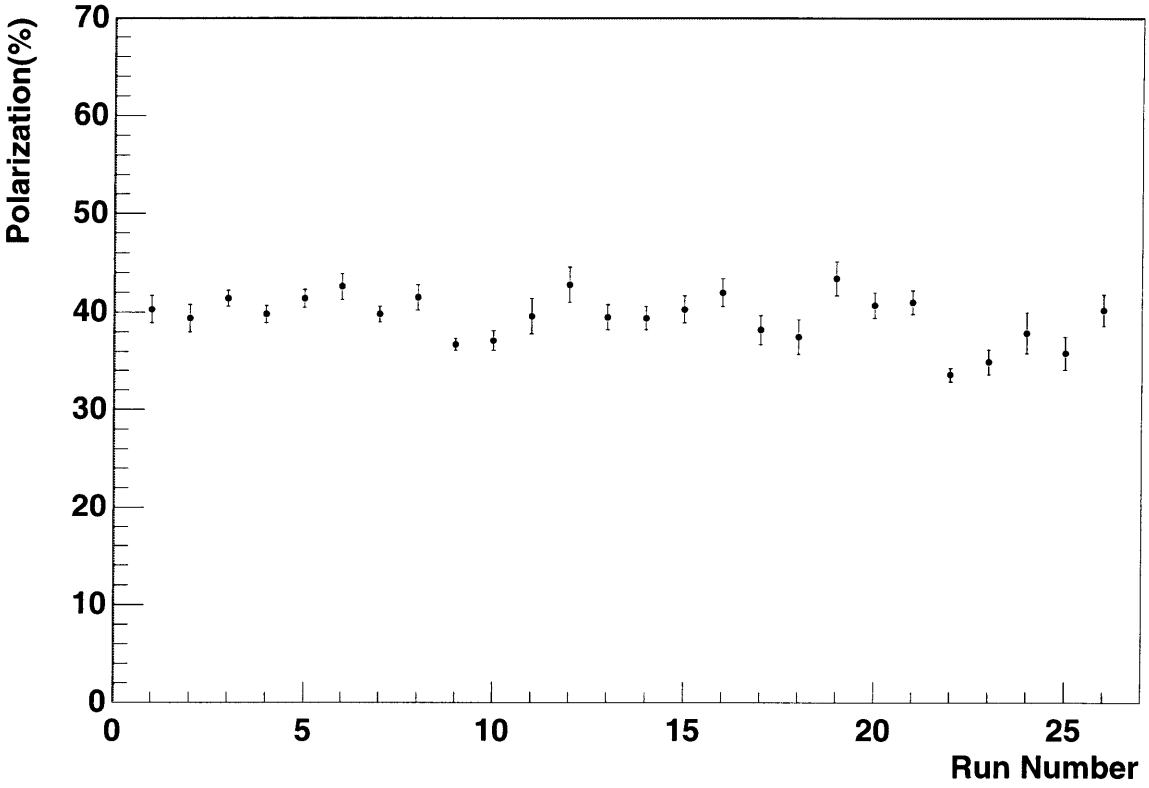

Figure 4-8: Measured beam polarization, plotted as a function of run number.

ness variations coupled with helicity correlated shifts in the electron beam can generate a systematic error in the measured asymmetry.

3. Uncertainty in the target polarization, which was about 1.25%. Beam heating effects can cause a local reduction in the polarization of up to 0.2%.

4. Uncertainty in target angle θ_T. This translates into a P_B uncertainty of 2.1%.

After all major sources of systematic uncertainties were combined together, the error is estimated to be 5.0%. Thus the final average beam polarization for this experiment was $38.1 \pm 1.8 \pm 5.0\%$.

In addition to beam polarization, it was also necessary to know the sign of the beam helicity. When a helicity signal was sent from the polarized source to indicate

the helicity state of the beam pulse, the definition of positive and negative helicity was arbitrary. The Møller polarimeter was used to determine the absolute sign of the helicity.

From Equation 2.12 one can see that the helicity asymmetry is negative when the incoming electron and the target electron have the same polarization direction. Since the magnetic field direction from the Helmholtz coils was known, so was the target polarization direction. Once the target polarization was known, the incoming electron polarization direction could be deduced from the sign of the measured asymmetry.

Chapter 5

$^2H(\vec{e}, e'p)$ Data Analysis

This chapter describes some specific details of the $^2H(e, e'p)$ data analysis that have not been presented in previous chapters. We concentrate on the time-of-flight corrections, missing mass determination, phase space matching, software cuts applied to the data, and asymmetry, cross section and response function extractions. We also discuss the systematic uncertainties for this experiment.

5.1 Time-of-Flight Corrections

The signature of a coincidence event between an electron and a proton is the time of flight. The time-of-flight (TOF) is the time difference in the coincident detection of an electron and a proton. A timing window of 110 ns was set in the hardware to identify raw coincidence events. The TOF TDC was started by an OOPS trigger and stopped by an OHIPS trigger. Ideally a TOF peak would be a delta function. However, it is typically broadened by the following:

1. Because of the finite acceptances of the spectrometers, particles travel different path lengths to reach the scintillators.

2. Particle speeds are different due to momentum differences.

3. The particles strike the scintillators at different locations.

4. Time walk in the discriminators due to the variable scintillator pulse height.

5. Electronic noise and instabilities.

After all the corrections were applied, the TOF peak widths were reduced and the signal-to-noise ratios were improved. Plots of raw and corrected TOF peaks for each OOPS are shown in Figure 5-1. The improvements in signal-to-noise are easily seen. In the next four subsections we discuss how each of these corrections was implemented.

5.1.1 OOPS Momentum

The momentum acceptance of each OOPS was about 10%. Flight times for protons traveling from the target to the scintillators varied considerably due to the momentum difference. The proton path length was calculated from the measured focal plane coordinates of the event and the TRANSPORT matrix elements as

$$\begin{aligned} l_P = l_0 \; &+ \; \langle l|\theta\rangle\theta_f + \langle l|\delta\rangle\delta \\ &+ \; \langle l|\theta^2\rangle\theta_f^2 + \langle l|\delta^2\rangle\delta^2 + \langle l|\theta\delta\rangle\theta_f\delta + \langle l|\phi^2\rangle\phi_f^2 \; . \end{aligned} \tag{5.1}$$

The TRANSPORT matrix elements used to calculate the proton path length are given in Table 5.1 [55]. The proton flight time is thus,

Table 5.1: OOPS matrix elements for time-of-flight corrections.

0^{th} order		1^{st} order		2^{nd} order	
l_0	457.0	$\langle l\|\delta\rangle$	0.031	$\langle l\|\delta^2\rangle$	0.730×10^{-3}
		$\langle l\|\theta\rangle$	0.077	$\langle l\|\theta^2\rangle$	0.860×10^{-3}
				$\langle l\|\theta\delta\rangle$	0.140×10^{-2}
				$\langle l\|\phi^2\rangle$	0.290×10^{-2}

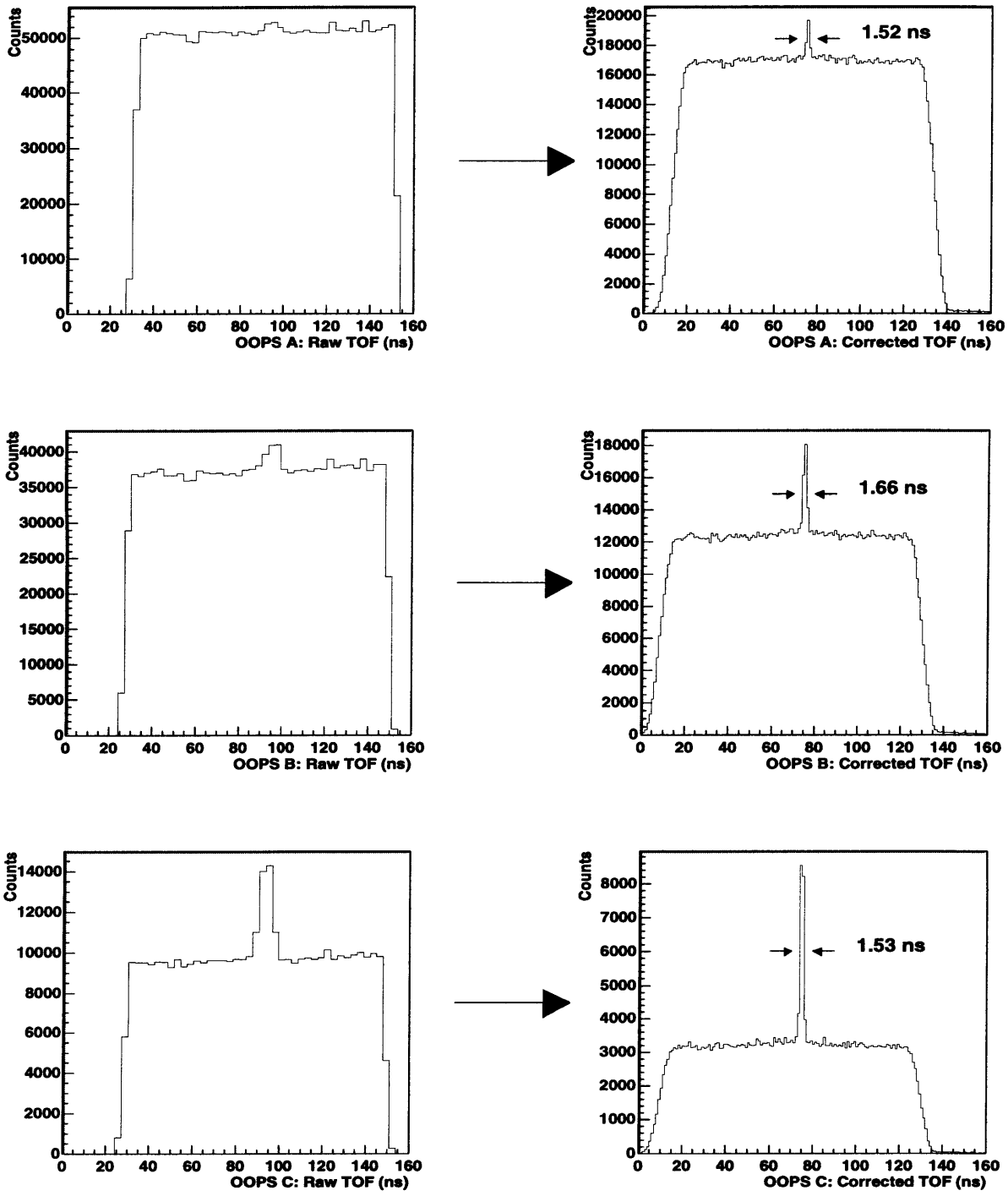

Figure 5-1: Time-of-flight corrections for OOPS A, B and C. The raw TOF and the corrected TOF histograms have different bin sizes.

$$t_P = \frac{l_P}{c\beta_P} , \tag{5.2}$$

where c is the speed of light. The time-of-flight was then corrected by calculating the time of the interaction. This time was subtracted from the OOPS start time and added to the TOF:

$$t_{TOF}^{corr} = t_{TOF}^{raw} + t_P . \tag{5.3}$$

5.1.2 OOPS Scintillator Timing

The OOPS trigger timing was determined by the left phototube signal of scintillator No. 2 (S2L). Because the particle hit point on scintillator No. 2 varies, this time also changes for each event. A software mean time correction was performed to correct this problem. The reasoning behind this correction can be found in [55].

For each delay line TDC reading, it was corrected as

$$t_D^{corr} = t_D - \frac{t_{S2L} + t_{S2R}}{2} , \tag{5.4}$$

where t_D and t_D^{corr} are original and mean-time corrected delay line TDC times, t_{S2L} and t_{S2R} are left and right TDC times of scintillator No. 2.

The mean-time corrected TOF is

$$t_{TOF}^{corr} = t_{TOF}^{raw} - \frac{t_{S2L} + t_{S2R}}{2} . \tag{5.5}$$

Another source of the TOF variation is time walk, which is due to the variation in the amplitude and rise time of the scintillator pulses. The time walk was corrected empirically as

$$t_{TOF}^{corr} = t_{TOF}^{raw} - \frac{41.94}{\sqrt{V_{S2L}}} , \tag{5.6}$$

where V_{S2L} is the S2L scintillator pulse height measured by the ADC.

5.1.3 OHIPS Path Lengths

A mean-timer module was part of the OHIPS trigger electronics. No software mean-time correction is needed for OHIPS.

The dominant OHIPS TOF correction comes from the electron flight path differences. Electron speed variations are not a problem since electrons travel with $\beta \approx 1$. Path lengths are calculated from the focal plane variables and TRANSPORT matrix elements. The path length for a given electron trajectory is given by

$$l_E = l_0 + \langle l|\delta\rangle\delta_e + \langle l|\theta\rangle\theta_t \ . \tag{5.7}$$

The flight time is

$$t_E = \frac{l_E}{c} \ . \tag{5.8}$$

The OHIPS path length TOF correction is

$$t_{TOF}^{corr} = t_{TOF}^{raw} - t_E \ . \tag{5.9}$$

The TRANSPORT matrix elements used for the TOF correction are given in Table 5.2

Table 5.2: OHIPS matrix elements for time-of-flight corrections.

$\langle l\|\delta\rangle$	1.45
$\langle l\|\theta\rangle$	-0.4166

5.2 Missing Mass Determination

Missing mass is an important experimental observable. In our case, it is the binding energy of the deuteron nucleus. The 2.2 MeV missing mass peak is a signature of the

$^2H(e,e'p)$ reaction. It is defined as

$$E_m = \omega - T_p - T_n \tag{5.10}$$

where T_p and T_n are proton and recoiling neutron kinetic energies. They are calculated as following:

$$T_p = \sqrt{P_p^2 + M_p^2} - M_p \ , \tag{5.11}$$

$$T_n = \sqrt{P_n^2 + M_n^2} - M_n \ , \tag{5.12}$$

$$P_n = \sqrt{P_p^2 - 2P_p q cos\theta_{pq} + q^2} \ , \tag{5.13}$$

where $P_p(P_n)$, $M_p(M_n)$ are the momentum and mass of the proton (recoiling neutron). Other variables are defined in Chapter 1.

There were a large number of accidental events compared to the number of true events, especially at the forward angle, as can be seen in the time-of-flight histograms of Figure 5-1. To subtract these accidental events, the following procedure was employed:

1. Three cuts were placed on the corrected TOF histogram. One was centered around the TOF peak at $\pm 3\sigma$, two other cuts were placed on either side of the TOF peak in the "flat" region of the accidentals.

2. Events from the TOF peak formed the missing mass "reals spectrum", and events from the TOF accidental region formed the missing mass "accidentals spectrum".

3. The missing mass accidentals spectrum was scaled by the ratio of the TOF cut-window widths and subtracted from the missing mass reals spectrum to form the missing mass trues spectrum.

The above procedure is demonstrated pictorially in Figure 5-2.

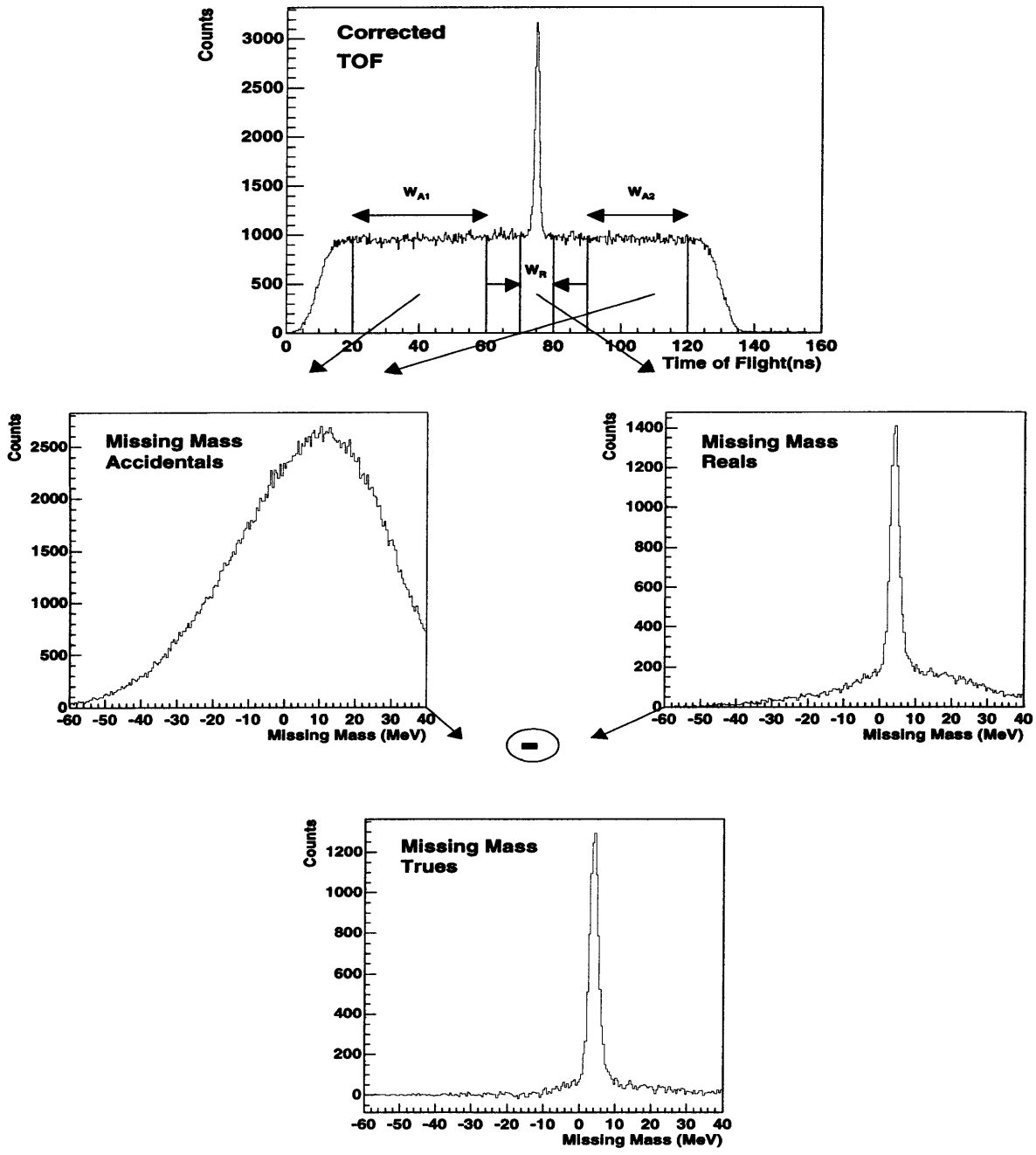

Figure 5-2: Procedure to subtract missing mass accidentals. Shown in the picture are data from the backward OOPS. The top panel shows the corrected TOF histogram with trues and accidentals cut windows. The middle panel shows the missing mass spectra under accidentals and trues cuts. The bottom panel is the background subtracted missing mass spectrum.

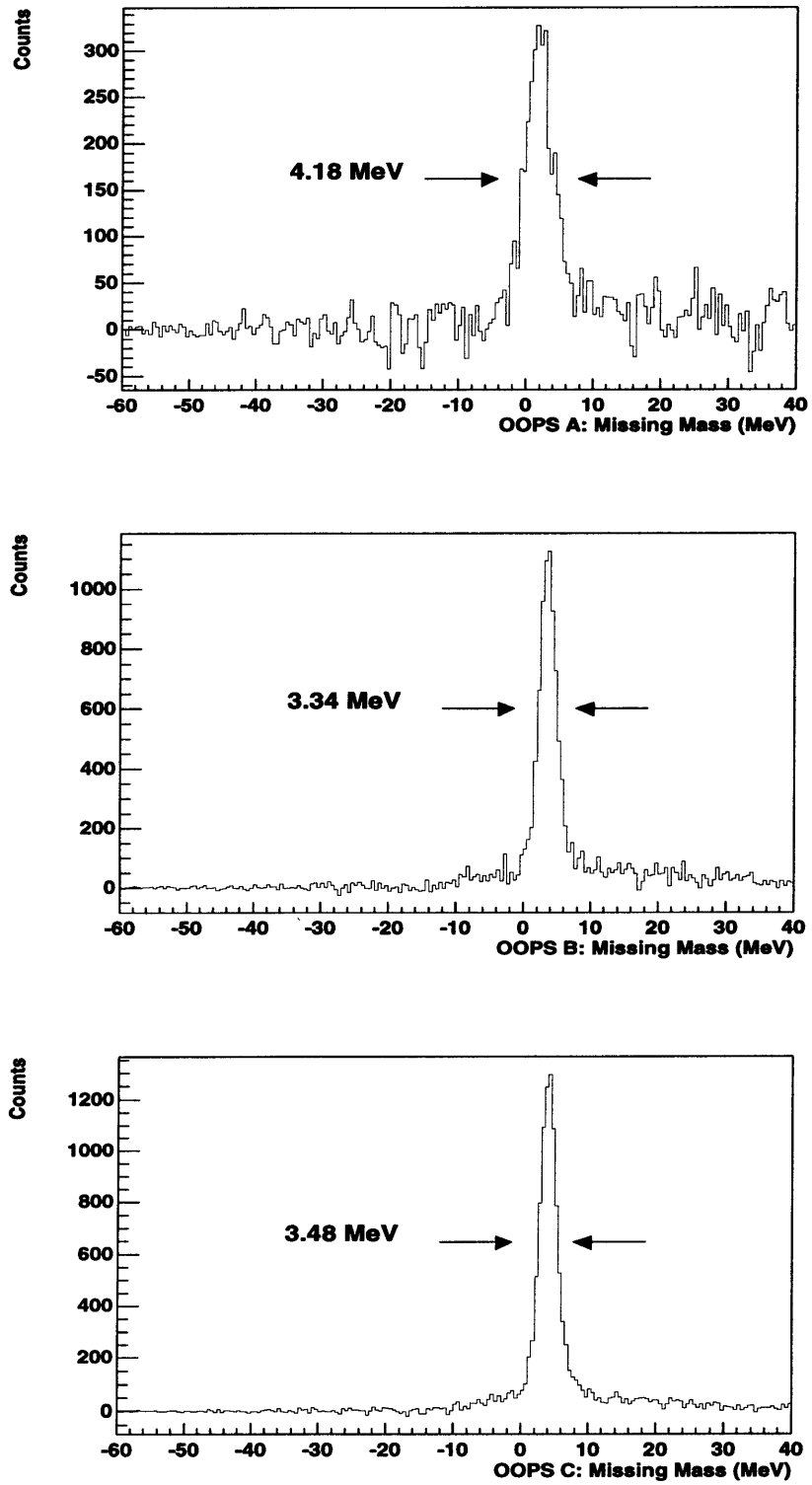

Figure 5-3: Background subtracted missing mass spectrum for OOPS A, B and C.

The background subtracted missing mass spectrum for each OOPS is shown in Figure 5-3. The FWHM of the missing mass spectrum is approximately 2.0 MeV for any particular run. But when all the runs were added together, the missing mass peaks became wider. This is mainly due to beam position changes and spectrometer dipole current fluctuations during the experiment. Furthermore, the missing mass peaks were not positioned exactly at 2.2 MeV. This is primarily due to the energy losses in the target and uncertainties in the δ matrix elements.

5.3 Phase Space Matching

From Equation 1.38 one can see that the $^2H(\vec{e}, e'p)$ coincidence cross section is a function of ω, q, θ_{pq} and ϕ_{pq}^{cm}. Ideally, the spectrometers would define pinpoint acceptances in the relevant kinematic variables. However, the particles in a realistic experiment are detected with finite acceptances, both in the angles and magnitude of the particle momenta. The measured cross sections are averaged over these acceptances. In order to extract f_{LT} and f_{TT} meaningfully, all these dependent kinematic variables have to be in the same ranges. Enforcing the proper kinematic restrictions usually involves software cuts on two or three sets of data. We refer to the procedure of determining and implementing these cuts as phase space matching.

Two-dimensional $\omega - \theta_{pq}$ histograms for the forward, backward and the out-of-plane OOPS are shown in Figure 5-4. One can easily see that the $\omega - \theta_{pq}$ phase space shapes for the forward and backward OOPS are very different. Only data in the matched central region were used to extract LT, TT asymmetries, cross sections and response functions.

The reason why the forward and backward OOPS have different $\omega - \theta_{pq}$ or $\omega - p_m$ dependences is illustrated qualitatively in Figure 5-5. When a scattered electron has energy e_1, the energy and momentum transfer are ω_1 and $\vec{q}_1$. The corresponding missing momenta for the forward and backward OOPS are p_{m1}^F and p_{m1}^B respectively.

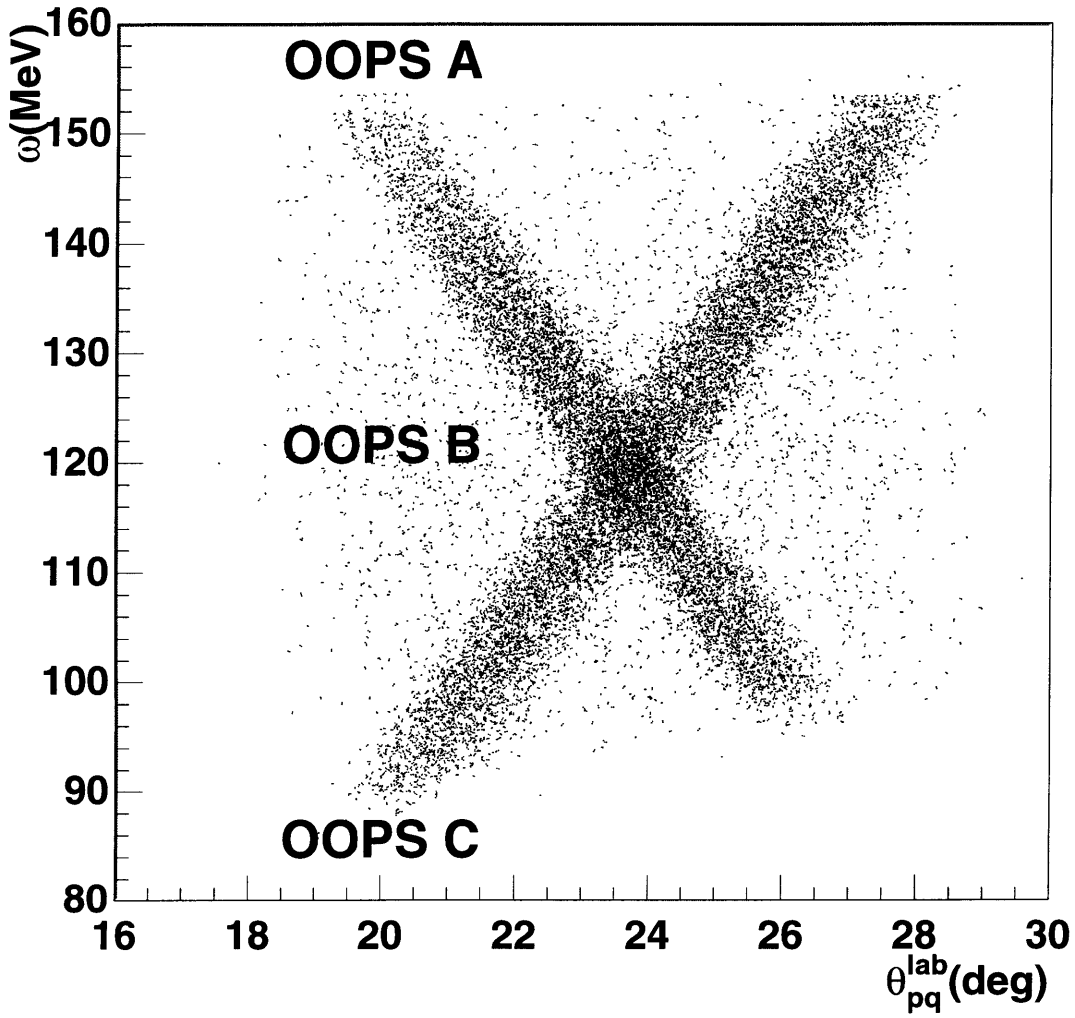

Figure 5-4: Scatter plots of $\omega - \theta_{pq}$ histograms for the forward (A), backward (C) and the out-of-plane OOPS (B).

If the scattered electron momentum is slightly lower, or the energy transfer ω_2 is slightly higher, the missing momenta become p_{m2}^F and p_{m2}^B. It is obvious from the diagram that $p_{m1}^F > p_{m2}^F$, while $p_{m1}^B < p_{m2}^B$. Therefore, $\frac{\partial\omega}{\partial\theta_{pq}} < 0$ at $\phi_{pq}^{cm} = 0°$ and $\frac{\partial\omega}{\partial\theta_{pq}} > 0$ at $\phi_{pq}^{cm} = 180°$. Thus the forward and backward OOPS $\omega - p_m$ phase space have different dependences. The different shape of the $\omega - p_m$ acceptance is entirely caused by the finite momentum acceptance of the electron spectrometer.

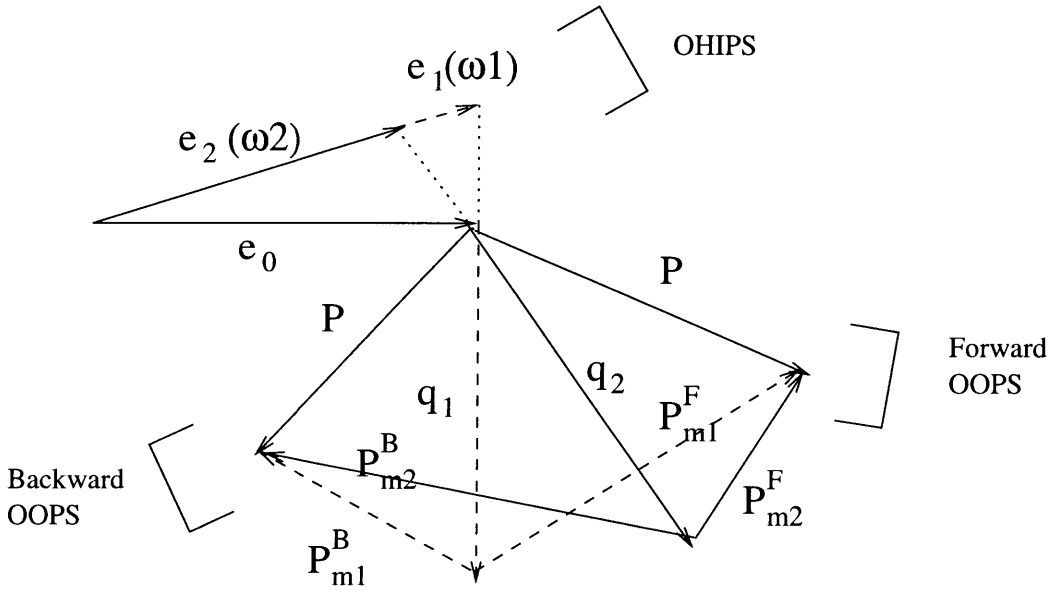

Figure 5-5: A qualitative diagram showing the $\omega - p_m$ acceptance difference between a forward and backward OOPS. See text for explanations.

A Monte Carlo simulation was used to match the phase space instead of the experimental data. The reason is that the experimental phase space was diluted and/or distorted by variation of the cross-section over the spectrometer acceptance and because of radiative effects.

A masking method was developed to match the phase space for different OOPS. It works as follows:

1. Each kinematic variable has a certain range. Each variable was divided into many bins. The number of bins are chosen properly for each variable. If the bin size is too small, a large number of Monte Carlo events have to be generated; if the bin size is too large, the matched phase space would not be accurately determined.

2. Perform Monte Carlo simulations of coincidence events between each OOPS and OHIPS. The simulated events are used to fill up all the bins.

3. If a bin contains more than one event from different OOPS, this bin will be regarded as lying inside the matched phase space, and it is masked as an 1. Otherwise it is masked as a 0.

4. Apply the masks to experimental data to match the phase space. The same masks were also used in the Monte Carlo simulation to calculate the coincidence acceptances.

This masking method can be used to match any number of variables for two or three OOPS's. It was necessary to match only ω, θ_{pq} and q for the LT and TT cross section and asymmetry extractions. There is no need to match ϕ_{pq}^{cm} at all. It is because ϕ_{pq}^{cm} is in the neighborhood of 0°, 90° and 180°, and the averages of $\cos\phi_{pq}^{cm}$ and $\cos 2\phi_{pq}^{cm}$ do not deviate significantly from the central values (less than 2%). Their effects on the response function extractions are much smaller than the statistical and systematic uncertainties.

5.4 Software Cuts

To ensure the quality of the data, several types of software cuts were applied. These are:

1. Generic Cuts. A series of generic cuts were applied on the odd-even signals, HDC TDC, OOPS and OHIPS LAM etc.. Cuts were also made on data type to

discriminate OOPS A, B and C, and on the helicity word to separate H^+ and H^- events.

2. Cut on good proton events. The definition of a good proton event is first, that the event must be a proton. This is ensured by putting a cut on the OOPS scintillator ADC spectrum, as shown in Figure 3-11. Secondly, the proton event must have a good track. This was achieved by cuts on x_d and y_d fitting resolution spectra, as shown in Figure 3-7.

3. Cut on good electron events. First, the analyzer determined that there was an unambiguous good track, which required an analyzable cluster with pivot wires in both chambers. Second, cuts were applied on the Cherenkov sum and lead glass sum to eliminate π^- events, as shown in Figure 3-12. Finally, a series of cuts were applied on the OHIPS x_t, y_t, θ_t and ϕ_t to remove extreme trajectories.

4. Time-of-flight and background cuts. The TOF and background cuts are described in Section 5.2.

5.5 Asymmetry Extractions

There are many advantages to measure asymmetries. The technique used is called STAM (Separation Through Asymmetry Method). Most of the systematic uncertainties, such as luminosity and acceptance volume, cancel out in the the calculation of an asymmetry. In this section, the $A_{LT'}$, A_{LT} and A_{TT} extractions will be discussed.

5.5.1 $A_{LT'}$ Extraction

The helicity dependent asymmetry (also called the fifth structure function asymmetry) was formed by taking the difference over the sum of true coincidence counts for each helicity:

$$A_{LT'} = \frac{N_t^+ - N_t^-}{N_t^+ + N_t^-} \ . \tag{5.14}$$

The true coincidence counts were identified by the characteristic peak in the background subtracted missing mass spectrum. The true counts were determined by subtracting the "accidentals" from the "reals", as shown in Figure 5-2:

$$N_t^\pm = N^\pm - A^\pm \ , \tag{5.15}$$

$$A^\pm = R^\pm A_b^\pm \ , \tag{5.16}$$

where $N^\pm$ is the total number of counts within the TOF peak window for each helicity and $A^\pm$ is the total number of accidental counts within the same TOF window , also for each helicity. $A^\pm$ is estimated by determining the number of accidental counts $A_b^\pm$ within the accidental windows that do not include the peak and multiplying by $R^\pm$, which is the ratio of the TOF peak window width to the accidentals window width for each helicity. $R^\pm$ is calculated as

$$R^\pm = \frac{W_R}{W_{A1} + W_{A2}} \ , \tag{5.17}$$

where W_R is the trues window width and W_{A1}, W_{A2} are the accidentals window widths.

The statistical error for $A_{LT'}$ is

$$\delta A_{LT'} = \frac{1 - A_{LT'}^2}{2} \sqrt{\frac{1}{N_t^+}\left(1 + \frac{1+R^+}{N_t^+/A^+}\right) + \frac{1}{N_t^-}\left(1 + \frac{1+R^-}{N_t^-/A^-}\right)} \ , \tag{5.18}$$

where $N_t^\pm/A^\pm$ is the trues to accidentals ratio within the trues window for each helicity ($N_t^\pm/A$ is also called the signal-to-noise ratio, S/N). Note that when the signal-to-noise ratio becomes bigger and bigger, the statistical error gets smaller and smaller; and when the signal-to-noise ratio approaches infinity, the subtraction error

disappears.

In order to reduce the statistical errors, the signal-to-noise ratios must be kept as large as possible. By using the corrected TOF histograms, the signal-to-noise ratios increase by at least a factor of 3. The background windows were also made as wide as possible.

The major systematic uncertainty for $A_{LT'}$ came from the accumulated charge asymmetry for oppositely signed helicities, which was very small (around 0.1%) and negligible when compared with the statistical errors.

Another source of the systematic uncertainty is the false asymmetry arising from helicity correlated differences in the beam parameters. Because of the way that the helicity states were generated during the experiment, the beam energy, position, angle and spot size were all slightly correlated with the helicity. Fast helicity reversal was achieved by reversing the voltage polarity of the Pockels cell. Changing this voltage can alter the angle and/or exit position of the transmitted laser light. There can also be a helicity correlated difference in the fraction of laser light which was transported to the GaAs crystal. The coincidence counting rate depends on the beam energy, the acceptance of the spectrometer can depend on the beam position and angle, and the background level in the detector may be sensitive to the beam position, size and halo. All these would cause helicity correlated false asymmetry. For example, the helicity correlated beam position shift was in order of $\sim$ 500 nm. However, all the false asymmetries were in order of ppm [85]. Compared with the statistical errors for this experiment, it is not significant.

The extracted asymmetries for OOPS A, B and C and their statistical errors are given in Table 5.3.

5.5.2 A_{LT} Extraction

The A_{LT} extraction is very similar to $A_{LT'}$. The differences are

Table 5.3: OOPS A, B and C helicity dependent asymmetries

Spectrometer	Asymmetry
A	0.039 ± 0.034
B	-0.030 ± 0.015
C	0.010 ± 0.012

1. Two OOPS were involved. One was at a forward angle, and one at a backward angle. To make the asymmetry meaningful, the phase space had to be matched for the two spectrometers, as discussed in Section 5.3.

2. Due to the different counting rates for the forward and backward OOPS, triggering and wire chamber efficiencies were also different. The true counts were corrected for the detector efficiencies.

3. Radiative correction factors could be different for two OOPS's. This had to be taken into account.

We repeat all the equations for $A_{LT'}$ but with modifications for A_{LT}.

$$A_{LT} = \frac{N_c^A - N_c^C}{N_c^A + N_c^C} , \tag{5.19}$$

where superscripts A and C indicate OOPS A (forward) and OOPS C (backward) respectively, $N_c^{A,C}$ are normalized true counts. They are calculated as

$$N_c^{A,C} = \frac{N_t^{A,C} \cdot f_{rad}^{A,C}}{\epsilon^{A,C} \cdot V^{A,C}} , \tag{5.20}$$

where $N_t^{A,C}$ are true counts in the background subtracted missing mass spectra, $\epsilon^{A,C}$ are overall OOPS detection efficiencies, $f_{rad}^{A,C}$ are radiative correction factors for OOPS A and C, and $V^{A,C}$ are coincidence phase space volumes for OOPS A and C. The

overall efficiencies $\epsilon^{A,C}$ are defined as

$$\epsilon^{A,C} = \epsilon_{ot}^{A,C}\epsilon_{oc}^{A,C} \ . \tag{5.21}$$

Here ϵ_{ot} and ϵ_{oc} are OOPS triggering and chamber efficiencies.

Similarly, the statistical error is

$$\delta A_{LT} = \frac{1 - A_{LT}^2}{2}\sqrt{\frac{1}{N_t^A}\left(1 + \frac{1 + R^A}{N_t^A/A^A}\right) + \frac{1}{N_t^C}\left(1 + \frac{1 + R^C}{N_t^C/A^C}\right)} \ , \tag{5.22}$$

where all the symbols have been previously defined.

The systematic errors for A_{LT} came from uncertainties in the OOPS detection efficiencies, coincidence phase space volumes and the radiative correction factors. The detection efficiencies were determined very accurately, and the radiative correction factor difference between forward and backward OOPS is very small, thus the major systematic error was caused by the uncertainty of the coincidence phase space volume.

For this experiment, the extracted A_{LT} and its statistical error are shown in Table 5.4.

Table 5.4: Extracted A_{LT}.

A_{LT}	-0.263 ± 0.035

5.5.3 A_{TT} Extraction

By following the same reasoning as in the previous section, we have

$$A_{TT} = \frac{N_c^A + N_c^C - 2N_c^B}{N_c^A + N_c^C + 2N_c^B} \ , \tag{5.23}$$

where superscript B indicates OOPS B (the out of plane OOPS).

$$N_c^{A,B,C} = \frac{N_t^{A,B,C} \cdot f_{rad}^{A,B,C}}{\epsilon^{A,B,C} \cdot V^{A,B,C}} , \tag{5.24}$$

$$\epsilon^{A,B,C} = \epsilon_{ot}^{A,B,C} \epsilon_{oc}^{A,B,C} , \tag{5.25}$$

and

$$\delta A_{TT} = \frac{1 - A_{TT}^2}{2} \left[\frac{N_t^A}{(N_t^A + N_t^C)^2}(1 + \frac{1 + R^A}{N_t^A/A^A}) + \frac{1}{N_t^B}(1 + \frac{1 + R^B}{N_t^B/A^B}) + \frac{N_t^C}{(N_t^A + N_t^C)^2}(1 + \frac{1 + R^C}{N_t^C/A^C}) \right]^{\frac{1}{2}} . \tag{5.26}$$

All the symbols are self-explanatory.

The extracted A_{TT} and its statistical error are shown in Table 5.5.

Table 5.5: Extracted A_{TT}.

A_{TT}	-0.008 ± 0.040

5.6 Absolute Cross Sections

A similar equation as in Section 4.6 was used to calculate the $^2H(e, e'p)$ cross sections.

The coincidence $^2H(e, e'p)$ cross section is calculated as

$$\sigma_{(e,e'p)} \equiv \frac{d\sigma}{d\omega_e \, d\Omega_e \, d\Omega_p} = \frac{N_c}{\Delta\Omega \cdot \frac{Q}{e} \cdot t \cdot \rho \cdot N_A} \cdot \frac{1}{\epsilon_{ot} \cdot \epsilon_{ht} \cdot \epsilon_{oc} \cdot \epsilon_{hc} \cdot \epsilon_{1/BB} \cdot \epsilon_{si}} \cdot f_{rad} , \tag{5.27}$$

where

N_c $\equiv$ Number of true coincidence events ,

$\Delta\Omega$ $\equiv$ $\Delta\omega_e \cdot \Delta\Omega_e \cdot \Delta\Omega_p$, the coincidence acceptance ,

Q $\equiv$ Total charge (coulomb) ,

e $\equiv$ Electron charge (1.602×10^{-19} coulomb/electron) ,

t $\equiv$ Equivalent target thickness ,

ρ $\equiv$ Target density ,

N_A $\equiv$ Avogadro's constant (6.02×10^{23} particles/mole) ,

ϵ_{ot} $\equiv$ OOPS trigger efficiency ,

ϵ_{ht} $\equiv$ OHIPS trigger efficiency ,

ϵ_{oc} $\equiv$ OOPS chamber efficiency ,

ϵ_{hc} $\equiv$ OHIPS chamber efficiency ,

$\epsilon_{1/BB}$ $\equiv$ One per beam burst veto efficiency ,

ϵ_{si} $\equiv$ OHIPS self-inhibit efficiency ,

f_{rad} $\equiv$ Radiative correction factor .

The coincidence cross sections were calculated for each helicity state and for each OOPS after matching phase spaces. The results are listed in Table 5.6.

Table 5.6: $^2H(\vec{e}, e'p)$ Cross Sections in $nb/MeV \cdot (sr)^2$. The first two rows show the helicity dependent cross sections without phase space cuts. The third row shows the cross sections within the matched phase space.

	OOPS A	OOPS B	OOPS C
σ^+	0.241 ± 0.011	0.318 ± 0.007	0.378 ± 0.006
σ^-	0.223 ± 0.011	0.338 ± 0.007	0.371 ± 0.006
σ	0.224 ± 0.016	0.309 ± 0.023	0.384 ± 0.011

The OHIPS triggering rate was used to monitor the luminosity for each run, which is shown in Figure 5-6. The fluctuation of the normalized yield is around 5%. It was caused by beam position changes and beam charge uncertainty.

Figure 5-7 shows the measured coincidence cross sections for OOPS A, B and C as a function of run number. It is an indication of the overall stability of the cross

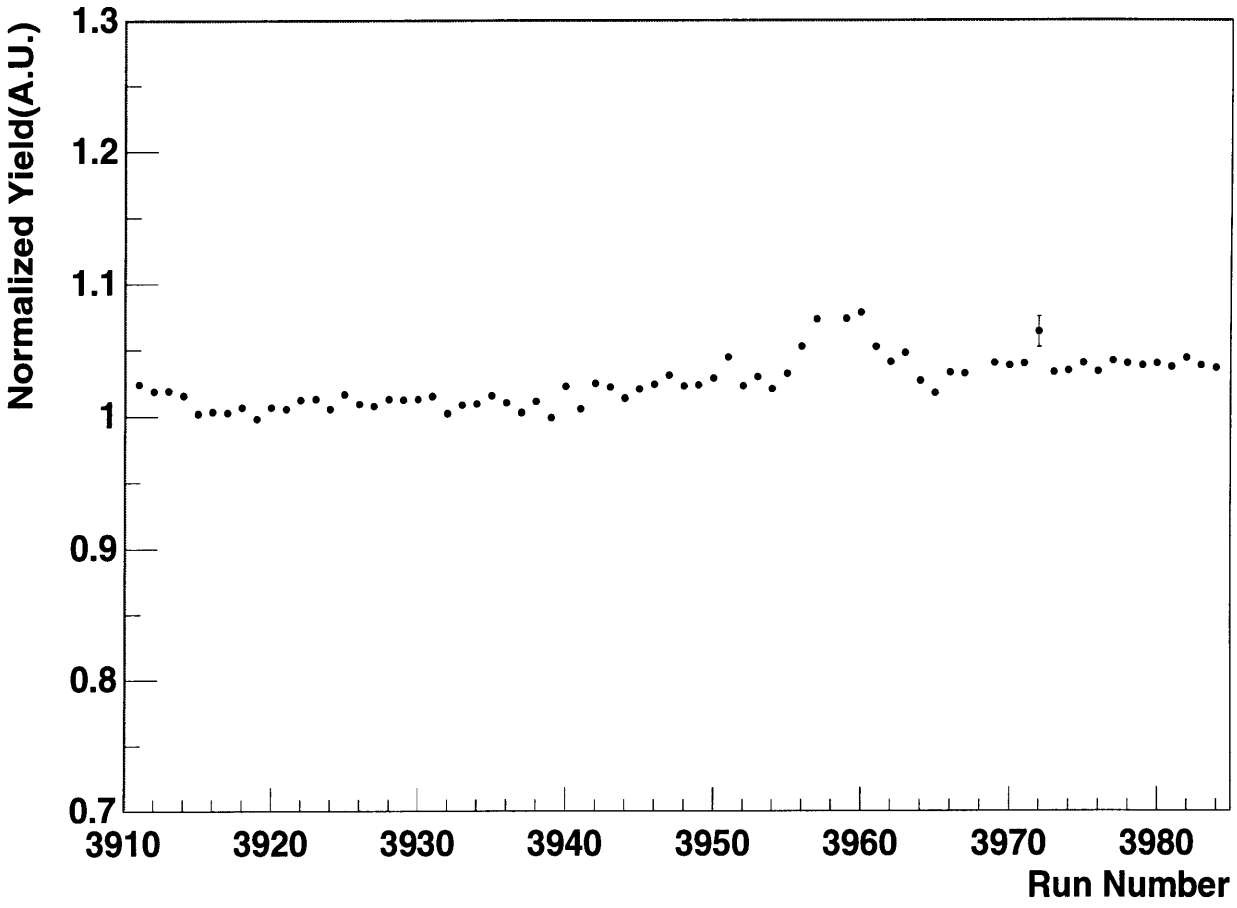

Figure 5-6: Normalized yield as a function of run number.

section measurements. A χ^2 test was performed on each set of cross sections. The results show that the fluctuations of the cross section measurement from run to run are mainly statistical (random), not systematic.

5.7 Response Function Extractions

As in Section 1.4, the response functions are defined as

$$f_{LT'} = \frac{\sigma^+_{\pi/2} - \sigma^-_{\pi/2}}{2CJ\rho_{LT'}P_B}, \tag{5.28}$$

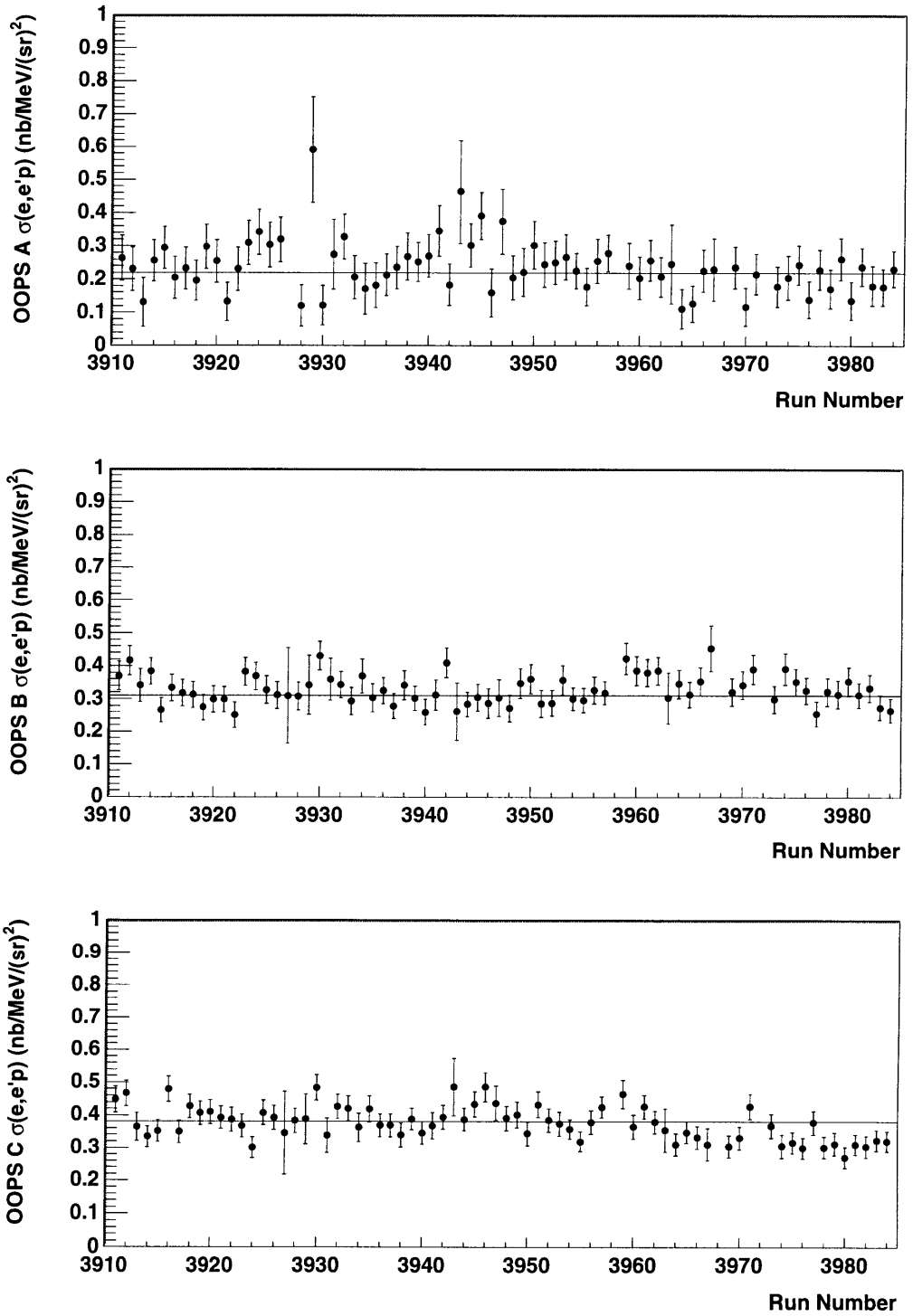

Figure 5-7: Measured coincidence cross sections between OHIPS and OOPS A, B and C as a function of run number. The horizontal lines are averaged cross sections.

$$f_{LT} = \frac{\sigma_0 + \sigma_\pi}{2CJ\rho_{LT}}, \tag{5.29}$$

$$f_{TT} = \frac{\sigma_0 + \sigma_\pi - 2\sigma_{\pi/2}}{4CJ\rho_{TT}}, \tag{5.30}$$

$$f_{L+T} = \frac{\sigma_0 + \sigma_\pi}{2CJ\rho_L}, \tag{5.31}$$

where all factors are previously defined and all the kinematics variables are averaged over the proper phase space by Monte Carlo simulations. Note that the Jacobian factors, $J's$, are in the denominators since we are dealing with the cross sections in the laboratory frame.

The statistical errors for $f_{LT'}$, f_{LT} and f_{TT} may be written as

$$\delta f_{LT'} = |f_{LT'}| \left[\left(\frac{1}{(\sigma^+_{\pi/2} - \sigma^-_{\pi/2})^2} (\delta^2\sigma^+_{\pi/2} + \delta^2\sigma^-_{\pi/2}) + \left(\frac{\delta P_B}{P_B}\right)^2 \right]^{\frac{1}{2}}, \tag{5.32}$$

$$\delta f_{LT} = |f_{LT}| \left[\left(\frac{1}{(\sigma_0 - \sigma_\pi)^2} (\delta^2\sigma_0 + \delta^2\sigma_\pi) \right]^{\frac{1}{2}}, \tag{5.33}$$

$$\delta f_{TT} = |f_{TT}| \left[\left(\frac{1}{(\sigma_0 + \sigma^2_\pi - 2\sigma_{\pi/2})^2} (\delta^2\sigma_0 + \delta^2\sigma_\pi + 4\delta^2\sigma_{\pi/2}) \right]^{\frac{1}{2}}, \tag{5.34}$$

$$\delta f_{L+T} = |f_{L+T}| \left[\left(\frac{1}{(\sigma_0 + \sigma_\pi)^2} (\delta^2\sigma_0 + \delta^2\sigma_\pi) \right]^{\frac{1}{2}}. \tag{5.35}$$

Table 5.7 gives the extracted response functions and their statistical errors.

Table 5.7: Extracted response functions in fm.

$f_{LT'}$	-0.0072 ± 0.0036
f_{LT}	-0.0071 ± 0.0009
f_{TT}	0.0003 ± 0.0016
f_{L+T}	0.0204 ± 0.0006

5.8 Systematic Errors

Systematic errors arise from inaccuracies in the system that are not related to statistics and counting times. The systematic uncertainties for the asymmetries and cross sections have been discussed briefly in the previous sections. Here we summarize the major sources of systematic uncertainties for this experiment. They are

1. The uncertainty in the beam energy: $800.0 \pm 0.8 MeV$.
2. The uncertainties of spectrometer angles due to alignment: $\pm 0.1^\circ$ for OHIPS and $\pm 0.06^\circ$ for OOPS.
3. Coincidence phase space volume: 5%.
4. Equivalent target thickness: 3%.
5. Radiative correction factor: 1%.
6. Beam polarization: 5%.
7. The uncertainty in the amount of charge on target: 0.1%.

It would be very difficult to calculate the dependences of systematic errors on each independent variable analytically. Instead, the approach taken here is mostly numerical. By changing one of the input variables in the analysis by the value of its uncertainty while keeping other variables fixed, the dependence of the final result on this uncertainty is obtained.

To estimate the systematic errors caused by uncertainty in the beam energy and spectrometer misalignments, the central kinematics of this experiment and Arenhövel's full cross sections were used.

The systematic errors for asymmetries, cross sections and response functions due to each major source are presented in Table 5.8.

From Table 5.8, one can see that the systematic errors for the asymmetries are much smaller than that of the cross sections or response functions. This is because

Table 5.8: Sources of error in the measurement.

Item	Fractional error (%)								
	E_e	θ_e	θ_p	V	t	f_{rad}	P_B	Q	Total
$A_{LT'}^{\pi/2}$	0.9	1.7	3.3	–	–	–	–	–	3.8
A_{LT}	2.2	1.7	0.8	–	–	–	–	–	2.9
A_{TT}	2.2	0.7	0.8	–	–	–	–	–	2.4
$\sigma_{\pi/2}^{+}$	2.5	1.0	1.2	5.0	3.0	1.0	–	0.1	6.6
$\sigma_{\pi/2}^{-}$	2.5	1.1	1.2	5.0	3.0	1.0	–	0.1	6.6
σ_0	1.7	0.5	1.0	5.0	3.0	1.0	–	0.1	6.3
$\sigma_{\pi/2}$	2.5	1.0	1.2	5.0	3.0	1.0	–	0.1	6.6
σ_{π}	2.8	1.4	1.4	5.0	3.0	1.0	–	0.1	6.8
$f_{LT'}^{\pi/2}$	2.2	2.5	0.8	5.0	3.0	1.0	5.0	0.1	8.5
f_{LT}	5.4	2.2	2.0	5.0	3.0	1.0	–	0.1	8.5
f_{TT}	0.9	1.1	0.3	5.0	3.0	1.0	–	0.1	6.1
f_{L+T}	3.2	0.5	1.1	5.0	3.0	1.0	–	0.1	6.8

many systematic uncertainties cancel out during the asymmetry calculations. It can also be seen that one of the major systematic errors is the uncertainty of phase space volume, which is rooted in the Monte Carlo simulation. If all the spectrometer responses are measured experimentally, the measured responses, instead of the Monte Carlo simulation, can be used to determine the phase space volume. This would greatly reduce the systematic uncertainty. Another improvement that can be done is to monitor the beam position accurately, which can provide precise information about the target thickness.

5.9 ω and θ_{pq} Dependent Cross Sections

It is interesting to look at the ω and θ_{pq} dependent $^2H(e,e'p)$ cross sections for different ϕ_{pq}^{cm} angles. We divided ω and θ_{pq} into five bins each and calculated the coincidence cross section for each bin. The results are shown in Tables 5.9 and 5.10. Because of the way the $\omega - \theta_{pq}$ phase space is populated, θ_{pq} is not fixed for ω dependent cross sections, and ω is not fixed for θ_{pq} dependent cross sections.

Table 5.9: ω dependent $^2H(e,e'p)$ cross sections in $nb/MeV \cdot (sr)^2$. Errors are statistical only.

ω Range (MeV)	OOPS A	OOPS B	OOPS C
93.6 – 103.6	0.325 ± 0.027	0.406 ± 0.015	0.655 ± 0.015
103.6 – 113.6	0.263 ± 0.018	0.377 ± 0.012	0.582 ± 0.013
113.6 – 123.6	0.239 ± 0.016	0.379 ± 0.012	0.404 ± 0.011
123.6 – 133.6	0.172 ± 0.013	0.289 ± 0.010	0.243 ± 0.009
133.6 – 143.6	0.151 ± 0.012	0.227 ± 0.009	0.165 ± 0.007

Table 5.10: θ_{pq}^{lab} dependent $^2H(e,e'p)$ cross sections in $nb/MeV \cdot (sr)^2$. Errors are statistical only.

θ_{pq}^{lab} Range (°)	OOPS A	OOPS B	OOPS C
21.0 – 22.0	0.162 ± 0.014	0.396 ± 0.015	0.599 ± 0.015
22.0 – 23.0	0.188 ± 0.015	0.331 ± 0.015	0.544 ± 0.013
23.0 – 24.0	0.224 ± 0.017	0.284 ± 0.014	0.395 ± 0.011
24.0 – 25.0	0.259 ± 0.020	0.238 ± 0.013	0.252 ± 0.009
25.0 – 26.0	0.306 ± 0.023	0.204 ± 0.013	0.185 ± 0.008

The ω dependent cross sections for OOPS C, compared with Arenhövel's full calculations, are shown in Figure 5-8.

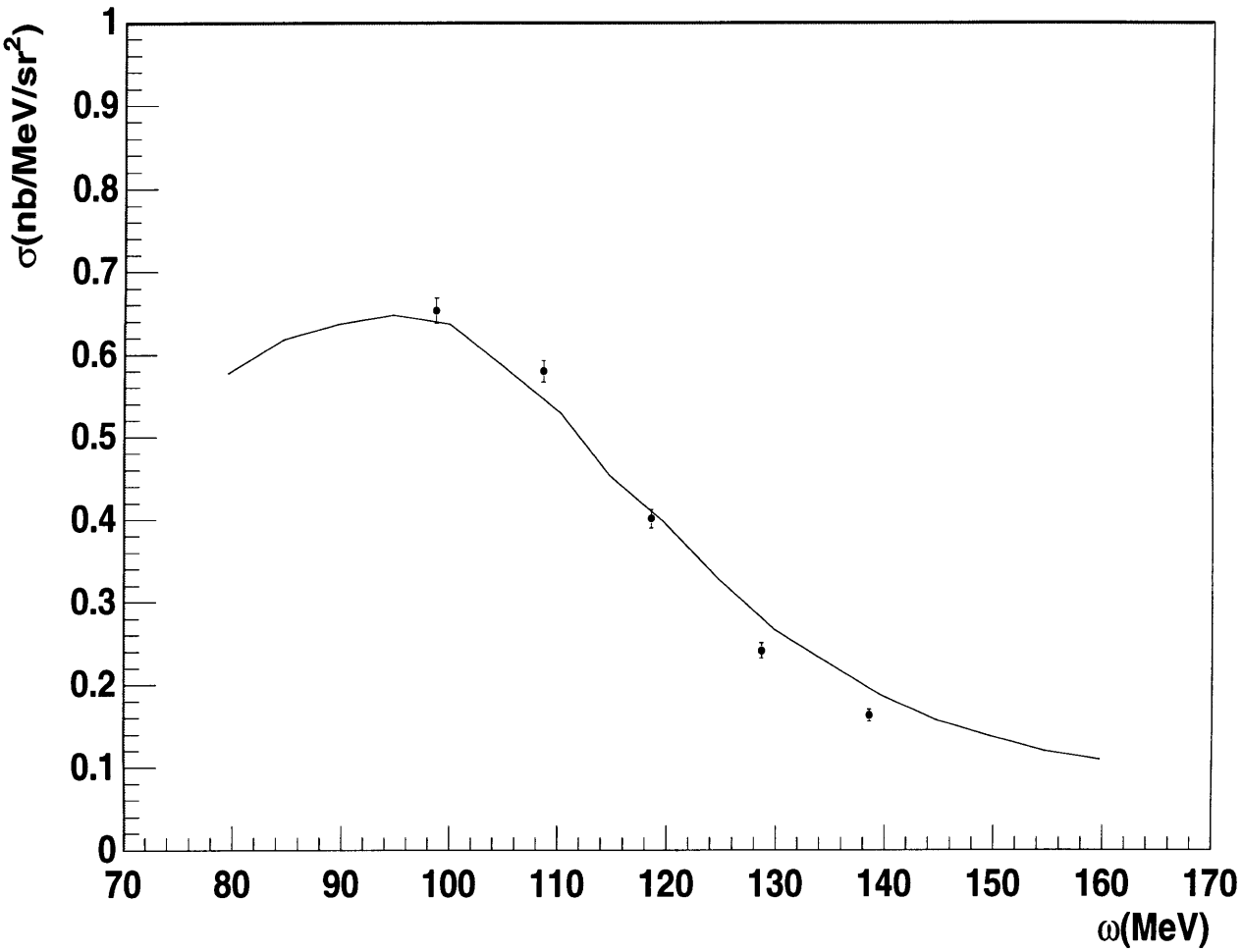

Figure 5-8: ω dependent cross section for OOPS C compared with Arenhövel's full calculation (solid line).

Chapter 6

Results and Discussion

In the previous chapter we presented details on the extraction of differential cross sections, asymmetries and response functions from the raw data. In this chapter we summarize these results and compare them with theoretical calculations. We conclude by discussing possible future directions for the out-of-plane spectrometry program.

6.1 Results

The final experimental results are summarized in Table 6.1. Listed in the table are cross sections, asymmetries and the corresponding response functions. Also presented are the ranges of ω, q, θ_{pq} and ϕ_{pq} over which the cross sections, asymmetries and response functions are extracted. For comparison, the Monte Carlo averaged theoretical calculations of Arenhövel *et al.* [34] are also given in the table. Only the full calculations (N+MEC+IC+RC) were used for the averaging.

To extract $A_{LT'}$ and $f_{LT'}$, the entire coincidence acceptance was taken for each individual OOPS. For the extraction of the LT and TT asymmetries and response functions, the data were masked to create an (ω, q, θ_{pq}) overlap among the $\phi_{pq}^{cm} = 0°, 90°$ and $180°$ data. The LT and TT cross sections, asymmetries and response functions were extracted from this overlapped region. The kinematic factors in the

Table 6.1: List of final results. Cross sections are in $\frac{nb}{MeV \cdot (sr)^2}$, asymmetries in %, and response functions in fm. Folded values are Arenhövel's full calculations averaged over experimental acceptance. ω, q, θ_{pq} and ϕ_{pq} are integration ranges over which the cross sections, asymmetries and response functions are extracted. The range of q is $472 - 505(MeV/c)$.

Item	Integrating ranges and extracted values				
	ω (MeV)	θ_{pq} $(^\circ)$	ϕ_{pq} $(^\circ)$	Extracted Values	Folded Values
σ_0^+	$95-155$	$19-27$	$-12-12$	$0.241 \pm 0.011 \pm 0.016$	0.2278
σ_0^-	$95-155$	$19-27$	$-12-12$	$0.223 \pm 0.011 \pm 0.015$	0.2278
$\sigma_{\pi/2}^+$	$88-155$	$18-29$	$80-100$	$0.318 \pm 0.007 \pm 0.021$	0.3213
$\sigma_{\pi/2}^-$	$88-155$	$18-29$	$80-100$	$0.338 \pm 0.007 \pm 0.022$	0.3349
σ_π^+	$86-155$	$19-29$	$165-195$	$0.378 \pm 0.006 \pm 0.025$	0.3728
σ_π^-	$86-155$	$19-29$	$165-195$	$0.371 \pm 0.006 \pm 0.024$	0.3725
σ_0	$109.0-128.2$	$22.6-22.8$	$-12-12$	$0.224 \pm 0.016 \pm 0.014$	0.2329
$\sigma_{\pi/2}$	$109.0-128.2$	$22.6-22.8$	$85-95$	$0.309 \pm 0.023 \pm 0.020$	0.2961
σ_π	$109.0-128.2$	$22.6-22.8$	$165-195$	$0.384 \pm 0.011 \pm 0.026$	0.3807
$A_{LT'}^0$	$95-155$	$19-27$	$-12-12$	$0.039 \pm 0.034 \pm 0.002$	0.0001
$A_{LT'}^{\pi/2}$	$88-155$	$18-29$	$80-100$	$-0.030 \pm 0.015 \pm 0.001$	-0.0207
$A_{LT'}^\pi$	$86-155$	$19-29$	$165-195$	$0.010 \pm 0.012 \pm 0.000$	0.0004
A_{LT}	$109.0-128.2$	$22.6-22.8$	–	$-0.263 \pm 0.035 \pm 0.008$	-0.2410
A_{TT}	$109.0-128.2$	$22.6-22.8$	–	$-0.008 \pm 0.040 \pm 0.000$	0.0178
$f_{LT'}$	$88-155$	$18-29$	$80-100$	$-0.0072 \pm 0.0036 \pm 0.0006$	-0.00486
f_{LT}	$109.0-128.2$	$22.6-22.8$	–	$-0.0071 \pm 0.0009 \pm 0.0006$	-0.00661
f_{TT}	$109.0-128.2$	$22.6-22.8$	–	$0.0003 \pm 0.0016 \pm 0.0000$	-0.00072
f_{L+T}	$109.0-128.2$	$22.6-22.8$	–	$0.0204 \pm 0.0006 \pm 0.0014$	0.02055

response function extractions were averaged over the corresponding phase space. The first error in the extracted values is statistical, and the second one is the systematic uncertainty.

6.2 Comparison with Theory

As presented in Chapter 1, Arenhövel and co-workers have performed systematic theoretical calculations of deuteron electrodisintegration [19, 20, 21, 22, 23, 24, 25]. A brief overview of Arenhövel's approach has been presented in Section 1.3. In the figures that follow, we explore the sensitivity of the cross sections, asymmetries and response functions, at the kinematics of our experiment, to the inclusion of meson exchange currents, isobar configurations and finally to the role of relativistic corrections. Given that our data involve averaging over finite acceptances, in both the electron and proton arms, similar averages were performed over the same kinematic acceptance for the theoretical results by Monte Carlo simulations. We present the following types of Arenhövel cross sections, asymmetries and response functions for comparison with our data:

1. The PWBA non-relativistic.
2. The normal (N) non-relativistic calculation.
3. The non-relativistic calculation including meson-exchange effects (N+MEC).
4. The non-relativistic calculation including both meson-exchange and isobaric contributions (N+MEC+IC).
5. The full calculation including meson-exchange, isobar configurations and relativistic corrections (N+MEC+IC+RC).

The deuteron initial state and the interactions of the outgoing n-p system in these calculations are based on the Paris potential [27]. Various calculations show very

little sensitivity to the choice of any realistic NN potential model [55]. This is not surprising, since each model, though constructed differently, was fitted to precise data, and consequently, should yield very similar results.

The IC effects are included in an Impulse Approximation (IA) framework. Since at our kinematics, these effects are expected to be small, such an approximation should be appropriate. However, in the Δ region, one may include the IC effects with a coupled-channel approach.

The comparisons of cross sections, asymmetries and response functions are presented in Figures 6-1, 6-2 and 6-3, respectively.

In these figures, the square boxes are the folded theoretical values; the horizontal bars represent the ranges over which the theoretical calculations are averaged. The solid dots are measured values in this experiment, and the vertical error bars are statistical errors.

Since three OOPS's were used in the experiment, the helicity dependent asymmetry was extracted for each individual OOPS. Figure 6-4 shows $A_{LT'}$ as a function of the out-of-plane angle ϕ_{pq}^{cm}.

6.3 Discussions

From Figure 6-1 to 6-4, one can see that the data generally agree with Arenhövel's full calculations very well. By looking at the cross section curves as a function of ϕ_{pq}^{cm} in Figure 6-1, it can be seen that the cross section is more sensitive to FSI at $\phi_{pq}^{cm} = 180°$ than at $\phi_{pq}^{cm} = 0°$. In contrast, the cross section is more sensitive to the relativistic corrections at $\phi_{pq}^{cm} = 0°$ than at $\phi_{pq}^{cm} = 180°$. At all angles, MEC and IC contribute significantly to the cross section. Our data show that one needs to include MEC and IC in the cross section calculations even at the quasi-elastic kinematics.

The data for the A_{LT} asymmetry and the f_{LT} response function are well described by the full calculations which include relativistic corrections. This agrees with the

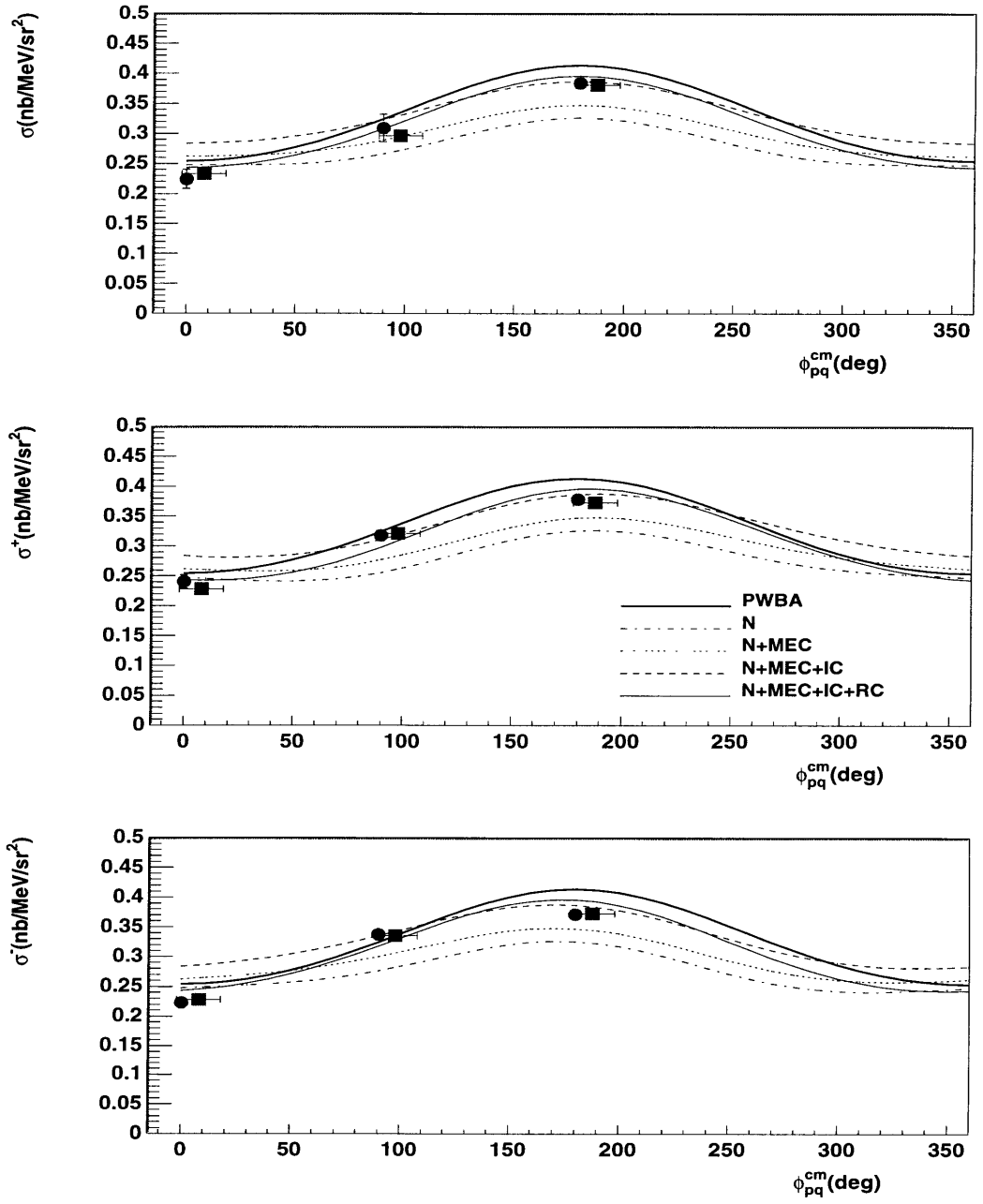

Figure 6-1: Measured cross sections (solid dots) compared to Arenhövel's calculations, plotted as a function of out-of-plane angle ϕ_{pq}^{cm}. The square boxes are the folded theoretical calculations, which are shifted to the right to avoid overlapping with the solid dots. The horizontal bars represent the ϕ_{pq}^{cm} ranges over which the theoretical calculations are averaged. The top figure shows the total cross sections within matched phase spaces for OOPS A, B and C. The middle figure is the cross section for electron helicity $h = +1$, and the bottom one with $h = -1$. The electron polarization used in the calculations is $P_e = 38.1\%$.

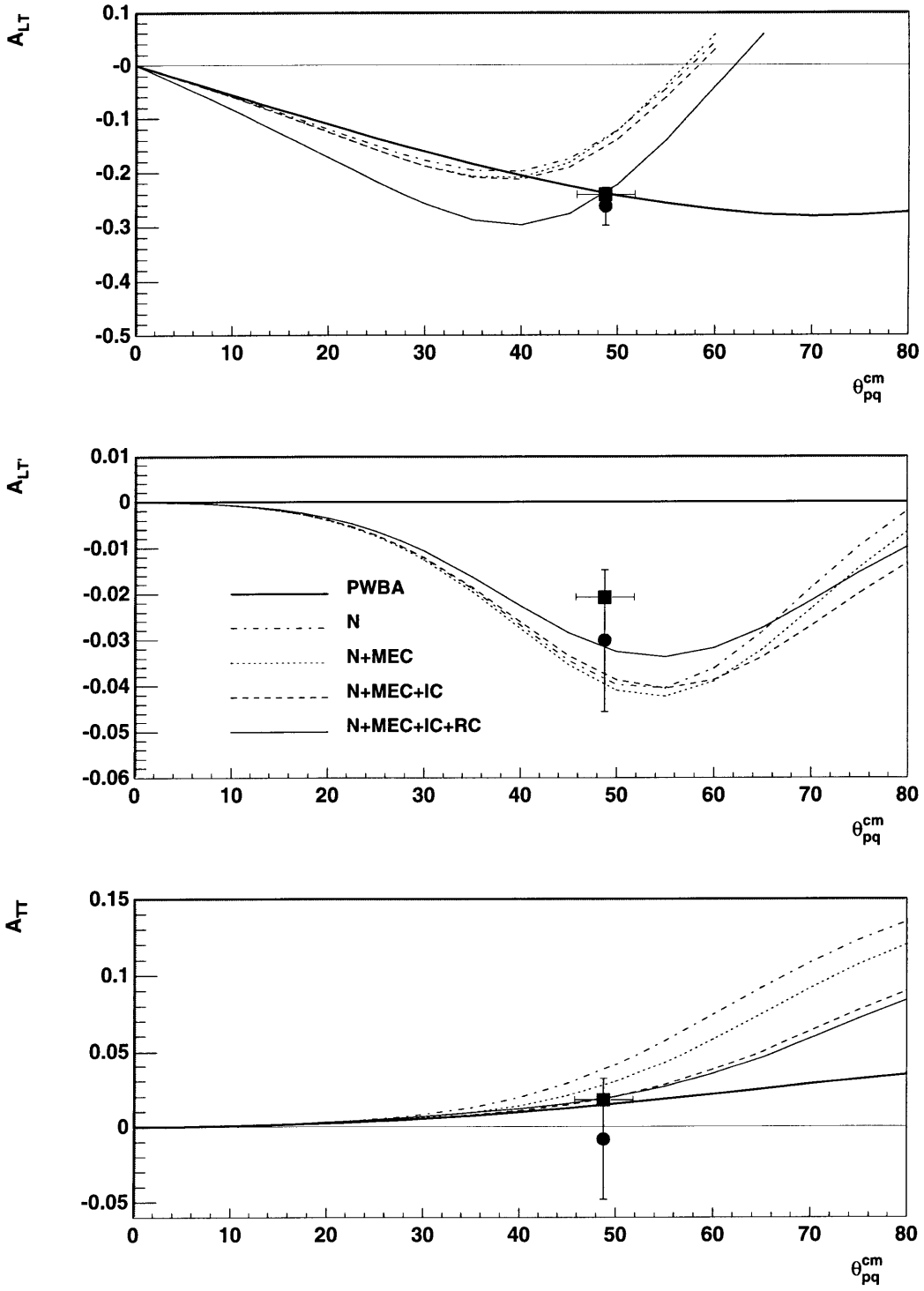

Figure 6-2: Measured asymmetries (solid dots) compared to Arenhövel's calculations, plotted as a function of the azimuthal angle θ_{pq}^{cm}. The square boxes are the folded theoretical calculations. The horizontal bars represent the θ_{pq}^{cm} ranges over which the theoretical calculations are averaged.

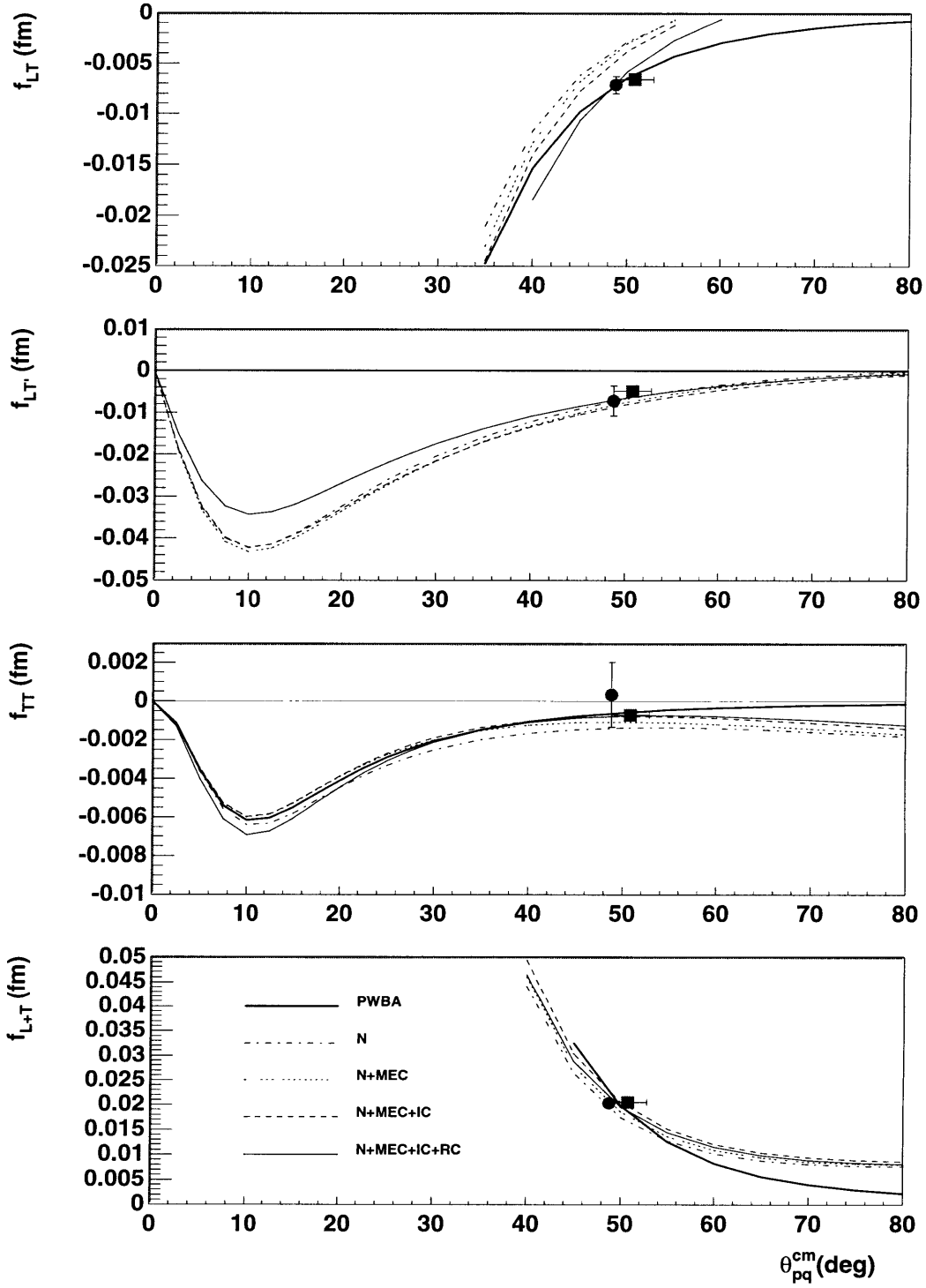

Figure 6-3: Measured response functions (solid dots) compared to Arenhövel's calculations, plotted as a function of the azimuthal angle θ_{pq}^{cm}. The square boxes are the folded theoretical calculations, which are shifted to the right to avoid overlapping with the solid dots. The horizontal bars represent the θ_{pq}^{cm} ranges over which the theoretical calculations are averaged.

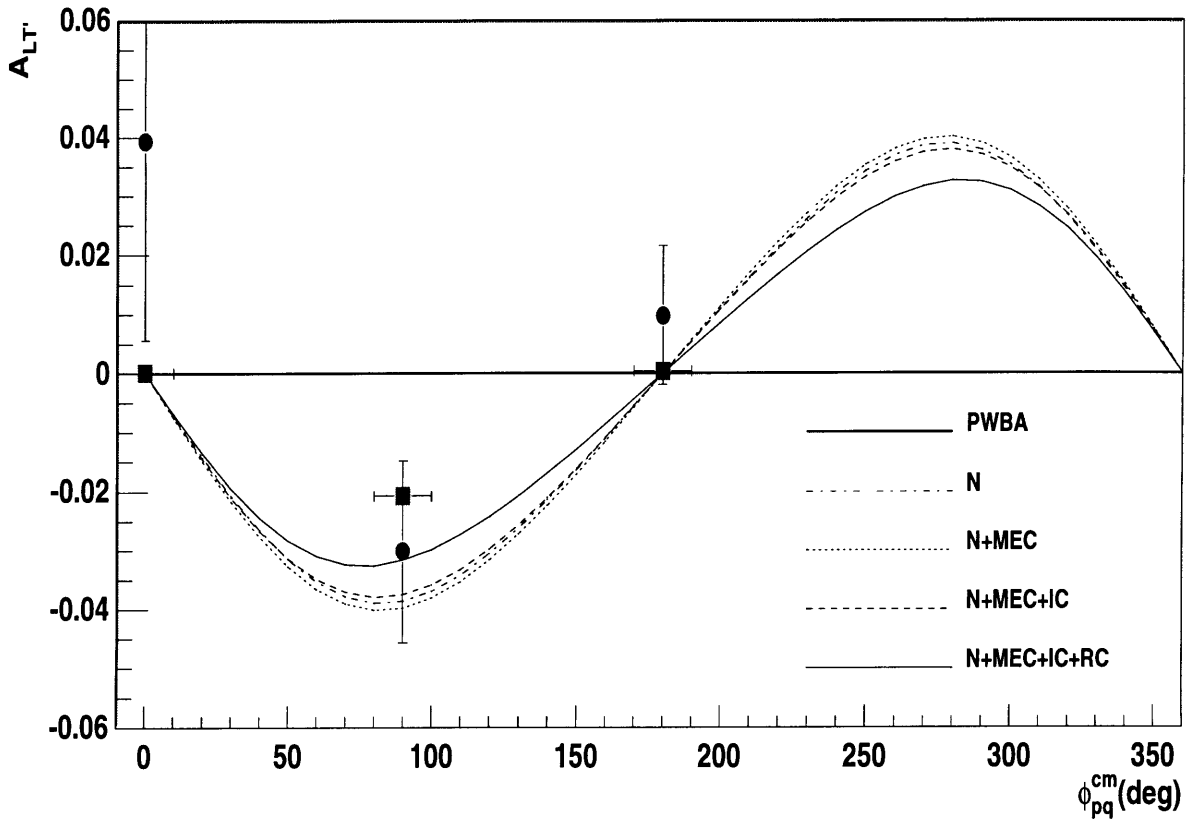

Figure 6-4: Measured $A_{LT'}$ (solid dots) as a function of the out-of-plane angle ϕ_{pq}^{cm}, comparing with Arenhövel's calculations. The square boxes are the folded theoretical calculations. The horizontal bars represent the ϕ_{pq}^{cm} ranges over which the theoretical calculations are averaged.

early findings from Bonn [39], Saclay [40], NIKHEF [38] and Bates [41], as discussed in Chapter 1. At the kinematics for this experiment, the PWBA and N+MEC+IC+RC results are the same. The asymmetry and the response function agree with both calculations. This is attributed to the fact that the inclusion of MEC and IC cancel the FSI effects at $\phi_{pq}^{cm} = 180°$ and the RC effects at $\phi_{pq}^{cm} = 0°$. However, when we move to the higher missing momentum (or larger θ_{pq}^{cm}) region, these two curves diverge rapidly, which means the FSI becomes more important. Other A_{LT} and f_{LT} measurements [61] conducted at Bates with varying missing momentum confirm this. It would be interesting if we could selectively turn on or turn off the FSI in the theoretical calculations to determine which part of the FSI (spin-spin or spin-orbit or both) comes into play at high missing momenta.

In PWBA, the initial and final state wave functions are treated as plane waves. In this case the hadronic tensor is completely symmetric. The helicity dependent asymmetry $A_{LT'}$ and response function $f_{LT'}$, which arise from the contraction of the antisymmetric part of the leptonic tensor with the antisymmetric part of the hadronic tensor, are identically zero. What we measured are clearly non-zero at $\phi_{pq}^{cm} = 90°$, which shows that the final state interactions play an important role here. This is seen in the difference between the N and PWBA curves in the plot. However, the contributions of MEC, IC and RC are small.

It is also interesting to observe the ϕ_{pq}^{cm} dependence of the $A_{LT'}$ asymmetry as displayed in Figure 6-4. The $\sin\phi_{pq}^{cm}$ dependence is predicted in Equation 1.38. Due to the $\sin\phi_{pq}^{cm}$ factor in the helicity dependent term, the asymmetry $A_{LT'}$ vanishes at $\phi_{pq}^{cm} = 0°, 180°$. This is confirmed by these measurements.

We know A_{TT} and f_{TT} are very small at our kinematics. The measurements also confirm this. However, due to the small asymmetry and low statistical accuracy, no firm conclusions can be drawn. For higher missing momenta, it is expected that the isobar configurations will play a bigger role and the asymmetry would become more sensitive to these effects. This becomes more obvious in the "dip" or Δ region, as described in [67]. With a continuous electron beam available in the near future, more accurate measurements are planned. However, our data demonstrate that A_{TT} and f_{TT} can be measured precisely using the unique OOPS facility at Bates.

6.4 Conclusions

In summary, the following conclusions can be made as a result of the measurement of the deuteron response functions f_{LT}, $f_{LT'}$ and f_{TT}:

1. The data (cross sections, asymmetries and response functions) agree with Arenhövel's full calculations within the statistical uncertainties.

2. The non-relativistic description of the longitudinal-transverse interference response function of the reaction falls short. The relativistic calculations describe the data much better than the non-relativistic calculations. Therefore, a relativistic description of the longitudinal-transverse interference response function f_{LT} is essential.

3. The calculated response functions at these kinematics are relatively insensitive to meson exchange currents and isobar configuration effects. However, the data indicate that one needs to include these small effects even for the quasi-elastic kinematics.

4. The helicity dependent asymmetry $A_{LT'}$ is non-zero within a confidence interval of $\pm 2\sigma$, which indicates that the helicity dependent response function $f_{LT'}$ is very sensitive to the final state interactions.

5. It is possible to measure f_{TT} with controlled systematic and statistical uncertainties.

6.5 Outlook

As stated in Chapter 1, this experiment is only a small part of a much more ambitious program to systematically measure all deuteron response functions at various kinematics[14, 15]. With the completion of the fourth OOPS module, together with a support system which permits all four OOPS modules to be arrayed azimuthally about a symmetry axis in the scattering plane, more comprehensive measurements can be conducted with fully controlled systematic uncertainties. Future improvements at the Bates accelerator facility, such as increasing the duty factor to 100% with the newly constructed pulse stretcher ring and doubling the beam polarization by using strained gallium-arsenide crystals, will significantly reduce the statistical errors for asymmetry and structure function measurements. These measurements will definitely

help constrain theoretical deuteron electrodisintegration models. A proposed setup of the OOPS cluster system is shown in Figure 6-5.

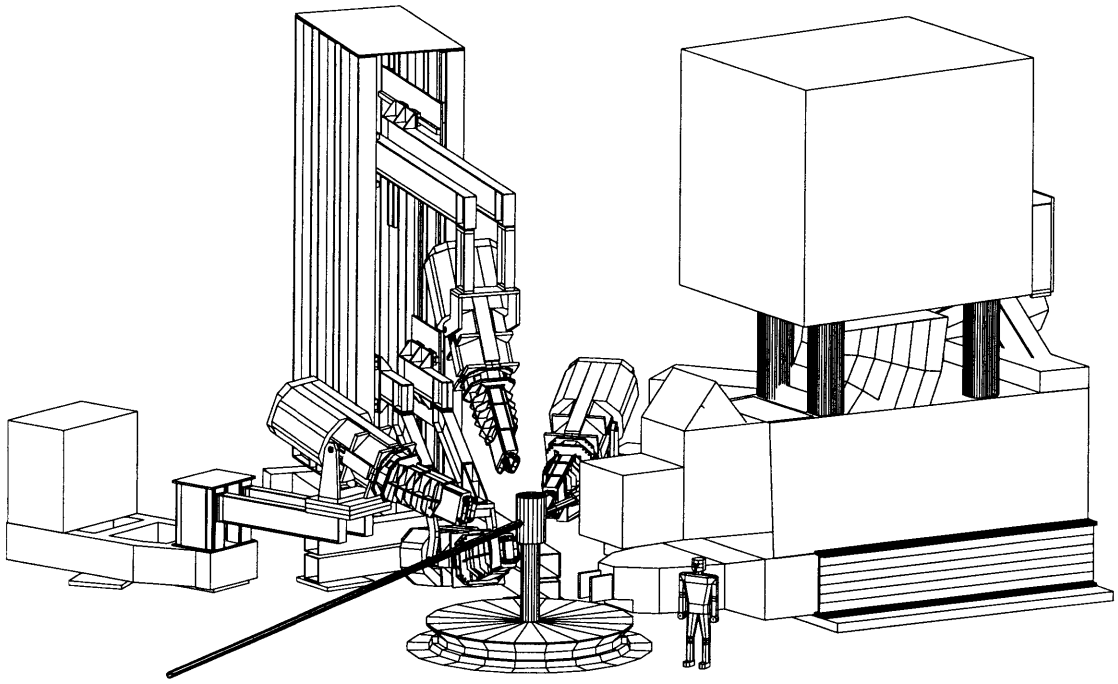

Figure 6-5: A proposed arrangement of a cluster of OOPS spectrometers with the OHIPS spectrometer in the South Hall at Bates in a typical out-of-plane $(e, e'p)$ geometry.

The kinematics of the remaining deuterium program at Bates [87] are summarized in Table 6.2. For this program, the physics goal is focused at the high missing momentum or large θ_{pq}^{cm} region where the deuteron D-state dominates and where accurate measurements of the ${}^2H(\vec{e}, e'p)$ interference response functions will place important constrains on the different models of the NN interaction. By performing the systematic studies over a broad kinematic range, such as proposed, the role played by various interaction effects would also be well quantified.

The primary goal of the OOPS program at Bates is to study the $N \rightarrow \Delta$ transition on the proton via the $H(\vec{e}, e'p)\pi^0$ reaction [86]. The study of the $N \rightarrow \Delta$ transition in the nucleon provides a deep insight about hadronic physics, which involves the resonant quadrupole excitation of the Δ. In Spring 1998, part of the original $N \rightarrow \Delta$

Table 6.2: Kinematical quantities for future measurements.

Kin	E_e (MeV)	ω (MeV)	q (MeV/c)	q^2 (fm^{-2})	E_{np} (MeV)	θ_{pq}^{cm} $(^\circ)$	p_r (MeV/c)
4A(Δ)	800	265.0	438	3.14	217	34.8	315
2B(QE)	800	118.6	486	5.72	56	78.5	300
3B(dip)	800	155.0	414	3.79	110	61.4	290
4B(Δ)	600	265.0	438	3.14	217	70.6	442

proposal, $H(\vec{e}, e'p)\pi^0$ [86] and $H(\vec{e}, e'\pi^+)$ [91], were completed at Bates. Two OOPS spectrometers were used for the simultaneous measurements of $R_{LT'}$ and R_{LT} response functions. The data analysis is underway.

In addition, several new experiments have been approved by the Bates PAC with high scientific grades, which will use the unique OOPS facility. These experiments would require CW beams to achieve high statistical accuracy. They would also benefit greatly from a high polarization beam. These experiments fall into four physics categories:

1. Studies of the quadrupole component in the $N \rightarrow \Delta$ transition:

   - Exp 87-09 $H(\vec{e}, e'p)\pi^0$ [89].
   - Exp 97-05 $H(\vec{e}, e'p)\gamma$ [90].
   - Exp 97-04 $H(\vec{e}, e'\pi^+)n$ [91].

2. Studies of the electromagnetic currents in the deuteron:

   - Exp 89-14 $^2H(\vec{e}, e'p)n$ [87].
   - Exp 89-10 $^2H(\vec{e}, e'p)n$ [88].

3. Studies of the generalized polarizabilities of the proton through virtual Compton scattering:

   - Exp 97-03 $H(e, e'p)\gamma$ [92].

4. Studies of few-nucleon systems:

   - Exp 97-06 $^3\vec{H}e(\vec{e}, e'd)p$ [93].
   - Exp 97-01 $^4He(\vec{e}, e'p)t$ [94].

Besides the already approved experimental programs which will utilize the OOPS facility, the versatility of the OOPS spectrometry system opens the door to several other areas of investigation. Aside from natural extensions of any $(\vec{e}, e'p)$ program, it is important to note that OOPS has shown its capability as a more general hadron detector, allowing for $(\vec{e}, e'd)$, $(\vec{e}, e'\pi^+)$ and $(\vec{e}, e'\pi^-)$ measurements. Such π^- and π^+ capabilities enables us to carry out a complete set of production measurements from the deuteron, $^2H(\vec{e}, e'\pi^-)pp$ and $^2H(\vec{e}, e'\pi^+)nn$, to other few-body systems, such as $^3\vec{H}e(\vec{e}, e'\pi^+)t$ and $^3\vec{H}e(\vec{e}, e'\pi^\pm)X$.

Combining this general hadron detection capability with other laboratory facilities opens other interesting possibilities. One example is to utilize a $^3\vec{H}e$ target in conjunction with the above mentioned pion-production experiments. Also intriguing is the possible combination of the Focal Plane Polarimeter (FPP) [10, 13] on OHIPS with the use of the out-of-plane OOPS as electron spectrometers to allow access to virtually all the interference response functions in $(\vec{e}, e'p)$ reactions. While to date none of these ideas for potential expansion have been thoroughly investigated or developed into PAC proposals, they are noted here to indicate the possible new directions and to show the promise of continuing extensive and fruitful physics programs which can follow the current experiment.

Appendix A

OOPS and OHIPS Matrix Elements

A.1 OOPS Matrix Elements

The OOPS target quantities are calculated as

$$\begin{aligned}\delta_{\rm t} = \delta_0 \;\; &+ \;\; \langle\delta|x\rangle x_f + \langle\delta|\theta\rangle\theta_f + \langle\delta|x\theta\rangle x_f\theta_f + \langle\delta|\theta^2\rangle\theta_f^2 \\ &+ \;\; \langle\delta|\theta y^2\rangle\theta_f y_f^2 + \langle\delta|y^2\rangle y_f^2 + \langle\delta|\theta^2\rangle\theta_f^2 \;,\end{aligned} \tag{A.1}$$

$$\begin{aligned}\theta_{\rm t} = \theta_0 \;\; &+ \;\; \langle\theta|\theta\rangle\theta_f + \langle\theta|x\rangle x_f + \langle\theta|x\theta\rangle x_f\theta_f + \langle\theta|x^2\rangle x_f^2 \\ &+ \;\; \langle\theta|xy\rangle xy + \langle\theta|x\theta^2\rangle x_f\theta_f^2 + \langle\theta|x^2\theta\rangle x_f^2\theta_f \;,\end{aligned} \tag{A.2}$$

$$\phi_t = \phi_0 + \langle\phi|y\rangle y_f \;. \tag{A.3}$$

All positions are in *cm*, angles in *mrad* and δ in %. The OOPS δ, θ and ϕ matrix elements are given in Table A.1, A.2 and A.3, respectively.

Table A.1: OOPS δ Matrix Elements.

δ Matrix Elements	OOPS A	OOPS B	OOPS C
δ_0	0.28	0.00	-0.03
$\langle\delta\|x\rangle$	4.64	4.39	4.46
$\langle\delta\|\theta\rangle$	-4.25×10^{-3}	-4.42×10^{-3}	5.57×10^{-3}
$\langle\delta\|x\theta\rangle$	2.57×10^{-2}	2.15×10^{-2}	2.02×10^{-2}
$\langle\delta\|\theta^2\rangle$	7.71×10^{-5}	1.15×10^{-4}	7.29×10^{-5}
$\langle\delta\|\theta y^2\rangle$	4.48×10^{-5}	-3.50×10^{-5}	-2.29×10^{-5}
$\langle\delta\|y^2\rangle$	-1.04×10^{-3}	7.03×10^{-4}	3.48×10^{-3}
$\langle\delta\|\theta^2\rangle$	0.00	0.00	2.11×10^{-5}

Table A.2: OOPS θ Matrix Elements.

θ Matrix Elements	OOPS A	OOPS B	OOPS C
θ_0	-0.19	3.34	0.08
$\langle\theta\|\theta\rangle$	-0.27	-0.28	-0.28
$\langle\theta\|x\rangle$	-4.26	-4.08	-3.58
$\langle\theta\|x\theta\rangle$	-3.69×10^{-2}	-2.83×10^{-2}	-2.89×10^{-2}
$\langle\theta\|x^2\rangle$	0.32	0.00	0.36
$\langle\theta\|xy\rangle$	-7.65×10^{-3}	0.0	0.0
$\langle\theta\|x\theta^2\rangle$	0.00	0.00	-1.41×10^{-4}
$\langle\theta\|x^2\theta\rangle$	0.00	0.00	2.56×10^{-3}

Table A.3: OOPS ϕ Matrix Elements.

ϕ Matrix Elements	OOPS A	OOPS B	OOPS C
ϕ_0	0.00	0.00	0.00
$\langle\phi\|y\rangle$	1.10	1.09	1.10

A.2 OHIPS Matrix Elements

The OHIPS matrix elements were obtained in the chamber coordinate [61]. The chamber offsets are corrected as

$$x_c = x_{ch} + 0.4 \ , \tag{A.4}$$

$$\theta_c = \theta_{ch} - 783.1 - 1.605x_c + 0.0017x_c^2 \ , \tag{A.5}$$

$$y_c = y_{ch} - 0.24 - 0.0022x_c + 0.0002x_c^2 \ , \tag{A.6}$$

$$\phi_c = \phi_{ch} + 3.74 + 0.093x_c - 0.0007x_c^2 \ , \tag{A.7}$$

where x_{ch}, θ_{ch}, y_{ch} and ϕ_{ch} are raw particle positions in the chamber coordinate; x_c, θ_c, y_c and ϕ_c are offset corrected particle coordinates.

The OHIPS target variables are calculated as

$$\delta_t = \sum_{k,l,m,n} \langle \delta | x_c^k \theta_c^l y_c^m \phi_c^n \rangle x_c^k \theta_c^l y_c^m \phi_c^n \ , \tag{A.8}$$

$$\theta_t = \sum_{k,l,m,n} \langle \theta | x_c^k \theta_c^l y_c^m \phi_c^n \rangle x_c^k \theta_c^l y_c^m \phi_c^n \ , \tag{A.9}$$

$$y_t = \sum_{k,l,m,n} \langle y | x_c^k \theta_c^l y_c^m \phi_c^n \rangle x_c^k \theta_c^l y_c^m \phi_c^n \ , \tag{A.10}$$

$$\phi_t = \sum_{k,l,m,n} \langle \phi | x_c^k \theta_c^l y_c^m \phi_c^n \rangle x_c^k \theta_c^l y_c^m \phi_c^n \ . \tag{A.11}$$

Possible values of k, l, m, n and the matrix elements are given in Table A.4. All units are standard: positions in cm, angles in $mrad$ and δ in %.

Table A.4: OHIPS Matrix Elements.

k	l	m	n	$\langle\delta\|x_c^k\theta_c^l y_c^m\phi_c^n\rangle$	$\langle\theta\|x_c^k\theta_c^l y_c^m\phi_c^n\rangle$	$\langle y\|x_c^k\theta_c^l y_c^m\phi_c^n\rangle$	$\langle\phi\|x_c^k\theta_c^l y_c^m\phi_c^n\rangle$
0	0	0	0	8.936×10^{-1}	$0.000 \times 10^{+0}$	$0.000 \times 10^{+0}$	$0.000 \times 10^{+0}$
0	0	0	1	$0.000 \times 10^{+0}$	$0.000 \times 10^{+0}$	-6.916×10^{-2}	$-1.097 \times 10^{+0}$
0	0	0	2	1.320×10^{-4}	$0.000 \times 10^{+0}$	$0.000 \times 10^{+0}$	$0.000 \times 10^{+0}$
0	0	1	0	$0.000 \times 10^{+0}$	$0.000 \times 10^{+0}$	-7.987×10^{-1}	5.273×10^{-1}
0	0	1	1	$0.000 \times 10^{+0}$	2.636×10^{-2}	$0.000 \times 10^{+0}$	$0.000 \times 10^{+0}$
0	1	0	0	6.180×10^{-3}	$-1.289 \times 10^{+0}$	$0.000 \times 10^{+0}$	-2.424×10^{-2}
0	1	0	1	$0.000 \times 10^{+0}$	$0.000 \times 10^{+0}$	-1.542×10^{-3}	-4.281×10^{-3}
0	1	0	2	-3.857×10^{-6}	-1.204×10^{-4}	$0.000 \times 10^{+0}$	$0.000 \times 10^{+0}$
0	1	1	0	$0.000 \times 10^{+0}$	$0.000 \times 10^{+0}$	$0.000 \times 10^{+0}$	1.221×10^{-2}
0	1	1	1	$0.000 \times 10^{+0}$	8.027×10^{-4}	$0.000 \times 10^{+0}$	$0.000 \times 10^{+0}$
0	2	0	1	$0.000 \times 10^{+0}$	$0.000 \times 10^{+0}$	4.571×10^{-5}	1.167×10^{-4}
0	3	0	1	$0.000 \times 10^{+0}$	$0.000 \times 10^{+0}$	$0.000 \times 10^{+0}$	1.656×10^{-6}
1	0	0	0	1.658×10^{-1}	$0.000 \times 10^{+0}$	$0.000 \times 10^{+0}$	$0.000 \times 10^{+0}$
1	0	0	1	$0.000 \times 10^{+0}$	$0.000 \times 10^{+0}$	-1.680×10^{-3}	-5.709×10^{-3}
1	0	1	2	$0.000 \times 10^{+0}$	$0.000 \times 10^{+0}$	$0.000 \times 10^{+0}$	5.346×10^{-5}
1	1	0	0	1.769×10^{-4}	3.237×10^{-3}	$0.000 \times 10^{+0}$	$0.000 \times 10^{+0}$
2	0	0	0	-2.099×10^{-4}	$0.000 \times 10^{+0}$	$0.000 \times 10^{+0}$	$0.000 \times 10^{+0}$
3	0	0	0	$0.000 \times 10^{+0}$	$0.000 \times 10^{+0}$	$0.000 \times 10^{+0}$	-7.709×10^{-5}
5	0	0	0	8.210×10^{-9}	$0.000 \times 10^{+0}$	$0.000 \times 10^{+0}$	$0.000 \times 10^{+0}$

Appendix B

OOPS and OHIPS TURTLE Models

TURTLE(Trace Unlimited Rays Through Lumped Elements) is a computer program designed to simulate charged particle transport systems. The version used in this thesis is non-standard. It was heavily-modified by J. Mandelville [69], which includes a modified input file structure and some new options [73].

Though three OOPS modules were used in the experiment, only one OOPS TURTLE model was used in the simulations, because they have identical designs and the measured properties for three OOPS modules are also almost identical [61].

B.1 OOPS TURTLE Model

```
(This is a TURTLE deck for Joe Mandeville's version of the program.)
(DESIGN-MOMENTUM 0.625)

(This is an OOPS module deck which is presumably used as one
(spectrometer in a coincident simulation.)
```

```
(Use second order optics and enforce aperture in the magnets.)
SECOND ON
APERTURES ON
(Give the dipole vertical and horizontal width/2.)
(Following slits are more restrictive, so these are effectively)
(ignored.)
DIPOLE-APERTURE 15.24,4.1275
(See the TURTLE manual for fringe fields; this is unclamped)
(Rogowski.)
FRINGE-FIELD .7,4.4

(Write the target coordinates to the output file.)
 DETECTOR

(Shift any target positions here. E.g., shift y for an)
(offset beam spot.)
(SHIFT 0. 0. 0. 0. 0. 0.)

(Drift to the target chamber window)
DRIFT 0.254
(scattering chamber window)
(     ---  mass [MeV], L/L_r)
( Kapton dens = 1.42 )
( CH2    dens = 0.92 -- 0.95 g/cm^3  L_r = 44.8 g/cm^2  )
(air                                 L_r = 30420 cm     )
(MULTIPLE-SCATTER 938.0 1.04E-4)

(Drift through air )
```

```
DRIFT 1.0423
(air--multiple scattering)
(MULTIPLE-SCATTER 938. 3.2873E-3)

(spectrometer entrance window )
(MULTIPLE-SCATTER 938. 1.04E-4)

(The vertical acceptance of the front collimator during the)
(Feb. 1991 test run is used below.  This corresponds to an)
(aperture of +-31mr in theta_target.)
 RECTANGULAR-SLIT 1  4.1778
(With the collimator insert used for the data cycle later in the)
(spring of 1991, the acceptance in theta_target was reduced to)
(+-25 mr.)
(RECTANGULAR-SLIT 1  3.24075)
(The horizontal acceptance is +-12 mr.)
 RECTANGULAR-SLIT 3  1.5634
 DETECTOR

(Drift to the effective field boundary of the dipole somewhere)
(inside the front collimator.)
 DRIFT .058958

(O O P S    D I P O L E)
(Model the OOPS dipole.  The total distance is 1.317366 m, and)
(the field is 6 kG.  We have partioned the dipole into many parts
(to include the baffles as slits.)
(beginning of dipole field inside front collimator)
```

```
OFFSET-RECTANGULAR-SLIT 1    -4.22          4.17
POLE-FACE-ROTATION           12.8616
Dipole                        0.059959      6.0       0.00000
(end of top of front collimator)
OFFSET-RECTANGULAR-SLIT 1    -4.36          +4.40
OFFSET-RECTANGULAR-SLIT 3    -1.72          +1.72
Dipole                        0.018385      6.0       0.00000
(end of bottom of front collimator)
OFFSET-RECTANGULAR-SLIT 1    -7.30          +4.50
Dipole                        0.284477      6.0       0.00000
(1st top baffle)
OFFSET-RECTANGULAR-SLIT 1    -6.10          +11.23
Dipole                        0.068472      6.0       0.00000
(2nd top baffle)
OFFSET-RECTANGULAR-SLIT 1    -6.33          +10.45
Dipole                        0.081898      6.0       0.00000
(1st bottom baffle, 3rd top baffle)
OFFSET-RECTANGULAR-SLIT 1    -6.61          +6.46
Dipole                        0.070855      6.0       0.00000
(2nd bottom baffle)
OFFSET-RECTANGULAR-SLIT 1    -11.39         +6.67
Dipole                        0.038675      6.0       0.00000
(4th top baffle)
OFFSET-RECTANGULAR-SLIT 1    -6.90          +8.11
Dipole                        0.020247      6.0       0.00000
(3rd bottom baffle)
OFFSET-RECTANGULAR-SLIT 1    -8.18          +6.89
Dipole                        0.050833      6.0       0.00000
```

```
(4th bottom baffle)
OFFSET-RECTANGULAR-SLIT 1   -11.28          +7.03
Dipole                       0.044326       6.0       0.00000
(5th top baffle, 5th bottom baffle)
OFFSET-RECTANGULAR-SLIT 1    -7.31          +7.17
Dipole                       0.040070       6.0       0.00000
(6th bottom baffle)
OFFSET-RECTANGULAR-SLIT 1    -9.11          +7.28
Dipole                       0.037596       6.0       0.00000
(7th bottom baffle)
OFFSET-RECTANGULAR-SLIT 1   -11.07          +7.40
Dipole                       0.036304       6.0       0.00000
(8th bottom baffle)
OFFSET-RECTANGULAR-SLIT 1   -12.90          +7.51
Dipole                       0.022248       6.0       0.00000
(6th top baffle)
OFFSET-RECTANGULAR-SLIT 1    -7.66          +8.34
Dipole                       0.013061       6.0       0.00000
(9th bottom baffle)
OFFSET-RECTANGULAR-SLIT 1    -8.27          +7.63
Dipole                       0.035989       6.0       0.00000
(10th bottom baffle)
OFFSET-RECTANGULAR-SLIT 1    -9.94          +7.73
Dipole                       0.037747       6.0       0.00000
(11th bottom baffle)
OFFSET-RECTANGULAR-SLIT 1   -11.62          +7.83
Dipole                       0.041258       6.0       0.00000
(7th top baffle, 12th bottom baffle)
```

```
OFFSET-RECTANGULAR-SLIT 1    -8.07          +7.96
Dipole                        0.046455       6.0       0.00000
(13th bottom baffle)
OFFSET-RECTANGULAR-SLIT 1   -10.05          +8.08
Dipole                        0.055635       6.0       0.00000
(14th bottom baffle)
OFFSET-RECTANGULAR-SLIT 1    -12.31         +8.27
Dipole                        0.070104       6.0       0.00000
(15th bottom baffle)
OFFSET-RECTANGULAR-SLIT 1   -12.05          +8.45
Dipole                        0.142960       6.0       0.00000
POLE-FACE-ROTATION              8.8616
(end of dipole field -- still inside vacuum box)
OFFSET-RECTANGULAR-SLIT 1   -10.15         +12.98

(The end of the rear flange of the dipole vacuum box)
DRIFT .089060
ELLIPTICAL-SLIT  1   8.62    3   8.62
RECTANGULAR-SLIT 3   3.33248

DRIFT .012692
(A circular lead collimator between the dipole and quad kills)
(bad rays before they enter the quad.)
(The front of the ring collimator)
ELLIPTICAL-SLIT  1   8.62    3   8.62

DRIFT .063492
(The end of the ring collimator)
```

```
ELLIPTICAL-SLIT  1   8.62    3   8.62

(The dipole-quad distance for the North Hall OOPS is slightly)
(shorter than the design value.  This is presumably taken up here)
(in the bellows.)
DRIFT .049446
(DRIFT .039446   --This is the value for the North Hall OOPS)

(The beginning of the quad pipe.  This is the end of the <7")
(diameter region; the pipe inner diameter is <8".)
ELLIPTICAL-SLIT  1   8.62    3   8.62

DRIFT .048804

(O O P S    Q U A D R U P O L E)
(Model the OOPS quadrupole.  The total length is .6925 m.)
(The dipole/quad field ratio for the Feb. 1991 test run is)
(1.185027.)
(The dipole/quad field ratio for the OOPS design is 1.185972.)
(Note that this slightly changes the design field below to 5.05914.)
QUADRUPOLE .115417 5.063176 9.995
QUADRUPOLE .115417 5.063176 9.995
QUADRUPOLE .115417 5.063176 9.995
QUADRUPOLE .115417 5.063176 9.995
QUADRUPOLE .115417 5.063176 9.995
QUADRUPOLE .115417 5.063176 9.995

DRIFT .123635
```

```
(The end of the quad vacuum pipe)
ELLIPTICAL-SLIT 1 9.995 3 9.995

DRIFT .076215
(The front edge of the OOPS rear vacuum collimator)

(The lead plate number 6)
RECTANGULAR-SLIT 1  6.8707
RECTANGULAR-SLIT 3  11.430
DRIFT 0.04445

(The lead plate number 5)
RECTANGULAR-SLIT 1 6.4389
RECTANGULAR-SLIT 3 11.9253
DRIFT 0.04445

(The lead plate number 4)
RECTANGULAR-SLIT 1 6.0007
RECTANGULAR-SLIT 3 12.433
DRIFT 0.04445

(The lead plate number 3)
RECTANGULAR-SLIT 1 5.5753
RECTANGULAR-SLIT 3 12.9413
DRIFT 0.04445

(The lead plate number 2)
RECTANGULAR-SLIT 1 5.1943
```

```
RECTANGULAR-SLIT 3 13.4493
DRIFT 0.04445

(The lead plate number 1)
RECTANGULAR-SLIT 1 3.7503
RECTANGULAR-SLIT 3 12.9286
DRIFT 0.0381

(The back side of plate number 1)
RECTANGULAR-SLIT 1 3.7503
RECTANGULAR-SLIT 3 12.9286

(The rear window flange of the quad vacuum box extension)
DRIFT .052507
RECTANGULAR-SLIT 1  5.08
RECTANGULAR-SLIT 3 17.78

(O O P S    D E T E C T O R   S Y S T E M)
(Note that the HDCs for the North Hall are off center.  Future OOPS)
(modules will not be this way.)

DRIFT .050033
(The 1st HDC intersects the center of the focal plane)
RECTANGULAR-SLIT 1 6.5
RECTANGULAR-SLIT 3 14.0
(When we are reconstructing data or wish for some other reason to)
(save the standard focal plane variables, we must include a DETECTOR)
(card here)
```

```
(since this is normal position in z for the focal plane variables.)
DETECTOR 0.03 3. 0.03 3.

DRIFT .127
(The 2nd HDC)
RECTANGULAR-SLIT 1 7.0
RECTANGULAR-SLIT 3 15.5

DRIFT .127
(The 3rd HDC)
RECTANGULAR-SLIT 1 8.0
RECTANGULAR-SLIT 3 17.0

DRIFT .0753
(The 1st scintillator)
RECTANGULAR-SLIT 1 8.890
RECTANGULAR-SLIT 3 19.05

DRIFT .0508
(The 2nd scintillator)
RECTANGULAR-SLIT 1 8.890
RECTANGULAR-SLIT 3 19.05

DRIFT .0762
(The 3rd scintillator)
(The trigger requires that all three scintillators were hit.)
(Generally, we just check to see that the last scintillator was hit.)
RECTANGULAR-SLIT 1 8.890
```

```
RECTANGULAR-SLIT 3 19.05

(Put a detector card here to see if particles make it this far.)
(Call this the trigger.)
DETECTOR
(This is a TURTLE deck for Joe Mandeville's version of the program.)
(DESIGN-MOMENTUM 0.2691)
```

B.2 OHIPS TURTLE Model

```
(This is an OHIPS module deck which is presumably used as one)
(spectrometer in a coincident simulation.)
(It is in the HIGH RESOLUTION or NORMAL MODE, which is defined)
(by -Q +Q)
(The LOW RESOLUTION or HIGH THETA ACCEPTANCE mode is defined)
(by +Q -Q)

(This file is derived from the following sources:)
( 1: Thesis of Robert Steven Turley Feb 1984     )
( 2: A drawing file of Dave Costa depicting the design OHIPS)
(    detection system)
( 3: Dan Tiegers 1.77M OHIPS Turtle file         )

(Use second order optics and enforce apertures in the magnets.)
 SECOND    ON
 APERTURES ON

(Write the target coordinates to the output file.)
```

```
 DETECTOR

(Shift any target positions here.  E.g., shift y for an)
(offset beam spot.)
(SHIFT 0. 0. 0. 0. 0. 0.)

(first drift space)
(scattering chamber vacuum)
 DRIFT 0.254
(scattering chamber window  )
(     ---  mass [MeV], L/L_r)
(MULTIPLE-SCATTER 0. 0.9200 )



(spectrometer entrance window )
(MULTIPLE-SCATTER 938. 1.04E-3)
(vacuum to quads collimator --- Tieger collimator)
(DRIFT 1.311)
(vacuum to quads collimator --- Vellidis collimator)
(DRIFT 1.152)
 DRIFT 1.3153



(--- Front window ---)
(The vertical   acceptance is 17.46 cm.)
 RECTANGULAR-SLIT 1  8.65
(The horizontal acceptance is  7.62 cm.)
 RECTANGULAR-SLIT 3  3.75
```

```
(--- 19.255 cm thickness ---)
 DRIFT   0.19255
(--- Rear window ---)
(The vertical   acceptance is 19.70 cm.)
 RECTANGULAR-SLIT 1  10.0
(The horizontal acceptance is  9.84 cm.)
 RECTANGULAR-SLIT 3  4.3

 DETECTOR

( ---  O H I P S  F I R S T  Q U A D R U P O L E  --- )
(drift to the entrance of the first quad)
 DRIFT   0.2406
(vacuum pipe)
 ELLIPTICAL-SLIT  1.   13.97   3.   13.97
(negative field for "high resolution"  mode)
(---- NEG field for "normal"   mode)
(QUADRUPOLE 0.708 -1.65012 15.24)
(---- POS field for "reverse"  mode)
 QUADRUPOLE 0.708  1.86913 15.24


( ---  O H I P S  S E C O N D  Q U A D R U P O L E  --- )
(drift to the entrance of the second quad)
 DRIFT 0.1307
(vacuum pipe)
 ELLIPTICAL-SLIT  1.   13.97   3.   13.97
(positive field for "high resolution"  mode)
```

```
( ---- POS field for "normal"  mode)
(QUADRUPOLE 0.708  0.63626 15.24)
( ---- NEG field for "reverse"  mode)
 QUADRUPOLE 0.708 -1.80225 15.24

(vacuum pipe)
 ELLIPTICAL-SLIT  1.   13.97   3.   13.97

DRIFT 0.262175
(transition piece)
 RECTANGULAR-SLIT 1 20.32
 RECTANGULAR-SLIT 3 9.525



( ---  O H I P S  D I P O L E  --- )
(drift to the entrance of the dipole)
 DRIFT 0.2508
(vacuum pipe)
 RECTANGULAR-SLIT 1 21.2725
 RECTANGULAR-SLIT 3 9.6043
(Give the dipole vertical and horizontal width/2.)
(The subsequent slits are more restrictive, so these are)
(effectively ignored.)
 DIPOLE-APERTURE 20.32,9.6043
(See the TURTLE manual for fringe fields; this is unclamped)
(Rogowski.)
 FRINGE-FIELD 0.7,4.4
(dipole field)
```

```
 POLE-FACE-ROTATION 0.0
 DIPOLE     3.     3.5339  0.0
(vacuum pipe)
 RECTANGULAR-SLIT 1 20.32
 RECTANGULAR-SLIT 3 9.6043
(clamped Rogowski)
 FRINGE-FIELD 0.4,4.4
 DIPOLE     0.9898 3.5339  0.0
 POLE-FACE-ROTATION  0.0
(vacuum pipe)
 RECTANGULAR-SLIT 1 20.32
 RECTANGULAR-SLIT 3 9.6043

(Drift 1.626 m to the center of the focal plane)
(DRIFT 1.626)
 DRIFT 0.534
(vacuum pipe)
 RECTANGULAR-SLIT  1 38.1
 RECTANGULAR-SLIT  3 8.6
 DRIFT 0.457
(vacuum pipe)
 RECTANGULAR-SLIT  1 38.1
 RECTANGULAR-SLIT  3 15.3

(multiple scattering on exit)
(MULTIPLE-SCATTER 0. 0.9200 )

( ---  O H I P S  D E T E C T O R  S Y S T E M  --- )
```

```
(vdcx)
( Wire chamber --VDC 1-- Low momentum side )
 DRIFT  0.4106
 OFFSET-RECTANGULAR-SLIT 1    -21.0  1000
 RECTANGULAR-SLIT 3 8.89

( Wire chamber --VDC 2-- Low momentum side   )
 DRIFT 0.04625
 OFFSET-RECTANGULAR-SLIT 1    -33.5  1000
 RECTANGULAR-SLIT 3 15.0

(Center of focal plane:center of VDCX1)
 DRIFT 0.17828
 DETECTOR .03 3. .03 3.
(measurement errors: dx,dy = .03 cm ; dth,dph = 3 mr)

( Scintillator --S1-- Low momentum side  )
 DRIFT 0.03556
 OFFSET-RECTANGULAR-SLIT 1    -23.556  1000
 RECTANGULAR-SLIT 3 15.0

( Drift to the center of VDCX2)
DRIFT 0.121285

( Wire chamber --VDC 1-- High momentum side )
( No cut on y)
 DRIFT 0.0677
```

```
 OFFSET-RECTANGULAR-SLIT 1     -1000  22.45

(Drift to the center of S1)
DRIFT 0.026594

( Wire chamber --VDC 2-- High momentum side )
( No cut on y)
 DRIFT 0.2049
 OFFSET-RECTANGULAR-SLIT 1     -1000  29.92

( Scintillator --S1-- High momentum side )
 DRIFT 0.010668
 OFFSET-RECTANGULAR-SLIT 1     -1000  21.556

( Scintillator --S2--  )
 DRIFT 0.26703
 RECTANGULAR-SLIT 1 30.48
 RECTANGULAR-SLIT 3 10.16

( The Cerenkov detector )
 DRIFT 0.11270
 RECTANGULAR-SLIT 1 61.27750
 RECTANGULAR-SLIT 3 23.8125
 DRIFT 0.71999
 RECTANGULAR-SLIT 1 61.27750
 RECTANGULAR-SLIT 3 23.8125
 DRIFT 0.08573
 RECTANGULAR-SLIT 1 61.27750
```

```
 RECTANGULAR-SLIT 3 23.8125



( Scintillator --S3--  )
 DRIFT 0.13452
 RECTANGULAR-SLIT 1 38.56
 RECTANGULAR-SLIT 3 11.43

(Put a detector card here to see if particles make it this far.)
(Call this the trigger.)
 DETECTOR

( PbG )
( DRIFT 0.07810)
( RECTANGULAR-SLIT 1 36.67252)
(RECTANGULAR-SLIT 3 12.5)
( DRIFT 0.20955)
( RECTANGULAR-SLIT 1 36.67252)
( RECTANGULAR-SLIT 3 12.5)
```

Appendix C

Event Data Structure

This appendix describes the details of the event structures. Each event word has 16 bits, except for the scaler word, which is 24-bit long and occupies two 16-bit words. Event 5 is the scaler event. Event 8 is the coincidence event which has all the electron and proton tracking information. Event 10 contains all the beam information, like beam charge, helicity and positions. Event 13 monitors the cryogenic target temperatures and pressures.

C.1 Event 5 Data Structure

There were total 184 scalers in Event 5. Many of them were redundant, which provided self-consistent checks.

Table C.1: Event 5 Data Structure (continued on next page)

Scaler Index	Content	Scaler Index	Content
1	BT3 BIC	2	OOPS A S1L
3	OOPS A S1R	4	OOPS A S2L
5	OOPS A S2R	6	OOPS A S3L
7	OOPS A S3R	8	OOPS A S2LL
9	OOPS A S2RL	10	OOPS A S1L&S1R

Table C.2: Event 5 Data Structure (continued from previous page)

11	OOPS A S2L&S2R	12	OOPS A S3L&S3R
13	OOPS A PRESCALE	14	OOPS PRESCALE OR
15	OOPS RETIMING OR	16	OOPS LIVE
17	COMPUTER BUSY	18	OOPS B S1L
19	OOPS B S1R	20	OOPS B S2L
21	OOPS B S2R	22	OOPS B S3L
23	OOPS B S3R	24	OOPS B S2LL
25	OOPS B S2RL	26	OOPS B S1L&S1R
27	OOPS B S2L&S2R	28	OOPS B S3L&S3R
29	OOPS B PRESCALE	30	EVENT 5
31	UNUSED	32	CLOCK
33	OOPS TRIGGER	34	OOPS C S1L
35	OOPS C S1R	36	OOPS C S2L
37	OOPS C S2R	38	OOPS C S3L
39	OOPS C S3R	40	OOPS C S2LL
41	OOPS C S2LR	42	OOPS C S1L&S1R
43	OOPS C S2L&S2R	44	OOPS C S3L&S3R
45	OOPS C PRESCALE	46	OOPS A S1&S2&S3
47	OOPS A S1&S2	48	OOPS B S1&S2&S3
49	OOPS B S1&S2	50	OOPS C S1&S2&S3
51	OOPS C S1&S2	52	COINCIDENCE
53	OHIPS PILOT	54	OHIPS LIVE
55	OHIPS TRIGGER	56	FINAL TRIGGER
57	UNUSED	58	OOPS A 1XT
59	OOPS A 1XB	60	OOPS A 1YL
61	OOPS A 1YR	62	OOPS A 2XT
63	OOPS A 2XB	64	OOPS A 2YL
65	OOPS A 2YR	66	OOPS A 3XT
67	OOPS A 3XB	68	OOPS A 3YL
69	OOPS A 3YR	70	OOPS B 1XT
71	OOPS B 1XB	72	OOPS B 1YL
73	OOPS B 1YR	74	OOPS B 2XT
75	OOPS B 2XB	76	OOPS B 2YL
77	OOPS B 2YR	78	OOPS B 3XT
79	OOPS B 3XB	80	OOPS B 3YL
81	OOPS B 3YR	82	OOPS C 1XT
83	OOPS C 1XB	84	OOPS C 1YL

Table C.3: Event 5 Data Structure (continued from previous page)

85	OOPS C 1YR	86	OOPS C 2XT
87	OOPS C 2XB	88	OOPS C 2YL
89	OOPS C 2YR	90	OOPS C 3XT
91	OOPS C 3XB	92	OOPS C 3YL
93	OOPS C 3YR	94	CLOCK
95	OOPS A SINGLE W/ CB	96	OOPS SINGLE OR W/ CB
97	OOPS RETIMING OR W/ CB	98	OOPS LIVE W/ CB
99	COMPUTER BUSY (CB)	100	OOPS B SINGLE W/ CB
101	OOPS FINAL TRIGGER W/ CB	102	OOPS C SINGLE W/ CB
103	OOPS A FIRED W/ CB	104	OOPS B FIRED W/ CB
105	OOPS C FIRED W/CB	106	OHIPS PILOT
107	OHIPS PRESCALE	108	COINCIDENCE
109	OHIPS LIVE	110	OOPS A & OHIPS
111	OOPS B & OHIPS	112	OOPS C & OHIPS
113	UNUSED	114	UNUSED
115	UNUSED	116	UNUSED
117	UNUSED	118	OHIPS S1L PMT
119	OHIPS S1R PMT	120	OHIPS S2L PMT
121	OHIPS S2R PMT	122	OHIPS S3L PMT
123	OHIPS S3R PMT	124	OHIPS C1
125	OHIPS C2	126	OHIPS C3
127	PBG 1	128	PBG 2
129	PBG 3	130	PBG 4
131	PBG 5	132	PBG 6
133	PBG 7	134	PBG 8
135	PBG 9	136	PBG 10
137	PBG 11	138	PBG 12
139	PBG 13	140	PBG 14
141	OHIPS S1 MT	142	OHIPS S2 MT
143	OHIPS S3 MT	144	OHIPS FAST CLEAR
145	OHIPS READ	146	OHIPS TRIGGER
147	BLANK	148	2 MS
149	TRIGGER READ	150	TRIG 2 MS OR 1BB
151	OHIPS PILOT	152	H+
153	EVENT 5	154	BEAM BURST
155	BEAM BURST W/ CB	156	OOPS A PRESCALE & H-
157	OOPS B PRESCALE & H-	158	OOPS C PRESCALE & H-

Table C.4: Event 5 Data Structure (continued from previous page)

159	OHIPS PRESCALE & H-	160	OOPS PRESCALE OR & H-
161	COINCIDENCE & H-	162	OOPS LIVE & H-
163	OHIPS LIVE & H-	164	OOPS TRIGGER & H-
165	OHIPS TRIGGER & H-	166	MASTER TRIGGER & H-
167	OOPS A PRESCALE & H+	168	OOPS B PRESCALE & H+
169	OOPS C PRESCALE & H+	170	OHIPS PRESCALE & H+
171	OOPS PRESCALE OR & H+	172	COINCIDENCE & H+
173	OOPS LIVE & H+	174	OHIPS LIVE & H+
175	OOPS TRIGGER & H+	176	OHIPS TRIGGER & H+
177	MASTER TRIGGER & H+	178	OHIPS PILOT & H-
179	UNUSED	180	UNUSED
181	UNUSED	182	UNUSED
183	UNUSED	184	UNUSED

C.2 Event 8 Data Structure

Event 8 had variable length. It could be an OOPS or OHIPS single event, it could also be a coincidence event among OHIPS and more than one OOPS. The event type was determined by the latch word. The following table only lists the single coincidence event (only OHIPS and one OOPS fired) data structure. The OHIPS DCOS had variable word length, the maximum number of words was 60.

Table C.5: Event 8 Data Structure (continued on next page)

Word Number	Content
1	LATCH 1
2	DATA TYPE
3	OOPS LAM
4	OOPS SCINT ADC 1L
5	OOPS SCINT ADC 1R
6	OOPS SCINT ADC 2L
7	OOPS SCINT ADC 2R
8	OOPS SCINT ADC 3L
9	OOPS SCINT ADC 3R

Table C.6: Event 8 Data Structure (continued from previous page)

10	OOPS CHAMBER ADC 1Y O-E
11	OOPS CHAMBER ADC 1X O-E
12	OOPS CHAMBER ADC 2Y O-E
13	OOPS CHAMBER ADC 2X O-E
14	OOPS CHAMBER ADC 3Y O-E
15	OOPS CHAMBER ADC 3X O-E
16	OOPS SCINT TDC 1L
17	OOPS SCINT TDC 1R
18	OOPS SCINT TDC 2L
19	OOPS SCINT TDC 2R
20	OOPS SCINT TDC 3L
21	OOPS SCINT TDC 3R
22	OOPS SCINT TDC 2LL
23	OOPS SCINT TDC 2RL
24	OOPS CHAMBER TDC 1YL
25	OOPS CHAMBER TDC 1YR
26	OOPS CHAMBER TDC 1XT
27	OOPS CHAMBER TDC 1XB
28	OOPS CHAMBER TDC 2YL
29	OOPS CHAMBER TDC 2YR
30	OOPS CHAMBER TDC 2XT
31	OOPS CHAMBER TDC 2XB
32	OOPS CHAMBER TDC 3YL
33	OOPS CHAMBER TDC 3YR
34	OOPS CHAMBER TDC 3XT
35	OOPS CHAMBER TDC 3XB
36	FLAG
37	TOF TDC LAM
38	TOF TDC 1
39	TOF TDC 2
40	TOF TDC 3
41	TOF TDC 4
42	TOF TDC 5
43	TOF TDC 6
44	TOF TDC 7
45	TOF TDC 8
46	FLAG

Table C.7: Event 8 Data Structure (continued from previous page)

47	HELICITY WORD
48	LATCH 2
49	FLAG
50	FLAG
51	FLAG
52	OHIPS SCINT TDC LAM
53	OHIPS SCINT ADC 1L
54	OHIPS SCINT ADC 1R
55	OHIPS SCINT ADC 2L
56	OHIPS SCINT ADC 2R
57	OHIPS SCINT ADC 3L
58	OHIPS SCINT ADC 3R
59	OHIPS CHERENKOV ADC 1
60	OHIPS CHERENKOV ADC 2
61	OHIPS CHERENKOV ADC 3
62	OHIPS CHERENKOV ADC SUM
63	OHIPS LEAD GLASS SUM
64	OHIPS SCINT TDC 1L
65	OHIPS SCINT TDC 1R
66	OHIPS SCINT TDC 2L
67	OHIPS SCINT TDC 2R
68	OHIPS SCINT TDC 3L
69	OHIPS SCINT TDC 3R
70	OHIPS CHERENKOV TDC 1
71	OHIPS CHERENKOV TDC 2
72	OHIPS CHERENKOV TDC 3
73	OHIPS SCINT 2 MT TDC
74	DCOS LAM
75-134	DCOS WORDS

C.3 Event 10 Data Structure

Event 10 contains the beam information. Event 10 scalers were used to record the relevant triggering counts event by event, such as OOPS and OHIPS singles, prescales and coincidence etc.. These scalers were very helpful to debug hardware problems.

Table C.8: Event 10 structure. Word 13 to 23 are scalers.

Word Number	Content	Word Number	Content
1	Møller halo	13	OOPS A prescale
2	Target halo	14	OOPS B prescale
3	Time slot scaler	15	OOPS C prescale
4	Helicity word	16	OHIPS prescale
5	Cerenkov 1	17	OOPS prescale OR
6	Cerenkov 2	18	Coincidence
7	Beam toroid 1	19	OOPS live
8	Beam toroid 2	20	OHIPS live
9	Beam position 1X	21	OOPS trigger
10	Beam position 1Y	22	OHIPS trigger
11	Beam position 2X	23	Master trigger
12	Beam position 2Y		

C.4 Event 13 Data Structure

Table C.9: Event 13 structure

Word Number	Content	Word Number	Content
1-17	Date & time	37	Space
18	Space	38-43	RTS2
19-23	DP2	44	Space
24	Space	45-50	RTS3
25-29	HP2	51	Space
30	Space	52-57	RTS4
31-36	RTS1	58	Terminator($)

Appendix D

Design and Implementation of the Analyzer

The analyzer was written in C++, which is built on two class hierarchies: the Q record class and the event class. The class structures are shown in Figures D-1 and D-2.

The Q record class is used to read and decode experimental raw data from storage devices. It consists of Q record header (base class) and seven subclasses (derived classes). They are BOT (beginning of tape) record, BOR (beginning of run) record, DAT (data) record, EOR (end of run) record, EOT (end of tape) record, CMT (comment) record and ERR (error) record. BOT and EOT indicate the beginning and end of the Q tape, BOR and EOR indicate the beginning and end of a run, which contain the information about run number, run time. CMT record maintains all the comment inputs from the experimentalists during the on-line data acquisition, ERR record has the system error messages. Each class (base or derived) has its own data members and methods to manipulate the data members. The most important method is "void handle()", which handles and decodes the input data stream. The decoded raw data are passed to the corresponding event class for further processes.

The event class hierarchy is straight forward. From Event Header (the base class), four event classes are derived: Event 5, Event 8, Event 10 and Event 13. Event 8 class

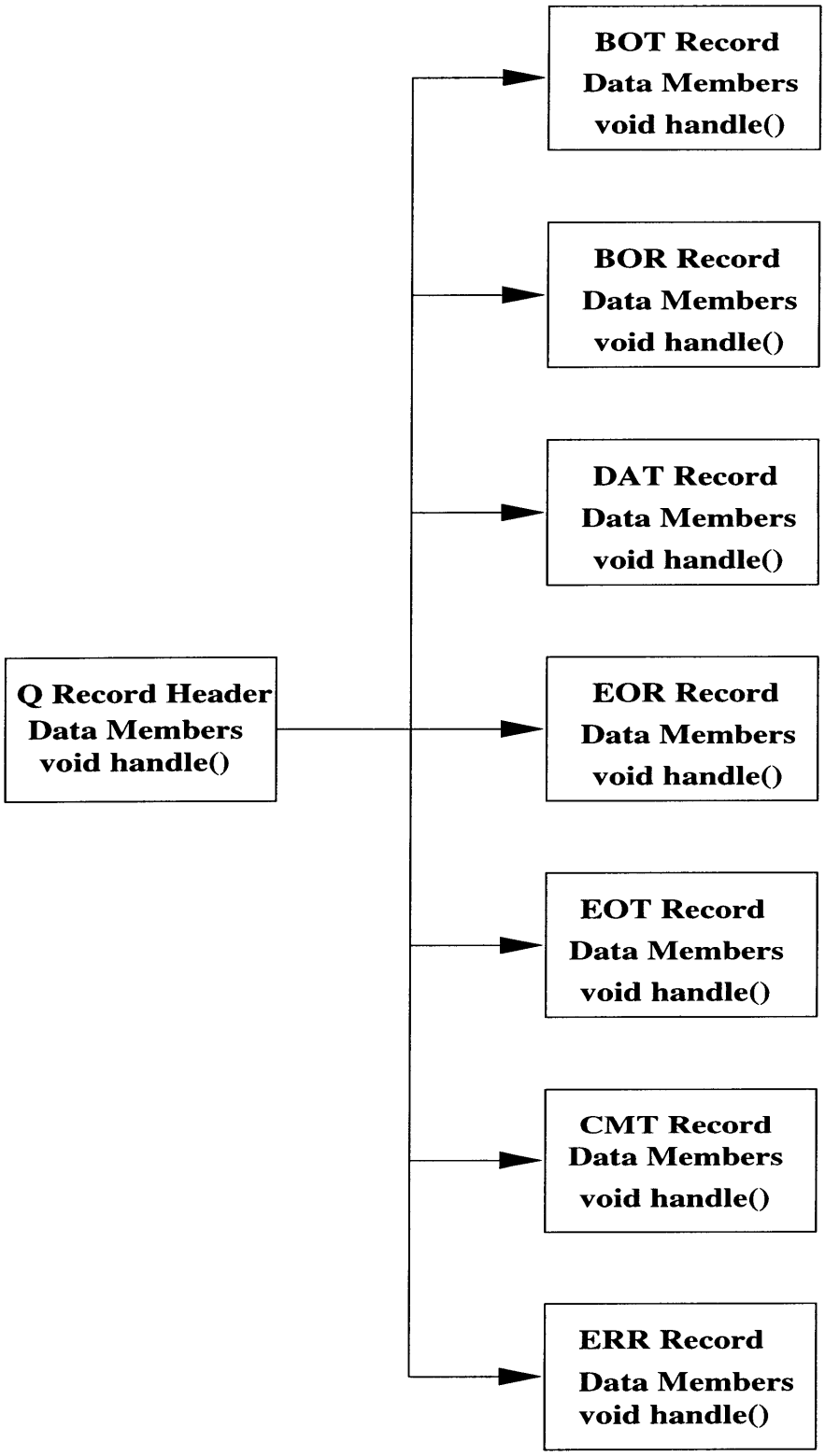

Figure D-1: Class hierarchy of Q record data structure.

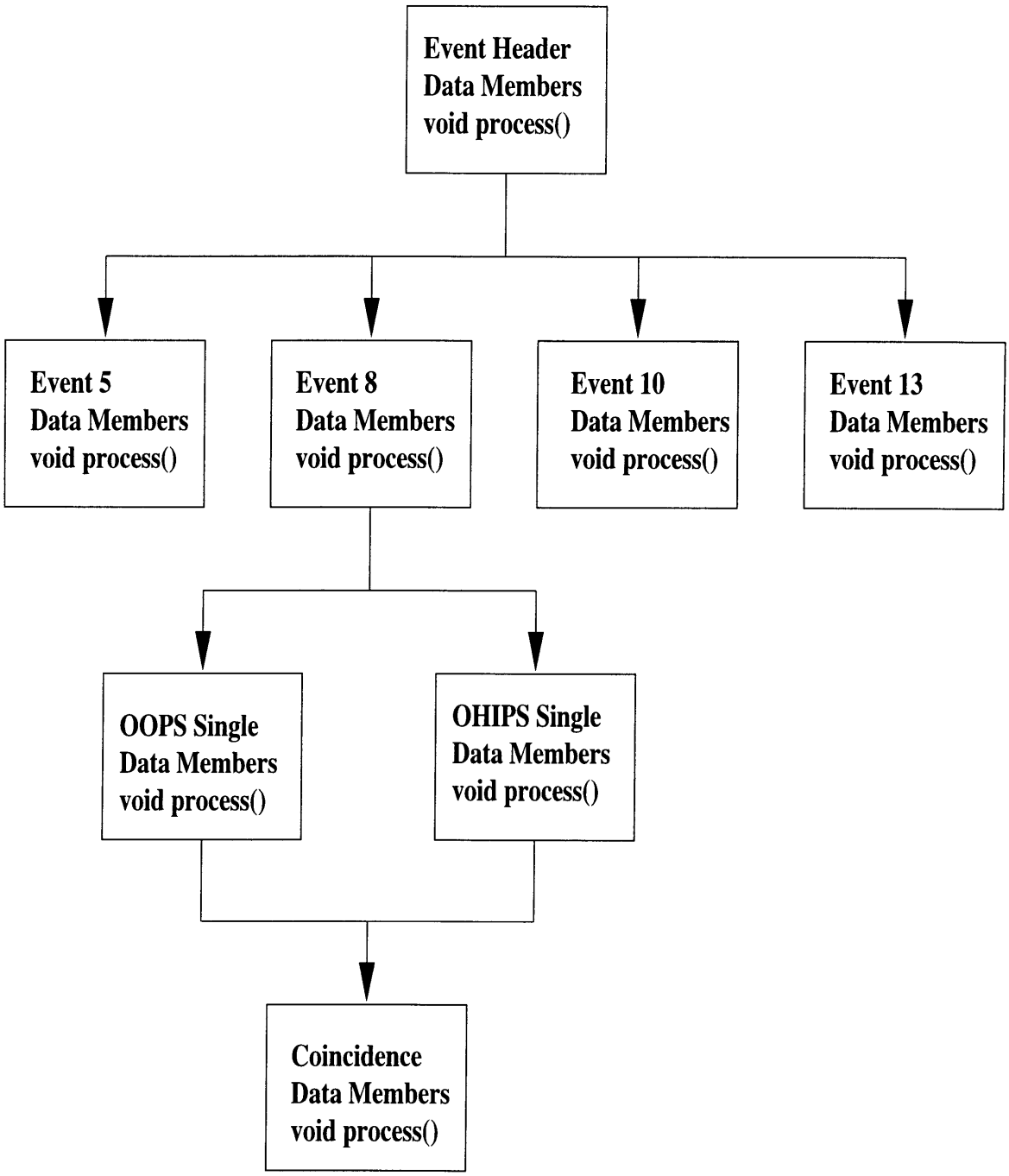

Figure D-2: Class hierarchy of event data structure.

contains the common data members for all the event 8's, from which OOPS single and OHIPS single event classes are derived. When OOPS single and OHIPS single are combined together, it constitutes a coincidence event. The multiple inheritance technique is used here. The data members in each class reflect the event data structures in Appendix C. The "virtual" method "void process()" has all the details about how to analyze each event, and is used in each event class to process data event by event, then write the analyzed data to a NTP file, also event by event.

The analyzer was developed on a Pentium PC running Red Hat Linux. The C++ complier used was gnu gcc, version 2.7.2.1.

Appendix E

OOPS Collaboration

R. Alarcon, J. Comfort, S. Dolfini, C. Mertz, A. Young

Arizona State University

M. Epstein, D. Margaziotis

California State University–LA

N. Kaloskamis, A. Karabarbounis, C. Papanicolas, C. Vellidis

University of Athens

W. Boeglin

Florida International University

A. Sarty

Florida State University

S. Williamson

University of Illinois

R. Hicks, X. Jiang, R. Miskimen, G. Peterson, J. Shaw

University of Massachusetts

A. Bernstein, W. Bertozzi, J. Chen, M. Distler, G. Dodson, K. Dow, M. Farkhondeh, S. Gilad, K. Joo, D. Jordan, S. Kowalski, C. Kunz, M. Pavan, D. Rowntree, S. Soong, D. Tieger, C. Tschalaer, W. Turchinetz, G. Warren, J. Zhao, Z.-L. Zhou

Massachusetts Institute of Technology

L. Weinstein

Old Dominion University

A. Hotta, H. Miyase, T. Miura, T. Suda, T. Tamae

Tohoku University

Bibliography

[1] I. The *et al.*, Phys. Rev. Lett. **67**, 173 (1991).

[2] TJNAF proposal E-94-018, E. J. Beise and S. Kox *et al.*, 1994.

[3] E. Passchier, Ph.D. Thesis, University of Utrecht, 1996 (unpublished).

[4] E. L. Tomusiak and H. Arenhövel, Phys. Lett. B **206**, 187 (1988).

[5] T. Eden *et al.*, Phys. Rev. **C50**, R1749 (1994).

[6] F. Klein *et al.*, Nucl. Phys. **A623**, 323c (1997).

[7] NIKHEF proposal 97-01, M. Ferro-Luzzi and J.F.J. van den Brand *et al.*, 1997.

[8] BALST proposal at the South Hall Ring of the MIT-Bates Linear Accelerator Center, 1991 (unpublished).

[9] TJNAF proposal E-93-026, D. Day *et al.*, 1993.

[10] R. W. Lourie *et el.*, IUCF Scientific abd Technical Report, 135 (1992-1993).

[11] B. D. MilBrath and J. I. McIntyre *et al.*, Phys. Rev. Lett. **80**, 452 (1998).

[12] K. Joo, Ph.D. thesis, MIT, 1997.

[13] G. A. Warren, Ph.D. thesis, MIT, 1997.

[14] Research Proposal to the Bates Linear Accelerator Center; *"A Program to Determine the Five Deuterium* $(\vec{e}, e'p)$ *Response Functions* $(f_L, f_T, f_{LT}, f_{TT}, f_{LT'})$*"*, 1989, Experiment #89–14.

[15] Research Proposal to the Bates Linear Accelerator Center; *"Measurement of the* $(\vec{e}, e'p)$ *Electrodisintegration of the Deuteron"*, 1989, Experiment #89–10.

[16] B. Frois and C. N. Papanicolas, Annual Review of Nuclear and Particle Science **37**, 133 (1987).

[17] A. S. Raskin and T. W. Donnelly, Ann. Phys. **169**, 247 (1986).

[18] A. S. Raskin and T. W. Donnelly, Ann. Phys. **191**, 78 (1989).

[19] W. Fabian and H. Arenhövel, Nucl. Phys. **A314**, 253 (1979).

[20] H. Arenhövel, Nucl. Phys. **A384**, 287 (1982).

[21] H. Arenhövel, W. Leidmann, and E. L. Tomusiak, Z. Phys. **A331**, 123 (1988).

[22] H. Arenhövel, W. Leidmann, and E. L. Tomusiak, Phys. Rev. C **46**, 455 (1992).

[23] G. Beck and H. Arenhövel, Few-body Systems **13**, 165 (1992).

[24] T. Wilbois, G. Beck and H. Arenhövel, Few-body Systems **15**, 39 (1993).

[25] F. Ritz, H. Göller, T. Wilbois and H. Arenhövel, Phys. Rev. C **55**, 2214 (1997).

[26] R. Machleidt *et al.*, Physics Reports **149**, 1 (1987).

[27] M. Lacombe *et al.*, Phys. Rev. C **21**, 861 (1980).

[28] B. Mosconi and P. Ricci, Nucl. Phys. **A517**, 483 (1990).

[29] J. M. Laget, Canadien Journal of Physics **62**, 1046 (1984).

[30] M. J. Zuilhof and J. A. Tjon, Phys. Rev. C **22**, 2369 (1980).

[31] S. Jeschonnek and T. W. Donnelly. Phys. Rev. C **57**, 2438 (1998).

[32] J. E. Amaro and T. W. Donnelly, Ann. Phys. **263**, 56 (1998).

[33] J. D. Bjorken and S. D. Drell, *Relativistic Quantum Mechanics*, McGraw-Hill, New York, 1964.

[34] H. Arenhövel, *Private communication*, 1996.

[35] C. N. Papanicolas *et al.*, Nucl. Phys. **A497**, 509c (1989).

[36] S. Gilad, W. Bertozzi and Z.-L. Zhou, Nucl. Phys. **A631**, 276c (1998).

[37] M. van der Schaar *et al.*, Phys. Rev. Lett. **66**, 2855 (1991).

[38] M. van der Schaar *et al.*, Phys. Rev. Lett. **68**, 776 (1992).

[39] F. Frommberger *et al.*, Phys. Lett. B **339**, 17 (1994).

[40] J. E. Ducret *et al.*, Phys. Rev. C **49**, 1783 (1994).

[41] D. Jordan, T. McIlvain *et al.*, Phys. Rev. Lett. **76**, 1579 (1996).

[42] E. Hummel and J. A. Tjon, Phys. Rev. C **42**, 423 (1990).

[43] J. A. Tjon, Few-body Systems Suppl. **5**, 17 (1992).

[44] E. Hummel and J. A. Tjon, Phys. Rev. C **49**, 21 (1994).

[45] B. Moscni, J. Pauschenwein and P. Ricci, Phys. Rev. C **48**, 332 (1993).

[46] W–J. Kasdorp, Phys. Lett. B **393**, 42 (1997).

[47] H. J. Bulten *et al.*, Phys. Rev. Lett. **74**, 4775 (1995).

[48] T. de Forest Jr., Nucl. Phys. A **392**, 232 (1983).

[49] A. Pellegrino *et al.*, Phys. Rev. Lett. **78**, 4011 (1997).

[50] S. M. Dolfini *et al.*, Phys. Rev. C **51**, 3479 (1995).

[51] C. Y. Prescott *et al.*, Phys. Lett. B **77**, 347 (1978).

[52] J. D. Jackson, *Classical Electrodynamics* (John Wiley & Sons, New York, 1975).

[53] M. Farkhondeh, G. Dodson, E. Ihloff and E. Tsentalovich, MIT-Bates polarized electron source, 1996(unpublished).

[54] D. V. Jordan, Ph.D. thesis, MIT, 1994.

[55] S. M. Dolfini, Ph.D. thesis, University of Illinois at Urbana-Champaign, 1994.

[56] C. F. Mertz, Ph.D. thesis, Arizona State University, 1998.

[57] The CRC Handbook of Chemistry and Physics, 72^{nd} Ed., 1991–1992.

[58] Chelton and Mann, Cryogenic Data Book, WADC Technical Report 59–8.

[59] S. M. Dolfini *et al.*, Nucl. Inst. Meth. A **344**, 571 (1994).

[60] J. Mandeville *et al.*, Nucl. Inst. Meth. A **344**, 583 (1994).

[61] Alain Young, Ph.D. thesis, Arizona State University (in preparation).

[62] D. Jordan *et al.*, Internal report, Bates Linear Accelerator Center (unpublished).

[63] L. G. Atencio, J. F. Amann, R. L. Boudrie, and C. L. Morris, Nucl. Inst. Meth. **187**, 381 (1981).

[64] A. H. Walenta, Nucl. Inst. Meth. **151**, 461 (1978).

[65] G. MP-1, *Introduction to Q*, Los Alamos Meson Physics Facility, 1985, document No. MP-1-3401-3.

[66] J. Arrington *et al.*, Nucl. Inst. Meth. A **311**, 39 (1992).

[67] Jiang Chen, Ph.D. thesis, MIT (in preparation).

[68] Xiaodong Jiang, Ph.D. thesis, University of Massachusetts at Amherst, 1998.

[69] J. B. Mandeville, Ph.D. thesis, University of Illinois at Urbana-Champaign, 1993.

[70] Michael Distler, *Private Communication*, 1998.

[71] W. R. Leo, *Techniques for Nuclear and Particle Experiments*, 2nd Ed., Springer-Verlag, 1994,

[72] D. C. Carey, *TURTLE (Trace Unlimited Rays Through Lumped Elements): A Computer Program For Simulating Charged Particle Beam Transport Systems*, Fermilab National Accelerator Laboratory, 1978, NAL–64.

[73] F. B. Mandeville and C. Vellidis, *Manual of the program TURTLE–JBM*, 1998 (unpublished).

[74] C. Vellidis, *AEEXB:A program for Monte Carlo simulations of coincidence electron scattering experiments*, 1998 (unpublished).

[75] R. D. Evans, *The Atomic Nucleus*, McGraw-Hill, New York, 1955.

[76] J. Schwinger, Phys. Rev. **76**, 760 (1949).

[77] S. Penner, Nuclear Structure Physics, Proceedings of the 18^{th} Scottish Univ. Summer School in Physics, 1977.

[78] L. W. Mo and Y. S. Tsai, Reviews of Modern Physics **41**, 205 (1969).

[79] J. Friedrich, Nucl. Inst. Meth. **129**, 505 (1975).

[80] Y. S. Tsai, Review of Modern Physics **46**, 815 (1974).

[81] E. Borie and D. Drechsel, Nuclear Physics **A167**, 369 (1971).

[82] G. G. Simon *et al.*, Nuclear Physics **A333**, 381 (1980).

[83] K. A. Dow and M. Farkhondeh, *Magnetic Measurements of the Extraction Line and Energy Compression System Dipoles*, Bates/SHR 92-07, 1992 (unpublished).

[84] T. Zwart *et al.*, Nucl. Inst. Meth. **A384**, 299 (1997).

[85] B. A. Mueller, Ph.D. thesis, California Institute of Technology, 1997.

[86] Research Proposal to the Bates Linear Accelerator Center; *"Measurement of the Quadrupole Contribution to the $N \rightarrow \Delta$ Excitation"*, 1987, Experiment #87–09.

[87] Update of Experiment 89-14 to the Bates PAC Meeting, April 2-5, 1997.

[88] Update of Experiment 89-10 to the Bates PAC Meeting, April 2-5, 1997.

[89] Update of Experiment 87-09 to the Bates PAC Meeting, April 2-5, 1997.

[90] Research Proposal to the Bates Linear Accelerator Center; *"Measurement of the quadrupole contribution to the $N \rightarrow \Delta$ excitation through the $H(\vec{e}, e'p)\gamma$ reaction"*, 1997, Experiment #97–05.

[91] Research Proposal to the Bates Linear Accelerator Center; *"Extending the Bates study of the $\gamma^* N \rightarrow \Delta$ transition to the $p(e, e')X$ and $p(e, e'\pi^+)n$ reactions"*, 1997, Experiment #97–04.

[92] Research Proposal to the Bates Linear Accelerator Center; *"Virtual Compton scattering on the proton below pion threshold"*, 1997, Experiment #97–03.

[93] Research Proposal to the Bates Linear Accelerator Center; *"Measurement of A_x and A_z asymmetries in the quasielastic $^3\vec{H}e(\vec{e}, e'd)p$ reaction"*, 1997, Experiment #97–06.

[94] Research Proposal to the Bates Linear Accelerator Center; *"Study of the reaction mechanism in $^4He(e, e'p)^3H$ via a measurement of the response functions R_{TT}, R_{LT} and $R_{LT'}$ with OOPS"*, 1997, Experiment #97–01.